UNIVERSIDADE DE LISBOA
INSTITUTO SUPERIOR TÉCNICO

Development of a Directionality Detector and Radiation Hardness Assurance for RADEM, the ESA JUICE mission Radiation Monitor

Marco Gui Alves Pinto

Supervisor: Doctor Patrícia Carla Serrano Gonçalves

Thesis approved in public session to obtain the PhD Degree in
Technological Physics Engineering

Jury final classification: Pass with Distinction and Honour

2019

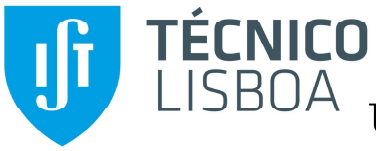

UNIVERSIDADE DE LISBOA
INSTITUTO SUPERIOR TÉCNICO

Development of a Directionality Detector and Radiation Hardness Assurance for RADEM, the ESA JUICE mission Radiation Monitor

Marco Gui Alves Pinto

Supervisor: Doctor Patrícia Carla Serrano Gonçalves

Thesis approved in public session to obtain the PhD Degree in
Technological Physics Engineering

Jury final classification: Pass with Distinction and Honour

Jury

Chairperson: Doctor Mário João Martins Pimenta, Instituto Superior Técnico, Universidade de Lisboa

Members of the Committee:

Doctor Pedro Miguel Félix Brogueira, Instituto Superior Técnico, Universidade de Lisboa

Doctor Ana Luísa Monteiro da Silva, Universidade de Aveiro

Doctor Patrícia Carla Serrano Gonçalves, Instituto Superior Técnico, Universidade de Lisboa

Doctor Wojciech Hajdas, Paul Scherrer Institute

Doctor Christian Poivey, European Space Agency

2019

Resumo

A "Exploradora das Luas Geladas de Júpiter", JUICE, é a próxima missão de classe L da Agência Espacial Europeia (ESA) ao sistema Joviano. Vai orbitar Júpiter e três das suas luas, Europa, Calisto e Ganimedes enfrentando um ambiente de radiação altamente variável e intenso, com uma grande população de electrões de energias elevadas, que podem levar à acumulação de doses de radiação ionizante significativas induzindo falhas no funcionamento de instrumentos. A maior parte das missões que visitaram este planeta, fizeram-no por curtos períodos de tempo, usando-o para manobras assistidas por gravidade no seu caminho para o sistema solar exterior. As únicas excepções até agora foram a missão Galileo e mais recentemente a missão Juno, ambas da NASA. O ambiente de radiação em Júpiter apenas foi medido durante um longo período de tempo pelo "Detector de Partículas Energético", EPD, a bordo da nave Galileo. A missão Juno não inclui nenhum monitor de radiação.

A missão JUICE incorporará o "Monitor de Electrões Resistente a Radiação", RADEM, que tem estado a ser desenvolvido no âmbito desta tese. O RADEM é um instrumento de baixa massa e baixa potência que contém quatro detectores: um detector de electrões; um detector de protões; um detector de iões pesados; e um detector de direcionalidade. Os três primeiros vão medir o espectro de energias da população de electrões, (Detector de Stack de Electrões - EDH), protões (Detector de Stack de Protões - PDH) e iões ((Detector de Stack de Iões - HIDH)). Estes são baseados em detetores de "stack" de Sílicio padrão adaptados para as energias das partículas existentes em Júpiter. Para complementar estes detetores, o Detector de Direcionalidade (DDH) vai medir a dependência angular dos fluxos de electrões existentes em Júpiter, permitindo assim evitar que se subestimem ou sobrestimem as doses de radiação durante a missão assim como melhorar os modelos do ambiente de radiação do sistema Joviano, com base nos dados da missão JUICE.

Nesta tese foram analisados quase todos os aspectos do processo de "Radiation Hardness Assurance" do RADEM. A tese envolveu o desenvolvimento do Detector de Direcionalidade, incluíndo a sua caracterização e testes em feixe, que permitirá especificar modelos de radiação mais precisos para futuras missões. Também envolveu a análise de radiação e optimização da blindagem do RADEM à radiação, da qual resultou a criação de um programa "open-source", GUIMesh, que permite converter geometrias STEP em GDML, um formato compatível com Geant4. As aplicações deste programa extendem-se à física nuclear, física de partículas e física médica.

No âmbito desta tese, também foi realizada a verificação da validade dos testes de ^{60}Co para componentes electrónicos utilizados em Júpiter. Estes testes mostraram que os efeitos do ^{60}Co em tecnologias de semicondutores usadas em aplicações espaciais são equivalentes aos efeitos de feixes de electrões com energias de 12 e 20 MeV de intensidades comparáveis. As implicações deste estudo na missão JUICE são são de extrema importância pois permitem manter as margens de radiação estabelecidas para a missão, evitando aumentar a quantidade de material (blindagem) e limitando a dose de radiação até à qual os testes de componentes são efectuados.

Palavras-chave: Jupiter, JUICE, ambiente de radiação, RADEM, Detectores de Partículas, Efeitos da radiação, Protecção radiológica, Componentes Electrónicos, Simulação de Monte Carlo, Geant4, GUIMesh, Detector de Direccionalidade, electrões.

Abstract

The JUpiter ICy moons Explorer (JUICE), ESAs next L-class mission to the Jovian system, will orbit the Jovian system for 3.5 years and study three of its moons, Europa, Callisto and Ganymede. It will face a highly variable and hazardous radiation environment, composed of a large electron population with energies much higher than those found in the Van Allen belts, that can lead to high cumulative ionizing doses in Electric, Electronic and Electromechanical (EEE) components and eventually cause instruments malfunction. The environment is related to the large complex magnetosphere of Jupiter, far extending into the orbit of Saturn.

The majority of missions that visited the planet, have done so briefly, using it for gravity assist maneuvers in their way to the outer solar system. The only exceptions so far were the Galileo spacecraft, and most recently the Juno mission both by NASA. Long-term observation of the radiation environment in Jupiter has been done mostly by the Energetic Particle Detector (EPD) in the Galileo spacecraft. Juno does not have any radiation monitor.

JUICE will carry the Radiation Hard Electron Monitor (RADEM) which is currently under development and is the main focus of this thesis. RADEM is a low power, low mass instrument that has four detectors: the Electron Detector Head; the Proton Detector Head; the Ion Detector Head; and the Directionality Detector Head. The first three will perform spectral measurements of the electron, proton and to some extent ion populations. They are all based on standard silicon stack detectors space technologies, extended to the higher particle energies. To complement these detectors, the Directionality Detector will measure the electron flux angular variability known to exist in Jupiter, avoiding in-situ under or over-estimation of radiation doses as well contributing to the development of radiation environment models based on JUICE mission data.

In this thesis, most aspects of the Radiation Hardness Assurance for RADEM were addressed. It covers the full development of the Directional Detector, including Geant4 simulations and beam tests, to optimize its design and to verify its performance. It also covers the radiation analysis and shielding optimization of RADEM, which resulted in the creation of the first open-source software, GUIMesh, to convert STEP geometries to GDML, a Geant4 readable format. This tool can also be used in a broad range of applications such as medical, nuclear and high energy physics.

The verification of ^{60}Co testing representativeness for EEE components flown to Jupiter was also assessed in the framework of this thesis. It was proved that ^{60}Co has similar effects on common semiconductor technologies used in space applications, as 12 and 20 MeV electrons of equivalent intensity. This result had major implications for the JUICE mission since it allowed to maintain the mission Radiation Design Margins and avoid over-testing and/or over-shielding.

Keywords: Jupiter, JUICE, Radiation environment, RADEM, Particle Detectors, Radiation Effects, EEE components, Radiation Hardness Assurance Monte Carlo simulations, Geant4, GUIMesh, Directionality Detector.

Acknowledgements

I would like to thank my supervisor Patrícia Gonçalves for all the teaching and opportunities. You helped me grow both as a scientist and as person during this PhD. I know I will carry your lessons in the future.

Thank you also to Pedro Assis for being as close to a co-supervisor as one can be. Your help was valuable for several aspects of this thesis as well as for personal growth.

I would also like to thank everyone of the Space Radiation Environment and Effects group at LIP for all the help and friendship, especially to Luísa Arruda for reviewing this thesis, Ana Luísa Casimiro for the support, and Jorge Sampaio for the fruitful discussions.

I extend these thanks to all the LIP personal namely, everyone in the ECRLAB and the Computing group. Special thanks to Miguel Ferreira, Zé Carlos, João Pina, João Paulo, Mário David and Nuno for all the help, as well as Natalia Antunes and João Pedro Santos for all the availability, comprehension and help. There are many others, Ruben Conceição, Liliana Apolinário, Bernardo Tomé but the list would just go on and on.

A special message to Gersende Prior that received me at LIP with open arms and introduced me to everyone. You were a big part in my growth and I am sure that my work ethic and my enthusiasm are at least in part thanks to you. Thank you for all the fish!

Thank you to all the students I have met in LIP over the years. To the first ones Márcia, João Espadanal, Ricardo Luz, Ana Sofia Inácio, Stefan Nae, Lia and Rute, thank you for introducing me to LIP and for welcoming me whole-heartadely. To the last ones, especially Ana Luísa Carvalho, Diogo Bastos, Ricardo Barrué and Júlia Silva thank you for handling for supporting me all the way.

A special thanks is also due to everyone at the Paul Scherrer Institute, especially Wojciech for taking care of everything that was needed during all of my stays, but also to Radek, Hualin, Patryk and Alankrita for all the help and friendship. It was incredible to learn with and about all of you.

From EFACEC my thanks go to Arlindo Marques for being available to help and clarify any doubts and for reviewing part of this thesis.

Many thanks also to everyone in the facilities used during the ECo60 test campaigns. This extends to Paula Matos from CTN to Alessandra Costantino, Michele Muschitiello and Christian Poivey from ESA/ESTEC. To the latter I also thank for being always available to help in other parts of my work.

To all my friends from Fadjojah city, you were all incredible during all these years. Thanks for all the support and for all the fun.

Thank you to both my parents and sister for enduring this struggle with me. You are and will always be the ones responsible for the person I have become and for how I handle all adversities that came my way.

Last but definitively not least, thank you Mariana Baptista. Thank you for being there every step of the way. Thank you for being my partner in crime and thank you for going through all of this with me. We will always have Llamas and Hawaii.

Contents

List of Figures

List of Tables

1 Introduction

Space is a fundamental part of modern society. Even though users might be unaware, multiple applications ranging from communication to navigation as well as to some fields of scientific research such as Earth Observation, are only possible due to the existence of man-made satellites orbiting Earth. However, technological (and biological) systems face several challenges in space. A combination of large temperature modulation, low pressure and a harsh radiation environment, makes it extremely hard to operate instruments continuously and without failure during their full life cycle. Radiation in particular can speed-up the degradation of Electric, Electronic and Electromechanical (EEE) components and materials [1][2][3][4][5], or lead to partial or complete failure of instruments, rendering a spacecraft inoperable [6][7]. Radiation is also a broad research topic in the scientific community, since both its origins, the Sun and other cosmic sources, and its modulation, influenced by the solar cycle and the magnetic fields of several bodies of the solar system, are still not fully understood.

The radiation environment in space can be branched into three components: Galactic Cosmic Rays (GCR), very energetic charged particles coming from outside the Solar System; Solar Energetic Particles (SEP), charged particles released from the Sun associated with Solar Flares (SF) or Coronal Mass Ejections (CME); and Trapped Particles (TP), charged particles trapped in cyclical motion in planetary magnetospheres [8]. While GCR and SEP are present across the entire Solar System with intensities and energy spectra modulated by the solar activity, trapped particles exist only around planetary bodies with magnetospheres such as the Earth or Jupiter. The presence of the Van Allen radiation belts surrounding the Earth, has been known since 1958 [9]. They consist mostly of protons between 100 keV to a few hundreds of MeV and electrons from tens of keV to 10 MeV. Protons with energies above 10 MeV are located mostly below 20000 Km, while the lowest energy protons can reach geosynchronous orbit, as it can be seen in Figure 1.1 (left side). For electrons, two different regions can be identified: the inner belt, populated by the higher energy electrons, and the outer belt, populated mostly by lower energy particles as show in the right side of Figure 1.1. A slot region between the two belts, where electron intensity is lower can also be identified [10][11].

While the Earth radiation environment has been studied extensively, the same is not true for the Jovian system. So far only the Galileo mission [13] and more recently the ongoing Juno [14] mission have been launched specifically to study the gas giant. Other

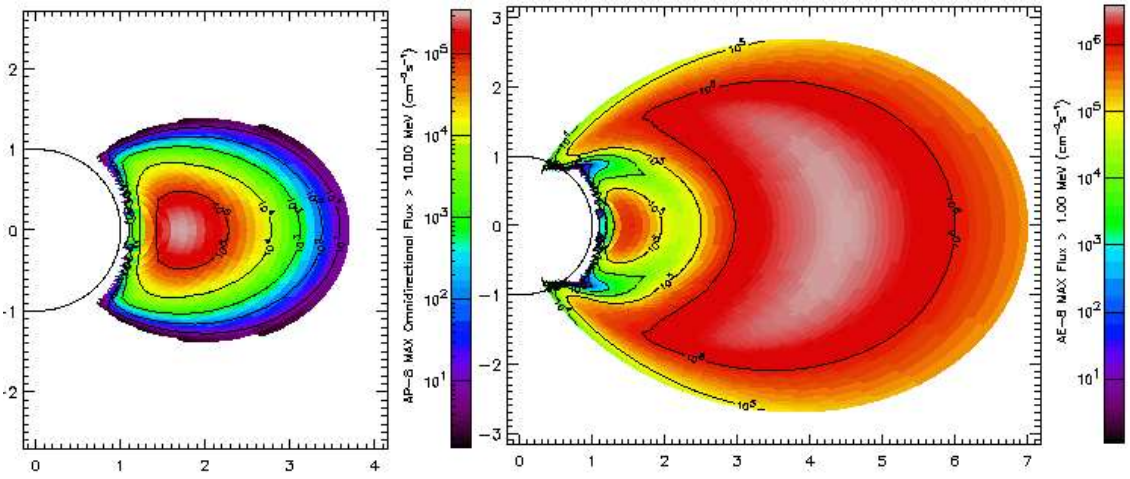

Figure 1.1: Proton (left) and electron (right) intensity according to the AP8 [10] (left) and AE8 [11] (right) models as a function of Earth radii for energies above 10 MeV and 1 MeV respectively. Credit: [12]

missions to the outer solar system such as the Pioneers [15][16], Voyagers [17], Ulysses [18], and others, had rendez-vous with the planet, the Juno mission does not carry any instruments capable of detailed radiation analysis, which means the Galileo spacecraft and its Energetic Particle Detector (EPD) has been the only source of long term data acquisition, regarding the radiation environment on Jupiter [13][19]. The EPD confirmed that the majority of the particle population on the Jovian system are electrons with energies much higher than those found on Earth's magnetosphere, with significant fluxes at energies higher than 10 MeV. This is mainly due Jupiter's magnetic field, which is much stronger than the Earth's and extends much further away from the planet with the magnetic tail reaching Saturn's orbit, trapping high energy particles [20].

1.1 Motivation

ESA's next class-L mission to the Jovian system, the Jupiter ICy moons Explorer (JUICE), will study the gas giant and three of its Galilean moons, Europa, Callisto and Ganymede for 3.5 years. It will orbit the gas giant and perform several fly-bys of Europa and Callisto before finally orbiting Ganymede at different altitudes [20].

1.1.1 Measuring Jupiter's Radiation Environment

The mission will carry the Radiation Hard Electron Monitor (RADEM) [21][22], to measure electron, protons and to some extent, ions. The instrument must be able to handle the high particle flux environment, up to $2 * 10^9$ particles/cm^2/s, and a large range of particle energies, 300 keV to 40 MeV electrons, and 5 MeV to 250 MeV protons, while complying with low power and low mass restrictions. RADEM has four detector heads: the Electron Detector Head (EDH) and the Proton Detector Head (PDH) which will perform

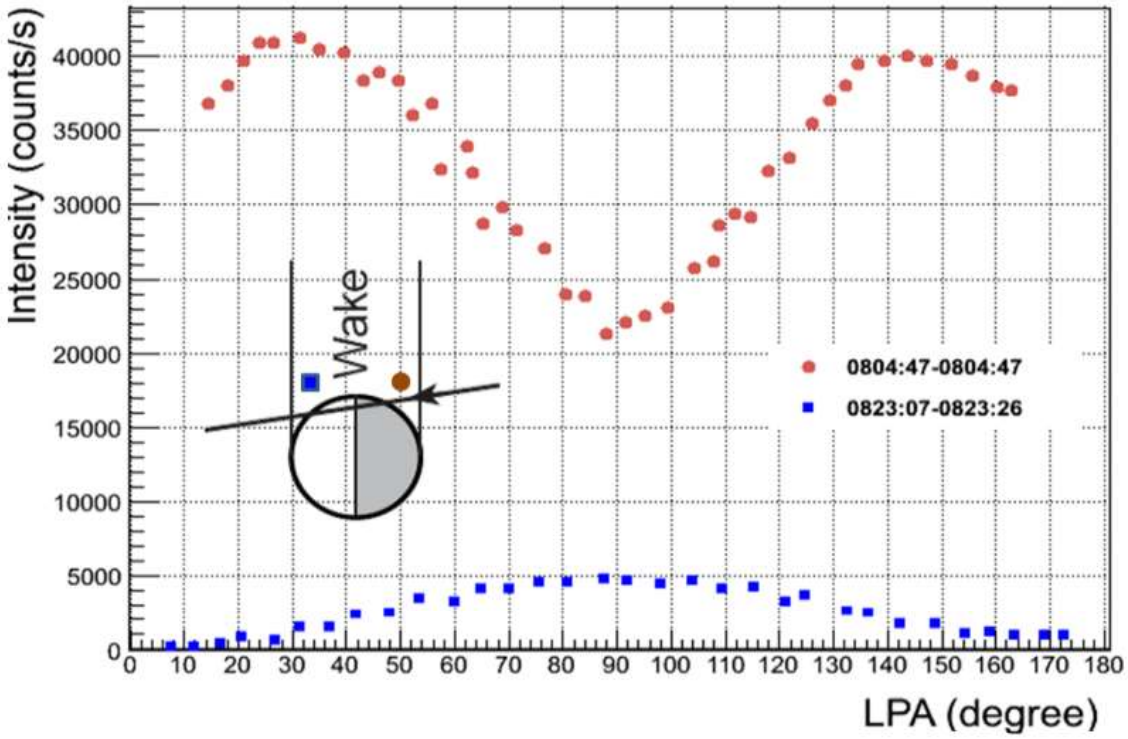

Figure 1.2: Flux angular variability as measured by the Galileo spacecraft at two different times, and therefore locations, of the Jovian system [25].

spectral analysis of electrons and protons respectively, the Ion Detector Head (IDH) which will measure and separate ions species up to Z=8, and the Directional Detector Head (DDH) which will measure the electron flux angular variability. The first three are based on the commonly used Silicon stack detectors concept present in the Standard Radiation Environment Monitor (SREM) [23] and Multi-Function Spectrometer (MFS) [24], adapted for the Jovian system particle energy ranges. The energy range of RADEMs detector heads surpasses that of the EPD carried by the Galileo mission, which was sensitive to electrons up to 11 MeV and protons up to 55 MeV [13]. The DDH on the other hand is a novel detector, necessary because of the flux angular variability measured by the EPD [25] as shown in Figure 1.2. The EPD itself was mounted on a rotational test-bed which allowed to perform angular analysis of the incoming particle flux. This method however, requires a large amount of mass, which is not allocated to RADEM. Therefore the best available option was to include a directionality detector.

1.1.2 Radiation Effects on EEE components

The harsh radiation environment of the Jovian system also constraints the EEE components used in the instruments aboard the JUICE mission, including RADEM. Degradation of semiconductors due to radiation is a known issue, which affects all spacecrafts and that must be considered from the early stages of their design. Radiation damage to EEE components can be branched into two categories: Cumulative and Single Event Effects (SEE).

Cumulative effects occur when the interaction of particles with the semiconductor material creates electron-hole pairs that do not re-combine due to the electric field within the device, and that become trapped in specific regions of a component (Ionizing radiation), or when it changes the location of an atom in the device lattice (non-Ionizing radiation). In space, these effects, which are mainly caused by electrons and protons, accelerate the aging of the components as a function of the Total Ionizing Dose (TID) and Total Non-Ionizing Dose (TNID) respectively. Single particles can also cause malfunction of components. SEEs occur when a single particle (usually a Galactic Cosmic Ray (GCR) ion though proton or even an electron induced SEE are possible) deposits enough energy on the sensitive part of a device causing a functional fault. SEEs can be either transient - the system recovers after charge collection - or persistent, some action must be taken in order to recover device operation. The latter can be catastrophic and lead to the destruction of the component and even of the system in which it is embedded [1][2][3][4][5][6][7].

To minimize the risk of mission failure, a thorough methodology called Radiation Hardness Assurance (RHA) must be followed. For this purpose, European missions follow the European Cooperation for Space Standardization (ECSS) norms [26]. Standards cover all aspects of RHA, from environment predictions, to dose and SEE rate calculation, and component selection and testing. Though these standards exist for interplanetary missions, the JUICE mission will be inside the Jovian magnetosphere exposed to its high energy high flux electron environment, which means that it is necessary to review existing methods of RHA. For instance, TID test standards refer to ^{60}Co as the ideal test source because it has been shown empirically that it gives the worst-case degradation for a given dose in comparison with the particles that compose the space radiation environment around the Earth. Damage to EEE components from this radiation has already been shown to be conservative when compared to the one induced in Earth orbit by radiation in the Van Allen belts [2]. In the Jovian environment however, electron fluxes are still significant at energies greater than 10 MeV, when compared with Earth's orbit as shown in Figure 1.3 [25]. At these energies, there has been some evidence that ^{60}Co might not lead to the worst-case degradation of components.

Careful consideration must also be taken when computing doses at component level. While both Sectorial Analysis and Monte-Carlo methods can be used, the former method is faster but over-estimates the dose, and consequently the increases shielding requirements, increasing the mass budget of instruments and of the spacecraft. This is especially true for electrons with energies found in Jupiter, which produce Bremsstrahlung radiation in the spacecraft materials, since the method simply estimates the amount of material that particles coming from a given direction must cross and not how they interact with the material or what secondaries they produce. Monte Carlo methods are more time consuming but are much more precise, since the physics processes involved in radiation interaction with matter are taken into account. This results in the reduction of the mass budget by considerable margins. TNID from electrons must also be considered in dose computations for the JUICE mission since, despite their low Non-Ionizing Energy Loss

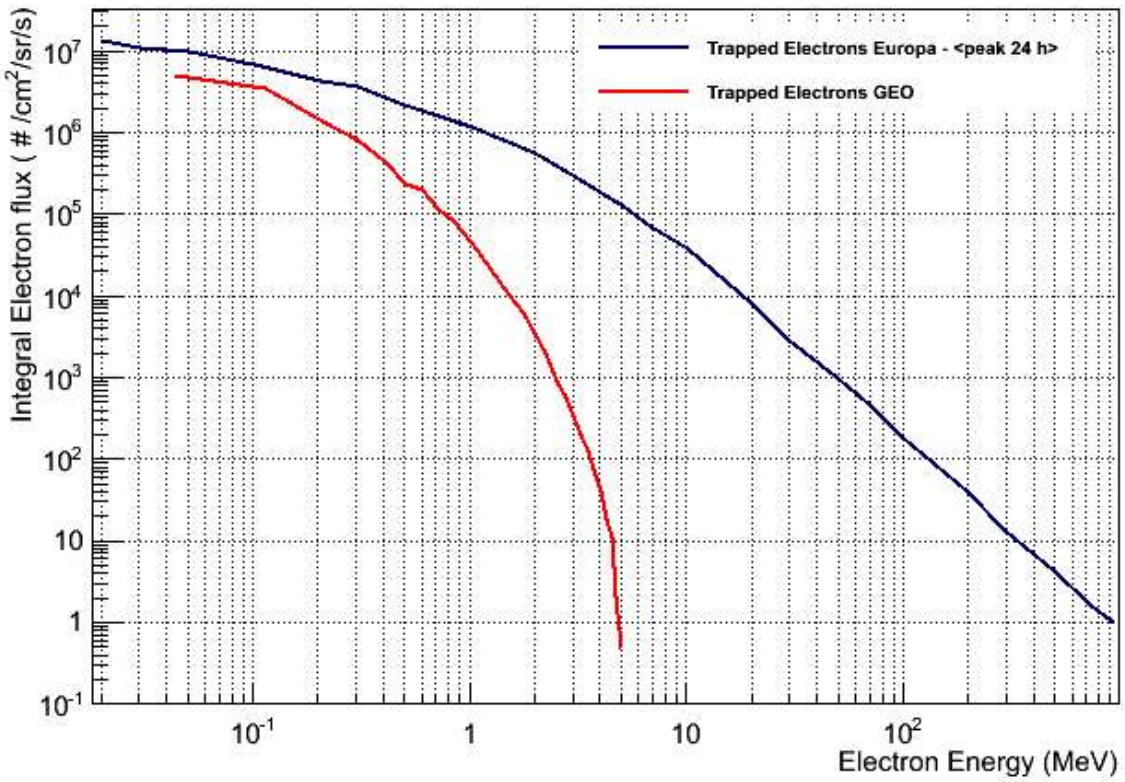

Figure 1.3: Comparison between electron fluxes in Europa <peak 24h> and Earth Geosynchronous orbit. Adapted from [25].

(NIEL), when compared to protons and neutrons, the fluxes at high energies are large enough that their contribution is non-negligible [27][28][29].

1.2 Objectives

The main objects of study in this thesis are the JUICE mission radiation monitor, RADEM and its Directionality Detector, DDH. RADEM performance depends on its detectors capability to measure radiation, with the DDH playing an essential role in the instrument, and the reliability of its EEE components when subjected to the harsh radiation environment around Jupiter.

1.2.1 Development of a Directionality Detector for RADEM

The DDH is a novel design developed in the context of this thesis for RADEM. The detector was designed to be a low power, low mass detector, capable of measuring the electron flux angular variability. Though the DDH concept does not allow for spectral analysis, it is able of performing flux angular measurements in a Field-Of-View (FOV) close to 2π sr (half the sky). In this thesis, the following activities concerning the DDH development will be discussed:

- Optimization of the DDH design concept, geometry and materials, using the Geant4 [30][31][32] simulation toolkit;
- Characterization of the response of the DDH, when subject to the Jovian system different space weather conditions and to the cruise phase radiation environment;
- Validation of DDH readout, the novel ASIC VATA466 [22], developed by IDEAS specifically for RADEM;
- Participation in the testing and calibration of RADEM Engineering Model (EM).

1.2.2 RADEM Radiation Hardness Assurance

RHA of RADEM must ensure instrument full operation during the whole mission. It requires dose level calculation for components, shielding optimization and testing of components not qualified for space. RADEM location in the JUICE spacecraft provides little shielding to the instrument, which means that a lot of effort has to be made to ensure safe operation, while maintaining the mass budget as low as possible. In this thesis all aspects of RHA for RADEM, except setting the environment specifications, were performed:

- A method to compute RADEM component doses for the whole mission was developed and optimized;
- Optimize RADEM shielding to keep component dose levels below sensitivity levels while maintaining its mass budget as low as possible;
- Assess SEE rate and impact on RADEM operation.

1.2.3 Verification of ^{60}Co testing representativeness of EEE components flown in JUICE

Another RHA contribution of this thesis not only to RADEM, but to the JUICE mission, and all future missions to Jupiter, was the verification of the ^{60}Co test standard validity for electron environments with energies higher than 10 MeV. As it was previously discussed, ^{60}Co tests are a conservative way to determine radiation sensitivity of EEE components in orbiting the Earth. To determine the test accuracy for components flown in the Jovian radiation environment, a series of irradiation campaigns with ^{60}Co and two electron energies (12 and 20 MeV), at low and high dose rates, were conducted separately, for components of different technologies.

1.3 Outline

In this thesis, Chapter 2 to 4 introduce the fundamental topics to the work here presented. In Chapter 2 a summary of the JUICE mission and its background is presented.

In Chapter 3, the physics and methods of radiation interaction with matter will be discussed. In Chapter 4 the radiation effects and hardness assurance for the JUICE mission are addressed.

Chapters 5-7 will be dedicated to the results of the work. In Chapter 5, all activities regarding the Verification of ^{60}Co testing representativeness for the JUICE mission will be presented. In Chapter 6 the radiation analysis and shielding optimization of RADEM is addressed. In the same Chapter, the development of the GUIMesh tool, which converts STEP geometries [33] into GDML [34] (a Geant4 [30][31][32] readable format), will also be reported. The development of the Directionality Detector of RADEM is presented in Chapter 7 and the conclusions and future work will be discussed in the final chapter.

2 Jupiter Icy Moons Explorer

Jupiter Icy Moons Explorer, JUICE, is the ESA next class-L mission to the Jovian system. The mission is inserted in the agency 2015-2025 Cosmic Vision science program [35]. It was selected as the first large mission of the program followed by Athena [36], an x-ray telescope, and LISA [37], a gravitational wave Laser Interferometer Space Antenna.

2.1 Motivation - Cosmic Vision

The Cosmic Vision is the ESA long-term plan created in 2005 for future missions. It consists of four major themes which drive mission selection based on scientific priorities:

- What are the conditions for planet formation and the emergence of life?
- How does the Solar System work?
- What are the fundamental physical laws of the Universe?
- How did the Universe originate and what is it made of?

JUICE addresses the two first topics via planetary exploration of Jupiter, a gas giant in its own right, which has directly impacted the evolution of our solar system and is an archetype to study the large number of gaseous planets discovered in the last two decades around other stars.

It will also study the three icy moons of the Jovian system, Europa, Callisto and Ganymede. Although these moons are far away from the Goldilocks zone, the interplanetary region where the conditions for the existence liquid water are met, it is believed that they have the conditions to sustain life: liquid water, complex molecules, energy source and long-term stability [20]. The existence of these deep habitats around gas giants are an on-going topic of discussion that may change our views on Astrobiology [38].

2.2 Mission Profile

JUICE is scheduled for launch in 2022, travel through the interplanetary space for 7.6 years including three Earth flybys, one Venus flyby and one Mars flyby, and tour the Jovian system for 3.5 years [20][28]. In Jupiter, the mission will enter an equatorial orbit

Table 2.1: JUICE mission phases. Adapted from [28].

Phase reference	Description	Duration (days)
Phase 0	Interplanetary transfer	2711
Phase 1	Transfer to Europa	458
Phase 2	Europa flybys	38
Phase 3	Jupiter high latitude phase with Callisto	248
Phase 4	Transfer to Ganymede	311
Phase 5a	Ganymede orbit insertion, elliptic orbits, and 5000 km circular orbit	152
Phase 5b	Ganymede 500 km altitude circular orbit	103
Phase 5c	Ganymede 200 km altitude circular orbit	30

for one year to study the Jovian system. Afterwards, it will flyby Europa three times on a 36 day period, transfer to a high latitude orbit around the planet for six months, where it will observe the planetary atmosphere and Callisto, before returning to an equatorial orbit for nine months in its way to its final target, Ganymede. The moon will be orbited at different altitudes, 5000, 500 and 200 km for a total of 280 days before crashing into the surface [20]. Table 2.1 contains the full mission phase description as well as planned duration.

The mission will be the third spacecraft to orbit the planet for a long period of time after the Galileo spacecraft which studied the planet from 1995 to 2003, and the JUNO mission that is orbiting the planet in a polar orbit since 2016. The chronology of all missions to Jupiter is shown in Figure 2.1. Most missions that visited the planet have done so by short periods of time on their way to the outer solar system. Long-term in-situ measurements are essential to study the time evolution of the system as a whole and to resolve spatial variability. Orbiter missions are necessary because unlike ground based observations, they give spatial resolution for long periods of time, and allow to monitor the system globally [20].

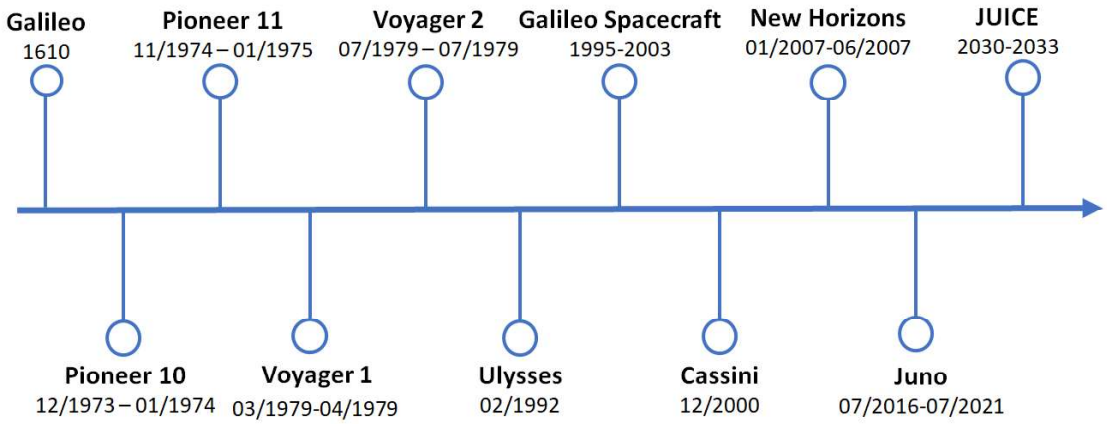

Figure 2.1: Chronogram of missions to Jupiter (and date of first observation).

2.3 Science Objectives and Instruments

Though there are still many questions, our knowledge of the Jovian system has greatly improved since Galileo first observed the four Jupiter moons with its name in 1610. Jupiter itself is a gas giant with a plethora of atmospheric processes variable in space and time. It has 63 known moons, four of which, the ones observed by Galileo, that are in part, responsible for the system evolution. The Galilean moons, Io, Europa, Ganymede and Callisto have an orbital radius of 5.99, 9.39, 14.97 and 26.33, Jupiter Radii (R_J=71.492 km) respectively. Callisto, Europa and Ganymede have icy shells and possible liquid water oceans beneath. Ganymede is a planetary body in its own right with a mass larger than Mercury and an intrinsic magnetic field. Io however, is a volcanic body and the main source of plasma in the system expelling ∼1000 kg of material per second [20].

JUICE main scientific objectives are to study the surface and sub-surface of the three moons, namely the sub-surface liquid water oceans. It will measure the ice shell thickness and explore the existence of water reservoirs or of actual oceans beneath it. In the case of Ganymede, the magnetic and induced fields are crucial to constraint the ocean thickness since the latter, is directly related a conducting fluid motion. For this reason, the moon magnetic field, plasma current and the planetary magnetic field have to be decoupled [20].

The mission will also study the moons tenuous atmosphere's which are thought to be a result of sputtering [20]. Sputtering products relay information from the material that composes its surface. JUICE will measure both the particle environment and the atmosphere to explore the dynamics of both. Furthermore, sputtering products from Europa are also one of the three main contributors, behind Io and Jupiter itself, to the total plasma material. Measurements of the atmospheric flow are essential to determine the coupling of the moon with the plasma and the high energy environment [20].

Jupiter is an object of study for the mission as well. The planet's atmospheric dynamics, composition and interaction with the moons, including gravitational and magnetic couplings, will be studied [20]. The mission will carry 11 scientific instruments to measure the gravity, particle environment and chemical composition. The full list of instruments can be found in Table 2.2. The instruments will allow to measure a broad range of wavelengths. Dedicated instruments to measure the magnetic field (J-MAG), the plasma environment (PEP) and gravity (3GM) are also included.

Table 2.2: List of scientific instruments in JUICE and their function.

Scientific Instrument	Name/Function
JANUS	Camera System
MAJIS	Moons and Jupiter Imaging Spectrometer
UVS	UV imaging Spectrograph
SWI	Sub-milimeter Wave Instrument
GALA	Ganymede Laser Altimeter
RIME	Radar for Icy Moons Exploration
J-MAG	A Magnetometer instrument for JUICE
PEP	Particle Environment Package
RPWI	Radio & Plasma Wave Investigation
3GM	Gravity & Geophysics of Jupiter and Galilean Moons
PRIDE	Planetary Radio Interferometer & Doppler Experiment

2.4 Jovian Radiation Environment

The radiation environment around planets is a result of local (planetary) and external (Solar and Galactic) processes. Radiation in space is hazardous to EEE components [2][4][6] and biological systems [39][38][40] but it also gives information about its origin and transport. As previously mentioned, there are three main contributors to the radiation environment: Solar Particle Events (SPE); Galactic Cosmic Rays (GCR); and Trapped Particles. The environment is populated by electrons, protons and ions in a large range of energies, from 100 keV (threshold between plasma and high energy environment [41]) to 10^{21} eV, the most energetic cosmic rays. The energies and particle types are summarized in Figure 2.2.

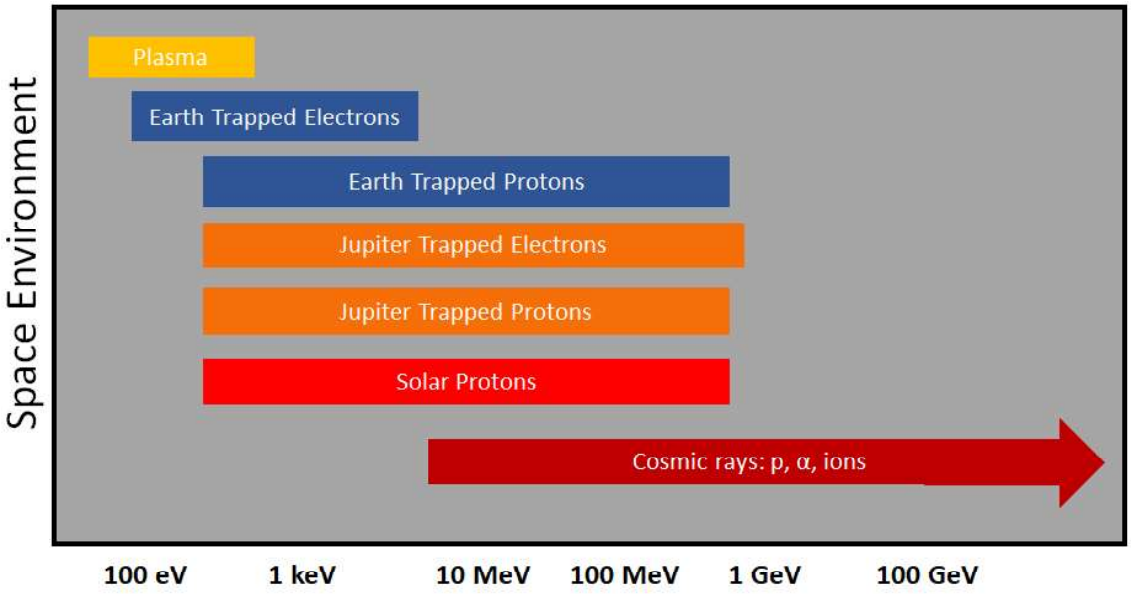

Figure 2.2: Space environment radiation sources and typical energies. Adapted from [42].

2.4.1 Jovian Magnetosphere

The magnetosphere is the main driver behind the plasma and energetic particle population around Jupiter, dictating many aspects of the system. In many ways, it is similar to other planetary magnetospheres such as the one in the Earth, Saturn, Uranus, Neptune and to some extent, Mercury [43]. Magnetospheres are related to planetary magnetic fields. Its size is directly related to the magnitude of the field, i. e., the stronger the magnetic field is, the larger is extent the magnetosphere, and to the solar wind pressure. This is the reason why the Jovian magnetosphere extends up to 5E+08 km, a length ~350 larger than the Earths magnetosphere, reaching the orbit of Saturn [44]. Jupiter's magnetic field strength is 4.2E-04 T at the equator, ~15 times larger than the Earth).

The magnetosphere is a complex system with different regions as it can be seen in Figure 2.3. The limits of the magnetosphere are the bow shock, the outermost layer between the magnetosphere and the interplanetary medium, and the magnetopause, the region where solar wind pressure matchs the magnetic field. These regions are variable in time and along the longitude of the planet. While the magnetosphere is compressed by the solar wind on the day-side, it is stretched into a long magnetotail in the night side. The magnetotail consists of two lobes, where few charged particles exist, separated by a plasma sheet of high particle density. Closer to the planet, its intrinsic magnetic field can be approximated by an off-center (0.1 R_J) tilted (9.6°) dipole. The magnetic field rotates with the planet finishing a full revolution every ~ 10 hours.[20]. Beyond (10-20 R_J), the dipole-like configuration is no longer true resembling a flat disk (magnetodisk).

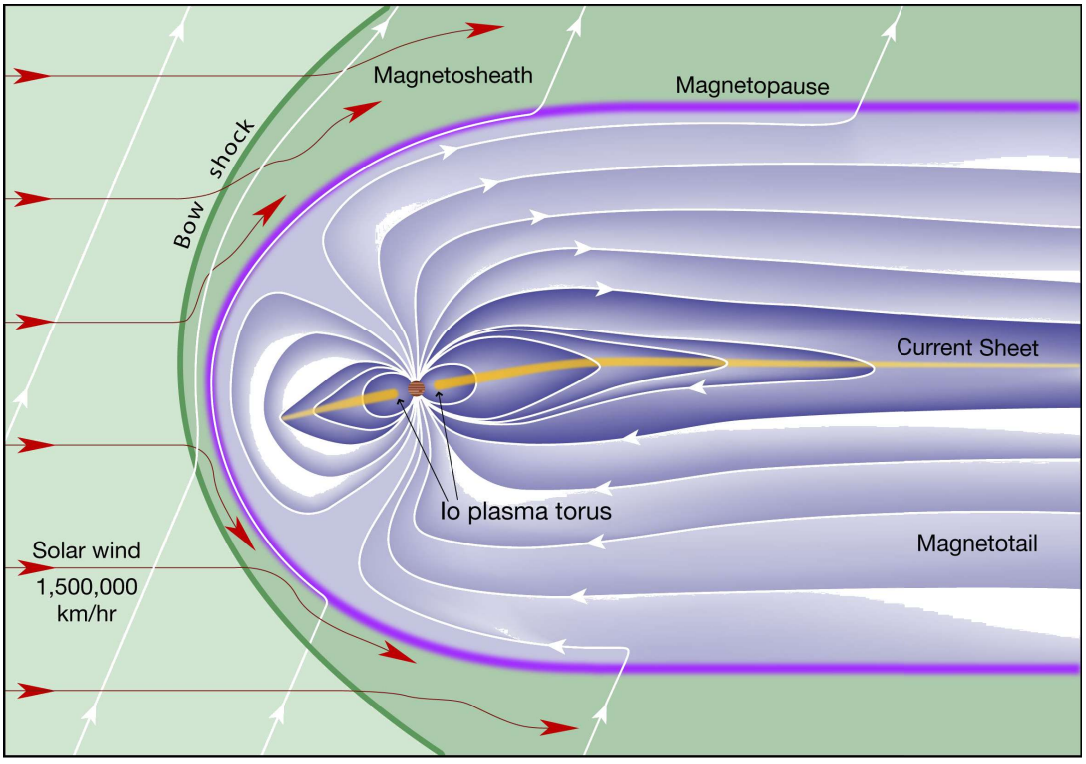

Figure 2.3: Schematic of the Jovian magnetosphere. From [45].

The magnetosphere can be divided into an inner dipole-like (<10-20 R_J) part, middle (20-40 R_J) part and outer (> 40 R_J) part [20][46]. In the inner part, plasma from Io (mostly sulfur and oxygen) and from Jupiter and Europa is accelerated by the rotating magnetic field. This, in combination with magnetic field ruptures and plasma instabilities can accelerate particles up to hundreds of MeV. The middle and outer part of the magnetosphere are radially stretched. While plasma in the inner and middle part of the magnetosphere is in co-rotation with the magnetic field of the planet, in the outer part plasma is slower by a factor of two or more.

It is in the magnetosphere that particles are accelerated to high energies (tens-hundreds of MeV). Up to ~10 MeV, particles are thought to originate in the solar wind or in the outer Jovian system and diffuse inward gaining momentum by conservation of the first and second adiabatic invariants [47][48]. Gyro-resonant electron acceleration from radio-frequency waves generated by thermal gradients has also been proposed as a mechanism to accelerate electrons to higher energies [47]. Betatron [49] and the Fermi mechanism [50] are thought to accelerate electrons to tens of MeV range which could explain the energy differences between trapped electrons in the Earth and in Jupiter based on the magnetic field strength and on the dynamics of the system.

Particles from the magnetosphere also interact with the moons in complex processes that include sputtering and injection of surface materials into the magnetosphere. Ganymede intrinsic magnetic field and sub-surface induced field also interact with the magnetosphere in a way that it is not yet fully understood. This is a key issue for JUICE which will separate all magnetic contributions at the moon.

2.4.2 Trapped Particles

Trapped particles are contained in the magnetosphere of planets, namely Earth and Jupiter. In Jupiter, they are thought to be originated from plasma emissions from the volcanic moon, Io and the icy moon Europa, accelerated in the Jovian magnetosphere. Electron and proton energies can reach ~100 MeV and ~1 GeV respectively. Particle fluxes decrease with the distance to the planet. At distances from the planet above 20 R_J, particles are concentrated mostly on the magnetodisk as it can be seen in Figure 2.4 for both electrons and protons [20][46][43]. Io and Europa as well as several smaller moons are deep inside the radiation belts. While Io, and to some extent Europa, feed the magnetosphere with ions, the smaller moons absorb the radiation in their orbit.

Ganymede is in an orbit where the particle content (type and energy) fluctuates. It also has its own magnetic field which means that it is shielded in part from the Jovian radiation. However it has been shown that it has its own trapped particles [25] as a result of its magnetic field. Callisto is the only of the four Galilean moons completely outside of the radiation belts and is the less unique moons regarding high energy particle interaction.

Several models of the Jovian environment have been developed over time. The first one was the Divine and Garret model [51][52] which was based on the Pioneer and Voyager missions [15] [16][17]. The Galileo mission data led to the development of GIRE [53], a

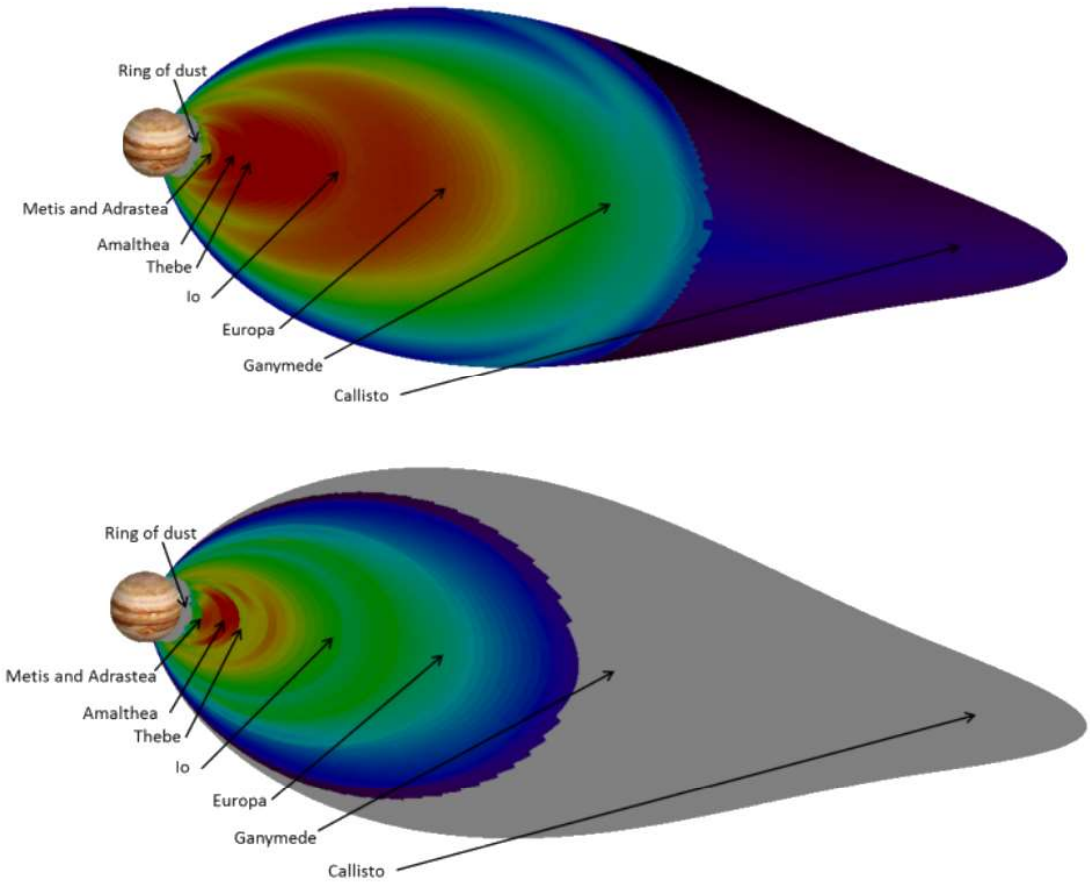

Figure 2.4: Jovian radiation belt (top panel: 10 MeV electron belts; bottom panel: 100 MeV proton radiation belt). From [43].

model which covered trapped electrons only from 8-16 R_J. A theoretical model, Salammbo [54] was also developed by ONERA, but no further long-term in-situ measurements have been done so far to further update the models.

For the JUICE mission a new, more precise, JOvian Specification Environment (JOSE) model was developed [46]. This model is based on flux long-term averages from the EPD instrument [13] of the Galileo spacecraft. In the model, particle fluxes up to L=20 are described by two parameters, the McIlwain magnetic field line equator distance, L, and B/B_{eq}, the ratio between the field magnitude in a location and the equator field strength along the same line. For L>20, the dipolar model is no longer valid. At these distances, the flux organizes in a current sheet. Here the flux is modeled as a function of the cylindrical radial distance to the planet, ρ, and $n_d s$, the normal distance to the current sheet. Proton modelling is mostly extrapolated from low energies because data from Galileo is limited to 1.25 MeV [46].

Both Ganymede and Europa are inside the trapped electron region. Electron fluxes are larger for regions closer to the planet. This means that the radiation environment in Europa is much harder than in Ganymede. Ganymede also has its own magnetosphere

which can trap particles and deflect low rigidity (momentum per unit of mass) particles.

Electron fluxes have been shown to have angular dependence. Figure 2.5 shows the angular distribution of two electron channels of the EPD in three different locations during a Ganymede flyby. Measurements showed that a trapped like angular dependence on the flux (maximum Local Pitch Angle (LPA) at 90°) can be seen in Ganymede orbit. Beam-like electron profiles which are thought to be injected particles that drift towards the moon surface have also been measured by the EPD. Anisotropies from plasma convection have also been observed [25]. Angular assessment of the particle environment inside the Jovian system is critical to understand their origin and transport, as well as modelling the particle flux.

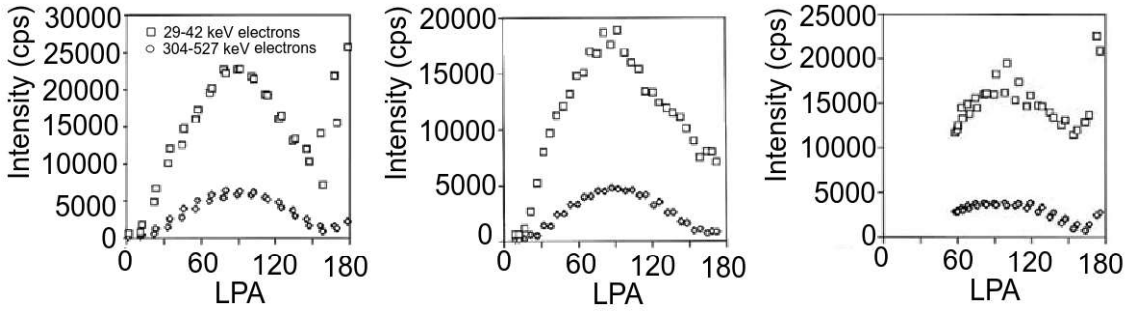

Figure 2.5: Electron Local Pitch Angle distributions in different locations of the Ganymede magnetosphere. In the left-most and right-most charts, close to 180°, a bump can be seen in the count rate indicating an electron beam in the direction of the moon surface. Adapted from [25].

2.4.3 Solar Particles Events

The Sun is constantly releasing particles to the interplanetary medium. These particles propagate in the Heliosphere making up the Solar Wind. The Solar Wind travels at up to ~800 km/s, ~0.25% of the speed of light. Its flux is modulated by the Solar Cycle that varies between 7 to 15 years. The cycle is associated with a change of solar activity and magnetic polarity. Higher Solar activity is directly related to the tilt of the Sun's magnetic field in relation to the Solar rotation [55]. The activity can be measured by the number of sunspots. The larger the number, the larger the solar activity. Daily measurements of the number have been done since 1749 [56]. Figure 2.6 shows yearly averages since 1860. As it can be seen duration and activity of each cycle differs. So far it is not possible to predict any of the two [55].

The Sun also produces Solar Energetic Particles (SEPs). They are associated with Solar Particle Events (SPEs) namely Solar Flares (SF) and Coronal Mass Ejections (CMEs). Both eject energetic protons with energies up to hunders of MeV and to some extension ions and electrons. The number of events is correlated with the solar activity.

SEPs travel across the interplanetary medium and interact with spacecrafts and astronauts. The power density of a SPE decreases with the distance from the Sun. Figure 2.7 shows the measurements made by Rosetta during the 2014-09-02 solar particle event.

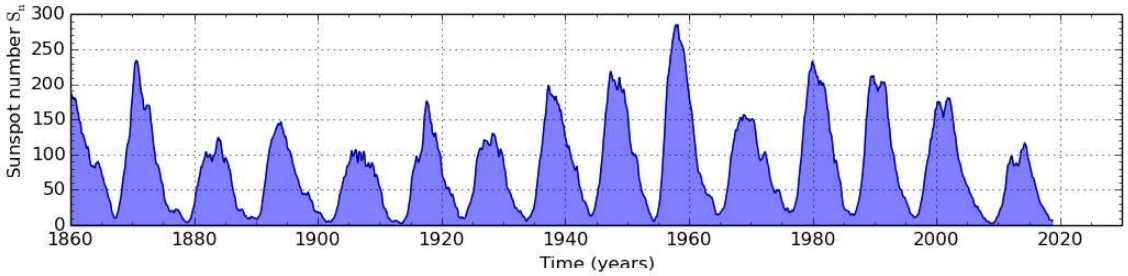

Figure 2.6: Sunspot yearly mean since 1860. From [57].

Despite its long distance to the Sun, both protons and electrons were measured by the Standard Radiation Environment Monitor (SREM) aboard the spacecraft. Therefore, even for missions far beyond Mars orbit, it is important to account for the presence of SPEs in the radiation environment.

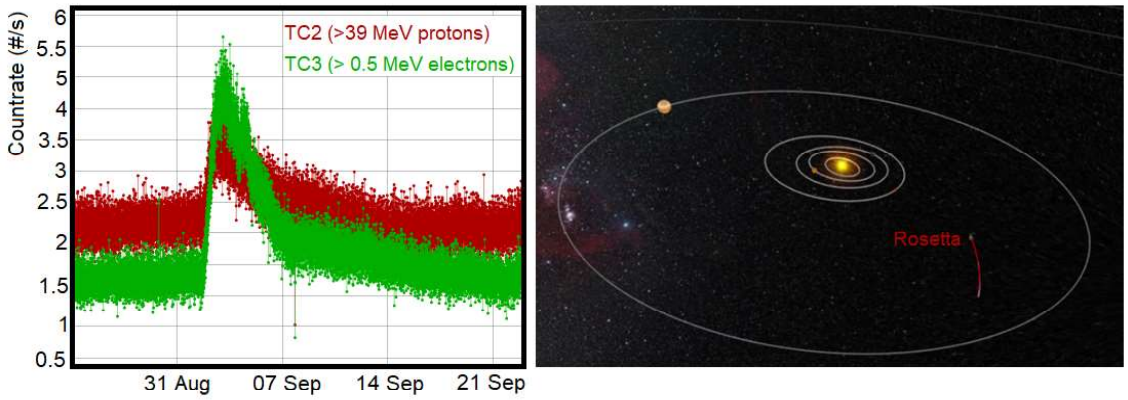

Figure 2.7: Rosetta SREM TC2 and TC3 channel measurements during the 2014-09-02 solar particle event (left) and its location in the solar system (right). From [58].

Although stochastic in nature, SPE occurrence is tied to the solar activity. At the solar maximum, these events are much more probable than in times of low solar activity. In each event the particle population and spectra may be different. This means that on top of being unable to predict short-term SPE occurrence, it is also impossible to model the particle flux. However, a modified Poisson statistic model developed by Burrell exists to determine the probability that a certain number of events will occur, during a certain time interval [59]. Regarding particles, data from several events has already been acquired. An important event is the 1989 one that is used as a worst-case for modelling purposes. There is also the possibility to model long-term fluxes assuming a period of time greater than a full solar cycle. The current standard model the ESP model [60]. The model averages data from 3 Solar Cycles at 1 A.U. However it does not model single events and does not take into account stochastic fluctuations of the radiation levels. Though the influence of SEPs in the Jovian system is apparently neglectable (evidence exists that it can cause short term effects on the Jovian magnetosphere), it is highly important for the interplanetary cruise phase of JUICE.

2.4.4 Galactic Cosmic Rays

The last contributor to the space radiation environment are Galactic Cosmic Rays. These are the most energetic particles consisting of protons (∼90%) and ion species with 2<Z<92 with different relative abundance. They are a constant, nearly isotropic low flux of particles (∼4 particles/cm^2/s in space) with galactic origins not totally well understood. These particles are accelerated in extreme environments such as Supernova explosions and then travel through the interstellar or the intergalactic medium to the Solar System. The energy vs flux as measured by several experiments is shown in Figure 2.8 [61]. Despite their low flux, they can cause severe damage to spacecrafts. The high energy end of the flux goes up to 10^{21} eV. Events in these energy range are so rare that they can be neglected from all JUICE mission considerations. Cosmic rays are also an important window to study the Universe as it can be inferred from the large number of experiments in the chart.

The cosmic ray flux is anti-correlated with the solar cycle. This means that the flux decreases when solar activity increases, i.e., the magnetic field strength increases. When solar activity decreases the flux increases. This is a consequence of the magnetic force exerted by the Heliosphere in cosmic rays up to ∼10 GeV. Particles with lower rigidity (momentum per unit of charge), are deflected by the magnetic field of the Sun. When the solar activity is larger, the magnetic field increases and deflection occurs for a larger range of particle energy. As a result, the cosmic ray flux decreases. Between solar maximum and minimum, the flux can vary by more than one order of magnitude depending on the particle and on the energy. This is especially true for particles with lower energies. At energies above ∼10 GeV/nucleon however, this effect is very small. Inside planetary magnetosphere flux decreases further [61] as the magnetic field increases. Short term variations driven by Solar Particle Events can also occur. This phenomenon, called Forbush Decreases, happens when an Interplanetary Coronal Mass Ejection carrying a magnetic field strong enough to deflect low energy GCRs [62][63]. The flux also lowers near planetary objects since they shadow part of the flux. In the Earth, both the magnetic field and the atmosphere protect the ground from GCRs.

While GCRs are not a feature of the Jovian environment per se, they are important for any mission in space. GCR are known to cause Single Event Effects (SEE) on electronics in Earth orbit, interplanetary cruise and in other planets [6][64][28]. Jupiter is no exception and careful considerations have to be taken into account. The problem with GCRs is that, although they are much less abundant than trapped particle, they are also highly energetic and can fully cross a spacecraft and hit its components. Their effect is mostly a function of their Linear Energy Transfer (LET). GCR models, including the one used for JUICE, ISO 15390 [65], give average fluxes depending on solar epoch (solar maximum or minimum). Fluxes are usually given behind 1 g.cm^{-2} because, despite the fact that the materials do not have significant impact on high energy GCRs, the lower energy particles loss of energy changes their LET. In this region the LET of a GCR increases increasing the probability that a SEE occurs. As in the Earth, the Jovian magnetosphere

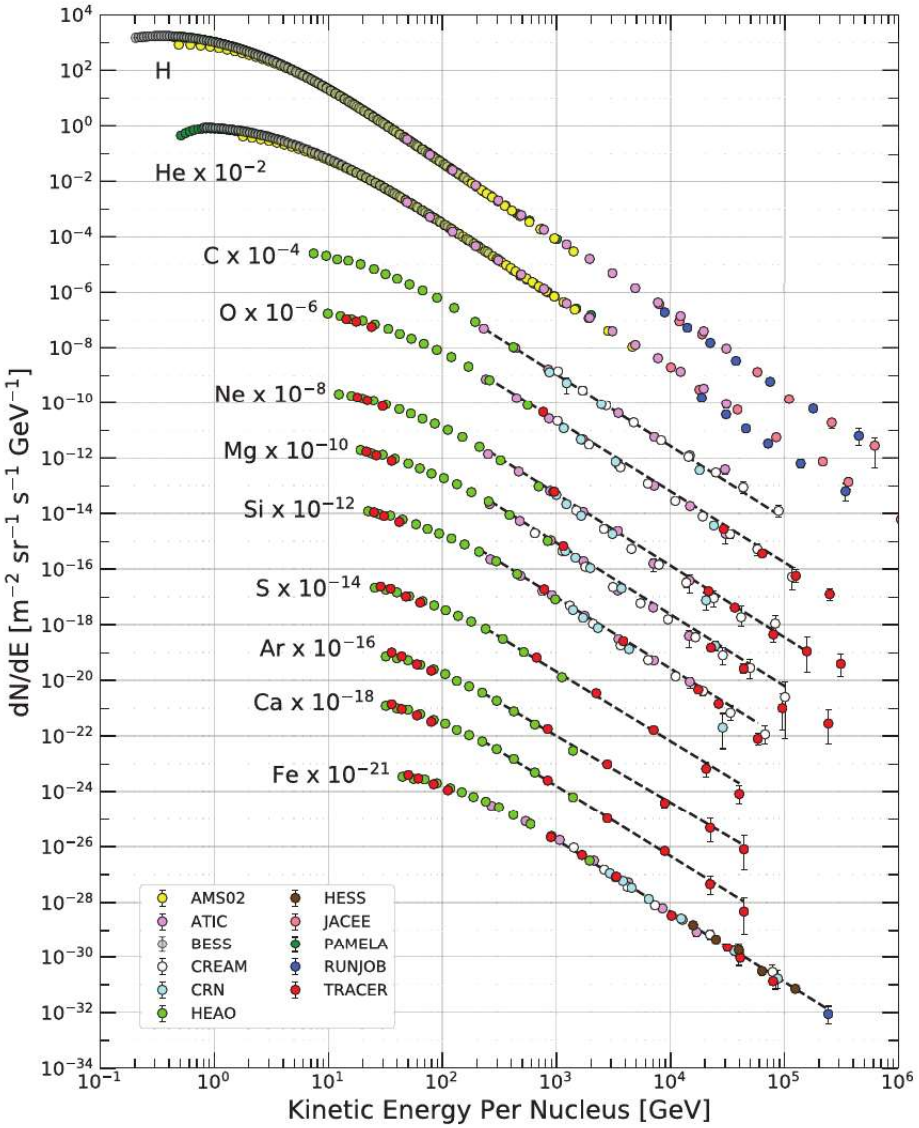

Figure 2.8: Primary cosmic radiation fluxes plotted as particles per energy-per-nucleus vs energy-per-nucleus. From [61].

and planet/moon shadowing lower the GCR flux.

Succinctly, solar particles, Galactic Cosmic Rays and trapped particles combine to form a complex and hazardous environment for any missions outside the Earth's atmosphere.

2.5 Radiation Hard Electron Monitor

RADEM is the Radiation Hard Electron Monitor currently in development for the JUICE mission. It is a low mass (1 kg excluding shielding), low power instrument with short bandwidth that will be responsible for in-situ radiation dose assessment, and for relaying large radiation level alarms to the spacecraft. Although it is considered a housekeeping instrument, it will also provide valuable scientific information regarding the ener-

getic particle population around the gas giant. An image of the latest STEP [33] geometry of RADEM can be seen in Figure 2.9 with the four detector heads, discussed below, in brown.

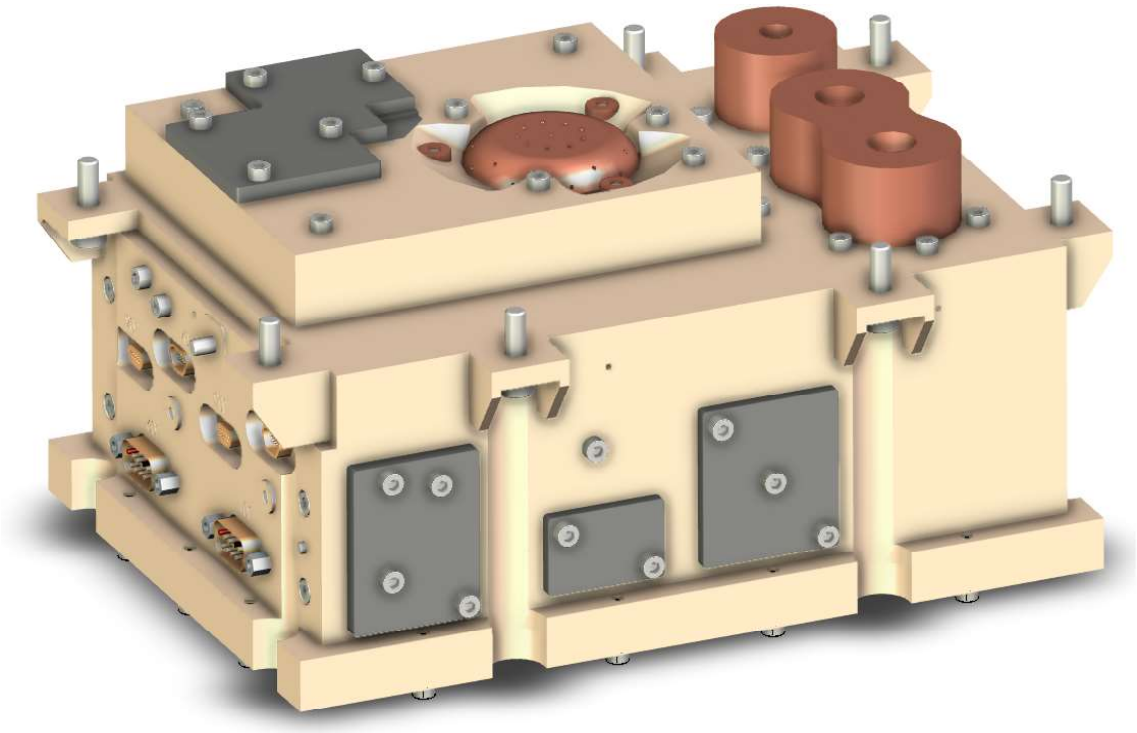

Figure 2.9: RADEM up-to-date step geometry. The four detector heads are in brown. Beige represents the Aluminum housing and gray the Tantalum shielding.

So far, only the Energetic Particle Detector (EPD) [13][19] aboard the Galileo spacecraft performed long-term measurements of the radiation environment in Jupiter. As it was discussed before, all other missions visited the planet only for a short time during gravity assisted maneuvers which did not allow them to collect substantial data for flux modeling, even when the mission carried a particle detector. The exception is the aforementioned Galileo and currently Juno. The latter however does not have radiation measuring capabilities, despite recent efforts to use the radiation induced dark current of its CMOS cameras, to constrain the particle population [14][66].

The EPD was a bi-directional telescope mounted on a rotating platform which gave it a 4π sr field-of-view. The two telescopes, the Low Energy Magnetospheric Measurement System (LEMMS) and the Composition Measurement System (CMS) were capable of measuring electrons with energies between 0.015 to 11 MeV, protons with energies between 0.08 to 59 MeV, and ion species up to Iron in different energy ranges [13]. The instrument had 10.5 kg of mass and 6W available, much more that what was assigned to RADEM. Despite this, has been increased as a consequence of this thesis for reasons that will become clear in Chapter 6. It proposes to extend the energy range measured by the EPD with larger mass and power restrictions. Its constraints do not allow the same concepts of the EPD to be used, namely the rotational system, but also the use of an artificial magnetic

fields such as the one in the LEMMS telescope [13].

2.5.1 Front-End Electronics

Before discussing the RADEMs detectors, it is important to understand the ASIC VATA466 [22] that was developed by IDEAS specifically for RADEM. The ASIC has 4 Low-Gain channels and 32 High-Gain channels. Each channel is coupled to a singular radiation sensitive device. The Low-Gain channel has a charge discriminator (Low-Threshold) programmable from 260 fC to 22.6 pC. The High-Gain channels have two charge discriminators (Low and High Threshold) programmable from 1.2 fC to 0.2 pC and from 15 fC to 1 pC respectively. Each channel is connected to a 22-bit counter that registers the pulse heights into an analog multiplexer. The threshold outputs of all channels are connected to 36 programmable coincidence pattern units with 68 inputs (32*2+4) that feed a 22-bit counter. The hold time of the coincidence units, Mono-stable Coincidence Time (MCT) can be selected as 50, 100, 200, 300, 400 or 600 ns. This allows a coincidence based count rate assessment of the radiation environment [22]. The gain of the device can also be adjusted. Figure 2.10 shows the block diagram of the ASICs.

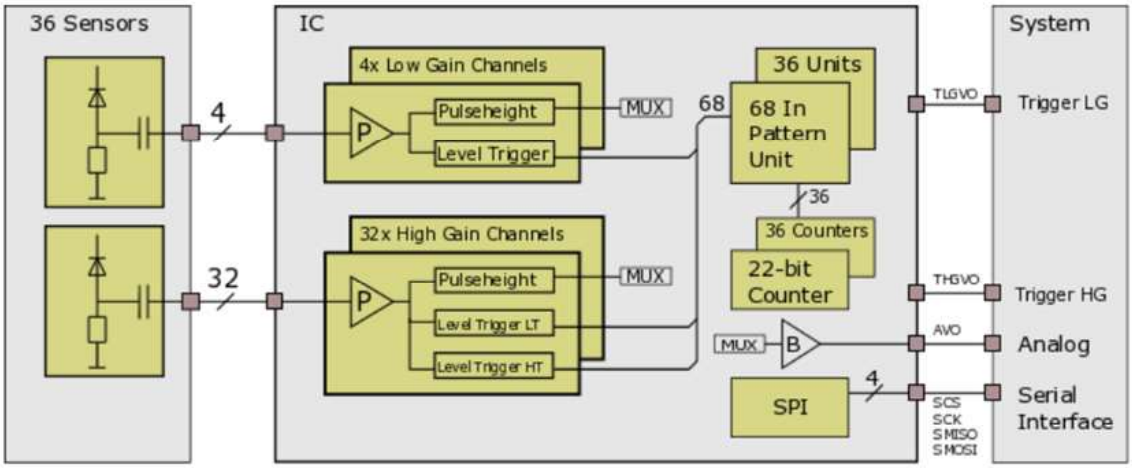

Figure 2.10: Block diagram with radiation sensors (left), the integrated circuit (ASIC, centre), and readout system (right). From [22].

The ASIC is radiation hardened against Single Event Upsets (SEUs), with triple-modular redundancy and parity check, and against Single Event Latch-ups (destructive modes of EEE components), with an external latch-up detection module which monitors the current and power-cycles the device if a programmed threshold is reached (see Chapter 4 and Chapter 6 for more information on radiation effects on semiconductor devices).

It also has an intrinsic calibration system that allows to connect each channel to an adjustable pulse generator. While it does not replace actual particle calibration, it can be used to perform functional analysis and adjust to any parametric changes during the mission that might have been caused by aging, or most likely, radiation.

2.5.2 Detectors

RADEM consists four detectors, the Electron Detector Head (EDH), the Proton Detector Head (PDH), the Heavy Ion Detector Head (HIDH) and the Directionality Detector Head (DDH). It is proposed to measure electrons from 0.3 to 40 MeV, protons from 25 to 250 MeV, and ions species from Helium to Oxygen with energies from 8 to ~670 MeV, at the large rates, due to the high particle fluxes of the Jovian system, $2*10^9$ electrons/cm^2/s and $2*10^8$ protons/cm^2/s. The Electron, Proton and Ion Detector heads are based on standard silicon stack detectors concepts such as the ones used in the Standard Radiation Environment Monitor (SREM) [23] and the Multi-Function Spectrometer (MFS) [24], extended to higher energies. Figure 2.11 shows a schematic of the stacked detectors. The radiation sensors are 300 μm thick custom-made n-well Silicon diodes in full-depletion mode, operated at 90V, with different radius. The aperture and dimensions of the detectors are related to the expected count rate from worst-case particle environment and the readout maximum rate (1MHz) of the ASIC, as well as the Total Ionizing Dose (TID) and the Displacement Damage Dose (DDD).

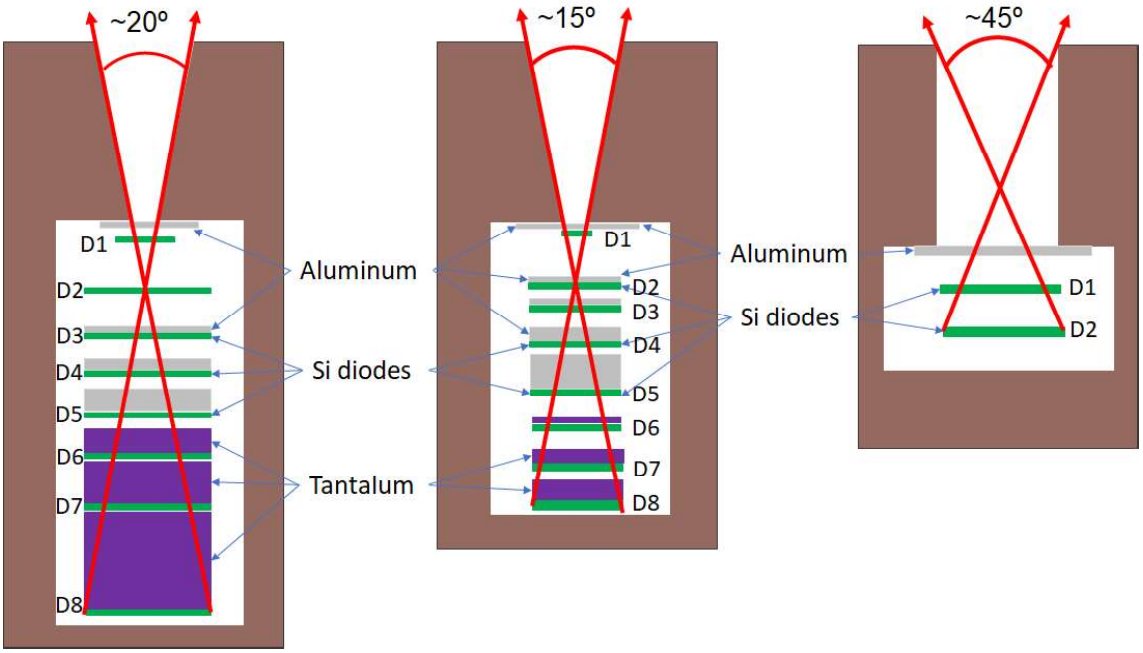

Figure 2.11: From left to right schematic of the PDH, EDH and HIDH.

2.5.2.1 Working Principle

In a stack detector, a particle loses energy in successive, increasingly thicker or denser, absorbers. The more energetic the particle is, the deeper in the telescope it can go. Silicon diodes are placed between absorbers to detect the passage of particles. The energy of a particle is then be inferred from the deepest Silicon diode that it interacts with. This is based on the stopping power of the particle of interest in the absorber materials and

on calibration measurements. The particle type, in this case electrons and protons, is differentiated by applying energy (pulse height) cuts with the front-end electronics. Low energy protons ($\leqslant$100 MeV) lose more energy than electrons in the small path they travel in the silicon diodes. High energy protons however, have similar signatures to those of electrons but since they lose energy in the stack, they can still be differentiated.

2.5.2.2 Electron Detector Head

The Electron Detector has eight Silicon diodes, identified as D1, D2, ..., D7, D8 or (EDH1, EDH2, .., EDH8) from top (aperture side) to bottom, interleaved by Aluminum and Tantalum absorbers. All dimensions of the telescope elements are described in Table 2.3. The detector is surrounded by an 8 mm copper collimator with a $\sim$15°aperture. The thickness and material of the absorbers is based on the energy range that is intended to measure. This detector head has a VATA466 ASIC [22] uniquely assigned to it. Each sensor diode is connected to an individual High-Gain channel of this ASIC. Readout coincidence patterns between the top most diode (D1) and the others diodes determine if a particle entered through the FOV of the detector and, if it did, what is the energy range. If a signal that is not detected in D1 but is detected another diode it is considered background as it could not have come from the telescope aperture. Its theoretical electron energy channels are: 0.35-0.5 MeV; 0.5-1.0 MeV; 1.0-2.0 MeV; 2.0-4 MeV; 4.0-7.0 MeV; 7-17.5 MeV; 17.5-35 MeV; and >35 MeV. These values are base on the Continuous Stopping Power Approximation (CSDA) which is not true. In fact, as it will be discussed in Chapter 3, radiation interaction with matter is stochastic which means that energy deposition and range of particles in a material is not single valued. For this reason the real energy channels require calibration to be determined.

2.5.2.3 Proton Detector Head

The Proton Detector Head also has eight silicon diodes, identified as D1, D2, ..., D7, D8 (or PDH1, PDH2,..., PDH8) from top (aperture side) to bottom, interleaved by Aluminum and Tantalum absorbers. All dimensions of the telescope elements are described in Table 2.4. The detector is surrounded by an 8 mm copper collimator with a $\sim$15°aperture. The thickness and material of the absorbers is based on the energy range that is intended to measure. The PDH shares a VATA466 ASIC with the HIDH. The Silicon diodes in the PDH are connected on a one-to-one basis to the High-Gain channels of the ASIC while the HIDH Silicon diodes are connected to the Low-Gain channels. The same principle of the EDH applies to the PDH. However, since the PDH is dedicated to measure proton energy, the energy cuts are higher in order to discriminate from electron interactions in the sensors and count only protons. High energy protons are differentiated from electrons because the later do not reach the same telescope depth as protons. Its theoretical proton energy channels are: 4-7 MeV; 7-12.5 MeV; 12.5-20 MeV; 20-35 MeV; 35-50 MeV; 50-80 MeV; 80-125 MeV and >125 MeV.

Table 2.3: EDH telescope mechanical and particle cutoff characteristics. Numbering is ordered from top (aperture) to bottom. Cutoff values were obtained from NIST data [67].

Telescope Element	Material	Diameter (mm)	Thickness (mm)	Cutoff energy (MeV)	
				proton	electron
Absorber 1	Al	14.5	0.4	6	0.35
Diode 1	Si	3	0.32	9	0.4
Absorber 2	Al	8	0.3	12.5	0.5
Diode 2	Si	6	0.32	15	0.7
Absorber 3	Al	6	0.9	17.5	1
Diode 3	Si	6	0.32	20	1.25
Absorber 4	Al	6	1.9	25	2
Diode 4	Si	6	0.32	27.5	2
Absorber 5	Al	6	3.8	40	4
Diode 5	Si	6	0.32	40	4
Absorber 6	Ta	6	1.2	50	7
Diode 6	Si	6	0.32	50	7
Absorber 7	Ta	6	1.7	65	17.5
Diode 7	Si	6	0.32	65	17.5
Absorber 8	Ta	6	2.1	80	35
Diode 8	Si	6	0.32	80	35

Table 2.4: PDH telescope mechanical and particle cutoff characteristics. Numbering is ordered from top (aperture) to bottom.

Telescope Element	Material	Diameter (mm)	Thickness (mm)	Cutoff energy (MeV)	
				proton	electron
Absorber 1	Al	13	0.2	4	0.15
Diode 1	Si	6	0.32	7	0.3
Diode 2	Si	12	0.32	9.5	0.45
Absorber 2	Al	14	0.4	12.5	0.6
Diode 3	Si	12	0.32	15	0.7
Absorber 3	Al	12	1.2	20	1.25
Diode 4	Si	12	0.32	25	1.5
Absorber 4	Al	12	3.3	35	3
Diode 5	Si	12	0.32	35	3
Absorber 5	Ta	12	2	50	10
Diode 6	Si	12	0.32	50	10
Absorber 6	Ta	12	4.8	80	>1000
Diode 7	Si	12	0.32	80	>1000
Absorber 7	Ta	12	10.8	125	>1000
Diode 8	Si	12	0.32	125	>1000

2.5.2.4 Heavy Ion Detector Head

The HIDH has only one aluminum absorber at the top of the telescope and two silicon diodes. It will measure ions from Helium to Oxygen with energies from few MeV up to 300-400MeV. All dimensions of the telescope elements are described in Table 2.5. Each of the two diodes are connected to the Low-Gain channels of the same ASIC as the PDH

because of the large energy deposition from ions when compared to protons and electrons.

Table 2.5: IDH telescope mechanical and particle cutoff characteristics. Numbering is ordered from top (aperture) to bottom. Electron and proton cutoffs are neglectable in the case of the HIDH because these ions have higher LET and because the diodes are connected to the Low-Gain channels of the ASIC.

Telescope Element	Material	Diameter (mm)	Thickness (mm)	Cutoff energy (MeV)	
				proton	electron
Absorber 1	Al	17	0.1		NA
Diode 1	Si	12	0.32	NA	NA
Diode 2	Si	12	0.32	NA	NA

2.5.2.5 Directional Detector Head

The Directional Detector will perform flux angular measurements of the radiation environment around Jupiter. It is composed of a single copper collimator with 28 apertures corresponding to different directions in the sky. Figure 2.12 shows a cut view of the detector. Detailed description of the detector is given in Chapter 7 along with all the work related to its development, characterization and validation. As it was discussed in Section 2.4, the DDH is of utmost importance for the JUICE mission to decouple radiation sources and precisely estimate the radiation flux in Jupiter.

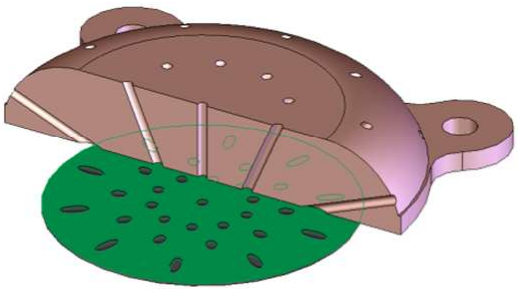

Figure 2.12: Cut view of the DDH. It consists of a single copper collimator with 28 holes correspondent to 28 directions. A pixelated sensor plane with diodes with geometrical shapes identical to the directions projection on the plane is used to detect the particles.

2.6 Summary

In this chapter, JUICE mission was introduced both from a scientific perspective and a radiation environment perspective. The mission has a broad range of scientific objectives that will focus on its moons and the planet itself. It is intended to study the sub-surface oceans of the three Galilean moons, their surface, and their interaction with the Jovian system. The moons have tenuous atmospheres that are thought to be a result of high

energy particles impact on the moons. Jupiter's atmosphere will also be studied as well as its system as a whole.

An important part of the Jovian system is the radiation environment, which is both dangerous for missions and a rich source of scientific data. Precise measurements of the particle population can give insight into the processes that created and accelerated them. Particle energy distribution is a direct result of the Jovian magnetosphere and its understanding is vital to study the interactions between Jupiter's magnetic field, the plasma environment and the high energy environment. Also, sputtering effects are important to map and comprehend the surface of the Jovian moons.

The space radiation environment is composed of three parts: Galactic Cosmic Rays (GCRs), Solar Energetic Particles (SEP) and trapped particles. The latter are one of the main hazards for the JUICE mission since they lead to high induced radiation doses. Radiation in the Jovian system is highly complex varying from a dipole-like inner region with high energy electrons (>10 MeV), the radiation belts, to a disk like region away from the planet. Radiation belts also exist around the moon Ganymede that has an intrinsic magnetic field. Measurements of the radiation environment are essential for the Radiation Hardness Assurance and to advance the knowledge about the Jovian systems.

RADEM will be the second instrument to measure the radiation environment in the Jovian system for an extended period of time. It is a low mass low power monitor with four detector heads specifically design to perform spectral analysis of the electron, proton and ion population during the mission, as well as measuring the flux angular variability. The latter is of utmost importance since different contributors to the radiation environment have different angular profiles. In Ganymede for instance both trapped-particles and beam-like fluxes exist with very different angular distributions. The energy range of RADEM extends that of the EPD [13] which will allow to construct better models and comprehend the mechanisms that accelerate particles up to high energies. The energy range also allows to make joint measurements with the PEP instrument which will study the plasma environment and correlate the measurements of the two instruments with the magnetic field measurements made by the J-MAG. It can then be said that RADEM is not only an important housekeeping instrument but also a valuable scientific tool.

3 Particle Transport in Matter

Particle interaction with the spacecraft materials and instruments may dictate the success of a mission. As it will be discussed in the next Chapters, dose levels in EEE components can cause short-term or definitive failure to a system, an instrument or even a spacecraft. It can also increase the noise of instruments and, in the case of this thesis, be the object of study. Therefore, it is of major importance to model and simulate radiation interaction with matter.

The processes that may occur when a particle transverses a material is dependent on its type, energy and on the medium properties. Particles of the space environment, mostly protons, electrons and ions, interact with the Coulomb field of atoms (electromagnetic interactions), and with their nuclei (nuclear interactions). Though plasmas are an important part of the solar system dynamics and a hazard to all spacecrafts, they are out of scope for this thesis and therefore will not be discussed.

3.1 Electromagnetic Interactions

Photons and charged particles lose most of their energy via electromagnetic interactions. These processes are the main cause of the Total Ionizing Dose (TID) in EEE components, and to some extend to the Total Non-Ionizing Dose (TNID). TID degrades components leading to parametric and eventual functional failure of components, systems and consequently instruments and spacecrafts [1][2] [3][4][5]. Radiation effects will be discussed in Chapter 4.

3.1.1 Photons

While photons do not contribute significantly for the space radiation environment, they can be produced by charged particle interactions in materials, namely high energy electrons. They are also used in ground-based TID testing of components since their non-ionizing contribution is neglectable [68], and since it has been demonstrated that they represent a worst-case damage analysis at the energies of ^{60}Co photon emission (1.17 and 1.33 MeV). There are three main processes by which high energy photons interact with matter: Photoelectric Effect, Compton scattering and Pair Production. To a much smaller degree, photons also interact via coherent (Rayleigh) scattering without loss of energy [69].

In this thesis we are interested in the overall attenuation in materials. Figure 3.1 shows the mass absorption coefficient, μ_m of all three main processes of photon interaction in Silicon and the total mass absorption in Silicon, Aluminum, and Tantalum. For Silicon, the photoelectric effect is the dominant process up to 60 keV and Compton scattering between 60 keV to 15 MeV photons. Though pair production is possible above 1.022 MeV, its cross-section only surpasses that of Compton scattering at higher energies. Its cross-section varies slowly with the atomic number. However, it is not constant. For high Z materials such as Tantalum, Compton scattering is the most probable process only for energies above 500 keV [69][70].

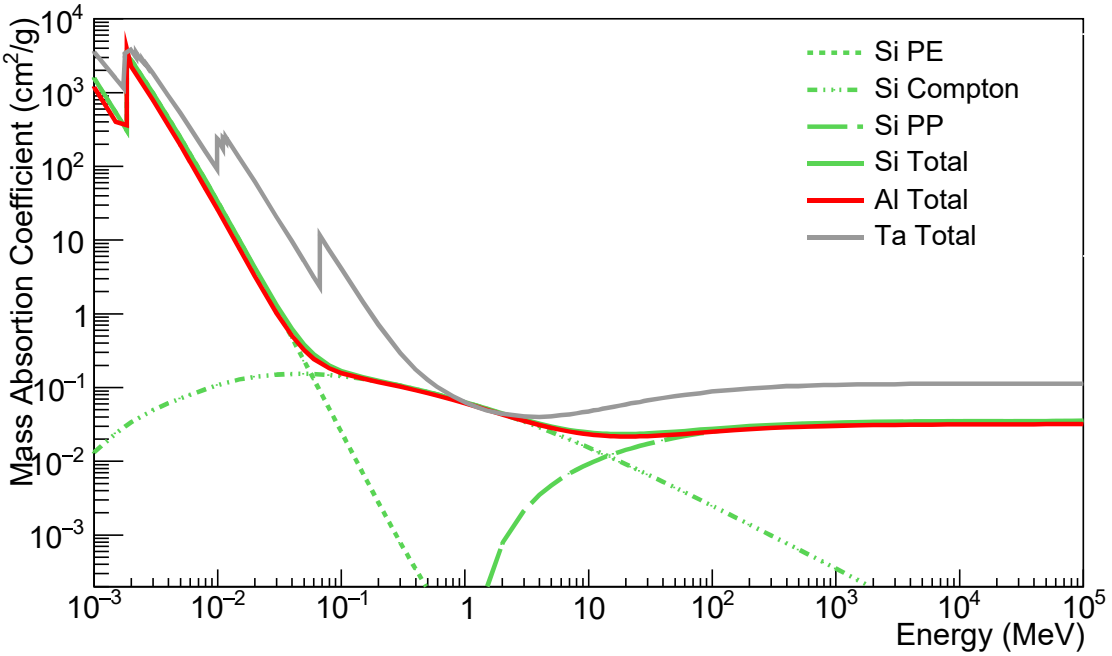

Figure 3.1: Photoelectric, Compton scattering, Pair Production and total mass coefficients in Silicon (green), and total mass absorption coefficient in Aluminum (red) and Tantalum (gray). Data from [70].

The mean free path of photons, λ, can be obtained from the mass absorption coefficient:

$$\lambda = (\mu_m \rho)^{-1} \tag{3.1}$$

Where ρ is the material density. λ does not vary much between materials with similar atomic numbers and densities. It is also in order of a few cm for Silicon and SiO_2. This is important for ^{60}Co testing which will be discussed in Chapter 4 [70].

3.1.2 Electrons

Electrons and positrons lose energy via collisional and radiative interactions. They are treated differently than heavy charged particles because of two reasons. First, their mass is of the same magnitude as the struck particle (electrons) or much lower (nucleus) which means that they lose much more energy per collision than heavier charged particles. Second

electrons have the same identity as the atomic electrons which cannot be distinguished and positrons can also annihilate with the selectrons. This has direct implications in the stopping power of the two particles. Since positrons have very limited relevance for this thesis, I will focus on electrons which are an important population of the space radiation environment as it was discussed in Chapter 2 [28][71][72].

3.1.2.1 Collisional Energy Loss

Collisional energy loss occurs between the incident particle and the atomic electrons or nucleus. They can either ionize the atom, excite it into a higher energy state, or even displace it from the lattice. At the energies that we are interested in however, the amount of energy loss means that excitation occurs only in a small fraction of the collisions. The average energy loss per unit of length, the stopping power, can be expressed as:

$$-\langle\frac{dE}{dx}\rangle\frac{1}{\rho} = \frac{1}{2}K\frac{Z}{A}\frac{1}{\beta^2}\Big[ln(\frac{m_e c^2\beta^2\gamma^2 m_e c^2(\gamma-1)/2)}{I^2}) + F(\tau) - \delta - 2\frac{C}{Z}\Big] \tag{3.2}$$

Where I, ρ, Z and A are the the mean excitation energy, density atomic number and mass numbers of the material respectively, $\beta = v/c$ and $\gamma = \frac{1}{\sqrt{1-\beta^2}}$, δ is the density correction term and C/Z the shell correction term. F(τ) is a function of the kinetic energy, τ, alone which is different for electrons and for positrons.

Notice that the the stopping power is proportional to the atomic number (Z) divided by the mass number (A). This ratio varies little along the periodic table which means that the collisional stopping power, normalized to the material density, is similar for all elements. This can be seen clearly between Silicon (Z=14) and Tantalum (Z=73) in Figure 3.2. However, it is linearly proportional to material density.

Ionization means that secondary electrons also need to be accounted for. The secondary electrons energy is a function of the scattering angle. Most collisions occur at small angles (soft collisions) which results in low energy transfer between the primary electron and the atomic one. For larger angles (hard collisions) a large fraction of the energy of the primary electron (up to half) can be exchanged. In these cases, the secondary electron can escape the medium. These secondaries are denominated as δ-rays. Electrons collisions with the Coloumb field of a nuclei does not ionize the medium. The energy loss in this collisions is denominated as Non-Ionizing Energy Loss, (NIEL). Despite representing a small fraction of the total energy loss, for the JUICE mission it has to be accounted for as it will become evident in Chapters 4 and 6.

3.1.2.2 Bremmstrahlung

Electrons can also be accelerated in the electrostatic field of atoms (most likely of the nucleus but also of the electronic cloud) and emit radiation. For low energy electrons (E>>$m_e c^2$) screening can be neglected. In this case, the energy loss via this process

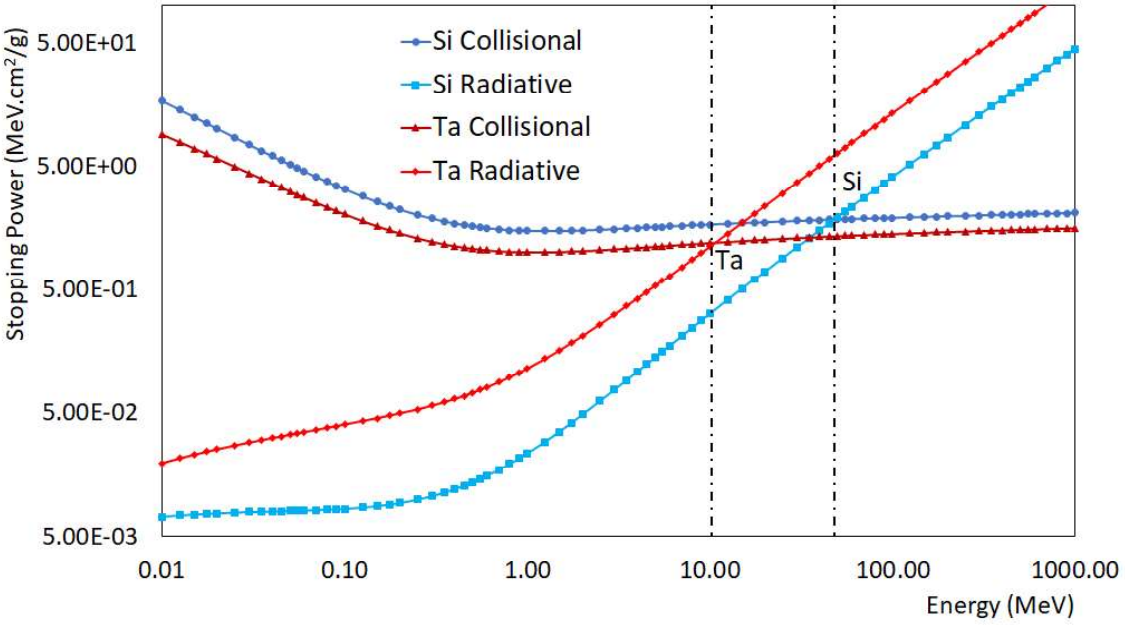

Figure 3.2: Electron collisional and radiative stopping power in Silicon and Tantalum. Data from [67].

(Bremsstrahlung) can be calculated as:

$$-\frac{dE}{dx}\frac{1}{\rho} = KZ^2E\left[ln\frac{2E}{m_ec^2} - 1/3 - f(Z)\right] \tag{3.3}$$

If the logarithm term is ignored, the energy loss increases linearly with the energy. At high energies however, the screening effect from the electron cloud must be considered and the formula becomes:

$$-\frac{dE}{dx}\frac{1}{\rho} = KZ^2E\left[ln\frac{183}{Z^{1/3}} - 1/18 - f(Z)\right] \tag{3.4}$$

Radiative energy loss is proportional to Z^2 which means that it depends highly on the atomic number. In fact, if one looks at the critical energy, E_c, the energy at which radiative energy loss is equal to the collisional one, it becomes apparent that radiative energy loss becomes non-negligible at lower energies for high Z materials. This comparison can be seen in Figure 3.2 for Silicon and Tantalum. For both materials, the critical energy is 50 and 12.5 MeV respectively [67]. As a consequence, at these energies electrons lose more energy in high Z materials. This is a consequence of higher Bremsstrahlung interaction rates and energies. The photons produced can travel larger distances in materials and further ionize the medium. From this perspective, it can be concluded that low-Z materials are better at stopping electrons, per unit of mass, for energies below E_c. For higher energies high-Z materials are more efficient. Emitted photons from the interactions are not negligible especially for TID estimation.

3.1.3 Heavy Charged Particles

Charged particles such as protons and heavy ions also lose energy via Coulomb scattering with both atomic electrons and nuclei. For higher energies (>>20 GeV), such as the ones of Cosmic Rays, radiative losses are also important [69]. The average rate of energy loss can be described by the Beth-Bloch formula:

$$-\frac{dE}{dx}\frac{1}{\rho} = Kz^2\frac{Z}{A}\frac{1}{\beta^2}\left[ln(\frac{2m_ec^2\beta^2\gamma^2W_{max}}{I^2}) - 2\beta^2 - \delta - 2\frac{C}{Z} + zL_1 + z^2L_2\right] \quad (3.5)$$

Where W_{max} is the maximum energy transfer in a single collision, I is the mean excitation potential of the target material, and δ is the density effect correction required for high energies. The three right terms refer to low energy corrections. They are, from left to right, the shell corrections which corrects for the atomic binding, the Barkas correction that includes the decreased energy loss by negative particles, and the Both correction [69]. The Bethe-Bloch equation is valid for β>0.05. For lower energies the Andersen-Ziegler formulae is used. Figure 3.3 shows the proton stopping power in Silicon, Aluminum and Tantalum. The stopping power varies slowly with Z especially near the minimum ionizing energy (∼1 GeV in protons). However, it is proportional to the density of the material.

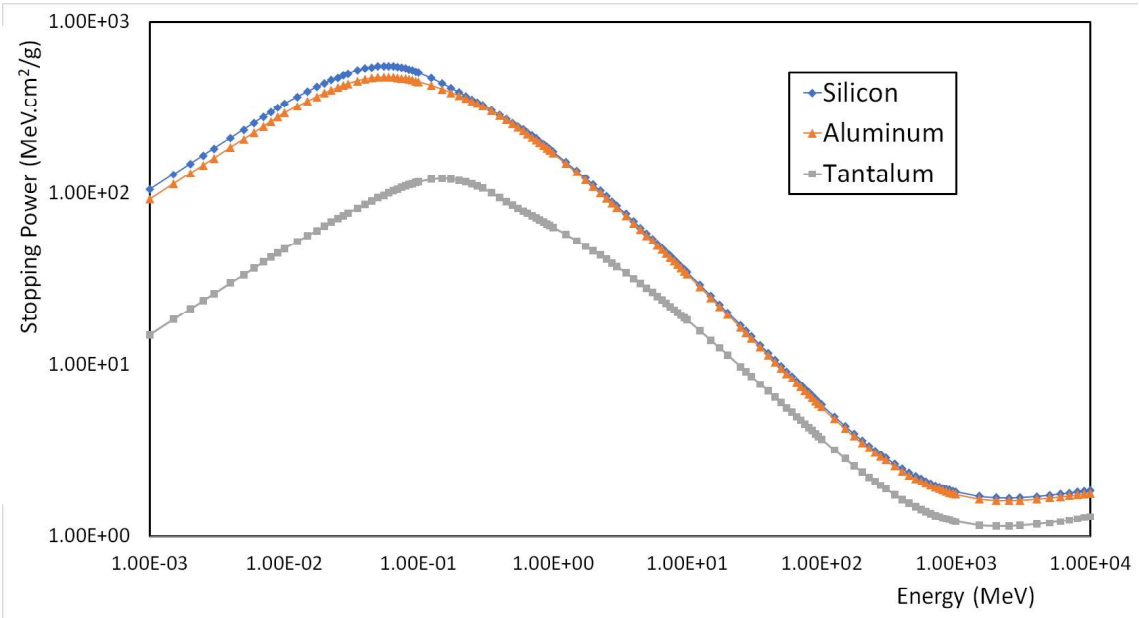

Figure 3.3: Proton stopping power in Silicon, Aluminum and Tantalum. Data from [73].

3.1.4 Straggling

So far we have discussed the average energy loss of charged particles in matter only. However, their path along a material consists of multiple collisions with atoms in the lattice, for which the energy loss in each collision is not always the same. Furthermore,

due to scattering, the path of the particles is not a straight line. Therefore, the energy loss of a single particle in a material follows a distribution which depends on the thickness of the target. For very thick absorbers, the energy loss follows a Gaussian distribution. In thin absorbers (such Silicon diodes) it can be shown that the energy of a particle crossing a material follows a highly-skewed Landau-Vasilov distribution, or more accurately a Bichsel function, as the one shown in Figure 3.4 [69][74]. In this case, the mean energy does not correspond to the peak since collisions of large energy loss (in the case of electrons up to half of their energy) are considered.

Let us define k as the ratio between the mean energy loss and the maximum energy transfer, W_{max}. For very low values of k (< 0.01), the distribution is equivalent to the one obtained by Landau. At very large values of k (>10), the distribution becomes Gaussian. Vasilov calculated the distribution for average values of k which matchs experimental data better since it drops one of Landau's assumptions: $W_{max} \rightarrow \infty$ [69]. This is the case of the Silicon diodes used in RADEM as it will become clear in Chapter 7. A consequence of Coloumb collisions is the ionization of atoms. Ejected electrons have very low energies for the most part. However, in large angle collisions, keV electrons can be released into the material. These particles, usually named δ-rays, can leave the initial volume and propagate to other regions.

It should be noted that Vasilov's theory does not take into account the binding energy of electrons nor the change in velocity in each collision.

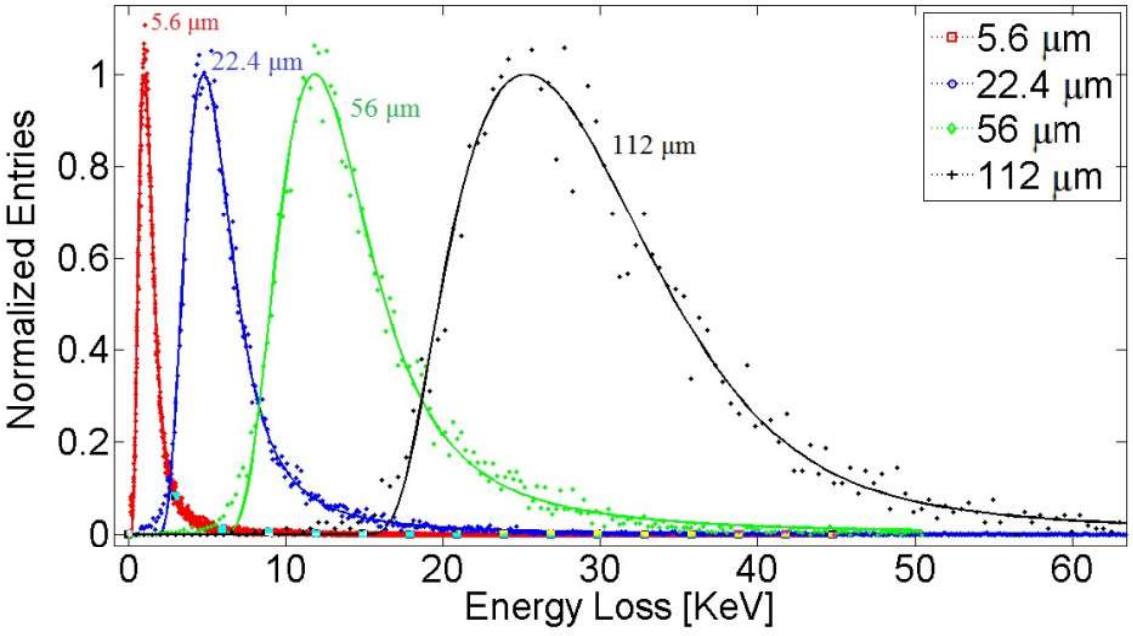

Figure 3.4: Energy loss distributions with fits for 12 GeV protons passing through several silicon thicknesses. From [75].

The range of a particle is also subject to straggling. While the range of a particle in a target material can be approximated with the Continuous Slow-Down Approximation (CSDA), because of the stochastic nature of energy loss it is actually a distribution and

not a single volume. If the target is thick enough, the distribution will resemble a Gaussian distribution as it can be seen in Figure 3.5. While straggling of heavy particles produces Gaussian distribution, electrons are much more susceptible to multiple scattering. Their path is much more chaotic which results in a very broad range distributions as it can be seen in Figure 3.6. This has large implications in detector response.

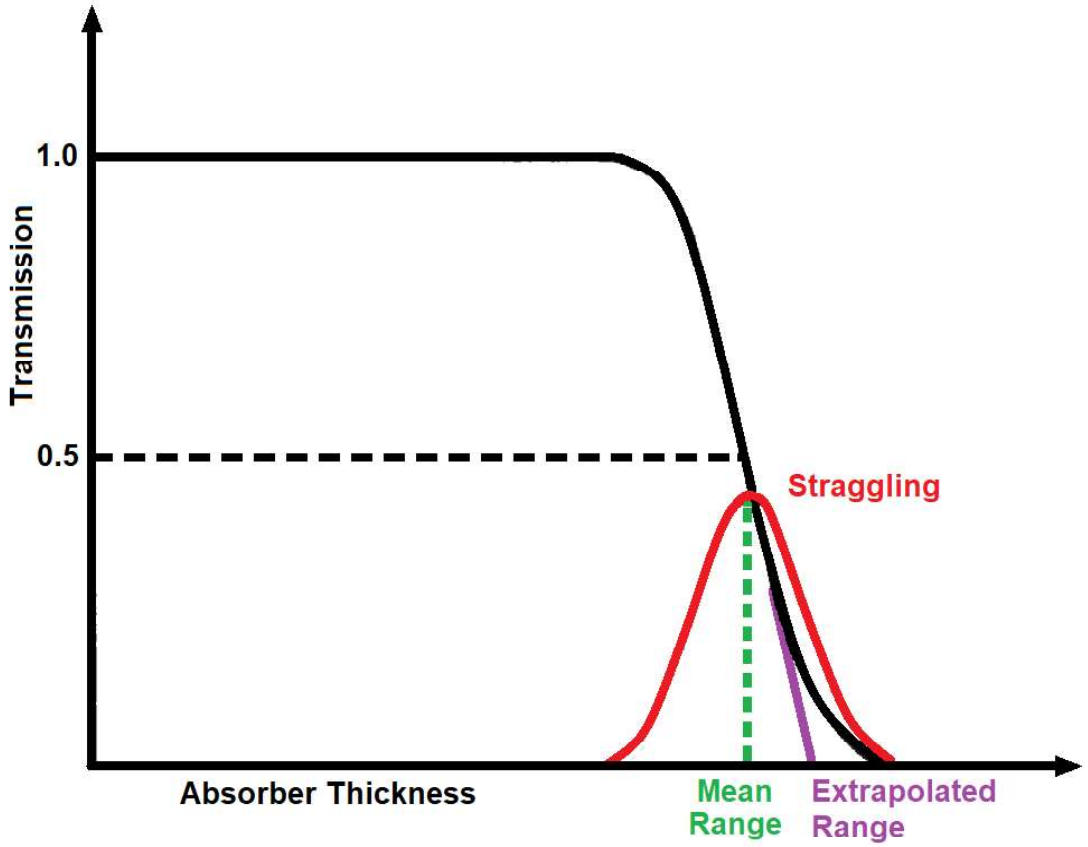

Figure 3.5: Typical transmission curve of heavy charged particles. The range is approximately Gaussian. Adapted from [69].

3.1.5 Multiple Coloumb Scattering

Coulomb scattering also affects the particle track. Unlike photons charged particles suffer a large number of collisions in a small path. It is then more useful to treat the problem as a series of collisions (Multiple scattering). Nevertheless it has be demonstrated already that single collisions between charged particle and an atom can be described with some degree of accuracy by the Rutherford formula:

$$\frac{d\sigma}{d\Omega} = z_2^2 z_1^2 r_e^2 \frac{\left(m_e c/\beta p\right)^2}{4sin^4(\theta/2)} \tag{3.6}$$

Where z_1 and z_2 are the charge of the two particles in the collision, r_e is the electron radius and θ is the scattering angle. The differential crossing section is inversely propor-

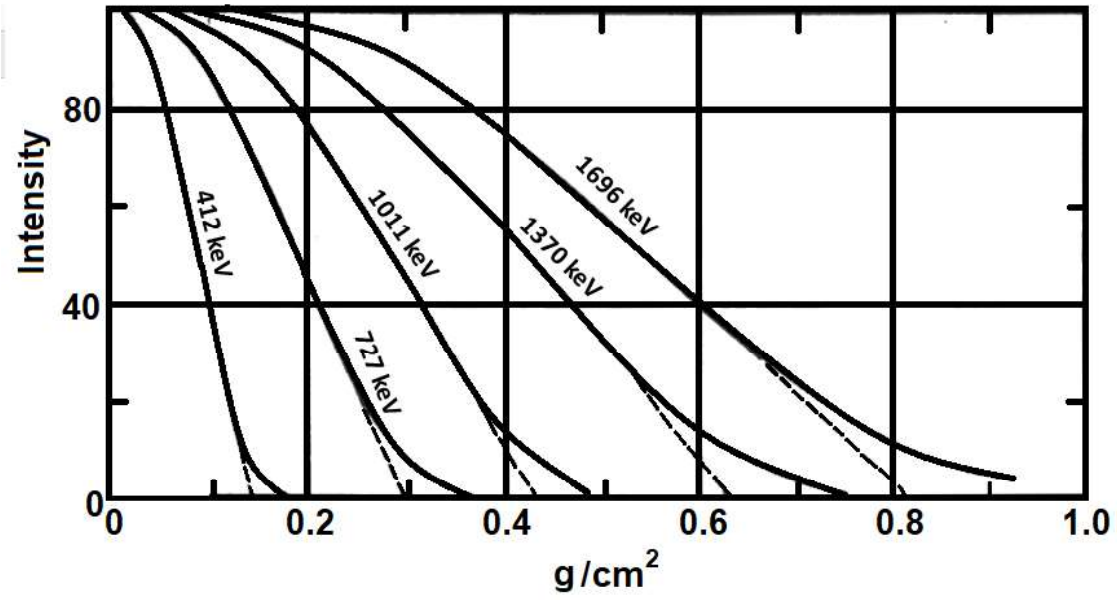

Figure 3.6: Range of electrons in Aluminum. Adapted from [69].

tional to the fourth power of the sin of the scattering angle meaning that most interactions result in small deflections. These are usually referred to as soft collisions. They can be treated statistically by Molière theory up to ∼30°[76]. For even smaller scattering angles (<10°), which account ∼98% of the collisions, the angular distribution can be described with a Gaussian distribution [61] [69].

There are two important quantities that need to be calculated: the change in direction θ_{space} and the deflection, y_{space}, from the initial line of entry. The track of a particle subject to Multiple Coulomb scattering in a target, projected into a plane, is described in Figure 3.7. Assuming a Gaussian distribution, θ_{plane} can be written as [61]:

$$\frac{1}{\sqrt{2\pi}\theta_0} exp\Big(-\frac{\theta_{plane}^2}{2\theta_0^2}\Big) d\theta_{plane} \tag{3.7}$$

Where $\theta_0 = \theta_{plane}^{rms}$. y_{space} can be calculated with the thickness of the material and the angle, Ψ, between the entry and exit points. Orthogonal projections are independent and can be treated the same way [61].

Larger angle scattering (hard collisions) is usually the result of single scattering and can be treated by the Rutherford formula with some corrections. Electrons are much more susceptible to large angle deflections since they have the same mass as their atomic counterpart. Nevertheless small angle and large angle deflections can be treated independently for electrons and for heavy charged particles [69][61].

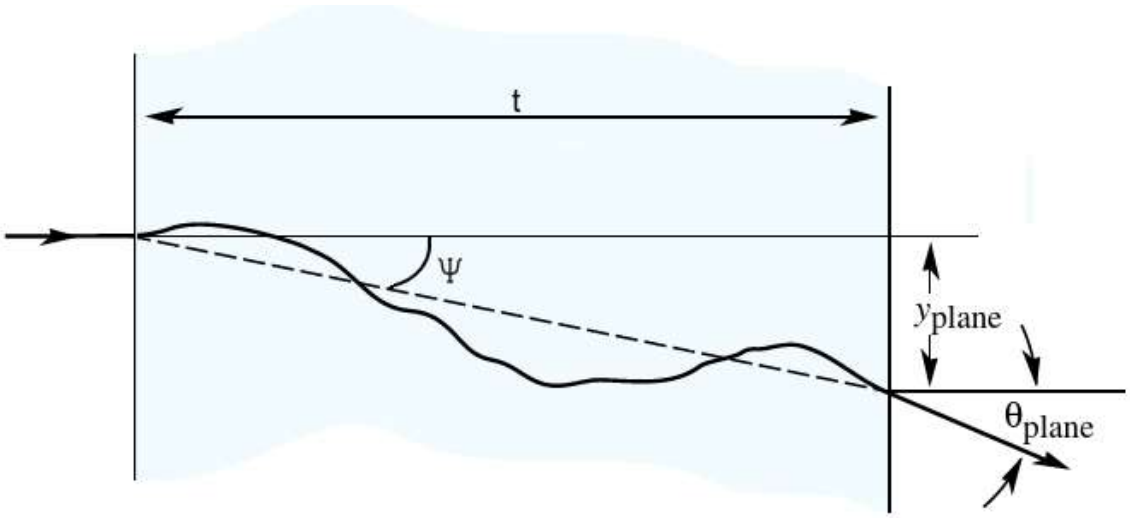

Figure 3.7: Projected Coulomb scattering in a plane. t is the thickness of the material, θ_{plane} and y_{plane} are the scattering angle and the deflection in the project plane respectively. Adapted from [61].

3.2 Nuclear Reactions

Hadrons can also interact with the atomic nucleus via the strong force. In the space radiation environment, protons and to some extent ions and neutrons are responsible for most nuclear interactions. While neutrons are chargeless, charged hadrons must overcome the Coulomb potential to interact directly with the nucleons. These interactions can be elastic or inelastic. Inelastic collisions can excite the nucleus (activation), break it, and/or produce secondary hadrons.

In space, hadronic collisions occur mainly between high energy cosmic rays and the atomic nucleus in materials of spacecrafts or for example in planetary surfaces. Hadronic collisions can produce electromagnetic showers consisting of pair production and electron-positron annihilation. Since the cosmic ray flux is much lower than that of trapped particles it was not is not considered in this thesis the only exception being Single Event Effect rate calculations. However these calculations are made based only on the initial particle energy and does take into account the physical processes of the interaction neither the secondaries that are produced.

Slow neutrons can also be captured by nuclei but they are not relevant for this thesis as well.

3.3 Monte Carlo methods for Particle Transport

Physical interactions must be simulated in different scenarios for a wide range of applications. This is usually done using Monte Carlo methods. Monte Carlo methods make use of pseudo-random number generators to determine the outcome of a series of statistical events. The idea is that outcome of consecutive probabilistic events can be computed

with a finite set of case-by-case analysis. Deterministic problems can also be solved by Monte Carlo methods if the solution to the problem is analytically impossible or very time consuming.

The Monte Carlo method was first proposed by Leclecrc in 1777. He determined experimentally the probability that a needle of length, l, dropped in a random position at a random angle, intersected the lines of a wooden floor composed of parallel stripes separated by a distance, d, as shown in Figure 3.8, as the ratio between the number of times the needles superposed with the stripes and the total number of throws.

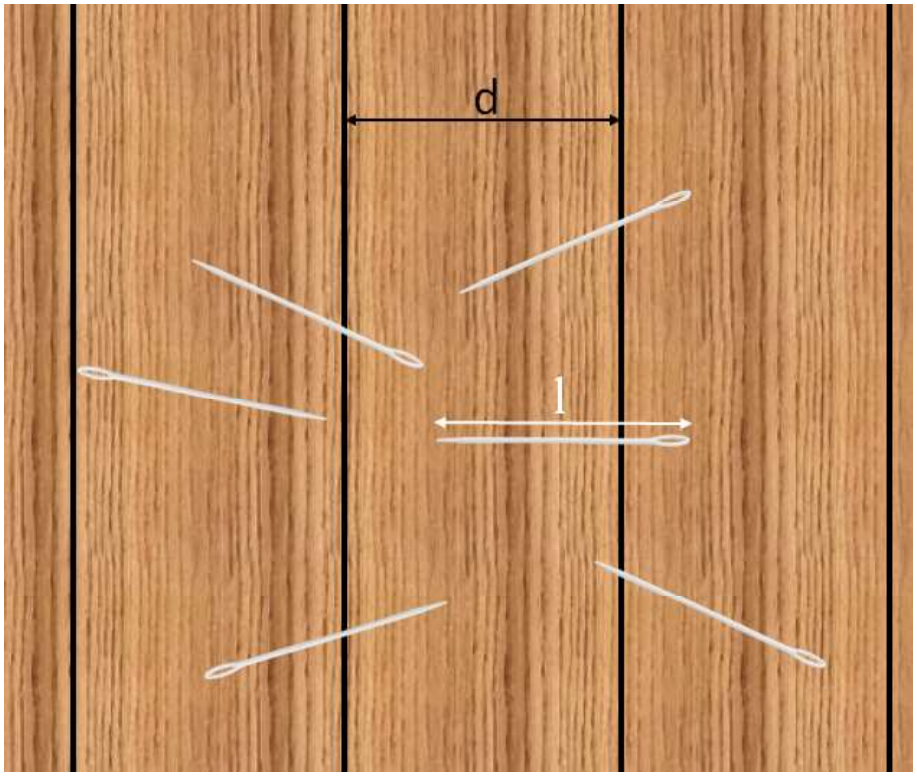

Figure 3.8: Buffon needle experiment.

Given that the needle length is smaller than the distance between stripes (l<d), then the probability, P, that the needle will cross a line is:

$$P = \frac{2l}{d\pi} \tag{3.8}$$

If the number of throws is large enough, P will be measured with high precision. Inverting the equation P can be used to calculate π. Computational speaking, the events can be simulated by generating two pseudo-random numbers, rand1 and rand2, with a uniform distribution between 0 and 1. The horizontal position, x, of the center needle can then be obtained by multiplying rand1 by the distance between the stripes. To obtain the angle, θ, rand2 is multiplied by 2π. Assuming that the left stripe is the origin of the horizontal axis, the two can then be used to determine if the needle intersects the stripes in the event. If one the two following conditions is true:

$$\begin{aligned} x - \tfrac{l}{2} cos\theta < 0 \\ x + \tfrac{l}{2} cos\theta > d \end{aligned} \tag{3.9}$$

Then, the needle crosses the stripes. P is the ratio between these events and the total number of events. Although pseudo-number generators are deterministic and periodic, state-of-the-art generators can compute a very large number of values (2^{64-1}) before re-starting the cycle.

3.3.1 Particle transport

In particle transport, the Monte Carlo method is equivalent to the Boltzmann Transport Equations. Though the equations can be solved analytically in some cases, for geometrical complex systems the time to find the solutions far surpasses the Monte Carlo method [42]. In Monte Carlo particle transport we need to obtain the probability that a particle will travel a distance x without interacting. First let us write the probability that a particle will not interact between x and x+dx, P(x, x+dx) [69]:

$$P(x, x + dx) = P(x)(1 - wdx) \tag{3.10}$$

Where wdx is the probability that a particle will interact between x and x+dx. Assuming dx to be very small (much smaller than x), we can re-write the former equation as:

$$P(x) + \frac{dP}{dx}dx = P - Pwdx \tag{3.11}$$

Solving for P:

$$P = Ce^{-wx} \tag{3.12}$$

where C is a constant. Since, by definition P(0)=1, C is also 1. w can be shown to be the inverse of the mean free path, λ:

$$w = \frac{1}{\lambda} = \sigma\eta \tag{3.13}$$

Where σ is the total cross-section of the particle in a give material and η is the number density of the material. The distance traveled by a particle between collisions can then be obtained 3.12:

$$x = -\lambda ln(1 - P) \tag{3.14}$$

Since P is a uniform distribution between 0 and 1, the distance of a particle to the next collision can be calculated by generating a pseudo-random number between 0 and 1. λ can be obtained from empirical databases or by theoretical models. Considering that a particle does interact after a given distance, the nature of the interaction must also be addressed. If the particle has n-modes of interaction in the material, then, the sum of the

probability of all processes must be equal to one:

$$\sum_{i}^{n} \frac{\sigma_i}{\sigma} = 1 \tag{3.15}$$

Finally, the probability of interaction of each process can be distributed between 0 and 1 according to the ratio $\frac{\sigma_i}{\sigma}$ as it can be seen in Figure 3.9. A good example of this are gamma-rays. A 4 MeV gamma interaction ratios in Silicon are 1.22E-02, 8.91E-01 and 1.08E-01 for the Photoelectric effect, Compton Scattering and Pair Production respectively. The probability distribution can then be converted to a Cumulative Density Function: [0,1.22E-02[for the Photoelectric effect, [1.22E-02, 8.91E-01[and [8.91E-01,1] for the same three processes [70]. Assuming that the generated number was 0.5, then the particle would interact via Compton scattering.

Following process selection, the dynamics of the interaction has to be resolved. For Compton scattering the angle of scattering must be calculated based on the angular probability.

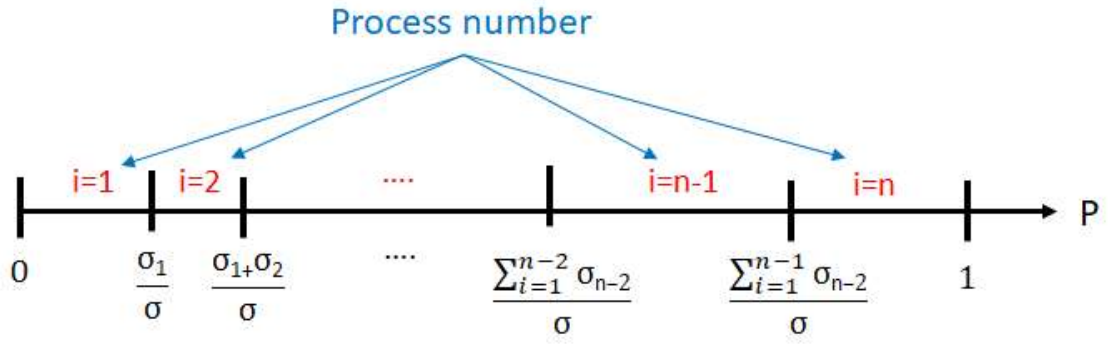

Figure 3.9: Process probability distribution.

This is the basis of Monte Carlo particle transport. Depending on the particle and the energy different assumptions and methods have to be applied. For instance, electrons and protons have a very small mean free path which makes it impractical to simulate all collisions. In this case, different methods exist such as the multiple Coulomb scattering model which computes the net scattering of several collisions [42][76][77][78]. Another issue is the generation of secondaries and the energy cutoff. It is not practical to follow each particle down to rest. Monte Carlo codes usual allow users to select the energy cutoff, the energy below which it is considered that a particle loses all its energy in the volume it is located, or range cutoff, which instead considers the mean free path of the particle [42][32].

It can be concluded that there are two major areas in Monte Carlo particle transport: Geometry and Physics. Implementation of both is not always trivial and can vary from code to code [30][31][32][79][80].

3.4 Geant4

Geant4 is a multi-purpose particle transport simulation toolkit [30][31][32]. The toolkit is built in the Object Oriented language C++ succeeding Geant3 [42]. The full source code can be read and edited which is extremely useful because any user can evaluate and modify features, physics models, and methods of the toolkit. Originally the code was developed for High Energy Physics with applications in particle physics, cosmic rays, astrophysics and others [30][42]. The toolkit is in continuous development. Recently it expanded the range of applicability to radiobiology with the introduction of a low energy physics list - Geant4DNA [32]. Though other codes to compute particle transport in materials such as MCNPX [79] and FLUKA [80] exist, access to the source code and/or the extent of physics databases may be limited.

3.4.1 Physics Models

As it was discussed before, an important part of the Monte Carlo methods is the physics models. These models calculate the probability and dynamics of interactions between a particle and the medium depending on the particle type, energy and target material. Geant4 offers a broad range of physics models from eV to PeV [32]. Physics models can be combined to form a physics list, a compilation of processes and models that are employed in the propagation and interaction of particles. This is extremely useful because no single model can accurately reproduce the physics processes of all particles for all energies. Geant4 allows users to select their own physics list or to use a pre-built reference list. Pre-built lists have the advantage of being optimized for specific applications and of having been validated up to some degree by the developers. For shielding studies in the fields of high energy, and space science/engineering, there is a pre-built physics list named "Shielding". The Shielding Physics list is an extension of the QBBC [44] which is already recommended for medical and space applications with the addition of high precision neutron tracking below 20 MeV. The Physics List can be divided into three categories: Electromagnetic; Hadronic; and Decay [42][32][81].

Electromagnetic

The "Shielding" Physics uses Geant4 standard Electromagnetic physics processes and particles. It is valid for gammas, charged leptons and several hadrons such as protons and ions. For gammas all the main processes are included between 0 and 100 TeV. Electron and positrons are treated up to 100 TeV including both Ionization (Moller-Bhabha formulation [82]) and Bremsstrahlung (Seltzer-Berger models [83][84]). Protons are treated with the Bragg model below 2 MeV (cross-sections from NIST [73]) and the Bethe-Bloch formulation is used above this energy.

An important aspect of the physics list is Coulomb multiple scattering calculations. Unlike photons, where the mean free path is large and collisions can be treated discretely,

charged particle scattering occurs in very short paths. To optimize the computing time, a condensed history of multiple scattering is used [42]. The net result of multiple scatterings is calculated over a step length. The final direction and displacement with relation to the path of the particle is calculated for each step. This method is combined with a single scattering method for hard collisions. The two processes (single and multiple scattering) compete based on their probabilities for a given particle/energy/material combination. Up to 100 MeV, Geant4 uses the Urban model [85]. Above this energy it resorts to the WentzelVI model [86].

Hadronic

Hadronic interactions are diverse and no single model exists that fully describes the full list of processes it involves. Geant4 splits the hadronic component into four main processes: elastic, inelastic, capture and fission. At energies up to a few GeV, inelastic scattering of protons and neutrons is treated by the Binary Light Ion Cascade [87] and the Bertini Intra-Nuclear Cascade [88], which considers that the primary particles interact with individual nucleons of the nucleus. For higher energies it is handled by the Fritiof parton model [89][90]. Gammas photo-nuclear interaction is also included as well as electron virtual photon exchange with the nucleous via the Bertini Cascade model. Neutron capture is also included.

Elastic scattering is treated for both protons and neutrons from 0 to 100 TeV. Other hadrons are modelled with different levels of detail. [81]

Decay

The "Shielding" physiscs list includes all ion decay processes in Geant4 database as well as long-lived hadron and letpon decays [81].

3.4.2 Geometry and Navigation

For particle transport the path of particles inside a number of volumes has to be calculated as well. Geometries in Geant4 can be described through several classes, which reproduce simple geometric shapes such as parallelepipeds, spheres and cylinders among others, and by combining them via Boolean operations. For more irregular solids, geometries can also be defined by boundary representation such as splines, b-splines or tessellated surfaces [32].

For tracking purposes, one needs to locate the particle inside a solid, and to calculate the distance and the position of the next boundary inside the same solid. Different geometries require different techniques. Calculation of the position of a particle inside a sphere for instances is of $O(1)$. In fact, in this case both the position, and the boundary intersection location can be calculated with the solid boundary conditions, $x^2 + y^2 + z^2 < r^2$. For complex geometries such as tessellated solids the method is much more complicated. It is a multiple step process linearly proportional to the number of facets, n, $O(\mathrm{n})$ [91]. This has important consequences in the framework of this thesis because most volumes are

defined as tessellated solids. Although the method is slower it allows to describe complex geometries which is not always possible with regular solids.

3.5 Summary

In this Chapter the relevant processes of the interaction of particles with matter in space were introduced along with the techniques that enable to track the particle path in a given volume. This is an important field not only for space but for all applications where radiation is present. Radiation interaction with matter is a broad subject which does not need to be extensively discussed here.

Monte Carlo simulation for particle transport is a powerful tool that has been developed over the years. Progress in computational power has increased the range of applications. However, it requires thoroughly validation and does not, in any circumstance, replace experimental measurements. It also does not describe nature in its entirety but in an approximate useful way.

Geant4 is one of the most popular Monte Carlo codes for particle transport. It has a large history of use in high energy physics and has proven to be adequate for space applications. Several engineering tools based on Geant4 are recommended for use in European Cooperation for Space Standardization (ECSS) norms [26].

4 Radiation Effects and RHA of EEE Components flown to Jupiter

Spacecraft systems rely heavily on semiconductor technologies to perform their required function for the entire mission lifetime. However, Electric, Electronic and Electromechanical (EEE) components are known to degrade to the point of malfunction when subject to large cumulative, or instant, absorbed doses of radiation. Exposure to the space radiation environment affects devices in different ways related to component type and mode of operation. Therefore, thorough understanding of the mechanisms, effects and response of components to radiation, is essential to launch a successful mission. In this chapter, the basic aspects of semiconductor devices and the effects of radiation as well as the activities that compose the Radiation Hardness Assurance (RHA) process will be presented.

4.1 Semiconductor technologies

Semiconductor materials are crystalline structures made of elements in the 14^{th} group of the periodic table such as Silicon and Germanium. These materials have electrical conductivity between that of metals and insulators. Complementary binary compounds such as Gallium Arsenide can be semiconductors as well. Semiconductors have a small forbidden bandgap, between the valence and conduction bands, where the Fermi level lies. To improve electrical conductivity, the bandgap width can be decreased by the addition of impurities to the material via ion implantation for example (doping). These impurities are known as donors if they have more valence electrons than the semiconductor material or acceptors if they have less. While donors populate the conduction band with electrons pushing the Fermi level away from the valence band (n-type semiconductor), acceptors contribute with holes putting the Fermi level closer to the valence band (p-type semiconductor). Holes are atoms that lost one of its valence electrons and that, for the purposes of electric conductivity, behave as positively charged particles moving through a semiconductor. Both electrons and holes are considered the charge carries in n-type and p-type semiconductors respectively. Doped semiconductors have better electrical conductivity than intrinsic (pure) semiconductors.

The contents presented in this section are based mainly on [92] and [93].

4.1.1 P-N Junctions

N-type and p-type semiconductors are the basis of modern electronics. Both types can be combined to form a p-n junction. As a result of this junction, electrons will diffuse from the n-type region to the p-type region while holes diffuse in the opposite direction. As the particles diffuse, an increasingly stronger electric field is created, countering this movement until equilibrium is met (see Figure 4.1). Between the two types a new depletion region of very low conductivity, where the valence bands are filled, appears. If an increasingly positive potential is applied to the p-type, the depletion region size will decrease, and the material conductivity will rise linearly until it saturates. If a negative potential is applied however, the depletion region size will increase, and no current will pass. This is the principle of operation of a diode .

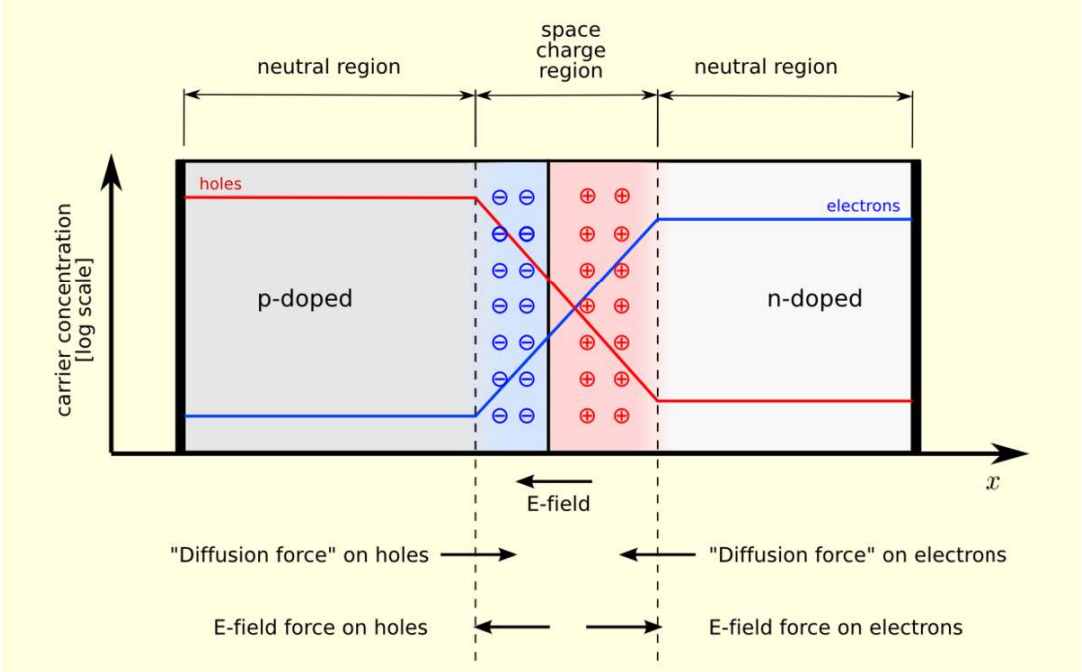

Figure 4.1: Schematic of the forces that act on electrons and holes and charge carrier concentration in a p-n junction.

More complex devices with multiple p-n junctions with broader applicability have been developed. Transistors are the most common of such devices. The first transistor was patented in 1926 by Julius Edgar Lilienfeld [94] but it was implemented for the first time only in 1947 by John Bardeen, Walter Brattain and William Shockley. Transistors revolutionized the field of electronics and are the building blocks of most EEE components. For this reason, its inventors were awarded the 1957 Nobel Prize in Physics [95]. The two most commonly used transistors are the Metal-Oxide-Semiconductor Field-Effect-Transistor (MOSFET) and the Bipolar Junction Transistor (BJT).

4.1.2 Metal-Oxide-Semiconductor Field-Effect Transistors

Metal-Oxide-Semiconductor Field-Effect Transistors (MOSFET) are a class of unipolar transistors that use electric fields to control its behavior. Its electric current is driven predominantly by one charge carrier in contrast to bipolar transistors where both charge carriers are responsible for it.

4.1.2.1 Basic Structure and Working Principle

MOSFETs are four-terminal devices with a p or n-type substrate and two highly doped n or p-type regions, the source and the drain, with a distance, l, between them, as shown in Figure 4.2. An oxide or an insulator, of thickness d, separates the device from the gate contact, usually a metal or polysilicon (SiO_2). A thick field oxide is also used to isolate devices within the same substrate.

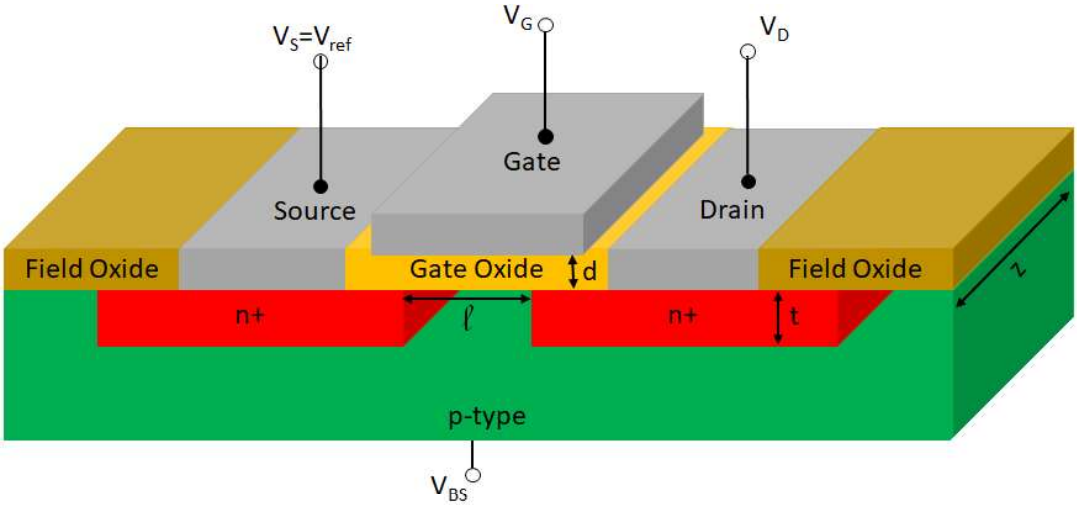

Figure 4.2: Basic structure of a n-type (NPN) MOSFET. The substrate is shown in green and the highly doped n channels are in red. The contacts with the Source, Drain and Gate are in gray, the Gate Oxide in yellow and the Field Oxide which separates devices in the same substrate in dark yellow. The thicknesses of the n channels, t, and Gate Oxide, d, gate length, l, and depth, z, as well as the doping of the n-channels, N_A, determine the properties of the MOSFET.

To understand the working principle of a MOSFET, the substrate and the source can be considered grounded though this is not necessarily true in all applications. If the Gate and the Drain voltages are zero (V_G=V_D=V_S=0) then no current flows through the device and two depletion zones are formed around the n-doped regions as a result of the p-n junctions. If a positive voltage is applied to the Gate, holes close to it will be pushed away creating a neutral layer in the oxide-substrate interface. If V_G is high enough (larger than the Threshold Voltage, V_{th}), a highly conducting inversion layer will appear connecting the two n+ regions. At this stage the MOSFET is considered "On". The voltage at which the inversion layer appears is lower for higher temperatures since more charge carriers move from the valence band to the conduction band. Further increasing V_G will alter its conductance. V_{th} is a function of the semiconductor bulk potential, Ψ_B,

permittivity, ϵ_S, elementary charge, q, impurity density, N_A, and the capacitance per unit of area, C_i, as given in equation 4.1:

$$V_{th} = 2\Psi_B + \frac{\sqrt{\epsilon_S q N_A \Psi_B}}{C_i} \tag{4.1}$$

Adding an additional voltage between the Source and Drain, puts the MOSFET in a state of non-equilibrium; that is, the Fermi level of electrons near the Drain is lowered, and a current, I_D, flows from the Source to the Drain. I_D increases linearly with V_D (ohmic region) until the conducting channel depth reduces to zero. At this point I_D remains constant (saturation region). Saturation voltage (V_{sat}) is strongly related to V_G as it can be seen in the I_D vs V_D curve shown in Figure 4.3. The current in the Drain of an ideal MOSFET can be shown to be:

$$I_D = \frac{l}{t}\mu_n C_i \left\{ \left(V_G - 2\psi_B - \frac{V_D}{2} \right) V_D - \frac{2}{3}\frac{\sqrt{2\varepsilon_S \mathrm{q} N_A}}{C_i} \left[(V_D + 2\psi_B)^{3/2} - (2\psi_B)^{3/2} \right] \right\} \tag{4.2}$$

Where l and t are the channel length and depth respectively. In the ohmic region, V_D is small enough that this equation becomes linear:

$$I_D = \frac{l}{t}\mu_n C_i (V_G - V_{th}) V_D \tag{4.3}$$

MOSFET doping, gate length and depth as well as drain and source thickness, can be manipulated in the manufacturing process to optimize its properties for specific applications. P-type MOSFETs have the same working principle but with reversed polarities.

4.1.2.2 Floating-Gate MOSFET

Different MOSFETs with altered structures also exist. Floating-Gate and Metal-Insulator-Oxide Semiconductors (MIOS) devices for instance are the two groups of non-volatile memories. Floating-Gate MOSFETs have an additional metal gate layered between a thin insulator in contact with the substrate and a thick insulator in contact with the gate metal contact as displayed in Figure 4.4. If a negative voltage is applied to the gate, charge carriers will cross the thin insulator into the metal but will pass through the thick insulator changing the threshold voltage of the device. The charge, and consequently the shift in threshold voltage, will remain in the metal between both insulators for tens of years with the device unpowered. Applying a positive voltage on the other hand will push the charge into the substrate returning the MOSFET to the initial state. The device can then be used as memory bit where its value depends on the existence of certain amount of charge (threshold voltage shift) [97]. These MOSFETs are the basic cell of Flash memories which can be of NOR and NAND type named due to their similarity to the gate logic with the same name. Bits are read as 1 when a NAND-type memory MOSFET gate charged and a 0 when it is not. The opposite applies for NOR-type memories.

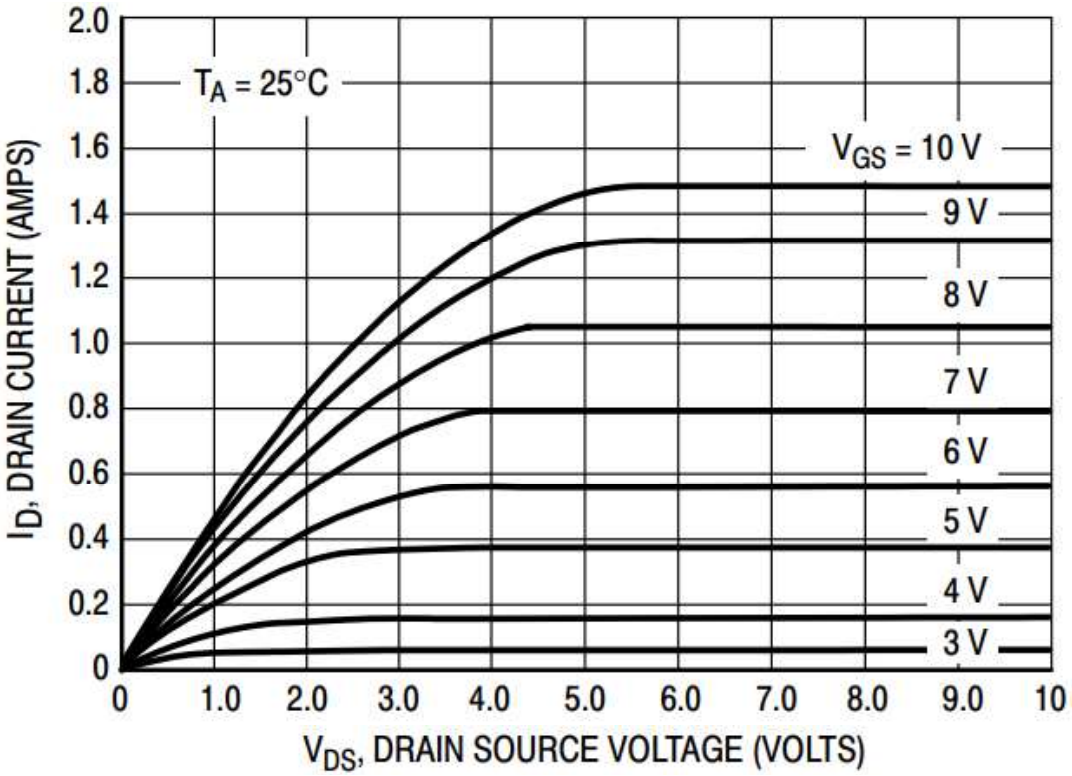

Figure 4.3: IV curve of a 2n7000G n-type MOSFET. It can be seen that the Drain current is limited by the Gate voltage [96].

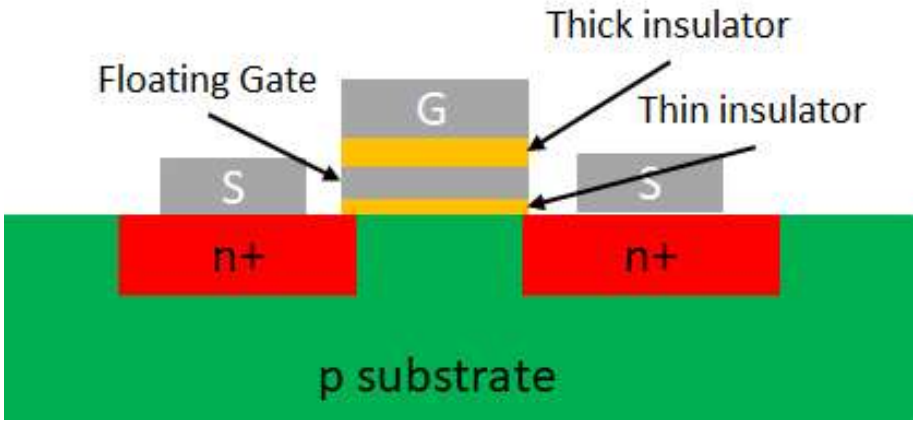

Figure 4.4: Floating-Gate transistor structure. A metal gate is layered between two insulators. The insulator closer to the device substrate allows charge to be injected into the floating gate when the voltage is applied to the Gate and contains it when this voltage is zero.

4.1.2.3 Complementary Metal-Oxide-Semiconductor

Complementary Metal-Oxide-Semiconductors (CMOS) are the most common Integrated Circuit (IC) devices used in logic and memory applications such as Static Random-Access Memories (SRAM), microprocessors and other digital and analogue circuits [98]. They were first patented by Frank Wanlass in 1963 [99]. CMOS combine both p-type and n-type MOSFETs forming highly dense circuits.

The simplest CMOS device, a logic inverter, built in a p-type substrate semiconductor, has two n-channels similarly to a p-type MOSFET, and a n-type well with two p-type channels separated from the n-channels in the substrate as shown in Figure 4.5. V_{DD}, the power supply voltage, is usually kept above the threshold voltage of the MOSFETs. When V_{in}=V_{DD}, the potential between the Source and the Gate of the PMOS (V_{GS}) is zero hence V_{out} is in open-circuit with V_{DD}. On the other hand, the Gate-to-Source voltage in the NMOS is equal to V_{DD} which means that the channel works as a resistor and V_{out} will become zero. In both cases the current in static mode is close to zero. This means that power consumption and heat dissipation are very low when the device is not switching modes.

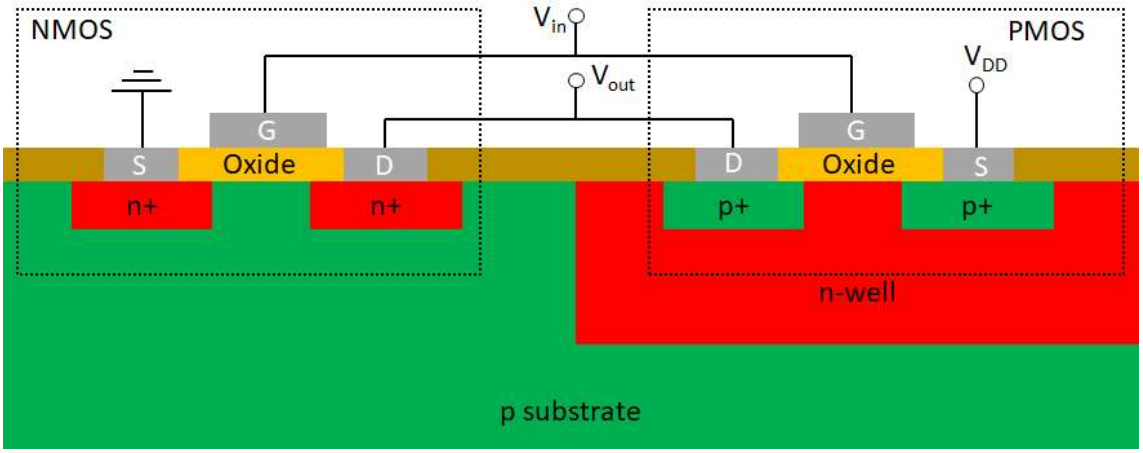

Figure 4.5: CMOS structure with the same color coding as Figure 4.2.

4.1.3 Bipolar Junction Transistors

Though CMOS are the most commonly used devices in ICs nowadays, Bipolar Junction Transistors (BJTs) were the premier component for several decades after its invention in 1948 at the Bell Telephone Laboratories. It is also used as a discrete device in many fields and is currently combined with MOSFETs or CMOS to form new technologies known as BiMOS or BiCMOS respectively. BJTs are three-terminal devices as displayed in Figure 4.6. These three regions known as Emitter, Base and Collector form two p-n junctions. This section will focus on npn BJT such as the one in Figure 4.6 but the same principle can be applied for PNP BJTs with reverse polarity. For reasons that will be clear later, the Emitter doping is much higher than the other regions hence there is no interchangeability between the Emitter and the Collector. The Base must also be made thinner than the other two regions and must be surrounded by the Collector. BJTs can operate in four working modes of operation depending on the potential applied to the p-n junctions as shown in Table 4.1. Despite this only three modes are commonly used since the Reverse Active mode has little application.

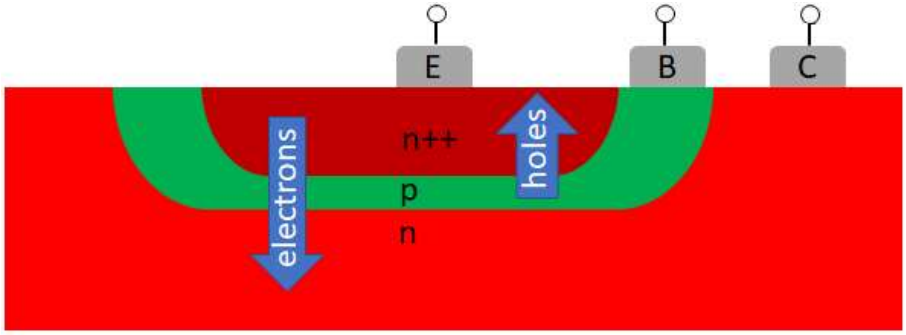

Figure 4.6: Bipolar Junction Transistor vertical structure. BJTs can also be made with a horizontal geometry.

Table 4.1: BJT operating modes.

Mode of operation	EB Junction	CB Junction
Active	Forward	Reverse
Cutoff	Reverse	Reverse
Reverse Active	Reverse	Forward
Saturation	Forward	Forward

4.1.3.1 Operation in Active Mode

When in Active Mode, V_{BE} >0, electrons from the emitter will be pushed towards the Base region while the holes will move on the opposite direction. The electron current will be much higher than the holes one due to the high impurity density in the Emitter. Also, since the base is thin, a large number of electrons will not recombine until they reach the Collector-Base Junction. These electrons are then swept from the Collector-Base junction to the collector region due to V_{CB} >0, originating the collector current I_C. The current can be modulated as:

$$I_C = I_S e^{\frac{V_{BE}}{V_T}} \tag{4.4}$$

Where I_S is the saturation current and V_T the thermal voltage. The saturation current itself is a function of the base width, intrinsic carrier density, cross-sectional area of the Base-Emitter junction, electron diffusivity and doping concentration of the Base. An important feature of BJTs is that I_C weakly depends on V_{CE} as long as it is positive. In fact, I_C can be controlled strictly with V_{BE}. Another important factor is that I_S, is inversely proportional to the base width, which means that this property can be manipulated in the manufacturing process to optimize it for different applications. The Base current on the other hand is composed of two components, the holes injected from the Base to the Emitter and holes that have to be supplied to it from the external circuit to replace the holes lost in recombination. I_B can be obtained with:

$$I_B = \frac{I_S}{\beta} e^{\frac{V_{BE}}{V_T}} = \frac{I_C}{\beta} \tag{4.5}$$

This means that I_B and I_C are correlated by a constant, β, known as the common-

emitter current gain. From the Kirchhoff laws one can determine then that the Emitter current, I_E, must be equal to the sum of the Base and Collector currents. I_E can then be written as a function of I_C:

$$I_E = \frac{\beta}{\beta + 1} I_C = \alpha I_C \tag{4.6}$$

Where α is the Common-Base current gain. This variable, as well as β and I_S , dictate the response of a transistor when a positive voltage is applied between the Base and the Emitter. this way the transistor can be used as an amplifier in a controllled manner.

4.1.3.2 Saturation and Cutoff Modes

Though V_{CE} is used at positive voltages, electrons can still go through the CB Junction if the voltage is slightly negative. However, at $V_{CB} \sim -0.4V$, the minority carrier density in the Base, electrons, starts to increase since it can no longer transverse the junction into the collector. This means that I_C starts to decrease until no electrons are collected and I_C reaches zero. This is considered to be saturation region. If on the other hand V_{BE} is lowered, electrons from the Emitter will stop to diffuse to the Base and consequently no current goes through the transistor (cutoff mode).

In a circuit as the one displayed in the left side of Figure 4.7, V_{CE} can be controlled with the Base. If the transistor is in cutoff mode (I_B=0), then I_C will be zero and V_{CE}= V_{CC}=3V. On the other hand, if I_B=30μA then $I_C R_C$=V_{CC} and consequently V_{CE}=0. This is the principle of operation of a logic switch. Observing the transfer curve on the right side of Figure 4.7 one can see that in the active region the BJT acts as an amplifier since I_C increases with I_B as described in the previous section.

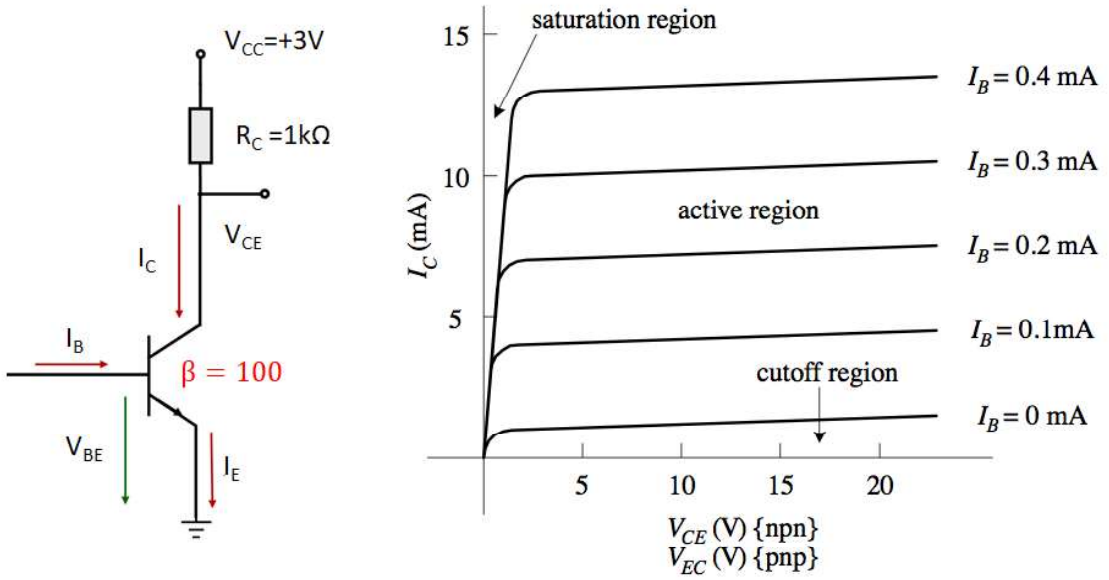

Figure 4.7: Common BJT circuit (left) and a typical transfer curve (right).

4.2 Total Ionizing Dose

Energetic particles from the space radiation environment lose energy crossing semiconductors devices by producing electron hole pairs (ionizing radiation) and/or by displacing atoms in the lattice (Displacement Damage) by Rutherford and nuclear scattering. The Total Ionizing Dose (TID) is defined as the absorbed energy of a material by ionizing radiation per unit of mass. It can be measured in SI units as Joule per Kilogram – Gray (1 Gy = 1 J/Kg); or CGS units erg per gram – rad (1 rad = 100 erg/g = 0.01 Gy). The deposited energy depends on the incident particle energy and type, as well as on the material. For this reason, values of TID must relate to the target material, e.g., 10 krad(SiO_2).

4.2.1 TID Mechanisms in MOS Devices

The mechanisms that lead to the degradation of MOS components due to ionizing radiation can be divided into four physical processes, as shown in Figure 4.8: production and recombination of electron-hole pairs in SiO_2; hole transport in the lattice; deep energy trapping in the SiO_2 bulk and close to the Si/SiO_2 interface; and radiation induced interface traps right at the $Si\text{-}SiO_2$ interface. The different time scales at which these processes occur, and correspondent annealing (de-trapping), dictate the type and magnitude of the effect seen in the MOS device operation [1][2][3].

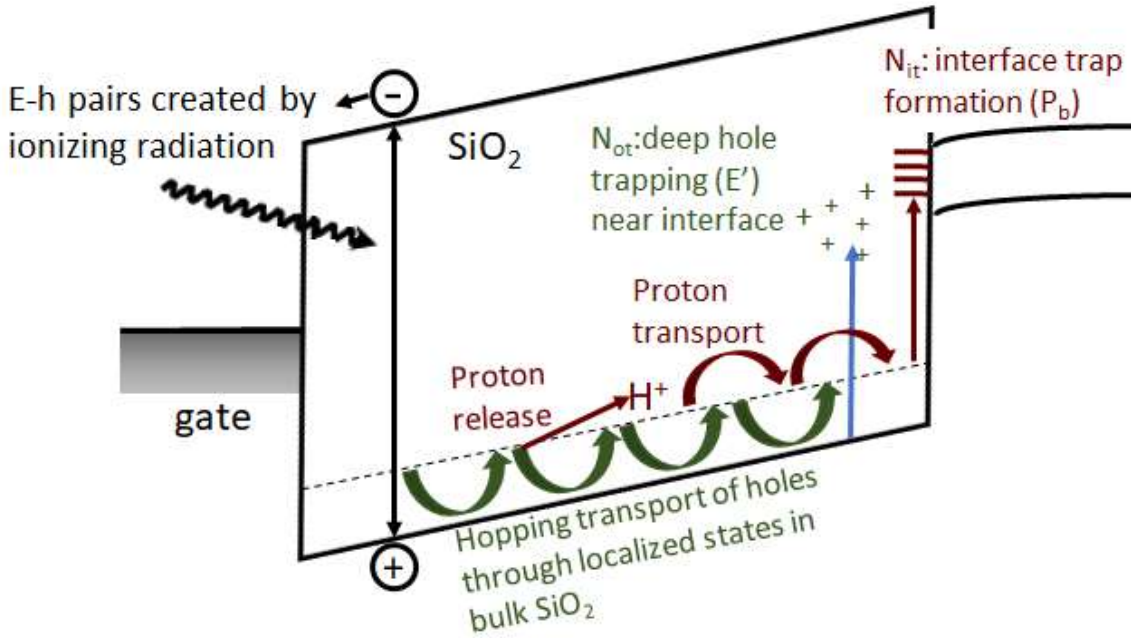

Figure 4.8: Schematic energy band diagram for MOS structure, indicating the major physical processes underlying radiation response. Adapted from [2].

4.2.1.1 Electron-Hole Production

Electron-hole pairs are generated when an incident particle, mostly electrons and protons in space, transfers enough energy to an electron so that it migrates from the valence to the conduction band. The minimum energy to excite an electron is known as the minimum ionization energy. It is equal to the energy bandgap of the semiconductor. Since the energy levels of the semiconductor are much lower than the energy deposited by a particle in the material, a single hit in the material produces a large number of electron-hole pairs from the valence band. Also, the valence and the conducting bands are semi-continuums, hence it is more important to consider the average ionizing energy which is slightly higher as shown in Table 4.2 for different materials.

Table 4.2: Minimum and average ionization energies for different semiconductors and SiO_2 at room temperature [56].

	Si	**Ge**	**GaAs**	**SiO_2**
Minimum Ionization Energy (eV)	1.12	0.7437	1.519	8.9
Average Ionization Energy (eV)	3.62	2.9	4.8	17

Electrons produced by ionizing radiation escape the oxide in a matter of picoseconds due to their high mobility. Some of them, however, recombine with holes. The net hole number depends on the magnitude of the electric field and on the initial line density of the produced charged pairs, which is a function of the energy and type of the incident particle. Lower densities result in lower recombination numbers and consequently a larger number of holes. The number of positively charged holes produces a positive electric field in the gate increasing the threshold voltage in pnp MOSFETs and decreasing it in npn MOSFETs [1][2][3]. The recombination problem cannot be solved analytically unless pairs are assumed to be far apart (geminate model) or very close (columnar recombination model) [2]. In Figure 4.9 the fractional yield of different radiation types as a function of the electric field in SiO_2 is shown. Notice that up to 3 MV/cm, ^{60}Co and 12 MeV electrons have the larger yields. Above this value, net pair separation increases slowly until no recombination occurs. 10 keV X-rays and 5 keV electrons display the same results for large enough electric fields. These results are a compilation of several studies over many years, but no single solution exists to predict the charge yield of irradiated components [2].

4.2.1.2 Oxide-Traps

There are two primary defect types in the oxide (SiO_2) (OT): shallow defects (or trap), located in the oxide bandgap within 1.0 eV of the valence band; and deep traps, 3.0 eV above the energy of the same valence band. Shallow traps are thought to be responsible for the hole transport mechanism, which frees Hydrogen atoms (originated from the passivation process) in the form of protons. Transport is highly dependent on the temperature, field and thickness of the oxide lasting several orders of magnitude

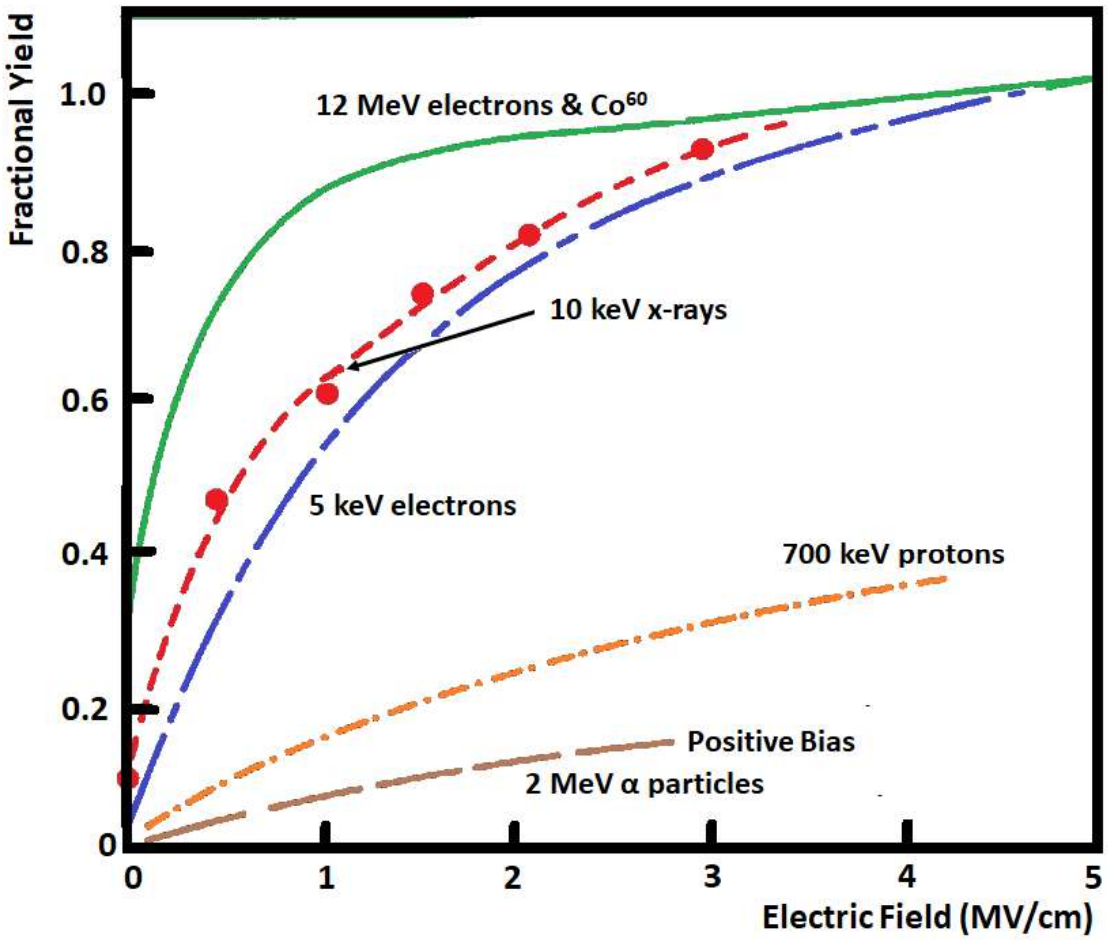

Figure 4.9: Fractional yield of holes generated in SiO_2 as a function of the electric field in the material. Adapted from [1].

in time. Deeper traps originate in oxide vacancies as a consequence of an incomplete oxidation process that leaves dangling bonds in Silicon. They are distributed along the whole oxide, but are in much greater numbers close to the Si/SiO_2 interface. Deep oxide-traps anneal over several years due to their long-term stability, depending on bias and temperature conditions. At lower temperatures, e.g., room temperature, a mechanism where an electron is exchanged between the trap and the Silicon substract via tunneling can occur. This forms a stable dipole structure, which neutralizes the trap. The probability that this occurs decreases with the distance to the interface. Traps closer to the interface, also known as border traps, form switch states which can exchange electrons with the substract depending on the surface potential. Non-switching (low probability) oxide traps form fixed states [1][2][3].

4.2.1.3 Interface-Traps

Another form of traps also exists exactly at the Si/SiO_2 interface (IT). These traps originate in tri-valent silicon atoms which are weakly bonded with hydrogen as a result of

a passivation process. It has been shown that holes produced by ionizing particles in the oxide can break the bonds in two ways: protons released by hole interaction with oxide defects containing Hydrogen interact with the bond producing H_2 and leaving a vacancy in the interface, which can then capture holes and electrons; and the holes themselves break the bond. Though the latter is possible, it has been shown that the former is the main cause of interface trap production [1][2][3]. These traps form promptly after a particle strikes the device and over time (thousands of seconds) as protons and holes travel to the interface. The trap build-up has implications in testing since at high dose rate saturation may not be achieved. Annealing occurs only at very high temperatures unlike in oxide traps, which is critical for total dose assessment [100].

The formation of these traps is heavily dependent on bias condition that favor the transport of protons to the interface. Interface traps act like border traps in the sense that they too exchange charges with silicon [1]. However, unlike oxide traps, interface traps add a negative charge in n-channel MOS devices causing a threshold shift in the opposite direction of the oxide traps, and a positive charge in p-channel MOSFETs. This effect can cause a rebound in V_{th} when the oxide traps anneal over time or at high temperature and the interface traps remain.

Figure 4.10 summarizes all traps types and states in a typical MOS. Notice that although border traps are located in the oxide, they behave similarly to the interface states switching charges with the substrate. Both fixed and switching traps affect the threshold voltage though the switching ones can be neutralized by biasing the gate. Interface traps also changes carrier mobility which in turn affect switching and drive current [100].

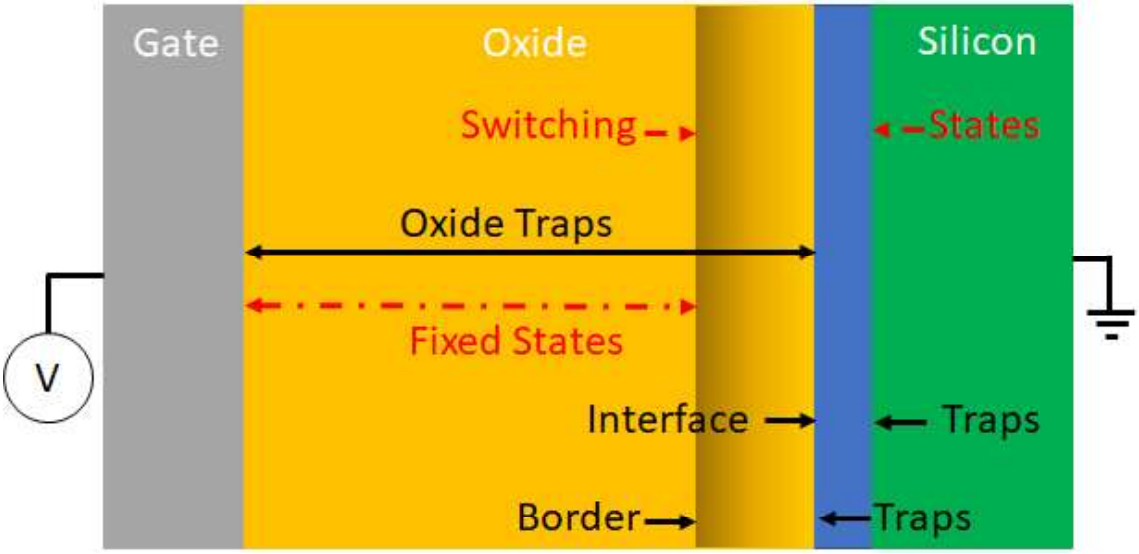

Figure 4.10: MOS structure and trap schematic. The Gate is in gray, the oxide in yellow/dark yellow, Silicon in green and the interface between the substrate and the oxide in blue. Sizes are not to scale. Three types of traps can be identified, oxide traps, border traps (a sub-set of oxide traps that can exchange charges with the substrate) and interface traps. Fixed states are found in the oxide only, while switching states are found in the oxide and in the interface.

4.2.1.4 Field-Oxide Traps

With the scaling of EEE components, the gate oxide thickness became smaller. Consequently, the number of gate traps as well as their effect has decreased substantially. This has increased the influence of trapping in the field oxide. These traps can create a channel between the drain and the source, which results in a large increase in leakage current, and between isolated devices leading to cross-talk [100].

4.2.2 TID Mechanisms in Bipolar Devices

The field-oxide is also of concern in bipolar devices especially in horizontal transistors where conduction is along the oxide. Oxide traps form in the same way for bipolar components as for MOS devices. In this components however, no voltage is applied to the oxide. Interface traps formed can exchange carriers with the base and increase the base current due to recombination. As a consequence the base current increases with no change in the collector current leading to a decrease in the gain. Interface traps can also create an inversion layer in p-doped regions which affects both the transistor gain and leakage current [100].

A critical feature of traps in bipolar technologies is their Enhanced Low Dose Rate Sensitivity (ELDRS). Though several theories exist to explain this behavior none can fully model these effects [101]. In general these models treat the problem as a reduced HDR effect which results from an increase in oxide trap recombination caused by the repulsive force between holes. This way protons are less prone to be released and consequently migrate towards the interface. At lower dose rates this effect is less pronunciated leading to larger numbers of interface traps [3] [102].

ELDRS effects are not easy to predict. The enhancement factor increases for lower dose rate, but at very low dose rates can decrease. It also leads to very long test times, which may not be compatible with a project schedule.

4.2.3 Effects

Summarizing, TID effects include a change in threshold voltage, leakage current and timing parameters in MOSFETs. Shift in the threshold voltage of MOS devices is the sum of oxide traps and interface traps as it can be seen in Figure 4.11. Oxide traps always decrease the threshold voltage since they hold positive charge. Interface traps exchange charges with the substrate hence they add to the oxide traps effect in PMOS, since most are positive, and subtract in NMOS devices since they have a higher probability of being negative. In Bipolar components radiation affects the gain of the device and increases the leakage current.

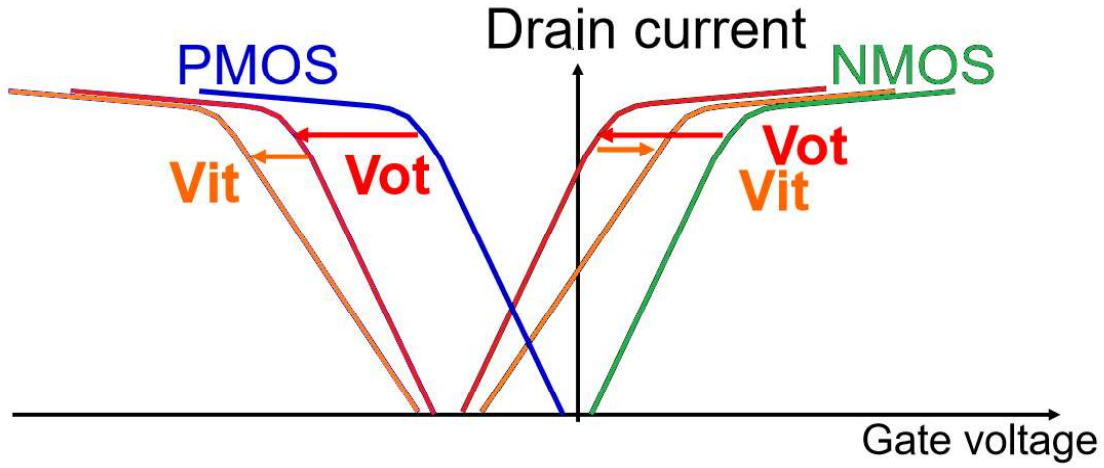

Figure 4.11: Oxide (OT) and interface (IT) traps effect on the threshold voltage of MOS devices. In PMOS devices (blue) both OT (red) and IT (orange) decrease the threshold voltage. In NMOS devices OT (red) and IT (orange) have the opposite effect. Adapted from [103]

4.2.4 Testing

To characterize and qualify EEE components to be flown in the space environment, military and national agencies developed testing standards: MIL-STD [104][105][106] and ASTM [107][108][109] in the US and ECSS 22900 [68][26][64] in Europe. For TID, both test standards consist of irradiating devices with ^{60}Co gammas in steps, measuring parameters of interest in-between, or continually (in-flux), which is preferred since it allows to obtain the full response of the device and avoid annealing effects. It is however technically challenging. ^{60}Co is chosen in detriment of particles predominant in the space environment such as electrons and protons, because it has been shown that its effect is conservative [2]. This has been demonstrated empirically and is mostly because ^{60}Co induces the lowest recombination yield as it was shown in Figure 4.9. It also has an advantage over X-rays since the absorbed dose is comparable between materials of different atomic number and densities which is not true at lower energies. This is not to say that it is the most representative of the environment but it does represent a worst-case condition.

Dose rates differ between standards though in all cases they are much higher than in the space environment as shown in Figure 4.12 [105]. For MOS components, High Dose Rates (HDR) are between 0.1 and 50 rad(Si)/s in ECSS 22900 [68] and between 50 to 300 rad(Si)/s in MIL-STD 1019 [105][68]. Higher dose rates have the benefit of bypassing annealing effects that can occur. However, they do not account for the build-up of interface traps, and the rebound effect that happens in NMOS devices. In these devices, the drift in threshold voltage caused by the oxide traps is partly compensated by the interface traps. If one allows the oxide traps to anneal, the effect from the interface traps in the threshold voltage, will become dominant and surpass in magnitude the one measured at the end of irradiation [102]. For this reason, both standards include one week of 100° C annealing to assess the worst-case effect of both trap types. MIL-STD 1019 requires a 50% margin on

the total dose levels [105].

There is also a concern about the worst-case bias conditions for irradiation. For qualification parts should be irradiated both unbiased and in worst-case condition. A good rule of thumb for end-users is to irradiate the parts in the same conditions they will be used, if possible [68][100].

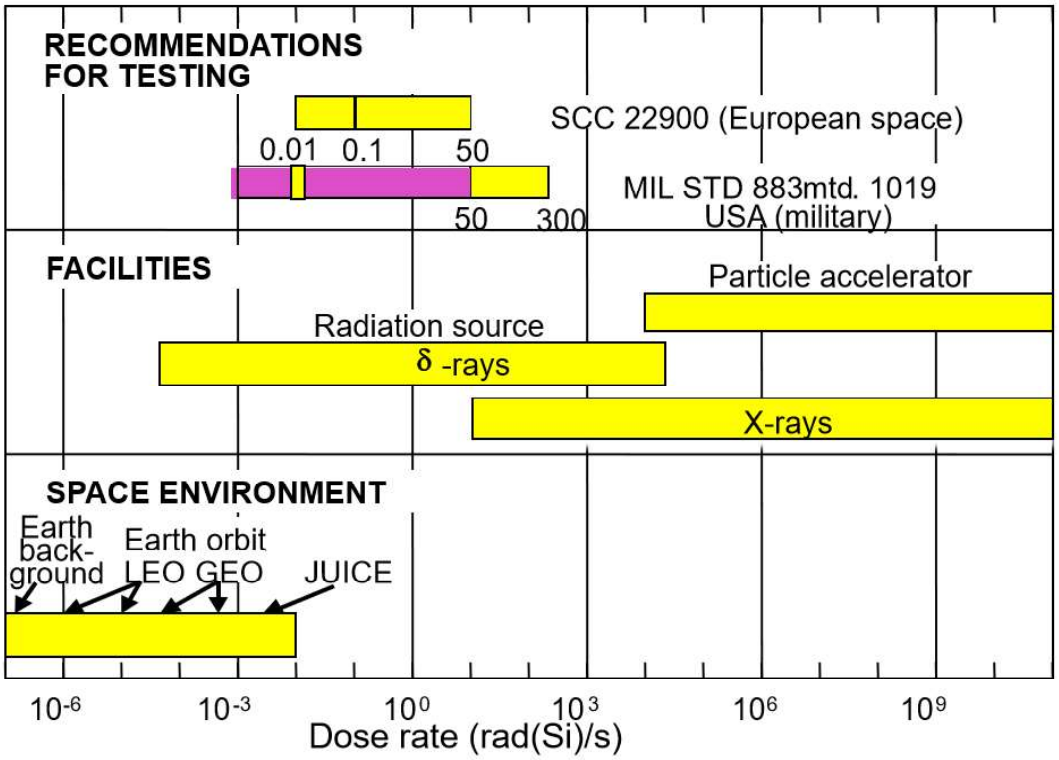

Figure 4.12: Dose rates in the space environment (bottom), facilities (middle) and recommended for testing (top). A gap exists between the space environment and the testing because of time constraints in project development. From: [100].

For bipolar devices ELDRS effect must also be considered when testing. It has been shown that a worst-case lower dose rate, which can be lower than 1 mrad(Si)/s, exists but it is dependent on several factors. This results in testing times that are not compatible with a spacecraft development schedule since it takes one year to reach 30 krad(Si) at this dose rate. As a compromise, MIL-STD 1019 allows testing to be done at a dose rate up to 10 mrad(Si)/s while in ECSS22900 it can be done up to 100 mrad(Si)/s. These methods are pragmatic in the sense that they can be used for the lifetime of a mission at the cost of increased risk that a component might have not been tested at their ELDRS limit [105][68].

Another important factor in testing is part-to-part variability. In fact, it is known that response to radiation varies successively more between different dies, wafers, lots and foundries [110][103]. The probability of survival of a part in a lot to a given dose is assumed to follow a log-normal distribution. One can then define a one side tolerance K_{TL}, as the number of standard deviations, σ, required for a part to have a survival probability of, P_S, with a confidence level, C [100]. ECSS22900 requires a minimum of 10 parts to be

tested, 5 unbiased and 5 in worst-bias conditions if known, and two used as references. This ensures that for P_S=C=90%, K_{TL} is 2 [26] which has implications in the Radiation Hardness Assurance (RHA) process. Even though this method is standard it has to be considered that there are cases where it might not bind the worst-case scenario. Recent studies have shown that a maximum likelihood method might be more suitable to bind a lot worst-case response [110].

4.3 Single Event Effects

Ionizing particles can also cause transient pulses in semiconductor devices known as Single Event Effects (SEE) which may result in temporary or permanent damage to components [6][7]. Though SEE have been a concern for spacecrafts for many years, the increased sensitivity of new technologies has brought this problem to ground operated devices as well [111].

4.3.1 Mechanisms

Unlike TID effects, SEEs are caused by electron-hole generation in the silicon lattice [6]. Unrecombined charges are transported by the force exerted by the electric field and/or by diffusion, forming a current (I) equal to [56]:

$$I = \sum_{i=e,h} qn_i m_i E + qD_i \nabla n_i \tag{4.7}$$

Where q is the elementary charge, n_i is the number of electrons/holes, m_i is its mass, E the electric field and D_i is the Diffusion Coefficient. The carriers generated this way, distort the field inside the silicon bulk, creating a channel to the p-n junction which allows them to propagate through the circuit (funneling) [112] [56]. Not all carriers generated this way are collected. The collected charge, Q_C, depends on several parameters related to the device such as sensitive volume size, bias conditions, doping density and others. It also depends on the incident particle energy and type.

Charge collection follows three steps in the charge collection: onset; prompt; and diffusion. This can be seen explicitly in Figure 4.13. Initially the particle strikes the device (onset) giving rise to a current up to a peak (prompt charge collection). The current rises and falls in a few picoseconds. However, it does not fall to zero immediately. For up to hundreds of picoseconds charge is still collected by diffusion [113].

Charged particles, especially ions, penetrate the material creating regions of high-density electron-hole pairs from its interactions with electrons in the material and also with the lattice atoms which can further ionize the medium and trigger other SEEs. The main variable of SEE capable particles is the Linear Energy Transfer (LET). The LET of a particle is a function of its mass, energy and density of the material it loses energy in. It is a measure of the rate of energy loss in a material varying very slowly as it loses

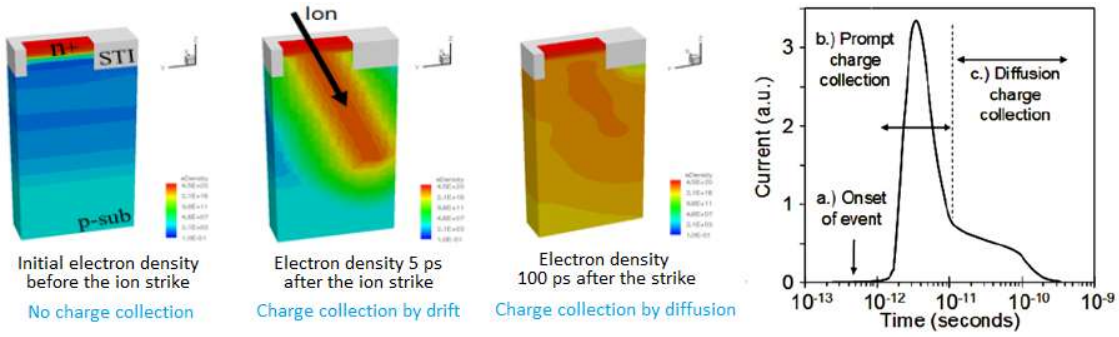

Figure 4.13: Electron density evolution during a SEE (three left images) and current in the device (right image). Adapted from [114] and [113].

energy until it reaches the Bragg peak where it loses most of its energy. This can be seen in Figure 4.14 for several ions of different energies in Silicon. Protons, neutrons (and electrons for the most sensitive technologies) can also cause SEEs in sensitive devices via indirect ionization processes [6]. In this case the particles undergo a nuclear reaction with a lattice atom which then ionizes the medium causing a SEE.

4.3.2 Types of Effects

There are a plethora of different SEE modes depending on component type and operation as enumerated in Table 4.3 [116]. They can be either destructive and non-destructive depending on their effect on the operating conditions of a device. Non-destructive effects though not critical, can still affect the normal operation of an instrument and/or spacecraft. Single Event Upsets (SEU) for instance can lead to loss of data or change in function of an instrument. It is also possible that more than one bit is affected (Multiple Bit Upset - MBU) which can severely jeopardize functionality. Single Effect Function Interrupts (SEFI) though also not destructive, require action in order to restore a system to normal operation.

Another issue are Integrated Circuits (IC) which can be sensitive to multiple SEE modes. For instance, a Field-Programable Gate Array (FPGA) can suffer SEUs and Single Event Latch-ups (SEL). Latch-ups are the result of the formation of a parasitic path connecting the ground to the power which result in the destruction of a device [117].

Table 4.3: Single Event modes and their effects. Top three types are non-destructive while the bottom three result in destruction of devices [118].

Error	**Effect**
Single/Multiple Event	Upset Single/Multiple bit corruption
Single Event Transient	Current pulse
Single Event Functional Interrupt	Interruption of normal operation
Single Event Latch-up	Latch-up
Single Event Burnout	Burnout
Single Event Gate Rupture	Rupture of the Gate

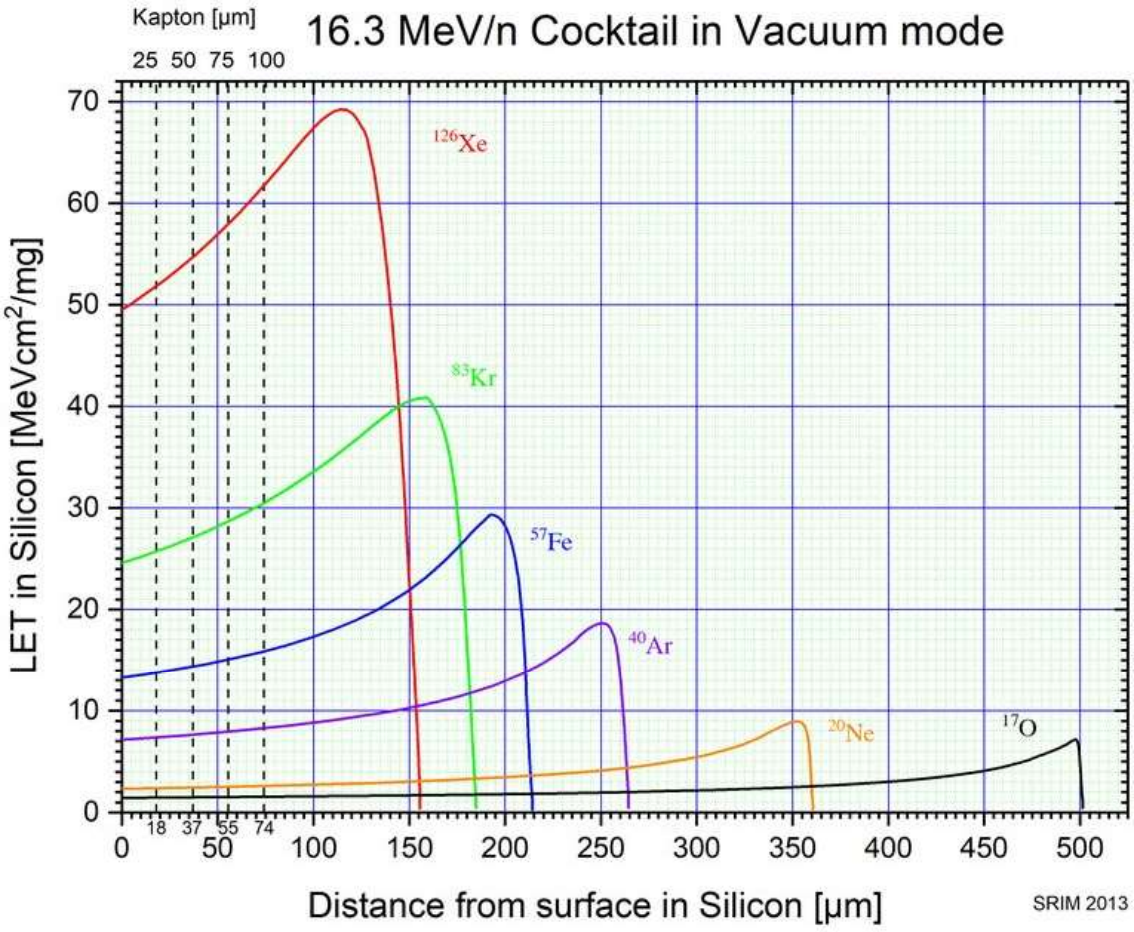

Figure 4.14: LET curves of 16.3 MeV/u cocktail ions in Silicon vacuum mode at the RADEF facilities. Vertical dash lines show the effective DUT surface positions when 25, 50, 75 and 100 μm of Kapton is added front of the DUT. From: [115].

4.3.3 Rate Calculation

An important aspect that determines the possibility of a SEE to occur is the sensitive volume of the device. While it is not trivial to obtain the exact sensitive volume, it has been shown that it can be approximated to a box with surface area S=X*Y, and thickness, Z (its shape is more complex though). It can also be assumed that the LET does not vary significantly for the whole track (this is true only for high energy particles). Q_c depends on the energy loss hence it is a function of the LET of an ion crossing the volume. Therefore, the critical charge can be described in terms of a LET threshold (LET_{th}). LET_{th} is defined as the minimum LET a particle must have in order to cause a SEE considering an ion with normal incidence to the surface of the sensitive volume. However, ions can cross the volume in any direction which means they will travel a larger path inside the sensitive volume, hence depositing more energy in the sensitive volume. It is then essential to define an Effective LET, LET_{eff} equal to the LET of the particle divided by the cosine of the incidence angle. While the true LET of the particle remains the same, for modeling purposes LET_{eff} allows to correct for the increased collected

charge in these cases. Assuming a sharp rise in the cross-section for occurrence of SEEs and a plateau corresponding to the surface area, CS_{sat}, the cross-section can be described as a 2-parameter Weibull distribution as the one shown in Figure 4.15. The fact that it is not simply a step function is due to the existence of several sensitive volumes with a distribution of LET_{th} and CS_{sat} [119][120].

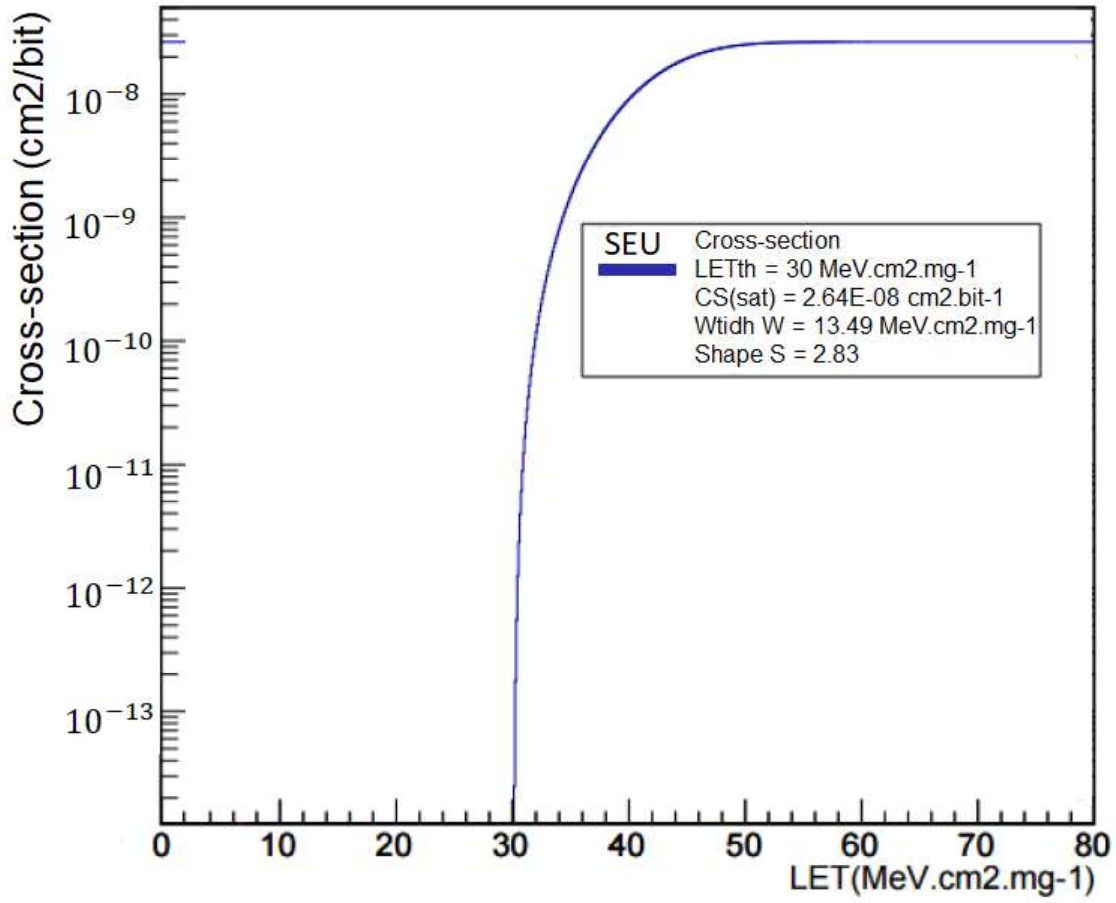

Figure 4.15: Typical SEU cross-section following a 2-parameter Weibull distribution.

The rate, R, at which SEEs occur under a flux Φ can be computed by either the Braford formula, the Pickel formula or the Blandford and Adamas formula [27]: -Braford formula:

$$R = \frac{A}{4} \int_{LET_{min}}^{LET_{max}} \frac{d\Phi}{d(LET)}(LET).P_{CL}(> D(LET)).d(LET) \tag{4.8}$$

-Pickel formula:

$$R = \frac{A}{4} \int_{D_{Min}}^{D_{max}} \Phi(> LET(D)).\frac{dP_{CL}(D)}{dD}.dD \tag{4.9}$$

-Blandford and Adams formula:

$$R = \frac{A}{4}\frac{E_c}{\rho} \int_{LET_{th}}^{LET_{max}} \frac{1}{LET^2}\Phi(> LET).\frac{dP_{CL}}{d(D(LET))}.D(LET).d(LET) \tag{4.10}$$

Where A is the total surface area and P_{CL} is the integral chord length distribution,

i.e., the probability of particles travelling through the sensitive region with a path length greater than D [27].

These equations can be solved numerically as long as the ion flux is known. Several tools exist for this purpose such as CRéME [121], SPACERAD [122], OMERE [123] and SPENVIS [12] [27]. For the ion population in space (Galactic Cosmic Rays) there are several models that were discussed already. Their LET does not vary significantly along their track in the spacecraft except for small energies. For this reason, 1 g.cm^{-2} aluminum shielding from the spacecraft should be considered according to [26]. For protons from Solar Particle Events (SEP) and radiation belts knowing the LET spectrum at part level is more complex. In this case one has to use either ray-tracing or Monte Carlo methods [27]. Moreover, the path length distribution is less meaningful since SEE induced by protons depends mostly on indirect ionization. This is also true for neutrons. The rate can then be calculated considering an angle dependence in ϑ:

$$R = \int_{E_{min}}^{E_{max}} \left\{ \frac{\partial \Phi}{\partial E \partial \theta}(E,\theta).\sigma_{nucleon}(E,\theta).sin\theta.d\theta \right\} dE \tag{4.11}$$

Where $\sigma_{nucleon}$ is the cross-section for nuclear reactions. When no data is available for protons, SEE rate can also be computed with heavy ion cross-sections by applying a factor of 10 [26]. Given the random nature of particles arriving to an area, the rate calculation must be seen only as an average rate. In fact, particle arrival, i.e. SEE occurrence, follows a Poisson distribution as follows [124]:

$$P(k;t) = e^{-Rt}\frac{(Rt)^k}{k!} \tag{4.12}$$

Where P(k;t) is the probability that k events occur after a time interval t, given a mean rate R. This is especially important to consider because it provides a way to calculate the probability that multiple errors occur. SEE rate prediction for all components that are sensitive to both non-destructive and destructive events, is essential to ensure that an instrument and/or spacecraft function correctly without interruption. Although it is possible to mitigate SEE probability it is not possible to completely avoid the risk of it happening.

4.4 Displacement Damage

Particles crossing silicon devices also interact with the lattice atoms via non-ionizing processes: nuclear elastic scattering; inelastic scattering; and nuclear capture. Protons are the main source of Displacement Damage (DD) in space but it can also be caused by neutrons, heavy ions, electrons and to a very small extent, gamma rays.

4.4.1 Mechanisms

Displacement damage occurs when an incident particles transfer energy to a Silicon atom, the Primary Knock-on Atom (PKA), though impurity atoms can also be dislodged this way, displacing it from the original position. This atom can recombine, create a stable Frenkel pair, a vacancy and an interstitial atom, or propagate. If given enough energy, a PKA can also scatter other atoms creating defect clusters. These clusters are the main cause of the effects seen in irradiated devices [4][5].

Cluster production depends not only on the incident particle type and energy but also on the material. This is because the PKA may be able to displace other atoms as well. The production of isolated defects and clusters can be modeled by Molecular Dynamics (MD) simulation in an accurate manner. In Silicon, the simulations show that the PKA is able to create both isolated and amorphous clusters as those seen in Figure 4.16. The amorphous structure of clusters is important because it changes the band-structure significantly when compared to isolated defects in a crystalline structure. Cluster may also contain high concentrations of bond defects caused by ion bombardment annealing [125].

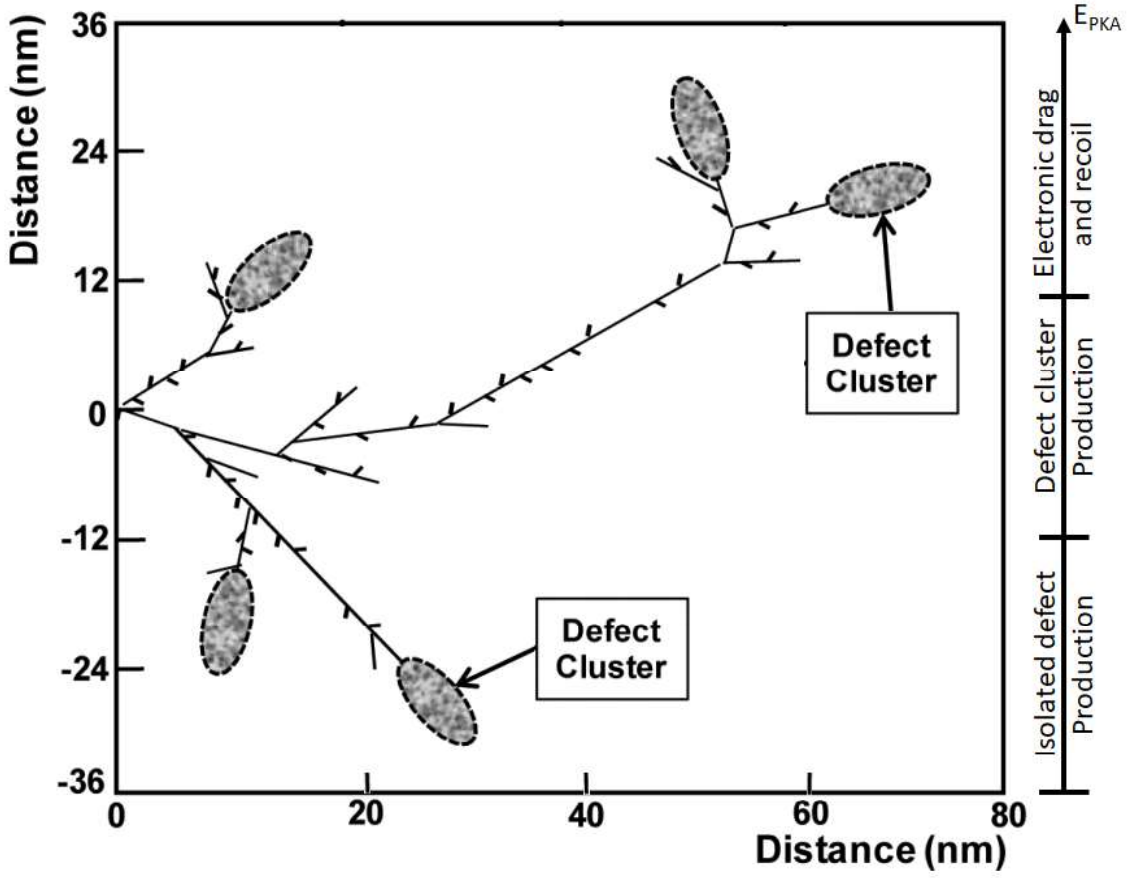

Figure 4.16: Conceptual illustration of the damage produced in Silicon by a 50-keV primary recoil atom. Isolated defects and amorphous defect clusters are shown. PKAs have three different energy regimes: Isolated defect production only; Cluster defect production only; and Electronic drag and recoil energy loss. Adapted from [5]

PKAs have three energy regimes as depicted in Figure 4.16: one from the displacement energy threshold (21 eV) up to the cluster production energy threshold (1-2 keV) where only isolated defects are created; another where cluster production occurs exclusively (from 1-2 keV to 10-20keV) [126]; and a third one for higher energies where PKAs loses energy to recoil production and/or electronic drag until it changes regime [5]. PKA favors the production of defect clusters slightly for energies >20 keV [5].

The PKA energy is highly dependent on the incident particle. While for electrons and low energy protons (¡10 MeV) Coulomb scattering dominates, which results in low energy PKA and consequently the production of isolated defects, for neutrons and higher energy protons interactions with PKA are mainly via nuclear reactions and nuclear scattering which generate a flat PKA spectrum with higher energies which resuls in the formation of a cascade of defects as seen in Figure 4.16.

4.4.2 Effects

Band structure changes caused by displacement damage increase thermal generation of carrier and carrier recombination lifetime, temporary trapping and reduction in majority carrier concentration. In MOS devices, Displacement Damage results in an increase in dark current in depletion zones of PIN diodes for example. In bipolar devices, the decrease lifetime of minority carriers decreases the gain of the components though for space applications, especially for the Jovian radiation environment, it is small when compared to TID effects [100][5].

4.4.3 Non-Ionizing Energy Loss (NIEL)

The Total Non-Ionizing Dose (TNID) or Displacement Damage Dose (DDD) can be defined in the same way as the TID as the absorbed energy per unit of mass, usually given as MeV/g, by a given material via non-ionizing processes. DDD can also be written as:

$$DDD(MeV/g) = \sum_{particles} \int \frac{d\Phi}{dE}\,(E)_{particle} * \mathrm{NIEL}_{particle}(E)\; dE \tag{4.13}$$

Where Φ is the particle fluence and NIEL (Non-Ionizing Energy Loss) is the rate at which the particle loses energy by displacing atoms in MeV.cm^2/g [5]. The expression is valid only for the cases where the NIEL does not vary significantly along a particle path in a material. Effects of DDD in components is a function of the NIEL alone. It depends on the particle type, energy and target material and has been calculated for different particles and energy regimes in Silicon by several authors [127][128][129]. Results for protons, neutrons and electrons can be seen in Figure 4.17. Neutron NIEL remains fairly constant for energies above 0.2 MeV since it only interacts via nuclear scattering. Protons have larger NIEL than neutrons up to 30 MeV. This is because for lower energies, Rutherford scattering dominates over nuclear interactions. For higher energies the nuclear cross-section dominates the interaction hence the plateau observed for both protons and

neutrons. Electrons on the other hand, scatter more with the atoms electronic cloud which means that only at higher energies they are able to interact with an atomic nucleus. A database of NIEL values is kept in [130]. Though it assumed that NIEL scaling can be used to assess damage from non-ionizing processes to components this is not always the case [5].

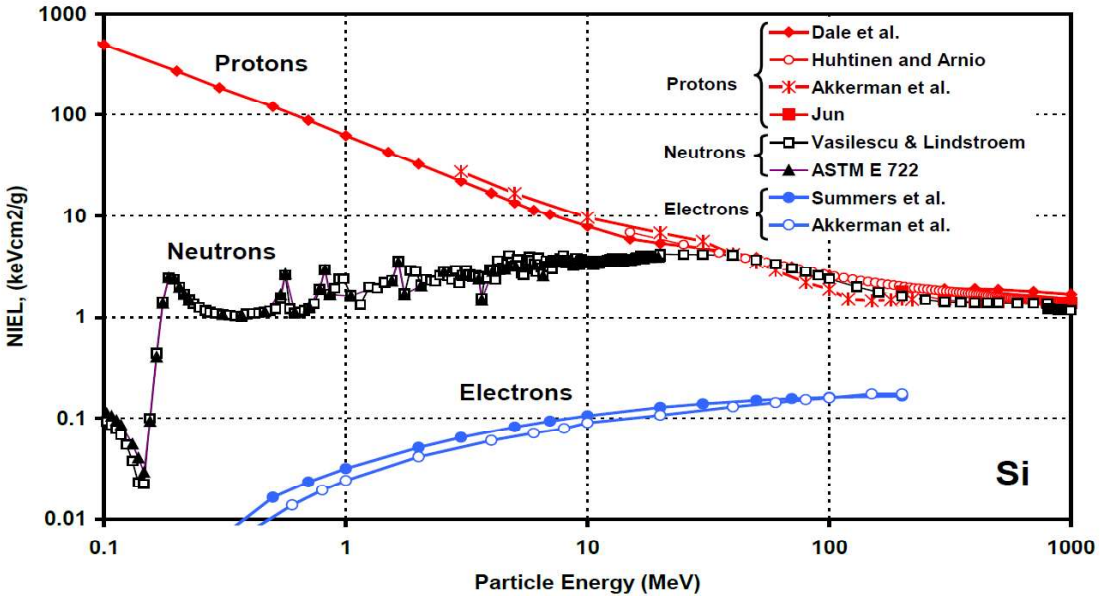

Figure 4.17: Electron, neutron and proton NIEL in silicon [116].

In the space environment, DDD is frequently dominated by protons. However, in environments with high fluxes of high energy electrons (>10 MeV) electron, such as the one expected for the JUICE mission, contribution to DDD is non-negligible.

4.4.4 Testing

Currently there are no standards for DD testing besides the neutron testing method 1017 described in [106]. Neutrons, protons and electrons can all be used, however both protons and electrons also induce TID effects. Since DDD effects are independent of bias, one solution to minimize this effect is to irradiate the components unbiased. Proton and ^{60}Co tests can also be combined to separate TID and DDD effects. Neutrons on the other hand do not contribute to TID but present technical problems regarding dosimetry, energy distribution and NIEL scaling. The latter is in fact an important factor in testing since it may not be reliable between different particles and/or energies. One solution is to perform tests with the most representative particle for a specific mission.

Similarly, to TID testing, tests are usually performed in fluence steps. Rates are not considered since there is no clear evidence for DDD rate effects so far [100][103].

4.5 Radiation Hardness Assurance

Considering all the radiation hazards discussed so far, strict Radiation Hardness Assurance (RHA) standards have been designed to ensure parts work within specification for a mission. Radiation Hardness Assurance composes of all activities performed to minimize risk associated with system failures due to radiation effects. It includes environment specification, part selection and testing, and TID, DDD and SEE level determination. An overview of the RHA process is displayed in Figure 4.18. Defining the particle environment and computing TID, DDD and SEE levels as well as assembling a database of candidate parts and their radiation test data should be done as soon as possible in the mission development to avoid costly changes. Selected parts are categorized as Hardness Non-Critical (accepted), Hardness Critical (requires lot acceptance tests) and Not Acceptable. Categorization depends on the Radiation Design Margin (RDM) determined for a mission. RDM is defined as the ratio between part failure levels and mission computed levels. If RDM is less than one, risk reduction actions must be performed. This can be done in multiple ways depending on the component and its application. Parts can also be rejected if no solution is found. If RDM is greater than one but less than two, lot acceptance tests must be performed on the flight lot. Other actions such as increasing the shielding might also be used in order to increase the RDM. This margin is essential given the uncertainties in the determination of the radiation environment and part-to-part variability as well as enhanced degradation from purely stochastic events [29][26].

4.5.1 Environment Specification

Environment specification is determined from the mission orbit and environment models which were already discussed in Chapter 2. It has three components: trapped particles; cosmic ray fluxes; and solar energetic particles. It can be done with several tools including SPENVIS [12] and Creme96 [121]. For the JUICE mission RHA the environment specification can be found in [28].

For the JUICE mission, trapped radiation belts fluxes are based on the JOSE model [46]. They are slit into six phases for electrons and five for protons as described in Table 4.4 of different duration that should be considered for TID and DDD calculations. Electrons have one additional phase because the shielding effect of the Ganymede magnetosphere was considered for the moon orbital phases. Average electron and proton fluxes for each phase as determined in [28] are displayed in Figure 4.19. Worst-case instantaneous fluxes of both particles are also shown. These are not important for TID and DDD considerations but are necessary to compute worst-case SEU rate from protons and to study the Directionality Detector Head (DDH) as it will become apparent in Chapter 6 and Chapter 7 respectively.

For SEE rate analysis the ISO 15390 cosmic ray model, discussed in Chapter 2, peak 5m, worst-week and quiet (solar minimum) at 1 A.U., shielded by 1 g.cm^{-2} aluminum for all phases including the interplanetary cruise as displayed in Figure 4.20 mst be used.

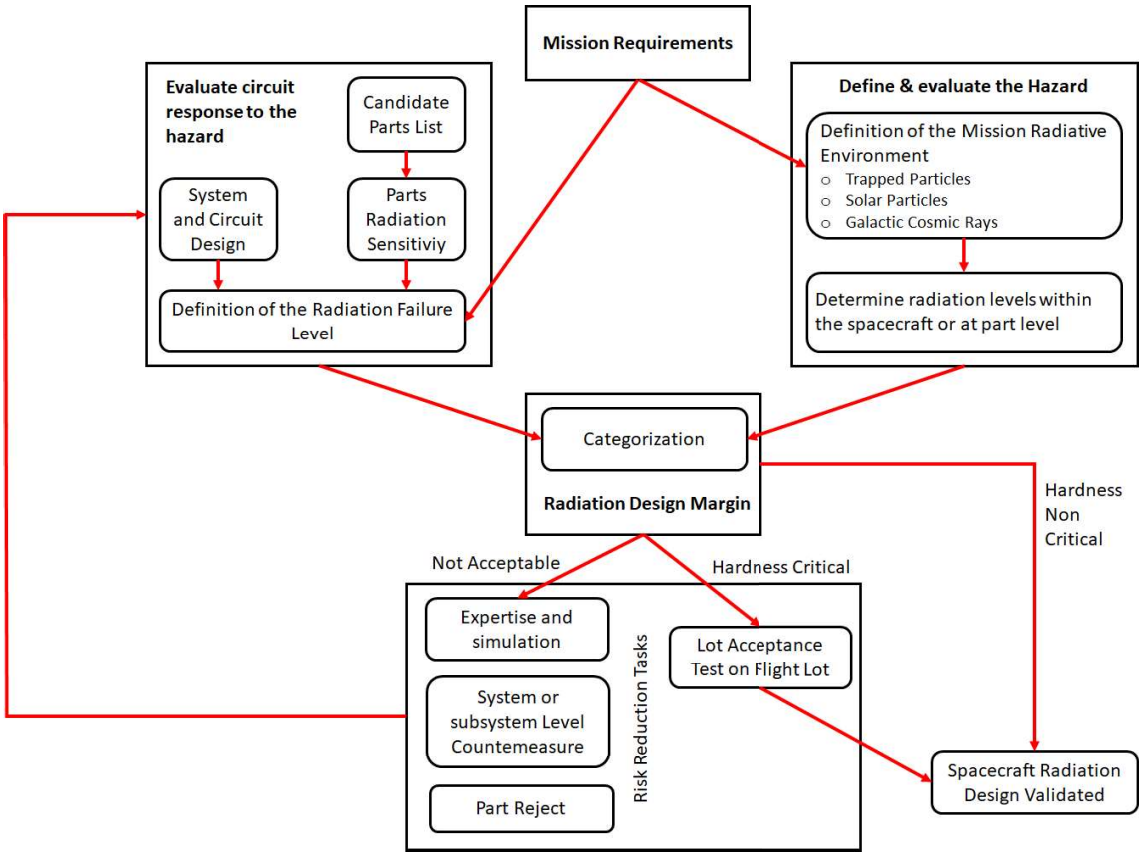

Figure 4.18: Overview of the Radiation Hardness Assurance process. Adapted from [29].

Influence of the Jovian magnetosphere in the GCR fluxes is not considered [28].

In the interplanetary cruise two other contributions are taken into account. The first is from protons originating in Solar Particle Events (SPEs) which were already discussed in Chapter 2. SPEs are unpredictable in time occurrence and in its characteristics. Nevertheless, long-term modeling is possible. For the JUICE mission, particles originating from such events are integrated over a seven-year period starting at the beginning of a solar maximum, at 1 A.U. with a 90% confidence level, according to the ESP model [60]. Flux variation across the solar system is not considered since it is not a trivial task and because the mission will spend most of its time further away from the sun even though a Venus flyby is planned [28]. The second contribution is from electrons from both SPEs and from Jupiter which dominates the electron environment at quiet times. These are modeled with the Interplanetary Electron Model (IEM) [131][132] which gives the cumulative fluences and worst-case fluxes. For dose calculations their contribution can be neglected [28].

4.5.2 Estimation of Radiative Quantities within the spacecraft and at part level

After defining the environment, TID, DDD and SEE levels within the spacecraft and/or at part level should be estimated. For SEEs this has already been discussed in section

Table 4.4: JUICE mission phase durations to be used in RHA calculations. From [28].

Phase	Duration (days)
1: Transfer to Europa	458
2: Europa flybys	38
3: Jupiter high latitude phase with Callisto	248
4: Transfer to Ganymede	311
5a: Ganymede 5000km altitude circular orbit	152 (300 for protons)
5b: Ganymede 500km altitude circular orbit	148 (0 for protons)

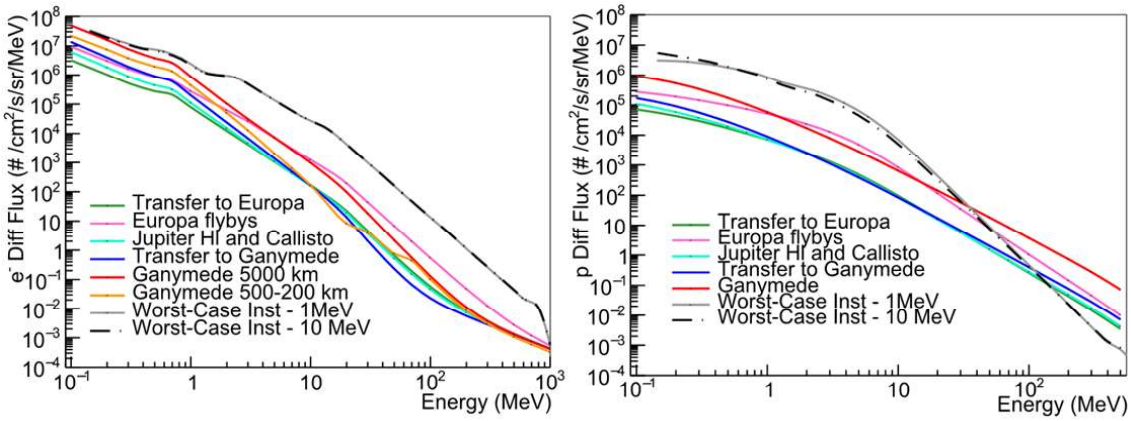

Figure 4.19: Electron and proton average differential fluxes expected for the orbital phases of the JUICE mission. Worst-Case instantaneous fluxes corresponding to the closest approximation to Jupiter are also shown. From: [21].

4.3.3. TID and DDD can be computed in similar ways with three different techniques of varying degrees of speed and accuracy: Dose-Depth curves; Sectoring; and Monte Carlo transport. The later has already been extensively discussed in Chapter 3 so it will not be addressed.

4.5.2.1 Dose-Depth Curve

Sector-based analysis leverages on the computation of a Dose-Depth Curve which specifies a quantity, dose or fluence, as a function of shielding thickness for a given radiation environment [27][26]. It is obtained for a specific material, usually aluminum, by solving the Boltzmann transport equations in a spherical volume or with Monte Carlo methods. Databases such as SHIELDOSE [133] already exist where convolution with the radiation environment of a given mission is performed. The dose obtained by this method for the minimum shielding offered by the spacecraft for a component is then considered as the worst-case. This is a first-order calculation that bypasses the actual geometry and materials of the spacecraft assuming that for shielding purposes, only the density of materials matter. For components close to the wall of the spacecraft a planar geometry should be used to obtain the Dose-Depth curve as well instead of the spherical shell [27][26].

TID results as a function of spherical Aluminum equivalent shielding, obtained with SHIELDOSE-2Q [133] for the JUICE mission are shown in Figure 4.21. One important

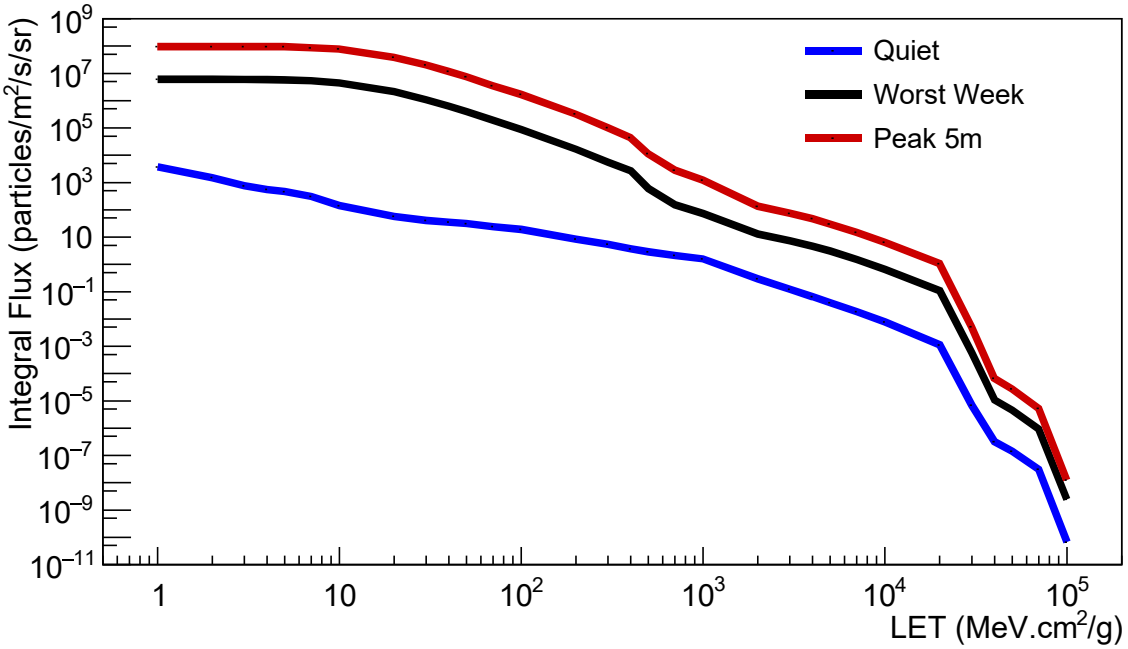

Figure 4.20: ISO 15390 quiet (solar minimum), worst week and peak 5m GCR Integral flux as a function of LET, at 1 A.U. with 1 g.cm^{-2} aluminum shielding. Adapted from [28].

result is that for more than 4 mm of Aluminum equivalent shielding, Bremsstrahlung is the second main contributor to TID and that, for more than 60 mm it is the main contributor. This means that assuming similar response for high and low Z materials is particularly inaccurate for the mission [28].

4.5.2.2 Sectoring

A way to improve this method is to lose the assumption that shielding is homogenous breaking the Field-Of-View of point into N sections, sec, (minimum 9X9) and attributing different shielding thicknesses to each of them. The thickness of each region is obtained by ray-tracing [27][26]. Ray-tracing consists of following M rays through all sections (>15 per section), from a central location, e.g. a component, registering the amount of material the ray transverses by summing the length (L) of all materials, mat, times material density (ρ_{mat}) and then converting it into aluminum equivalent:

$$t_{sec} = \frac{1}{\rho_{Al} M} \sum_{k=1}^{M} \left\{ \sum_{mats} L_{k,mat} \rho_{mat} \right\} \tag{4.14}$$

The dose coming from each section can then be obtained with the Dose-Depth curve (DDC):

$$dose_{sec} = DDC(t_{sec}) \tag{4.15}$$

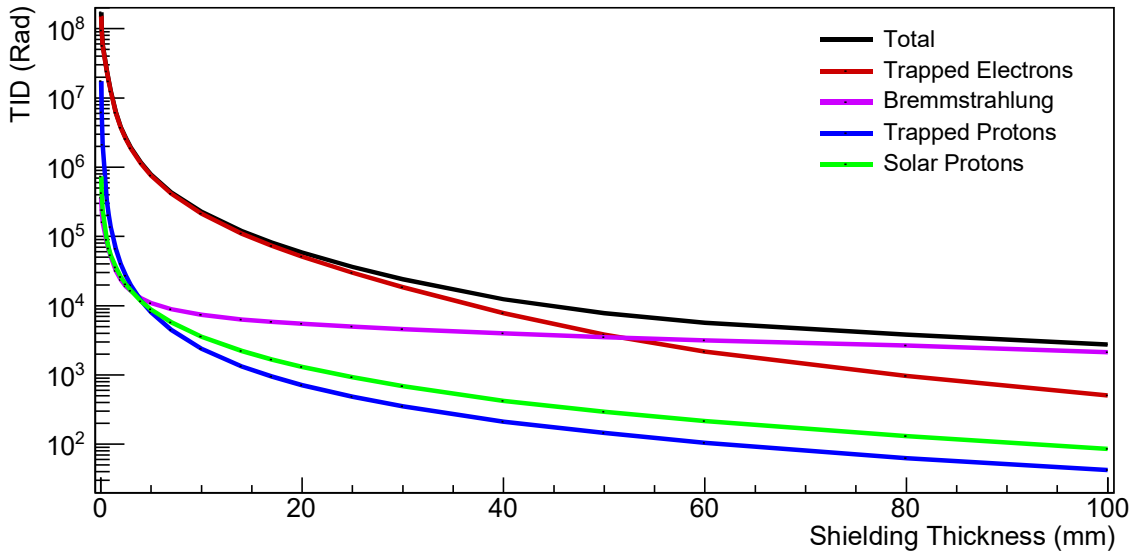

Figure 4.21: Dose in Si as a function of spherical Aluminum equivalent shielding as calculated by SHIELDOSE-2Q for the entire JUICE mission. Adapted from [28].

And the Total Dose can be obtained by summing the dose coming through each section (sec) weighted by its solid angle, α:

$$TotalDose = \frac{1}{4\pi} \sum_{sec} dose_{sec} \alpha_{sec} \tag{4.16}$$

Two techniques, NORM and SLANT, can be used to assess the length of the path crossed by a ray in a given material. The NORM technique considers that the ray crosses the material normal to the surface as shown in Figure 4.22. It is meant to account for the erratic scattering electrons in matter. The SLANT technique on the other hand considers a straight path in a material which better describes the behavior of protons [29].

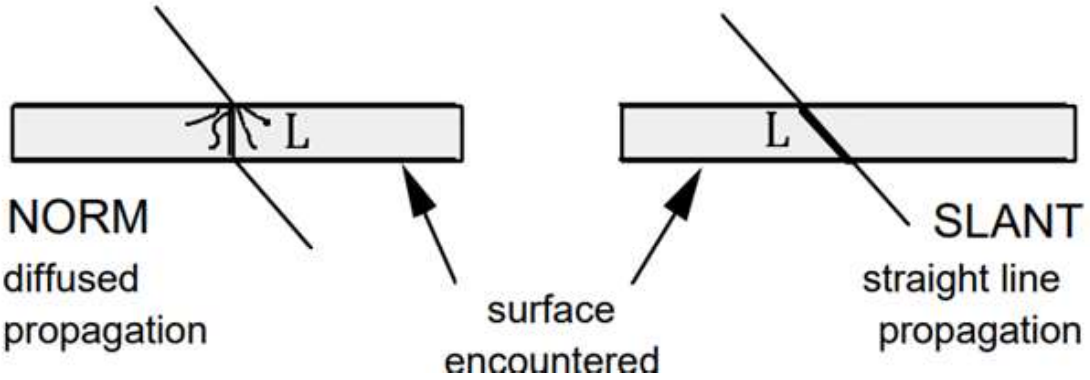

Figure 4.22: NORM and SLANT techniques for sector-based analysis. Adapted from [29].

Different DDCs should be used for the two methods in order to keep accuracy as high as possible. For the NORM technique a shallow sphere DDC must be used while for the SLANT technique a filled one is more correct. For electron dominated environments, espe-

cially high energy ones where Bremmstrahlung cannot be ignored as the JUICE mission, sectoring analysis has a high degree of inaccuracy. However, in the framework of this thesis, this technique has an important outcome. It can be used to obtain a 6-side box model of the spacecraft in terms of aluminum equivalent [27][26] which allows to speed-up Monte Carlo analysis.

4.5.3 Part Categorization

Another part of RHA is Part selection. In RADEM, all components except the ASIC VATA466 [22] and the custom-made Silicon diodes were selected from the JUICE Preferred Part List (JPPL) [134] which do not require testing as long as RDM is within specification (part list is given in Chapter 6). For components flown in the JUICE mission the RDM is two. The latter is due to uncertainties in the environment since measurements of proton fluxes have been restricted to low energies only. The ASICs however must be tested according to ECSS test standards. Due to their role on RADEM, test design for these components is critical to understand the instrument performance and reliability for the whole mission.

4.6 Summary

Radiation effects on components and RHA are a vast, continuously evolving subject. In this chapter an overview of these subjects was made with special emphasis on technologies and methods important for this thesis. There are however a number of new technologies such as FinFETs and 3D memories to name only a few which are the subject to recent investigations that were not addressed.

The Jovian radiation environment is hazardous for any mission. Missions to Jupiter are few and far between therefore a scrutinous RHA process needs to be done to minimize the risk of failure. Reliance on proven and tested components as well as the used precise methods to compute dose levels on components is of utmost importance. In the next two chapters, results concerning the radiation effects on components flown to Jupiter, namely the representativeness of ^{60}Co testing for components flown to Jupiter, as well as dose level calculations and shielding optimization methods and results for the Radiation Hard Electron Monitor (RADEM) which will fly in the JUICE mission (presented in Chapter II), will be discussed.

5 Verification of ^{60}Co Testing Representativeness of EEE components flown in the JUICE mission

It has been discussed in Chapter 4 that ^{60}Co is the preferred source for Total Ionizing Dose (TID) qualification of EEE components to be used in space. This is because it has been demonstrated empirically that for the same dose, ^{60}Co radiation affects components in a more pronounced manner when compared to other radiation sources. Theoretical models also predict a lower recombination yield for ^{60}Co (and for 12 MeV electrons) which results in a larger number of trapped charges in the oxide and therefore a larger radiation effect [2][135][136]. ^{60}Co is then referred to as the worst-case TID test conditions for components subject to the space radiation environment. TID testing is one of the most important parts of Radiation Hardness Assurance for space missions which has been successful in ensuring full spacecraft operation in a very large number of cases with few reported cases of TID induced failure [103].

5.1 Motivation and Objective

For Earth-bound missions, ^{60}Co emitted radiation is representative of the radiation TID environment. ^{60}Co decays into ^{60}Ni mainly by β^- decay (max energy of 0.31 MeV) followed by subsequent emission of two 1.17 and 1.33 MeV γ particles. These γ particles are highly penetrative reaching the Si and SiO_2 parts of the components. There, they interact mostly by Compton scattering, the process with highest cross-section at these energies and in these materials, as shown in Figure 5.1. Secondary electrons produced this way are ejected with a continuous energy spectra up to a maximum energy of $\sim$1MeV. While electrons of higher energies exist in Earth orbit, their fluxes above this energy are low.

As it was already shown in Figure 1.3, electron fluxes in Jupiter remain high for electron energies higher than 10 MeV when compared to Earth orbit. At these energies, electrons

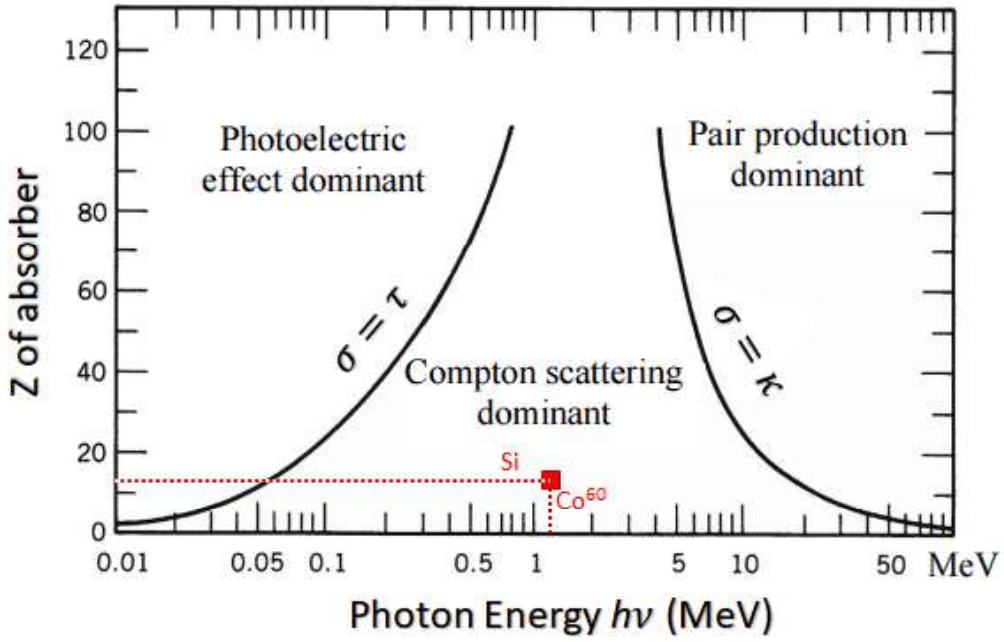

Figure 5.1: Compton scattering, photo-electric and electron-positron pair production dominated regions as a function of the atomic number, Z, of a material. Adapted from [137].

also interact with the materials via radiative processes (Bremsstrahlung) releasing photons into the material. Bremsstrahlung accounts for ∼15% of energy loss for 10 MeV electrons, ∼38% for 30 MeV electrons and >50% for 50 MeV electrons [67]. Secondary electrons from ^{60}Co on the other hand, lose energy mostly by collision. Because of this, it has been suggested that ^{60}Co might not represent the worst-case for environments with electrons of energies greater than ∼10 MeV. Furthermore, tests with both ^{60}Co and electrons showed that in some cases electrons might cause more damage to EEE components [138][139]. It is therefore of utmost importance to verify ^{60}Co testing representativeness for components flown to Jupiter (in JUICE and RADEM particularly), in order to confirm these tests are in fact a worst-case assessment of TID damage to components and that Radiation Design Margins (RDM) are enough to assure component reliability for the full mission duration.

For this reason, an extensive test campaign was performed with the objective of verifying if the ^{60}Co testing standards still apply to Jupiter. The tests were done in the framework of ESA contract "RFQ/3-13975/13/NL/PA" by irradiating commonly used technologies, to both ^{60}Co and two electrons energies > MeV as described in ECSS22900 [68]. The results presented in this chapter were presented and published in the "Data Workshop" session of the 2017 Nuclear and Space Radiation Effects on Components (NSREC) conference [140] and fully reported in [141].

5.2 Materials

To verify if ^{60}Co test standards are valid generically as Worst-Case scenario for the JUICE mission five commonly used technologies (Discrete and Integrated MOS and Bipolar devices) were irradiated with ^{60}Co and two electron energies (12 and 20 MeV) at High Dose Rate (HDR). ^{60}Co Low Dose Rate (LDR) tests were also done to compare the effects with the Enhanced Low Dose Rate Sensitivity (ELDRS) effect in Bipolar devices. All components were irradiated and characterized as specified in [68] since the objective was to validate the standard tests and not to study in full detail the mechanisms behind the radiation effects [141].

5.2.1 Test Components

The list of the components tested with their traceability information is given in Table 5.1. Traceability is essential in this study to ensure that possible differences between irradiated components were caused by the radiation and not by part-to-part variability inherent to the manufacturing process [110]. Part samples of each component type are shown in Figure 5.2 [141].

Table 5.1: List of tested components.

Component	A	B	C	D	E
type	Transistor Discrete MOS	FLASH-NAND Memory CMOS IC	Transistor Discrete Bipolar	OPAMP Analog IC non ELDRS	Shunt Voltage Analog ICs ELDRS
Reference	STRH100N10	MT29F32G08 ABAAAWP-ITZ	2N2222	LM124	LM4050WG 5.0-MPR
Manufacturer	STMicro Electronics	Micron	STMicro Electronics	Texas Instruments	Texas Instruments
Marking	520502101F BeO	29F32G0 8ABAAA	520100212	RM124AJRQMLV -JMO7C6273	LM4050WG 5.0-MPR
Date Code	1305A	1412	1345A	H7B1033W	HOB1022A
# of units	27	32	26	30	30

Figure 5.2: Component pictures from left to right, A through E.

5.2.1.1 Component A

Component A is a 100V N-channel MOS transistor manufactured by ST Microelectronics with the reference STRH100N10 [142]. The component was irradiated unbiased with

all leads tied to the ground. This is not its worst-case condition but it is still according to [68]. Electrical parameters measured are presented in Table 5.2 [141].

Table 5.2: Electrical parameters measured for Component A. From [141].

Characteristics	Symbol	Test Conditions	Limits		
			Min	Max	Un.
Gate-to-Source Leakage Current 1	I_{GS1}	VGS=20V, VDS=0V	-	100	nA
Gate-to-Source Leakage Current 2	I_{GS2}	VGS=-20V, VDS=0V	-100	-	nA
Drain Current	I_{DS}	VDS=40V, VGS=0V	-	10	μA
Gate-to-Source Threshold Voltage	$V_{GS(Th)}$	VDSVGS ID=1mA	2	4.5	V
Static Drain-to-Source On Resistance	$r_{DS(on)}$	VGS=12V, ID=24A	-	35	mΩ
Source-to-Drain Diode Forward Voltage	VSD	VGS=0V, ISD=48A	-	1.5	V

5.2.1.2 Component B

Component B is a 32 GBit commercial NAND-flash memory with reference MT29F32 G08ABAAAWP-ITZ manufactured by Micron [143]. This component was irradiated under static bias with V=3.3V (on). Two types of tests were performed: functional and electrical. Functional tests consisted in determining the error rates in holding values and in the operation of set/reset. These operations were tested at the same time with small statistical error by partitioning the chip and applying different tests to each part. The memories were partitioned in 64 blocks portions and tested as stated in Table 5.3 [141].

Table 5.3: Component B Partition Test Characteristics. From [141].

Partition #	Pattern	Type of test
1	All '0'	Static
2	All '1'	Static
3	Checkerboard	Static
4	Inv. Checker	Static
5	All '0'	Dynamic
6	All '1'	Dynamic
7	Checkerboard	Dynamic
8	Inv. Checker	Dynamic

In static tests, the memory was loaded with a specific pattern only once before any irradiation. In the dynamic tests the pattern is re-written every intermediate step. During re-writing, the partitions are tested for set/reset errors. The test sequences are as follows:

1. Prior to irradiation

   (a) Erase
   (b) Write patterns in all partitions
   (c) Read to validate
2. Irradiate Device Under Tests (DUTs)
3. Read all partitions to test data retention
4. Erase partitions 5 to 8 and test reset operation
5. Write patterns in partitions 5 to 8
6. Read partitions 5 to 8 to validate and to test set errors
7. Repeat points 2 to 6 for each irradiation step and points 3 to 6 for each annealing step.

Partition 2 and 6 were removed from testing due to the nature of NAND memories only allowing bits to flip from 0 to 1 (charged gate reads as 1). Besides the functional tests, the power supply current of the memory was also measured prior to irradiation, in between radiation steps, after radiation finishes and during the annealing, in standby and in read mode as listed in Table 5.4.

Table 5.4: List of electrical parameters measured for component B.

Characteristics	Symbols	Test Conditions	Limits		
			Min	Max	Un.
Standby current - VCC	ISB	CE# = VCCQ - 0.2V; WP# = 0V/VCCQ	-	50	uA
Array read current (active)	ICC1_A	-	-	50	mA

Reading all memory cells to check for errors is a very time consuming task which took ~2.5 hours to complete for all five irradiated samples while the ECS22900[68] requires that this period is limited to a maximum of two hours to avoid annealing effects. Since all components (A-E) were irradiated at the same time in each campaign, the characterization time of the memories posed scheduling issues with the other components. Therefore, irradiation of other components was not synchronized with the memories. As soon as their characterization was done, components were returned to the irradiation while memories remained outside for full characterization. They would then be placed under irradiation at the following step of the other components. This increased the time off-beam of the memories up to three hours which is larger than recommended but is compromise to minimize the impact of memory characterization in the test schedule.

5.2.1.3 Component C

Component C is a Bipolar Junction Transistor (BJT) from ST Microelectronics with reference 2N2222 [144]. This component was biased during irradiation according to its known worst-case condition ECSS Detail Specification No. 5201/002. The parameters listed in Table 5.5 were measured prior to irradiation, in between radiation steps, after radiation and during the annealing phase [141].

Table 5.5: Electrical parameters measured for Component C. From [141].

Characteristics	Symbol	Test Conditions	Limits		
			Min	Max	Un.
Collector-Base Cutoff Current	I_{CB}	V_{CB}=60V	-	10	nA
Emitter-Base Cutoff Current	I_{EB}	V_{CB}=3V	-	10	nA
Collector-Emitter Saturation Voltage	$V_{CE(sat)}$	I_C=150mA, I_{CB}=15mA	-	300	mV
Base-Emitter Saturation Voltage	$V_{BE(sat)}$	I_C=150mA, I_{CB}=15mA	-	1.2	V
Forward-Current Transfer Ratio	h_{FE1}	V_{CE}=10V, I_C=15μA	35	-	-
	h_{FE2}	V_{CE}=10V, I_C=100μA	75	-	-
	h_{FE3}	V_{CE}=10V, I_C=150mA	100	300	-
	h_{FE4}	V_{CE}=10V, I_C=500mA	40	-	-

5.2.1.4 Component D

Component D is an operational amplifier manufactured by Texas Instruments with reference LM124 [145]. This component was irradiated unbiased with all leads tied to ground as demonstrated to be the worst-case condition in [146]. The parameters listed in Table 5.6 were measured in all steps [141].

5.2.1.5 Component E

Component E is a shunt voltage reference manufactured by Texas Instruments with reference LM4050 [147]. This component was irradiated unbiased with all leads tied to ground according as shown to be the worst-case in [148]. The parameters listed in Table 5.7 were measured prior to irradiation, in between radiation steps, after radiation finishes and during the annealing phase [141].

5.2.2 Characterization

To characterize the components, a custom-made switch board (displayed in Figure 5.3), with 28 by-stable switches, connected to two Keithley Units (2636B – generic SMU and 2651a– Power SMU) providing a total of three channels, was used. The switch board was connected to Keithley 2636B digital IO in order to automatize all measurements. This was essential to decrease the off-beam time and avoid annealing effects between irradiation steps. A SOC development board from ARROW/ALTERA based on a Cyclone V was also used to interface the memory and perform the functional tests [141].

Table 5.6: Electrical parameters measured for Component D. From [141].

Characteristics	Symbols	Test Conditions	Limits Min	Limits Max	Un.
Power Supply Current	I_{CC}	V_{CC}+ = 30V, V_{CC}- = Gnd		3	mA
Input Bias Current	$\pm I_{ib}$	V_{CC}+ = 30V, V_{CC}- = Gnd, V_{CM} = +15V	-75	0.1	nA
Input Offset Current	I_{io}	V_{CC}+ = 30V, V_{CC}- = Gnd, V_{CM} = +15V	-15	15	nA
Input Offset Voltage	V_{io}	V_{CC}+ = 2.5V, V_{CC}- = -2.5, V_{CM} = -1.1V	-2.5	2.5	mV
Common Mode Rejection Ratio	$CMRR$		76		dB
Power Supply Rejection Ratio	$PSRR$	V_{CC}- = Gnd, V_{CM} = +1.4V, 5V $\leq V_{CC}+ \leq$ 30V	-100	100	uV/V
Voltage Gain	A_{vs}	V_{CC}+ = 30V, V_{CC}- = Gnd, 1V $\leq V_o \leq$ 26V, RL = 10kΩ	40		V/mV
Slew Rate: Rise	$+SR$	V_{CC}+ = 30V, V_{CC}- = Gnd	0.1		V/uS
Slew Rate: Fall	$-SR$	V_{CC}+ = 30V, V_{CC}- = Gnd	0.1		V/uS
Maximum Output Voltage Swing	$+V_{OP}$	V_{CC}+ = 30V, V_{CC}- = Gnd, V_O = +30V, RL = 10kΩ	27		V

Table 5.7: Electrical parameters to be measured for Component E.

Characteristics	Symbols	Test Conditions	Limits – Maximum tolerance 0 krad	30 krad	50 krad	100krad
Reference Voltage	V_R	I_R=74 μA	±5.0 mV	0.42%	0.67%	1.75%
		I_R=100 μA	±5.0 mV			
		I_R=1 mA	±8 mV			
		I_R=10 mA	±18 mV			
		I_R=15 mA	±20 mV			

All components were mounted in 5x5 cm^2 carrier boards to guarantee flux uniformity in all irradiations. These boards were designed in a way that allowed to connect them to the bias equipment and to the characterization setup. Three carrier boards with different components were used:

- carrier board with 5 samples of component A (Power Carrier)

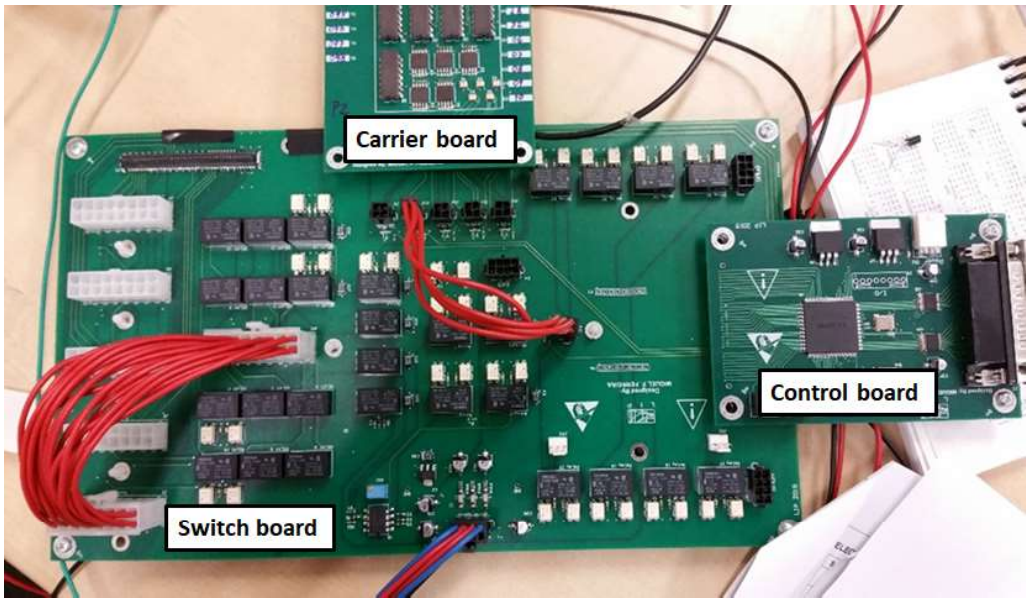

Figure 5.3: Switch board with a Generic Carrier board coupled to it. From: [141].

- carrier board with 5 samples of component B (Memory Carrier)
- carrier board with 5 samples of component C, 5 samples of component D and 5 samples of component D (Generic Carrier)

Each component sample was serialized with a unique ID according to the following form:

<irradiation type>-<component type>-<serial#>

Where <Irradiation type> indicates irradiation conditions (Co1, Co2, Eb1, EB2 or Eb3 - see next section) and the component type is according to 5.1 (A,B, C, D or E).

This ID is used when referring to a specific device for the remainder of this chapter. All components were characterized and irradiated at room temperature T_{room}=22±3 °C to minimize temperature related fluctuations and oxide-trap annealing.

5.3 Radiation Test Plan

Five irradiation campaigns including LDR and HDR ^{60}Co (Co1 and Co2) and HDR electron irradiations (Eb1, Eb2 and Eb3) were performed up to a total dose of ∼100 krad in water. During irradiation, components were biased in the worst-case conditions as specified in [68].

Components were characterized before, after and at four points during the irradiation. Measurements of irradiated components were performed under one hour to avoid annealing effects. Reference (unirradiated) components were also measured before, after and at some points during all irradiation campaigns. They were always kept in the same conditions as the irradiated samples to decouple the impact of external factors on the results.

5.3.1 ^{60}Co - Low Dose Rate

LDR ^{60}Co test campaign (code Co1) was performed at the ESA/ESTEC ^{60}Co facilities [149] with a dose rate of 280 rad/hour. Due to overlaps with other experiments, radiation steps were not equal but 23.73 krad, 20.42 krad, 24.11 krad, 26.07 krad and 19.37 krad respectively up to a total dose of 113.7 krad (measured using a Farmer Dosimeter with 0.66cc ionisation chamber credited with ISO-17025 [150]). All component types were irradiated in this test campaign.

5.3.2 ^{60}Co - High Dose Rate

The Co2 test campaign comprised of the irradiation of all the five type of components in CTN-IST (Campus Tecnológico e Nuclear–Instituto Superior Técnico) [151] using a ^{60}Co source at High Dose Rate (24 krad/hour) in 20 krad steps up to 100 krad (measured using a Farmer Dosimeter with 0.66cc ionisation chamber credited with ISO-17025 [150]).

5.3.3 Eb1 - 12 MeV e$^-$ High Dose Rate

Eb1 irradiation comprises the irradiation of all the five type of components using a 12 MeV electron beam from a medical Linear Particle Accelerator (LINAC) in Hospital Santa Maria (HSM) [152], with a 24 krad/hour dose rate in 20 krad steps up to 100 krad. Doses in LINACs are measured in water at the maximum ionizing depth as determined in [153]. This value is obtained by measuring the dose at different depths with a water phantom, creating a Dose-Depth Profile (DDP) such as the ones shown in Figure 5.4 measured in the RADEF LINAC [115] (the chart from the Hospital has very low resolution). The dose is then measured at a water depth corresponding to the maximum ionization percentage. For EEE components in ^{60}Co facilities, the dose is measured directly without water which means that the doses are not comparable. Since Silicon devices are very thin, it is then more accurate to use the former dosimetry method. For this reason, a conversion factor was applied to the dose given by LINAC operators, equal to the relative ionization at the surface obtained from the DDP and at the maximum of the profile. In Eb1 this factor was identified as 0.9 from the DDP given by the Hospital, which means that the irradiation was actually done at 21.5 krad/hour dose rate in 18 krad steps up to 90 krad (doses in water at the surface). The change in dose rate is small enough that no dose rate effects are expected.

5.3.4 Eb2 - 12 MeV e$^-$ High Dose Rate

Eb2 irradiation was done in the RADEF facilities [115] with a 12 MeV electron beam. Dose rate and total dose were the same as in Eb1 and the DDP was similar as well. Therefore, the correction factor (0.9) was used for both. In this campaign, only two samples of component C was irradiated and five samples of components D and E were

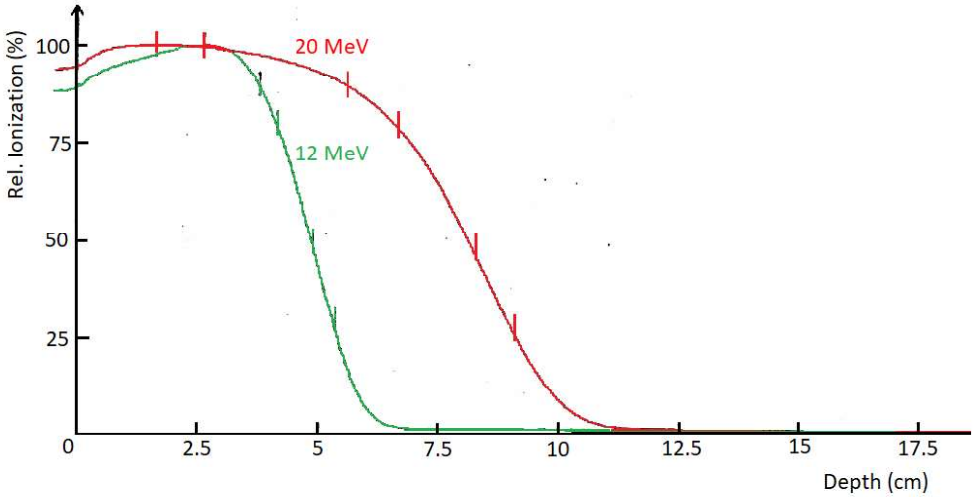

Figure 5.4: Dose-Depth profile for 12 and 20 MeV electron beams measured in the RADEF LINAC [115]

irradiated to compare to the results from Eb1. Component A and B were not irradiated. This allowed to correlate RADEF results with the Hospital without using all components.

5.3.5 Eb3 - 20 MeV e$^-$ High Dose Rate

Eb3 test campaign was also done in the RADEF facilities [115] with a 20 MeV electron beam. The correction factor in this case was found to be 0.95 which means that irradiation was done with a 22.7 krad/hour dose rate in 19 krad steps up to 95 krad. Five samples of component A, D and E were irradiated. Components B and C were not irradiated. A summary of the total number of each type of component irradiated in each test campaign is given in Table 5.8.

Table 5.8: Number of samples per component type used in each irradiation campaign. Notice that not all components were irradiated in Eb2 and Eb3 due to part availability. From [141].

Component	Co1	Co2	Eb1	Eb2	Eb3
A	5	5	5	0	5
B	5	5	5	0	0
C	5	5	5	2	0
D	5	5	5	5	5
E	5	5	5	5	5

5.3.6 Annealing Plan

After irradiation, the parts entered an annealing phase to study the effect of de-trapping. Samples irradiated were submitted to an annealing phase of 8 months unbiased at room temperature. The components were characterized weekly in the first month and once per month until the end of the annealing phase. This was done with all components

unbiased at room temperature because of logistic constraints. However, a consequence is that annealing is slower this way.

5.4 Irradiation Test Results

The full results of the irradiation test campaigns were already shown in [141] and published in [140]. As such, in this chapter only the most important results of each component will be discussed. Results are displayed with the template used in Figure 5.5. Relative parameter shift averaged over all samples of a given component type as well as the absolute values of each sample are shown. All error bars correspond to one sigma. Relative shift is more important because depending on component or parameter the initial value might fluctuate in a significant manner [141].

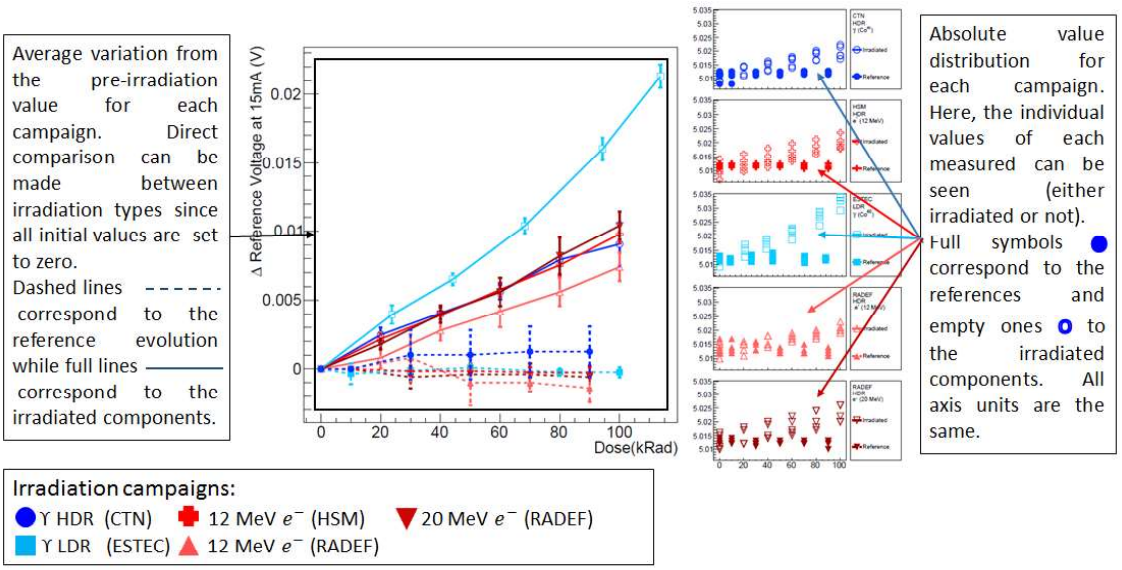

Figure 5.5: Guideline to the format of the results. From [141].

5.4.1 Component A – STRH100N10

Component A is a discrete MOSFET which means that the Gate-to-Source Threshold Voltage is the most affected parameter as it was discussed previously in Section 4.2.1. Figure 5.6 shows the shift in the parameter in the four test campaigns it was used (Co1, Co2, Eb1 and Eb3). No differences were observed between HDR ^{60}Co and both 12 and 20 MeV electron irradiations. A small Enhanced Low Dose Rate Sensitivity (ELDRS) effect is seen although it is not very significant. The same results were observed for the Drain Current. All other parameters showed no apparent shift. This means that for discrete MOS devices ^{60}Co can still be used to give the worst-case analysis in missions to Jupiter.

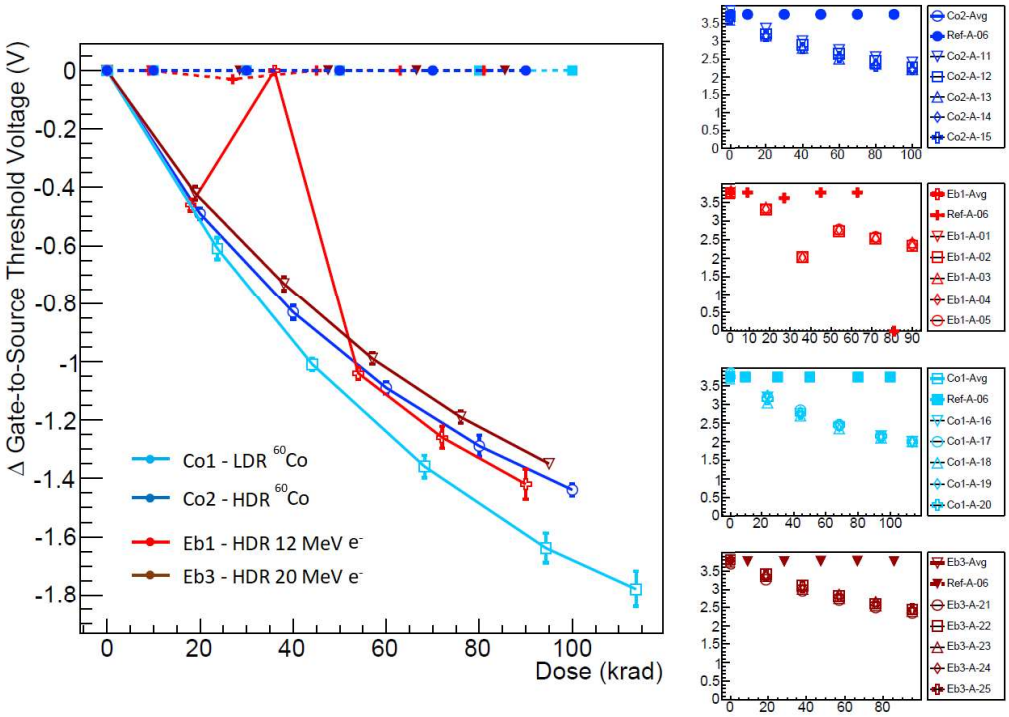

Figure 5.6: Component A Gate-to-Source Threshold Voltage variation (left side) and absolute values (right side). Blue points correspond to the HDR ^{60}Co CTN campaign, Red points to the 12 MeV e^- HDR Hospital campaign, Cyan points to the LDR ^{60}Co ESTEC campaign and Dark Red points to the 20 MeV e^- HDR RADEF campaign. The 40 krad point measured in Eb2 correspond to a faulty measurement. From [141].

5.4.2 Component B – MT29F32G08ABAAAWP

Component B is a commercial FLASH-NAND memory from Micron [143]. The main effects in this component is bit flipping (charging of the floating-gate of a cell MOSFET) and power consumption. Of the 13 samples tested, only one survived a full test campaign. Memories irradiated with electrons appeared to be less damaged than those subject to ^{60}Co irradiation.

In Co2 all samples were unresponsive after the third irradiation step (60 krad). In Co1, one sample remained functional up to 68.28 krad (three steps) while the other two stopped responding after the 44.15 krad mark. In Eb1 all samples were responsive after the third step, two after the fourth and one for the full test campaign. Moreover, Co1 bit error rate was also larger than in Eb1 as shown in Figure 5.7 for partition 0. The same results were obtained for other partitions electrical tests did not show significant change even after the memories were unresponsive.

There is no clear indication of the reason to the memories enhanced ^{60}Co sensitivity. The tests however suggest that standard ^{60}Co testing is representative of worst-case radiation effects on this technology and can be used safely for components flown in missions to Jupiter. However, it is noteworthy that this was done with a commercial component which is not manufactured with the same strict standards as qualified components. This

leads to greater part-to-part variability even inside the same lot. In fact, while one of the samples used in Eb1 managed to remained operational after receiving 90 krad, three of the samples subject to the same irradiation conditions were rendered unresponsive after 54 krad.

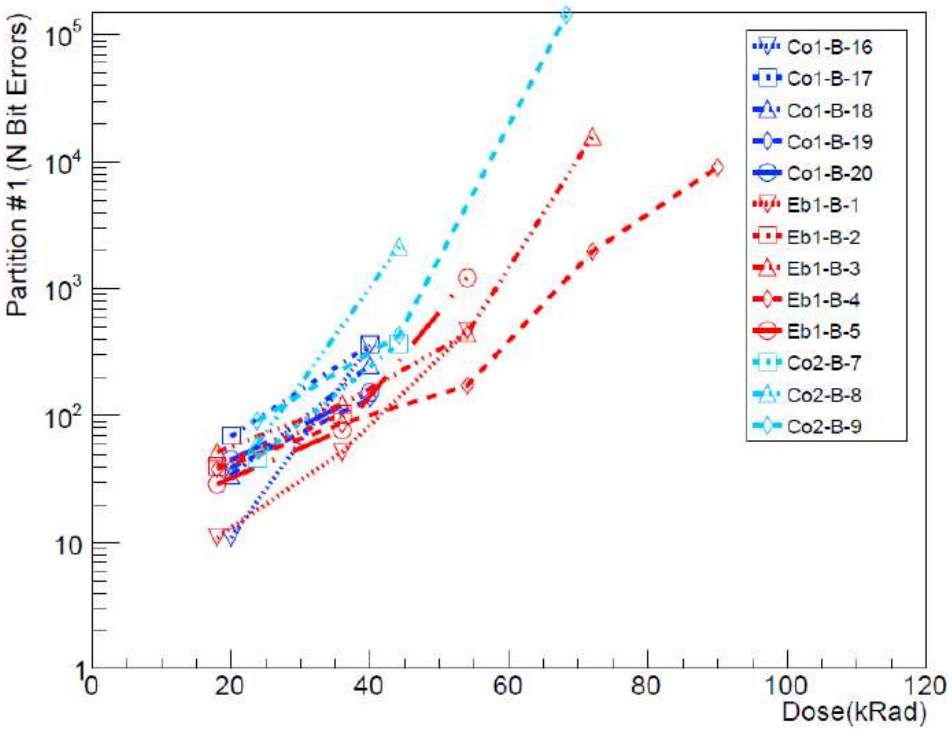

Figure 5.7: Component B number of bit errors in partition #1. Blue points correspond to the HDR ^{60}Co CTN campaign, Red points to the 12 MeV e$^-$HDR Hospital campaign and Cyan points to the LDR ^{60}Co ESTEC campaign. From [141].

5.4.3 Component C – 2N2222

Component C is a Bipolar Junction Transistor. For this components, the major effect should be the gain of the device as discussed in Section 4.2.1. In fact, as it can be seen in Figure 5.8, the Forward-Current Transfer Ratio decreases in a very significant manner. The degradation is equivalent in both ^{60}Co and electron irradiations in all regimes. The same is true for all other parameters. It is then safe to conclude that ^{60}Co can still be used as a worst-case test. The only noticeable effect is ELDRS which is expected in BJTs.

5.4.4 Component D – LM124

In component D, an OpAmp (analogue IC), unlike in all other components, degradation due to electrons was found to be larger than from ^{60}Co in the Input Bias and in the Common Mode Rejection Ratio parameters, as it can be seen in Figure 5.9 and Figure 5.10 respectively. In Figure 5.10 it can be seen that electron effects is greater in magnitude

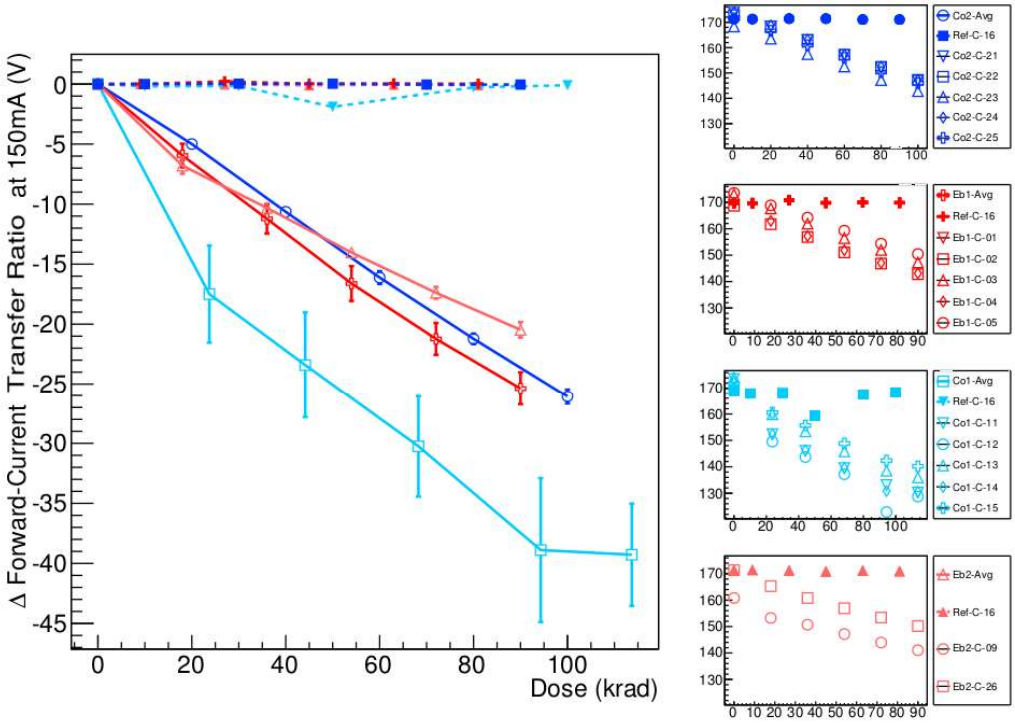

Figure 5.8: Component C Forward-Current Transfer Ratio (Ic=150mA) variation (left side) and absolute values (right side). Blue points correspond to the HDR ^{60}Co CTN campaign, Red points to the 12 MeV e^- HDR Hospital campaign, Cyan points to the LDR ^{60}Co ESTEC campaign and Light Red points to the 12 MeV e^- HDR RADEF campaign. From [141].

up to a dose of 55 krad in the case of Eb1 and Eb2 and that it starts to vary in the opposite direction for higher doses. In Eb2 the degradation is still larger than in ^{60}Co irradiations but smaller than in the other electron irradiations. Although it was expected that Eb1 and Eb2 would result in similar degradation of the components the fact that Eb1 is closer to Eb2 shows that inter-calibration between different LINACs might pose an issue in electron testing.

A way to explain the enhanced degradation of these parameters in electron irradiations is to consider the effects of Displacement Damage Dose (DDD) from electrons [128] or from neutrons produced in LINACs [154]. In another study [155], LM124 was tested by RUAG with protons and ^{60}Co to separate TID and DDD efects. Components in these tests were subject to different 50 MeV proton fluences,$P_{fluence}$ 1x10^{11}, 2x10^{11}, 3.5x10^{11} and 5x10^{11} p.cm^{-2}, and then irradiated with ^{60}Co until the combined TID from both irradiations reached 100 krad. TID from protons was computed into the total. In these tests, the Input Bias and CMRR parameters were particularly susceptible to DDD which further reinforces the aforementioned hypothesis. Complete extrapolation of the results is difficult since the particles used are different in type and energy hence NIEL scalability might not be valid. Also, components were not from the same lot which means that their response might not be the same. However, a qualitative comparison is still possible. First, one needs to evaluate the DDD from electron irradiation. TID deposited by an electron beam can be described as a function of the electron fluence, $\phi_{Electron(E)}$ as follows:

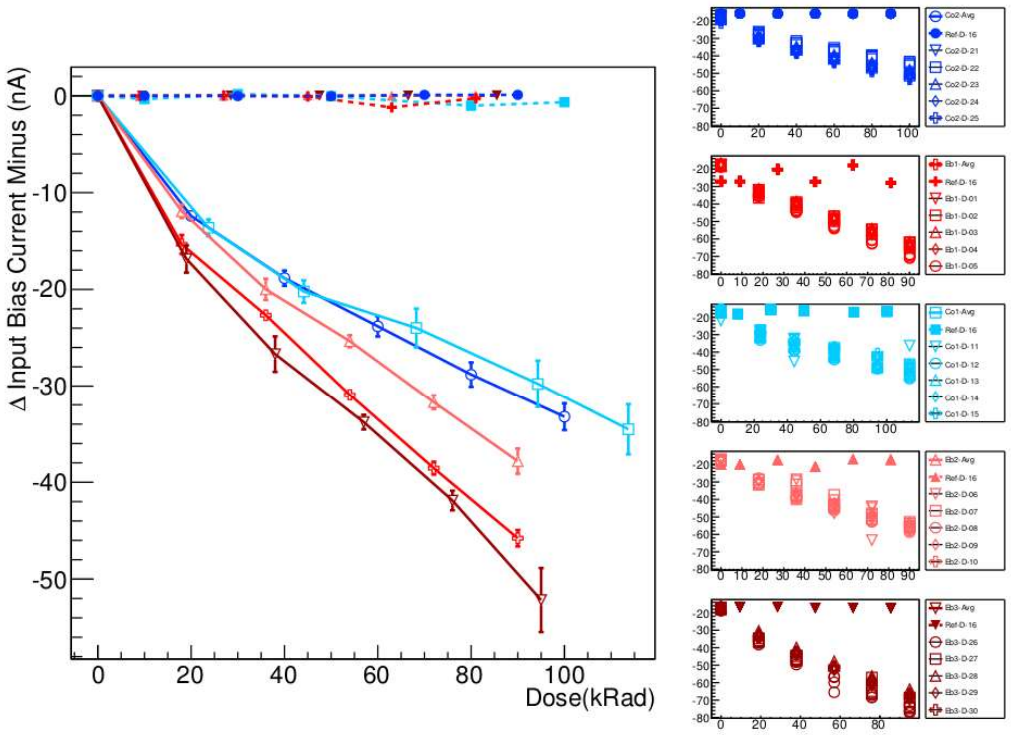

Figure 5.9: Component D Input Bias Current Minus variation (left side) and absolute values (right side). Blue points correspond to the HDR ^{60}Co CTN campaign, Red points to the 12 MeV e^- HDR Hospital campaign, Cyan points to the LDR ^{60}Co ESTEC campaign and Light Red points to the 12 MeV e^- HDR RADEF campaign and Dark Red points to the 20 MeV e^- HDR RADEF campaign. From [141].

$$TID = (\phi_{Electron(E)}.A).(\frac{dE}{dx}.th).\frac{1}{m} = \phi_{Electron(E)}.\frac{dE}{dx}.\frac{1}{\rho} \tag{5.1}$$

Where $\frac{dE}{dx}$ is the stopping power of the particle in Silicon and A, th, m and ρ are the surface area, thickness, mass and density of the device respectively. This formula is valid only if the stopping power does not change along the particle path. Since the components are thin and their density is not very large, this can be considered a good approximation for 12 and 20 MeV electron. The electron fluence can then be obtained as a function of TID:

$$\phi_{Electron(E)} = TID.\frac{dE}{dx}.\frac{1}{\rho} \tag{5.2}$$

And converted to a 50 MeV proton fluence:

$$\phi_{Eq.Proton(50MeV)} = TID.\frac{dE}{dx}.\frac{1}{\rho}.\frac{NIEL_{Electron(E)}}{NIEL_{50MeV\,Proton}} \tag{5.3}$$

Using the stopping power obtained with NIST [67] and the NIEL values from the SRNIEL database [130], the Eq. 50 MeV Proton fluence of 12 MeV electron irradiation (TID=90 krad), Eb1 and Eb2, and of 20 MeV electron irradiation (TID=95 krad), Eb3, is

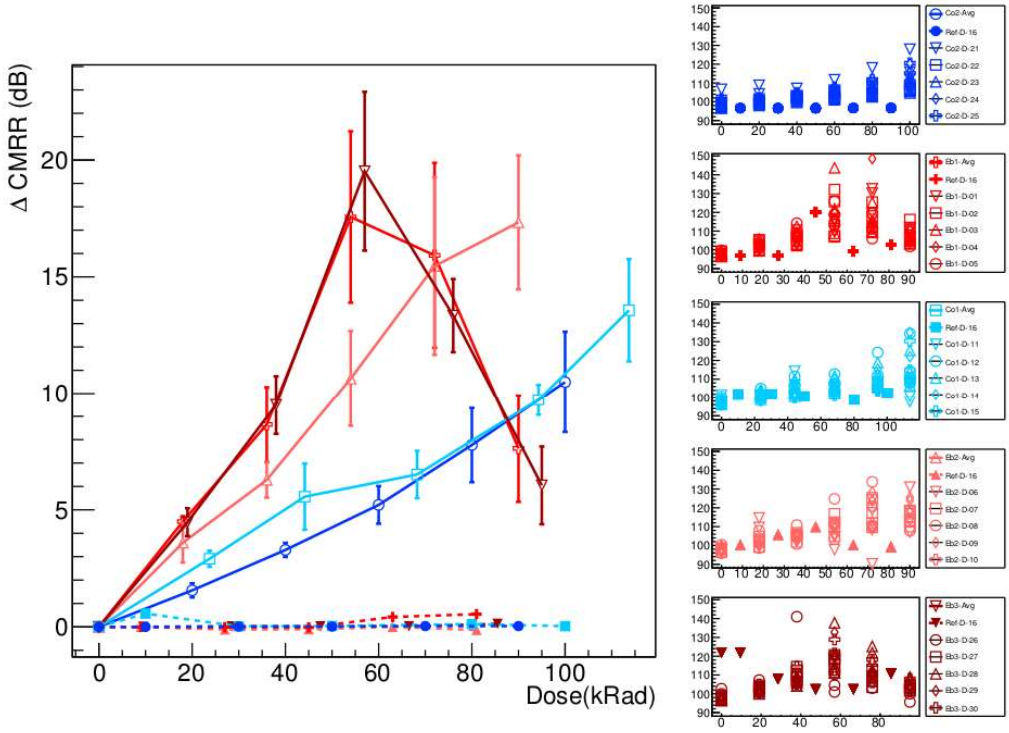

Figure 5.10: Component D Common Mode Rejection Ratio variation (left side) and absolute values (right side). Blue points correspond to the HDR ^{60}Co CTN campaign, Red points to the 12 MeV e^- HDR Hospital campaign, Cyan points to the LDR ^{60}Co ESTEC campaign and Light Red points to the 12 MeV e^- HDR RADEF campaign and Dark Red points to the 20 MeV e^- HDR RADEF campaign. From [141].

2.61x10^{10} $p.cm^{-2}$ and 2.93x10^{10} $p.cm^{-2}$ respectively. This is less than 30% of the smallest fluence tested in [155]. However these tests still show clear trends regarding the DDD effects. In the parameters that degraded similarly in electron and ^{60}Co irradiations such as the Voltage Offset, DDD has low effect for low fluences when compared to TID as it can be seen in Figure 5.11. In contrast, the drift of the Bias Current rises rapidly with DDD as it can be seen in Figure 5.12.

CMRR results from [155] on the other hand, show that the effect of DDD is contrary to that of TID. In fact, the tests in [155] with proton fluence of 1x10^{11} p.cm^{-2} results in a drift of 10(dB) in magnitude which is half of the drift due to ^{60}Co irradiation. This is indicative of what happened in this study. At first TID dominates the drift until after a certain threshold DDD takes over the effect. What is not clear is why initially TID and DDD combined results from electron irradiation had a larger effect than ^{60}Co. One possible explanation is the high variability in the measurements of all samples. In fact, even the references showed this variability which refers to a circuit issue. Furthermore, there is no evidence for enhanced electron sensitivity in other parameters of component D. Therefore this is not considered critical and ^{60}Co is deemed representative of worst-case radiation effects for these components.

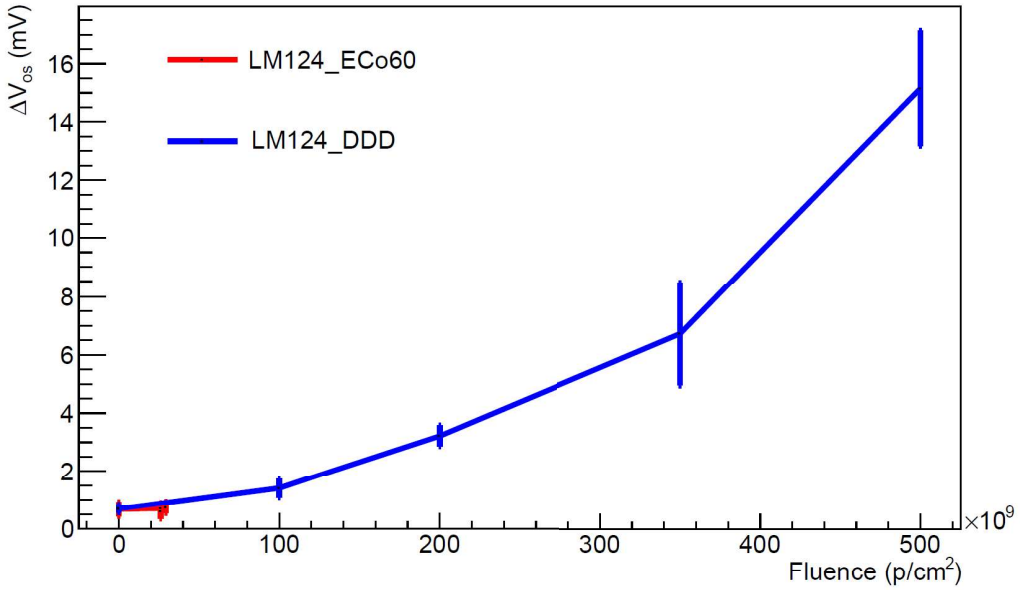

Figure 5.11: Voltage Offset drift obtained in this study and in [155]. Adapted from [141].

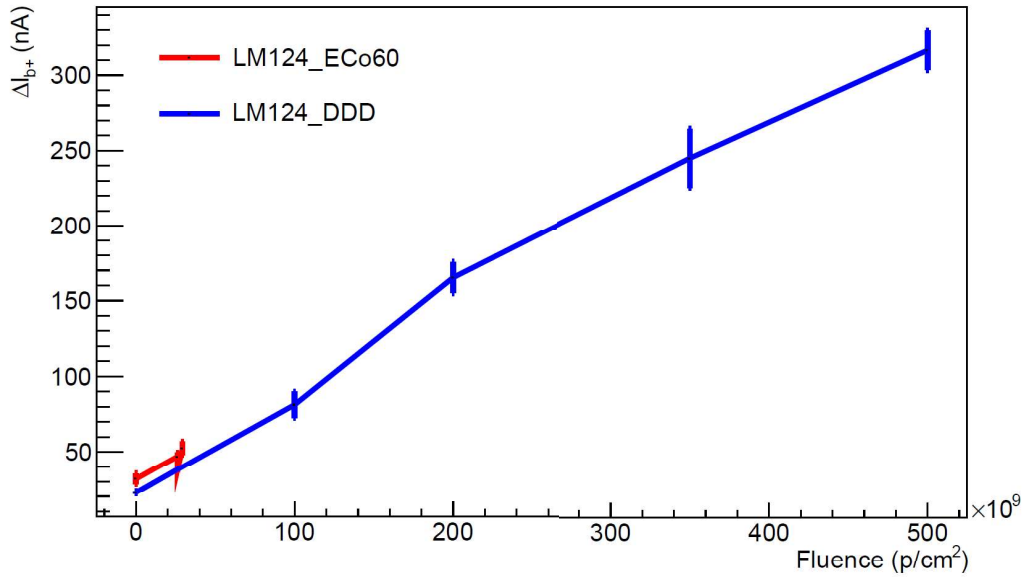

Figure 5.12: Input Bias obtained in this study and in [155]. Adapted from [141].

5.4.5 Component E – LM4050

Component E results also show that the difference between electron and ^{60}Co is small and that only ELDRS effects are visible as expected for this Bipolar device (see Figure 5.13). This is true for all parameters measured. It is noticeable however that the 12 MeV e^- irradiation campaign in HSM and the 20 MeV e^- irradiation campaign in RADEF have very similar results and that they are different from the 12 MeV e^- irradiation campaign in RADEF. This is consistent with the results obtained for Component D. These two components are the only ones that were irradiated in all conditions with a relevant number of samples, indicating that the two LINAC systems might need inter-calibration. Another

hypothesis is that this can also have been caused by neutron production in the targets and should be investigated especially regarding the medical applications of LINACs.

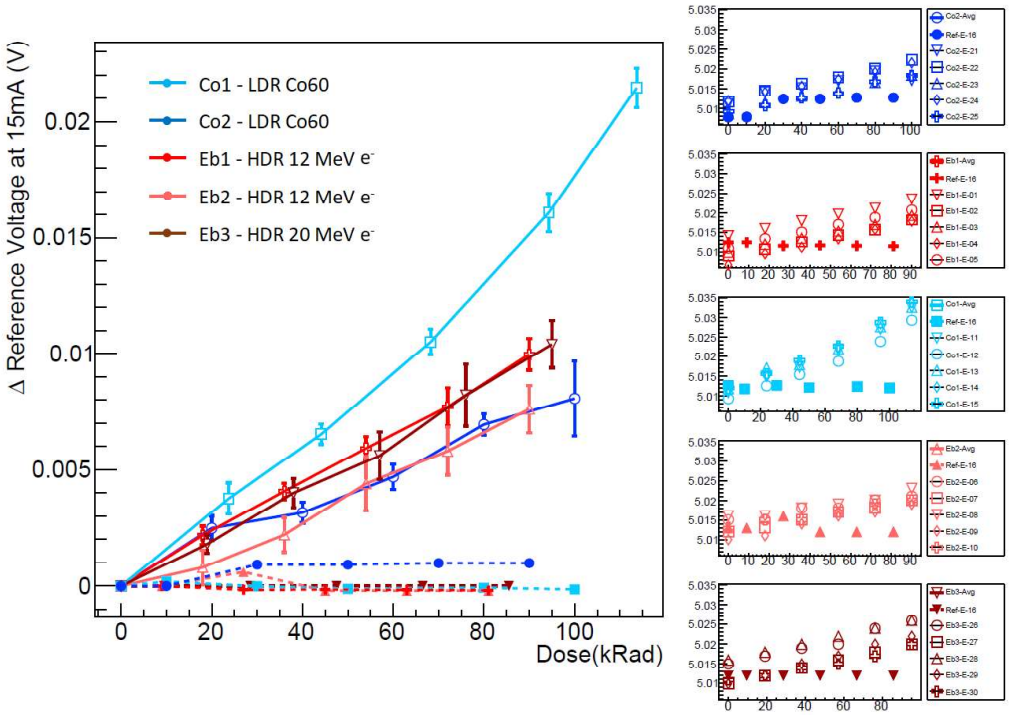

Figure 5.13: Component E Reference Voltage (Ir=15mA) variation (left side) and absolute values (right side). Blue points correspond to the HDR ^{60}Co CTN campaign, Red points to the 12 MeV e^- HDR Hospital campaign, Cyan points to the LDR ^{60}Co ESTEC campaign, Light Red points to the 12 MeV e^- HDR RADEF campaign and Dark Red points to the 20 MeV e^- HDR RADEF campaign. From [141].

5.5 Annealing Results

After irradiation, the components were subject to an annealing period of eight months. For logistic reasons, the components were kept unbiased for the whole period which slows down the process. The fact is that no annealing effects were observed in any of the components in this study. The only exception was the threshold voltage of component A which showed a slow recovery (formation of interface traps), small in magnitude, as it can be seen in Figure 5.14. This is explained by the fact that the samples were kept unbiased and at room temperature. This means that de-trapping, which is mainly achieved by thermal excitation of trapped charges, is a very slow process as observed. Annealing of oxide traps reverses the effect of irradiation since as N-MOS device interface traps have an opposite effect as it was discussed in Section 4.2.1. The fact that Co2 and Eb1 follow the same trend, though not conclusive, indicates that of ^{60}Co and electron irradiation result in the same trap profile meaning that for worst-case annealing assessment ^{60}Co is still valid.

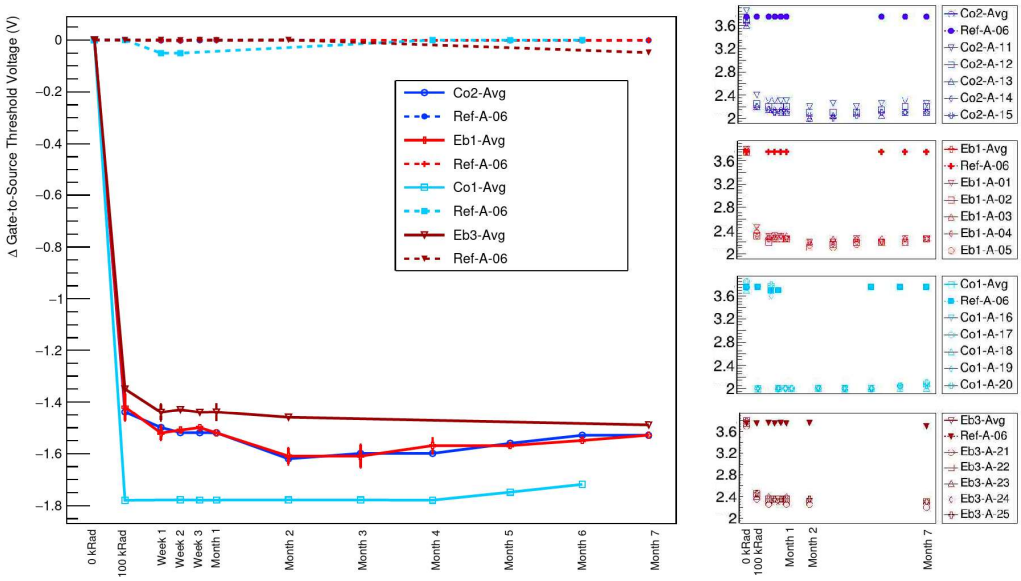

Figure 5.14: Component A Gate-to-Source Threshold Voltage annealing drift (left side) and absolute values (right side). Blue points correspond to the HDR ^{60}Co CTN campaign, Red points to the 12 MeV e$^-$ HDR Hospital campaign, Cyan points to the LDR ^{60}Co ESTEC campaign and Dark Red points to the 20 MeV e$^-$ HDR RADEF campaign. From [141].

5.6 Discussion

In this chapter the results of an extensive radiation test campaign to verify ^{60}Co testing representativeness for components flown in the JUICE mission is presented. Five key technology types, discrete and IC, MOS and Bipolar components, were irradiated with ^{60}Co at HDR in Campus Tecnológico e Nuclear - Instituto Superior Técnico, and at LDR in ESA/ESTEC facilities, as well as with 12 MeV and 20 MeV electrons in Hospital Santa Maria and RADEF - University of Jyvaskyla. All components bias conditions and electrical characterization were done as specified in [68] in order to address the problem at qualification level.

Components A, C and E showed no difference in the results confirming that for these technologies, ^{60}Co can be used to assess worst-case radiation effects for missions to Jupiter. For component B the same conclusion can be taken from the results but, in this case ^{60}Co degraded the components more than electrons. Although it does not affect the conclusions, it is noteworthy that the memories were of commercial origin which can induce larger part-to-part variability.

Component D, an Operational Amplifier showed enhanced degradation from electron irradiation in two parameters and no difference or no degradation in the others. The main hypothesis behind this result is that 12 and 20 MeV electrons have sufficient energy to penetrate the electronic cloud, and interact with the atomic nuclei, which translates into a low, but perceivable DDD effect. Also, it is also known that neutrons are also present in LINACs increasing the DDD in electron testing [154]. To determine this, the results obtained were compared to a study of combined TID and DDD effects with a proton beam and ^{60}Co on the same component (LM124) [155]. Although the device was not from the same lot, and the DDD in our study was much lower, a qualitative analysis was still possible. In fact, it was acknowledged that in the proton tests, the most sensitive parameters to DDD were the same that displayed enhanced degradation from electrons. Furthermore, in the proton tests, TID and DDD cause the Commom-Mode Rejection Ratio to drift in opposite directions. The same trend was observed in this study reinforcing the idea that DDD was responsible for the enhanced electron sensitivity. Considering also that only two parameters of LM124 showed this effect, it is safe to assume that ^{60}Co testing is representative of radiation effects on components flown to the Jovian system.

Another interesting result from this study was that the Eb1 test campaign with 12 MeV electrons in Hospital Santa Maria yielded very similar results as the 20 MeV electrons from the Eb3 test campaign in Jyvaskyla consistently. However, these results were different from the ones obtained in the Eb2 test campaign with 12 MeV electrons which is unexpected. Considering that both Eb2 and Eb3 were done in the same facilities (RADEF), some questions about the cross-calibration between different LINACs rose. In this case, the energies might correspond to different values or the neutron population might be different.

This project was successful in demonstrating the representativeness of ^{60}Co testing for the high energy electron environment found in Jupiter when compared to Earth's.

This result is relevant for worst-case conditions only but has an enormous impact for the JUICE mission. Knowing this assures that no further testing is required for all components that are planned to be used in the spacecraft while maintaining the same design margins. If the damage from electrons were found to be larger than ^{60}Co the whole Radiation Hardness Assurance process would have to be rethought to accommodate larger margins or to re-test the components used. In both cases this would have a major impact on the cost of the mission since the mass budget would have to be increased and/or testing of the components would have to be payed for. The latter case could also have major implications in the mission scheduling.

In the future it would be interesting to perform the same tests with different bias and with higher energy electrons in order to fully understand the differences between the mechanisms that govern ^{60}Co and electron effects in EEE components. Biased annealing or at high temperature should also be done to understand if trap evolution is the same in both cases.

6 RADEM Radiation Analysis and Shielding Optimization

An important aspect of Radiation Hardness Assurance (RHA) is the calculation of radiation quantities in sensitive components. These quantities must be within the operational limits of the components as determined by radiation testing and Radiation Design Margins (RDM). When the quantities are above these limits, actions must be taken in order to reduce the risk of malfunction as discussed in Section 4.5. The radiation margins for components from the JUICE Preferred Parts List (JPPL) and qualified components in instruments is 2 for both Total Ionizing Dose (TID) and Total Non-Ionizing Dose (TNID) [28]. The RDM is standard for flight-lot tested components in high reliability space missions. It allows to take into account the variability of the parts that compose the system and the stochastic nature of the radiation environment. In hindsight, they are also related to the work in the previous chapter in the sense that ^{60}Co testing was proven to be valid for the high energy electron environment in Jupiter and no additional testing and/or increased margins are necessary.

The Radiation Hard Electron Monitor (RADEM) is composed of more than one hundred sensitive EEE components. In this chapter, the methodologies used to compute TID, DDD and SEE at part level, as well as the mitigation decisions employed, when required, are discussed. All results are based on the Technical Notes [156][157][158] approved by ESA and AIRBUS under the ESA/ESTEC Contract 1-7560/13/NL/HB for the development of RADEM. GUIMesh, a tool developed for this purpose, published in [159] is presented.

6.1 GUIMesh

Before discussing the methods used to calculate the radiation levels in the RADEM EEE components, I will introduce and describe GUIMesh , a tool develped for this purpose, but that can be used in the development of any Geant4 application based on geometries described in STEP CAD formats. While the mechanical part of instruments is designed in Computer-Aided Design (CAD) tools, Geant4, the particle transport toolkit presented in Chapter 3 [30][31][32] does not have a parser to interpret the CAD standard file format STEP [33]. This may lead to loss of detail and under or overestimation of the quantities

under study, especially when the instruments have complex shapes, and/or a large number of volumes. Though several solutions have been proposed to import complex geometries from STEP files to Geant4, so far, only commercial options are available. Open-source programs with varying limitations also exist. While some of them, such as CADMesh [91][160] and STL2GDML [161] only interface Stereolithography (STL) [162], a CAD mesh format, files with Geant4, requiring previous effort from CAD users to convert solids into this format, others such as SW2GDML [163] which allows SolidWorks [164] geometries to be translated into the toolkit, work with those specific CAD formats only. These tools require that the instrument is designed with a specific CAD editor which is a major drawback since it might not be an option for the Geant4 users. Finally, there is a third category of tools, that converts STEP [33] files to GDML [34][165], the most widely used data exchange CAD format. These tools, namely FASTRAD [166], ESABASE2 [167] and STEP-Tools [168] are more versatile than those in other categories but they are neither open-source nor free [159].

In this work, FreeCAD [169], an open-source CAD editor with Python [170] scripting capabilities, was used to tessellate volumes from STEP files. Since FreeCAD libraries can be easily imported in Python, a Graphical User Interface (GUI) was programmed with Python. This application, GUIMesh, allows users to import STEP files using FreeCAD libraries, manage materials (STEP files do not include material information), mesh volumes, and export them to GDML files. Materials are chosen from the Geant4 material database based on the NIST [67] library or created by mixing materials listed in that database. Assignment of materials to volumes can be performed on a one-to-one basis or loaded from a CSV (Comma-Separated values) file. Meshing is performed via FreeCADs "tessellate" function which converts all surfaces into a mesh of triangles with a user-defined precision. A GDML file is written for each volume, to provide some flexibility. An additional GDML file is also written, the "mother" GDML, which is read by the GDML parser function in Geant4, providing the geometry tree so that multiple volumes can be integrated in the toolkit [159]. The work presented here was published in Computer Physics Communications [159].

6.1.1 Method

GUIMesh can be divided into three functionalities: CAD processing using FreeCAD to read step files and tessellate volumes, material management and GDML file writing.

6.1.1.1 Interface

The Graphical User Interface (GUI) built with Tkinter [171], a Python [170] extension, used to facilitate the procedure of converting STEP [33] geometries to GDML [34][165], is shown in Figure 6.1. It is composed of three panels. A menu with eight buttons, corresponding to different user options, a volume list of the imported STEP file, and a panel with the volume properties where the volume material as well as the maximum

meshing deviation (MMD) can be changed by the user. The user is also given the option not to write specific volumes to GDML. All these options can be applied to a single volume or to all of them simultaneously.

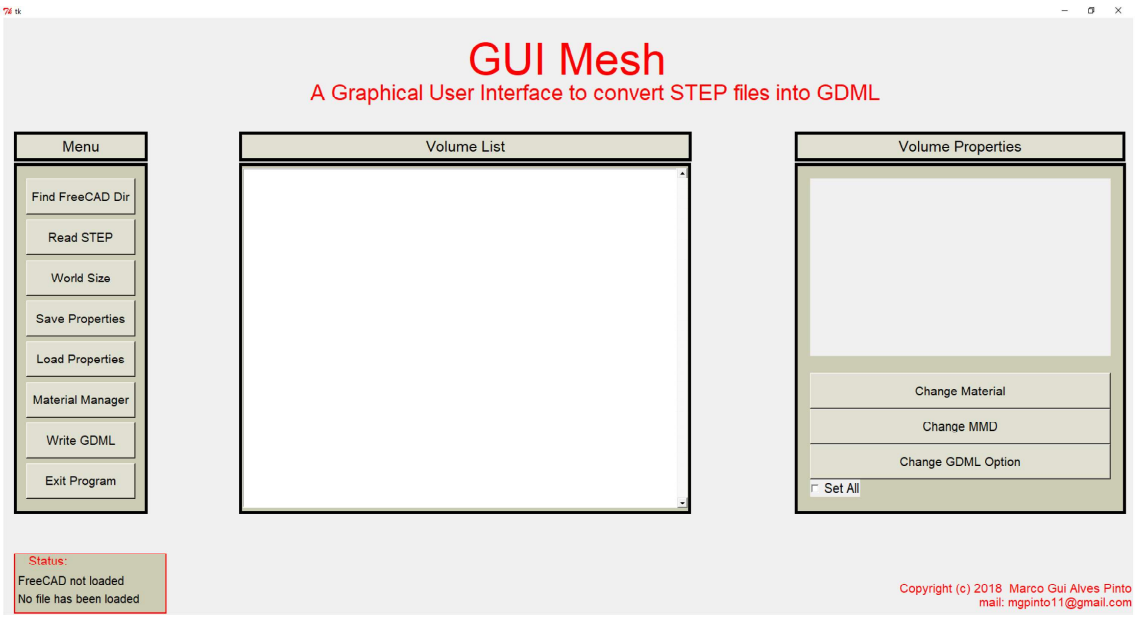

Figure 6.1: GUIMesh GUI. On the left side a menu with different functions is presented to the user as buttons. The middle panel displays the list of the loaded volumes. The right side is dedicated to volume editing. From [159].

6.1.1.2 CAD processing

GUIMesh imports FreeCAD libraries with Python 2.7. Both 0.15 and 0.16 versions of FreeCAD [169] are compatible with GUIMesh though volume names may differ from the original when volumes are imported. FreeCAD imports STEP files (.STEP and .STP extensions) via its "Import" module.

Tessellation of surfaces is performed by the FreeCAD standard meshing algorithm, which has one degree of freedom, the Maximum Mesh Deviation (MMD). The default value, 0.1 mm, can be changed for each volume individually or for the whole geometry. Lower MMD values provide better precision in the geometry description but require larger memory allocation and increased CPU time at simulation level, due to the increase in the number of triangles in the tessellation. The precision for planar surfaces does not change with MMD.

6.1.1.3 Material Definition

All (270) materials from the Geant4 NIST library are predefined in GUIMesh and can be accessed directly using their Name in the Geant4 Material Data Base (G4_H for Hydrogen, G4_He for Helium, etc.). These materials cannot be changed but they can be mixed to create new materials of a given name, density and number of elements, each

representing a fraction of the material composition. These new materials can be created, stored and loaded in the Material Manager window that is displayed in Figure 6.2. When loaded into GUIMesh all volumes are given a default material, Silicon (G4_Si), that can be altered directly in GUIMesh or latter in Geant4. In the former, materials can be assigned to volumes on a one-by- one basis, or uploaded through a CSV file containing all materials, where each line contains the volume name and the material name assigned to the volume, in the same order that is displayed in the GUI.

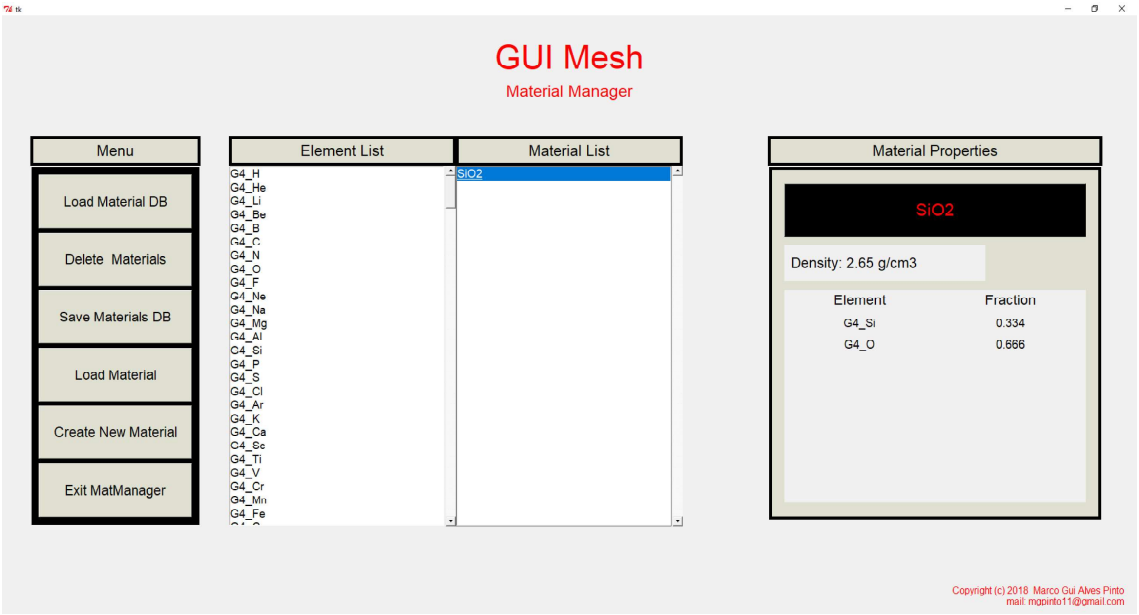

Figure 6.2: 2 Material Manager interface. Left side presents the user options regarding loading, saving, deleting and material. The middle section presents the session available elements (NIST materials [67]) and materials created by the used. The right side displays selected material properties. From [159].

6.1.1.4 GDML

GDML [34][165] is an XML-based language interchange format, designed to describe geometries for physics simulations. This format accepts both elementary shapes and tessellated solids. Tessellation was the method chosen for GUIMesh, since it allows to describe complex irregular solid [30][31][32].

GDML format is composed of five fields: define; materials; solids; structure and setup.

The field "define" is used to define different values that may be used in the rest of the file. Here is where the vertex positions of a given volume are registered. The field "materials" is used to define the materials assigned to the objects. NIST materials do not need to be defined in detail, since Geant4 will correctly interpret material included in the Geant4 Material Database reference. Any compound or mixture of materials however, may be defined in this field as a mix of NIST materials, each defined by the corresponding mass fraction in the compound or mixture.

The "solids" field corresponds to the geometric definition of volumes. The world volume

is defined as a simple box with dimensions defined in GUIMesh (default size is 1 m x 1 m x 1 m). Tessellated solids from the STEP file are registered as a series of triangles enclosing a surface with the vertex that are written in the "define" field.

The "structure" part defines the geometry hierarchy. Unlike in STEP files, where the hierarchy is flat, Geant4 has a geometric hierarchy where volumes are placed inside others with the world volume as the top geometry. Since in GUIMesh each volume is written in a separate file, each volume is the top most geometry in its file. For this reason, GUIMesh also writes an extra "mother" file, which defines the world volume and allocates the other GDML files (volumes) inside it. Material references are assigned to the corresponding volumes in their respective files. There is no limit to the number of physical volumes that can be assigned to the global geometry with this method. Finally, the field "setup" identifies the top volume. For each GDML file, the top volume corresponds to the volume defined in the field "solids". For the mother GDML file, the top volume is the world volume.

The geometry thus defined can then be imported into Geant4 by the GDMLParser function [165], with the mother file as argument.

6.1.1.5 Validation

To confirm that the volumes are correctly imported into Geant4, geometry, navigation and material tests were performed. Three test geometries were defined with 0.1 mm MMD: a cylinder with a 5 mm radius and 10 mm height; a torus with 10 mm outer radius and 5 mm radius section; and a 5 mm sphere, since due to their curved surfaces they are more prone to precision problems than plane geometries. Since we expect to import several volumes at once into Geant4, a system of two spheres, where a larger 5 mm radius sphere, with a 2 mm radius spherical hole in its center, encases a second sphere with the same size as the hole, is also tested. The sphere system was tested with several different MMDs. Figure 6.3 shows all tested solids in STEP format visualized with FreeCAD.

All solids imported into Geant4 were visually analyzed for correctness. The precision of the system with two spheres was also analyzed with the Geant4 test particle, the geantino, which is a "particle" that crosses the geometry and does not interact with any materials. 10E+05 geantinos were generated omnidirectionally from a point-like source located at the center of the sphere system. The positions where the geantinos changed volumes, from the inner sphere to the outer sphere, and from the outer sphere to the outside world, were recorded. Since the spheres are meshed, the radius of the sphere is not constant in all directions. The average and maximum values of the radii of both spheres for different MMDs were thus computed. Their masses were also calculated with Geant4 "GetMass" function and compared to the value obtained from FreeCAD libraries.

Particle navigation inside the geometries was also tested. Errors may occur in Geant4 due to particles getting stuck near triangular faces. A particle is considered stuck in the geometry when it does not change position for 10 consecutive steps. When this happens Geant4 slightly moves the particle by 10^{-7} mm. To account for navigation errors

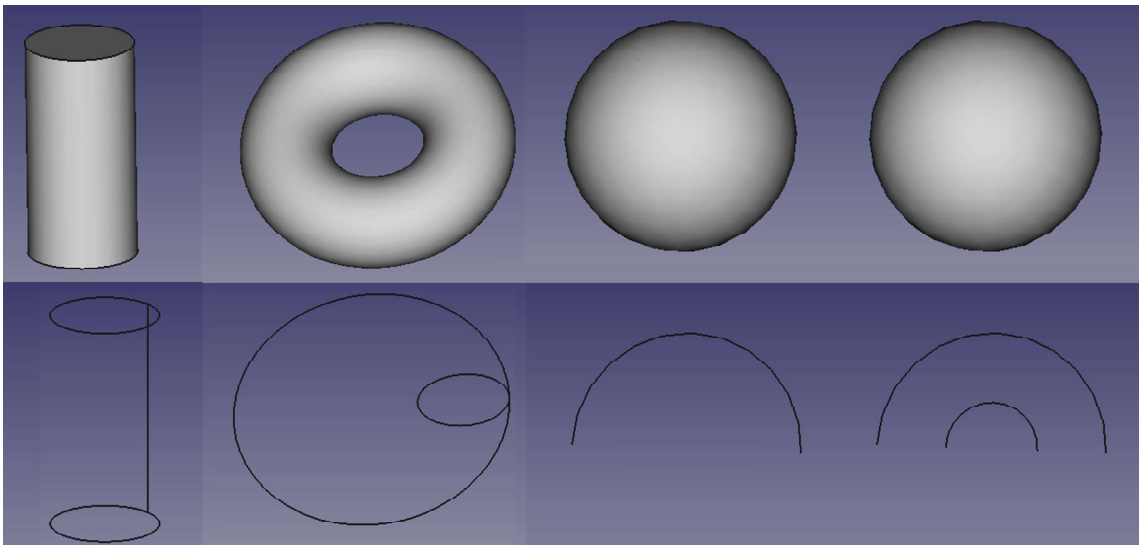

Figure 6.3: STEP format of all solids used in the tests, a cylinder, a torus, a sphere and a second sphere with a spherical hole in the middle to encapsulate another a sphere that fills it. Below each solid, a wire image of its volume can be found for clarity. From [159].

10E+5 geantinos were generated omni-directionally from a 8 mm radius spherical source surrounding the test volumes. All solids presented in Figure 6.3 were submitted to this navigation error test.

An additional test was performed to compare the distributions of energy deposited in meshed and Constructive Solid Geometry (CSG) spheres. This was done for each type of solid (meshed and CSG) with Silicon assigned to them, generating a parallel beam of electrons with a flat energy spectrum ranging from 100 keV to 500 MeV in a circular plane, with the same radius as the sphere (5 mm), 10 mm away from it, and registering the deposited energy in the volume. The same source was used to compare deposited energy in a cylinder filled with an elementary material, iron (Fe), and a composed material, silica (SiO_2), assigned to the volume with Geant4 and with GUIMesh.

A summary of the solids, and of their characteristics, used for each test is shown in Table 6.1. The total surface area to MMD ratio is also given since it can be used as reference for the mesh precision for a given shape. Notice that the precision is smaller in the 2 mm radius sphere than in the 5 mm radius sphere for the same MMD, since mesh deviation will be larger when compared to the total surface area. All tests showed in this paper were executed with Geant4.10.01.p02.

6.1.1.6 Benchmarking

To understand how tessellation affects simulation time and memory usage, 10E+05 geantinos runs with a point source located in the center of the geometry, but without any readout, were performed for the Sphere System mesh with the five MMD values mentioned in Table 6.1, as well as for a similar configuration, implemented with CSG solid class in Geant4. All simulations ran on a system with an Intel(R) Xeon(R) CPU E5540 @2.53

Table 6.1: Summary of the solids/tests performed. From [159].

Solids			Tests			
Shape	Mesh Max Deviation (mm)	Area/MMD (#/mm2)	Geometry Visual	Geometry Precision	Navigation	Energy Deposition
Cylinder	0.1	7.85E+03	X	-	X	x
Torus	0.1	1.97E+04	X	-	X	-
	CSG	-	-	-	-	X
Sphere	0.1	3.14E+03	X	-	X	X
	0.01	3.14E+04	-	-	-	X
Sphere	10	3.64E+01/5.03E+00				
	1	3.64E+02/5.03E+01				
System	0.1	3.64E+03/5.03E+02	X	X	X	-
	0.01	3.64E+04/5.03E+03				
Outer/Inner	0.001	3.64E+05/5.03E+04				

GHz with 4 GB available memory.

6.1.2 Results

Several tests to the imported geometry and to particle tracking inside the volumes as well as deposited energy were performed to validate the method. CPU time and memory usage were also compared using the sphere system mesh with different MMD values and for one defined by CSG with Geant4 user classes.

6.1.2.1 Geometry

All solids were successfully imported into Geant4. Figure 6.4 shows the imported solids, where all single volume geometries were meshed with 0.1 mm MMD. The two-sphere system was meshed with 10 mm, 1.0 mm, 0.1 mm, 0.01 mm and 0.001 mm to understand the effect of this parameter. The shape of the spheres is highly dependent on the MMD. In fact, in Figure 6.4 we can see that we can have a shape that no longer resembles the original sphere from Figure 6.3 (10 mm MMD) and good spherical approximations (0.1 mm, 0.01 mm and 0.001 mm MMD). The Geant4 "CheckOverlaps" function was used with 10E+05 test points. No overlaps were found in any case.

The average and maximum deviation of the radius in the meshed spheres are given in Table 6.2. As expected, both the average and maximum deviation become smaller for smaller MMD. It is also noticeable that the inner surface radius has a larger deviation than the outer one since both were meshed with the same MMD though their sizes are different. The mass calculated with Geant4 for the meshed geometries (with silicon as material) are compared with CSG/CAD in Table 6.2. Again, it can be seen that, the lower the MMD, the closer the mass is to the expected value. For the lower MMD spheres this difference is negligible. The mass value is always lower in the case of meshed geometries due to the nature of the mesh generation algorithms.

6.1.2.2 Navigation

Navigation tests showed no stuck events for all geometries, except the largest MMD sphere system where the percentage of stuck events was 2.84% $\pm$ 0.02%. This is due to the

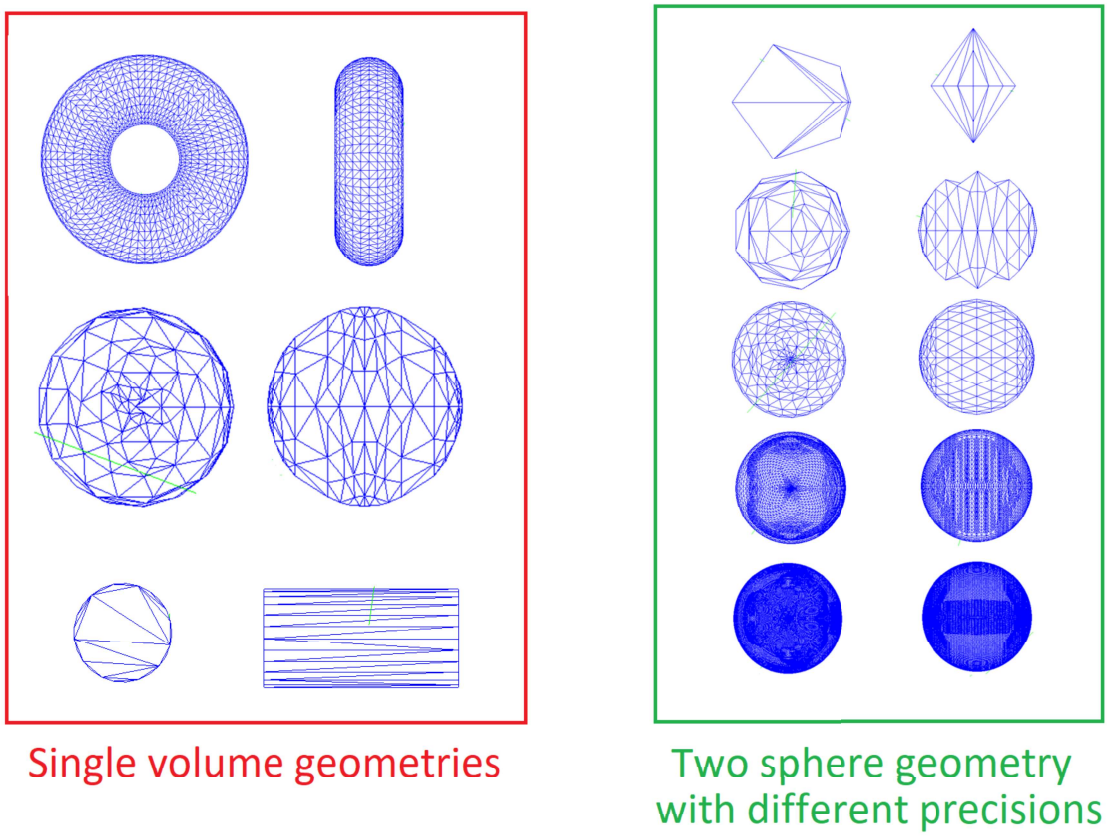

Figure 6.4: Solids imported with Geant4. In the red box the single geometry solids mesh with 0.1 mm MMD can be seen. In the green box the two-sphere system can be seen(only the outside sphere is visible) meshed with 10 mm, 1 mm, 0.1 mm, 0.01 mm and 0.001 mm from top to bottom. From [159].

existence of small angles between the triangle edges, which result in large sections of the solid where the dimensions are small enough to affect position determination by Geant4.

6.1.2.3 Deposited Energy

The distributions of the energy deposited by electrons, with energies ranging from 100 keV to 500 MeV, in three 5 mm radius spheres, two of them meshed with different precisions and a third defined using the Geant4 CSG sphere class, are shown in Figure 6.5. The lower precision meshed sphere (green line) shows different deposited energy when compared to the other two tested solids, although the total deposited energy differs from the two other cases by approximately 1%. It is noticeable that the deposited energy in this sphere has a step like behavior due to the transition and shape of its triangles. The other two energy profiles, for the more precise meshing and for the CSG sphere implementation, display an excellent agreement.

Element and compound material definition by GUIMesh were also tested. Deposited energy in the two tested materials, SiO_2 and Fe, has very good agreement between GDML and Geant4 implementation, as shown in Figure 6.6. Deposited energy in SiO_2 (green and

Table 6.2: Average and Maximum deviation from the mathematical surfaces of the sphere systems and mass deviation between CAD and Geant4. From [159].

MMD (mm)	Surface	Average Deviation (%)	Maximum Deviation (%)	Mass Deviation (%)
10	Outer (5mm)	41.4032	63.1302	74.36
	Inner (2mm)	41.403	63.1302	74.26
1	Outer (5mm)	5.0308	17.4846	12.88
	Inner (2mm)	11.5995	34.002	29.44
0.1	Outer (5mm)	0.8344	1.6554	2.29
	Inner (2mm)	1.7125	5.0685	5
0.01	Outer (5mm)	0.07	0.3052	0.11
	Inner (2mm)	0.166	0.7675	0.5
0.001	Outer (5mm)	0.0092	0.0326	0.03
	Inner (2mm)	0.02	0.0845	0.04

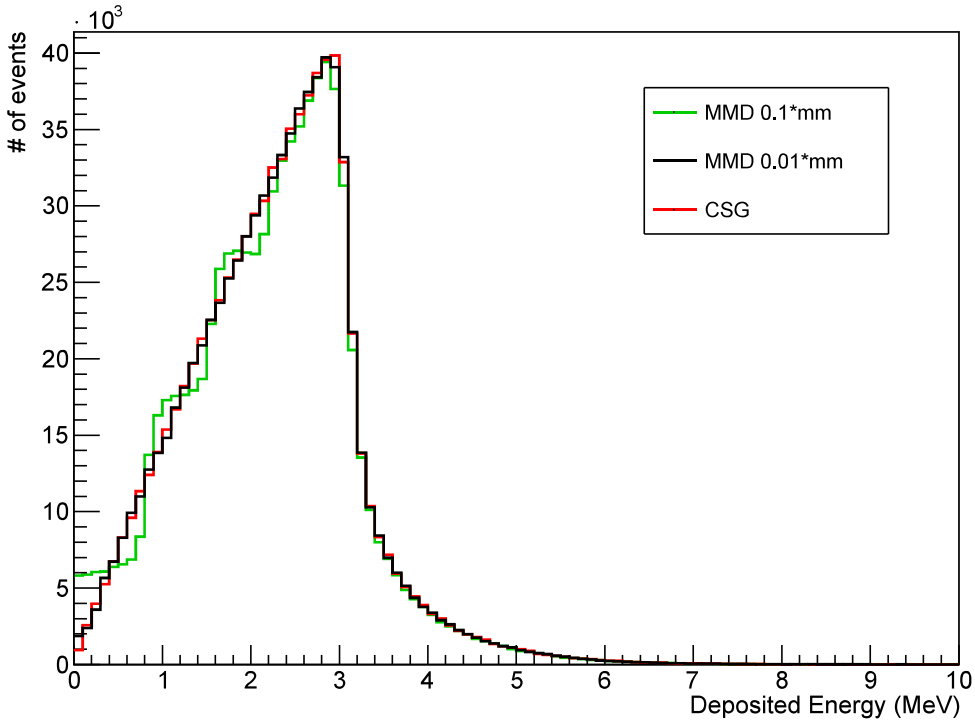

Figure 6.5: Comparison between the deposited energy of electrons in three spheres, two meshed with different precisions and one implemented with a Geant4 CSG class. Energy deposited in the 0.01 mm MMD sphere (black line) is similar to the deposited energy in the CSG sphere (red line). The energy spectrum in the 0.1 mm MMD sphere (green line) however is different due to its structural defects. From [159]

black) and in Fe (blue and teal) show the same behavior for the whole range of energies. Material properties reported by Geant4 after the geometry was loaded is also the same in both cases.

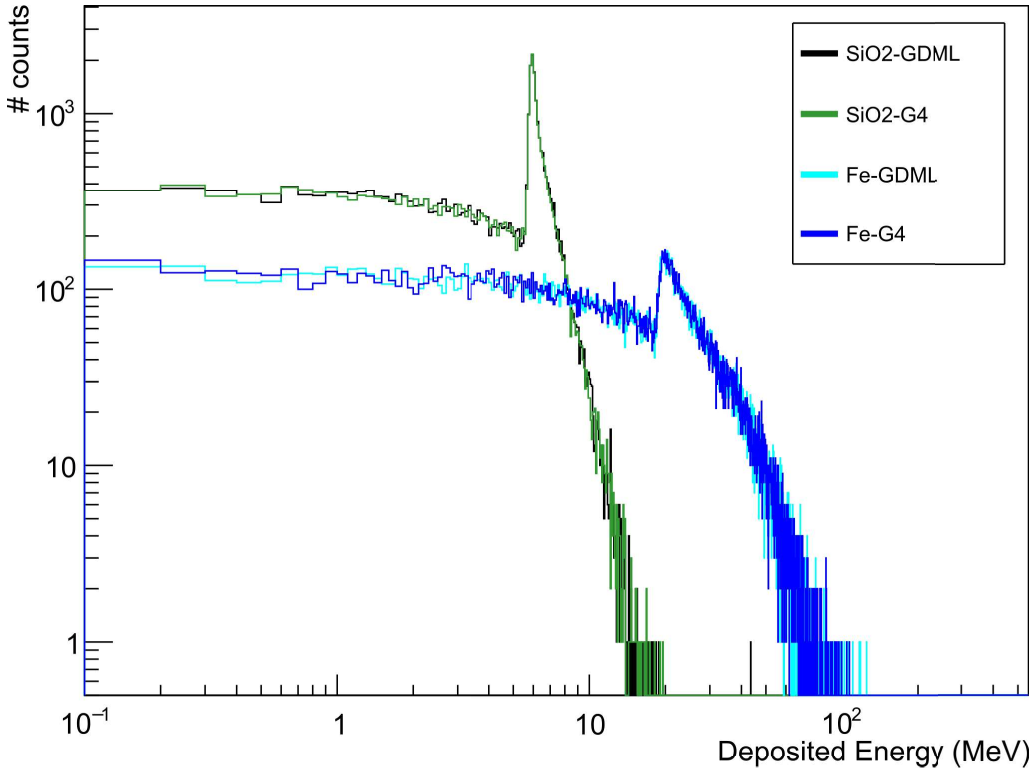

Figure 6.6: Comparison between the deposited energy of electrons in two materials, SiO_2 (green and black) and Fe (blue and teal), defined by Geant4 and by GDML. From [159]

6.1.2.4 Benchmarking

Benchmarking was done by performing ten runs, each with 10^5 geantinos, generated from the center of the sphere system with different implementations of varying precision meshed geometries and for a CSG implementation, all with the same material, Silicon. Figure 6.7 shows the CPU time and memory used to load the geometry as well as the CPU time for the whole simulation. Both the CPU time and memory increase exponentially for lower MMD. It is important to take this into account when the geometry is complex and/or there are a large number of volumes. Notice that CSG is always faster and requires less memory, even when compared to the sphere system meshed with the largest MMD value.

6.1.3 Discussion

Several geometries in STEP format were successfully imported into Geant4 via GUIMesh. No holes were found in the tessellated geometries. Also, no overlaps were detected since all triangles of the meshed solids are inside the original shape.

For curved surfaces, the shape form was shown to be highly dependent on the MMD. This is due to the MMD limiting the maximum distance from an edge of the mesh to the original surface that it describes, e.g., larger MMD values allow larger deviations from this surface. This results in finer tuning of the surfaces for lower MMD values, as the number

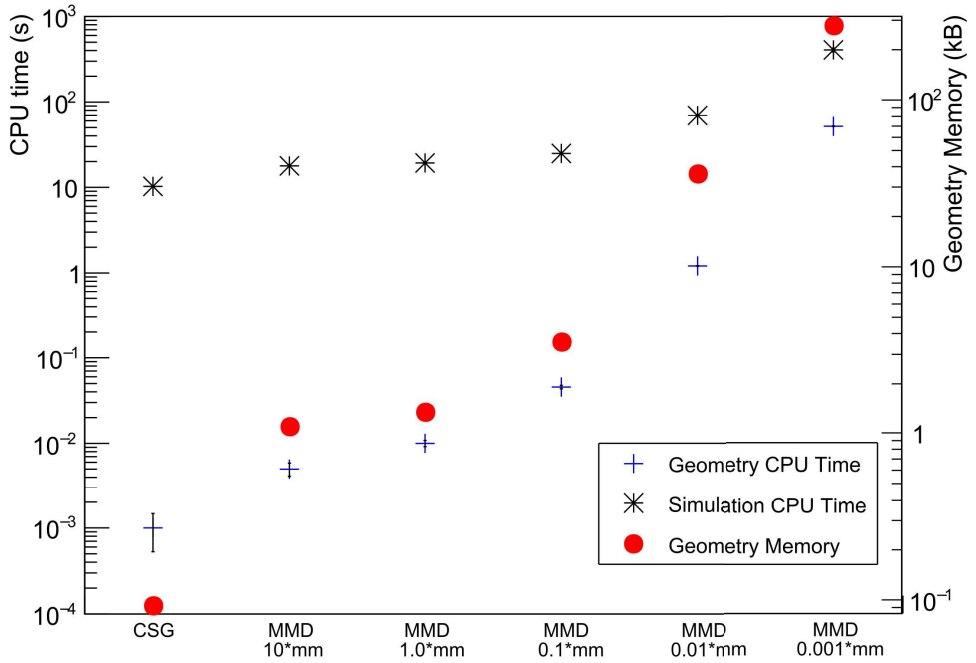

Figure 6.7: Comparison of CPU time for the whole simulation and to load the geometry between different mesh precisions of the sphere system and CSG solid. Memory required to load the geometry is also shown. From [159]

of triangles increases and their size decreases. Deviation, defined as the distance from the surfaces in Geant4 to the solids mathematical definition, was also computed and shown to be smaller or of the same order of magnitude as the MMD value. This means that for the same MMD, spheres with different radii will have different normalized deviations; hence when choosing the MMD one should also consider the size of the solids to be meshed. This is especially important since there is also a penalty in CPU time from the lack of geometry hierarchy inherent to CAD geometries.

Navigation errors resulting from "stuck" particles in some cases were studied. These happen when Geant4 is not able to compute in which volume the particle is located. No errors occurred in all geometries except the 10 mm MMD sphere system where the percentage of events displaying this behavior was under 3%. The distributions of deposited energy were found to depend on the meshing precision. In fact, while the distribution of energy deposited on a 0.1 mm MMD sphere displayed discontinuities, for the 0.01 mm MMD sphere results matched perfectly those obtained for the CSG sphere. This has to do with the path of particles going through the sphere. If one crosses the sphere at the center it will travel a longer path than one that goes through it at the edge. If the sphere is ideal as in a CSG solid, the linear distance is a smooth function dropping to zero at the limit. In the case of a meshed surface this function is no longer smooth. In fact, the function changes from triangle to triangle as can be seen in the meshed solid images. For more accurate tessellations this feature is less evident due to the decrease of the step

amplitude (smaller triangles). Scattering of electrons and the bin size of the deposited energy histogram also contribute to this effect. Mixed materials defined in GUIMesh were also validated.

Memory and time consumption were found to increase for solids meshed with lower MMD values, which means that for complex and/or large number of solids careful consideration should be made regarding solid precision.

6.1.3.1 Conclusions

GUIMesh enables users to import CAD geometries in STEP format into Geant4. A STEP file describing a global geometry is read by GUIMesh, and the geometry is meshed with a given Maximum Mesh Deviation and registered with the corresponding material in a GDML file structure, readable by Geant4. A set of test volumes were used to test GUIMesh performance in terms of geometrical accuracy, particle navigation errors and material implementation. It was concluded that geometry precision is highly dependent on the chosen value for MMD. Lower values of MMD result in more accurate geometries and fewer errors in particle tracking, at the cost of memory and processing time. No overlaps were found in the tested geometries and it was shown that material definition in GUIMesh successfully implements materials into Geant4.

GUIMesh can be a useful tool for all users of Geant4, allowing them to import STEP geometries of arbitrary size and complexity into the simulation toolkit. As it will be seen clearly it was a fundamental part of the radiation analysis presented in this chapter and of the characterization of the Directionality Detector presented in Chapter 7. It is also being used in the analysis of Multi-Functional Spectrometer (MFS) [24] and current studies of Component Technology Test Bed (CTTB) [172].

6.2 Geant4 Simulation

Now that GUIMesh was introduced let us continue to the quantification of the TID and the DDD in components. In Section 4.5 the two standard methods were discussed. As it was made clear, sector analysis is less accurate for electrons, especially for those with energies where Bremsstrahlung radiation is relevant such as the Jovian radiation environment. For this reason, it was decided to run Monte Carlo - Geant4 [30][31][32] simulations (version 4.10.01.p02) to calculates TID and DDD. Monte Carlo methods computing time scales with the complexity and size of the geometry of the problem. In the case of RADEM, there are 714 discrete volumes, plus the spacecraft which is much larger than the Radiation Monitor. This is a challenging computational problem but has other advantages besides computing more accurate doses. Monte Carlo simulation also allows to characterize the detector heads response to radiation and to obtain their response functions. Geometry description is essential to compute accurate dose levels, background and response of the detectors.

6.2.1 Spacecraft Description

The geometry of both the spacecraft and RADEM must be coded into Geant4. As it can be seen in Figure 6.8, the size and complexity of the spacecraft poses a significant time constraint for the simulations. There are some solutions to solve this issue. One of them is to assume the spacecraft volume is a homogeneous volume of Aluminum, with density equal to its total mass divided by its volume. Simplified Geant4 simulations showed however that almost no particles would cross the volume which is simply not true [156].

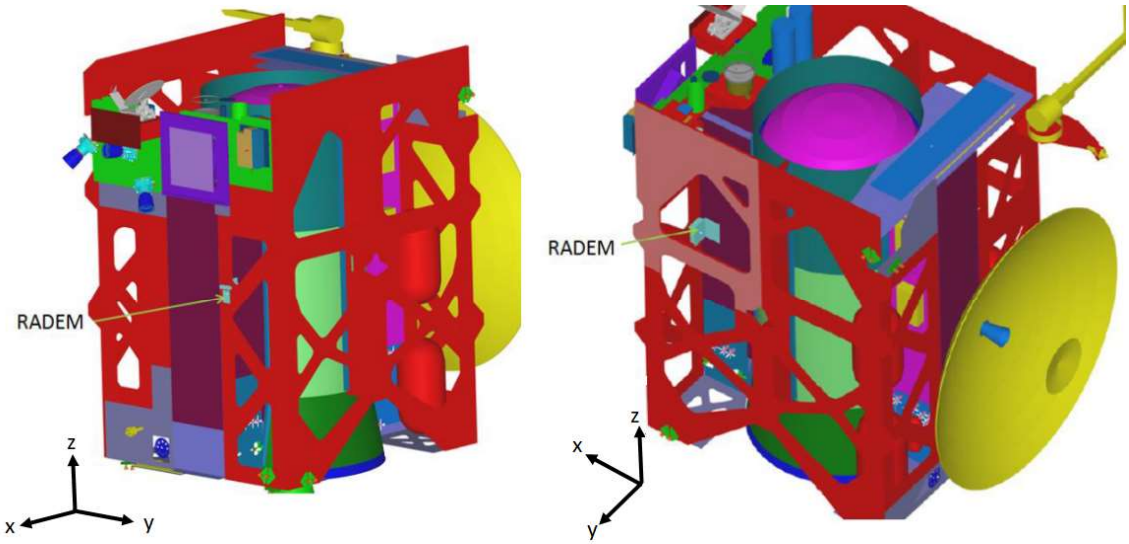

Figure 6.8: Two views of the JUICE Model, including RADEM location on JUICE +x panel.The model includes a support bracket, which is not included in the present analysis.

Another way is to simulated the spacecraft and save the particle spectra at the entrance of RADEMs volume. This spectra would then be used as input to simulate the RADEM instrument. This method is the most accurate one as it takes into account all volumes as well as the scattering of particles in the spacecraft. However it still requires that the whole spacecraft is simulated which takes a long time and is subject to modifications during the development stage. To compromise between time and accuracy, the spacecraft was converted to a 6-side box model as discussed in Section 4.5.2.2 and included in the RADEM model. The thickness of Aluminum in each face is given in Table 6.3 according to the axis defined in Figure 6.8. The model was agreed upon by Airbus, ESA, and the collaboration after it was proposed by the first, AIRBUS. As it can be seen the instrument will be open to the environment for the most part. The only exception is the -Y side which has 10 mm Aluminum equivalent shielding.

6.2.2 RADEM Model

The first model of RADEM was designed to be inside a vault with enough shielding to limit TID values to 50 krad(Si). Its outer walls had only 2 mm Aluminum thickness, which according to the environment specification [28] translates in a total dose of 3.8 Mrad(Si) (if

Table 6.3: S/C Aluminium equivalent shielding at RADEM faces. From [158].

Face	Eq. Shielding	Observations
-X	1 mm Al	3 mm are considered to represent the the support bracket
+X	0.5 mm Al	Representative to the CRFP wall
-Y	10 mm Al	2mm Al + 2mm Pb + equipment
+Y	0	
-Z	0.5 mm Al	Not coded into the simulation.
+Z	0	

spherical Aluminum shielding is considered - see also Figure 5.4). From the same source, one can also see that, to achieve TID levels required for the components, roughly 17 mm of Aluminum is required. Since the walls are actually slabs these values are overestimated.

One of the issues with space missions, is that the mass must be kept as low as possible. It is then essential to consider all volumes of RADEM which was the main reason for the development of GUIMesh[159]. The STEP file was provided by EFACEC and then converted to GDML with GUIMesh with a Maximum Mesh Deviation of 0.1 mm. This was the first time GUIMesh was used for modeling purposes outside of its proof-of-concept. The full geometry of the instrument already imported to Geant4 is shown in Figure 6.9. The spacecraft equivalent shielding (in red), coded at Geant4 level, was considered for all RADEM models.

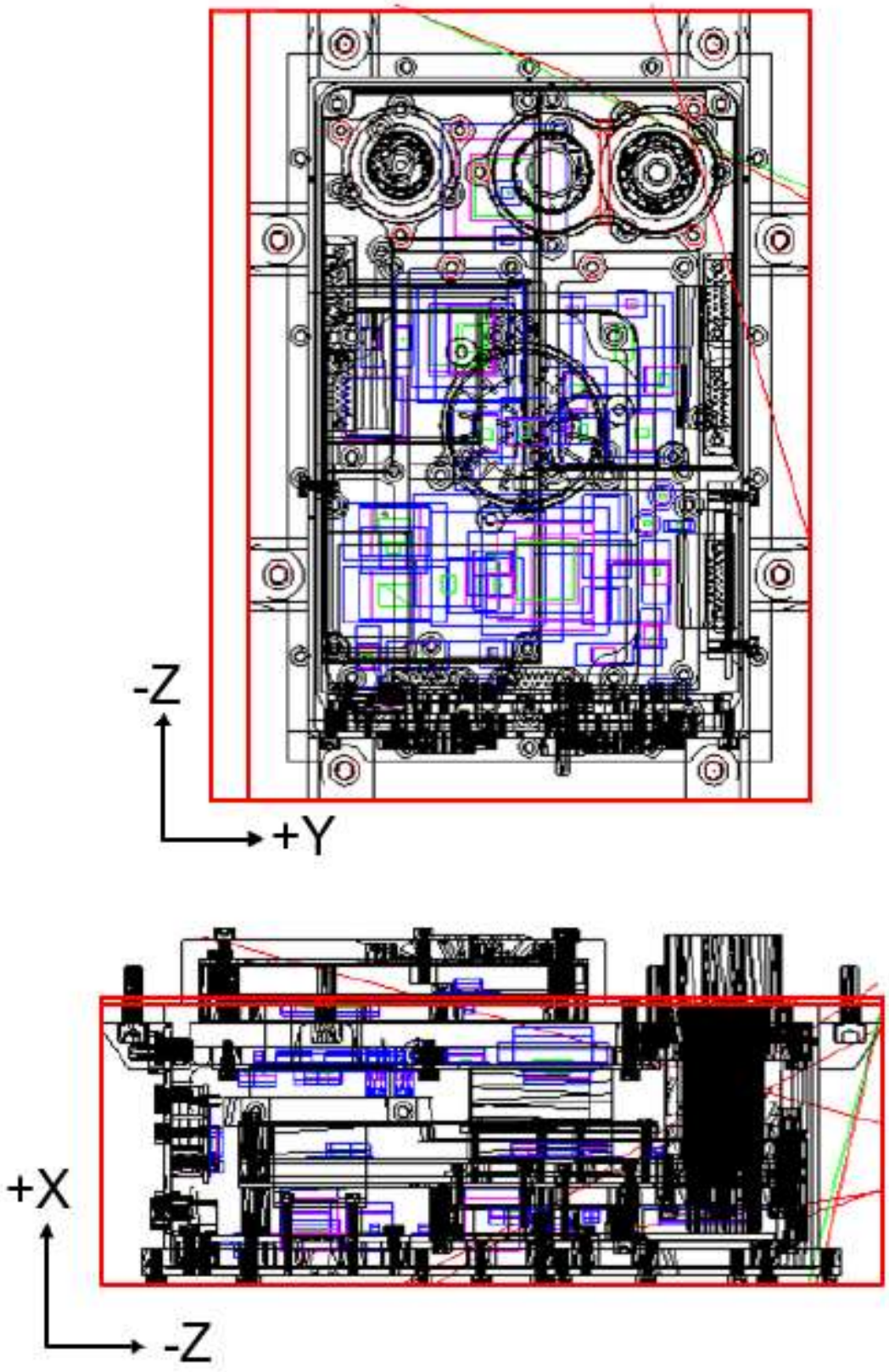

Figure 6.9: Visualisation of the GDML RADEM model imported into a Geant4 application without rotation. From [158]

6.2.3 Component Geometry

An important aspect of the geometry is the description of the EEE components. While the bulk of an active device is made from Silicon, TID effects are related to the dose in the oxide (SiO_2) as discussed before. However it is very difficult to assess the size of latter. Furthermore it has a relatively small size meaning the simulation would be very inefficient. Also, since the density of SiO_2 and Si are similar, which means that differences in the stopping power of electrons in the materials is small, it was considered that the sensitive part is the Si bulk. The dimensions of the Silicon and packaging were estimated from the components datasheet and/or Standard Microcircuits Drawing (SMD).

In the STEP file, components were represented by four regions as shown in Figure 6.10:

- a clearance region for shock and vibration required for mechanical simulations (no physical volume)
- a mechanical envelope for PCB design purposes (mass merged with component body – no physical volume)
- the component body (effective density assumed as a mixture of Al_2O_3 with Si)
- the Silicon die of the component, the sensitive part

In Geant4 neither the clearance (which is actually void) nor the mechanical envelope, which is small when compared to the envelope were coded.

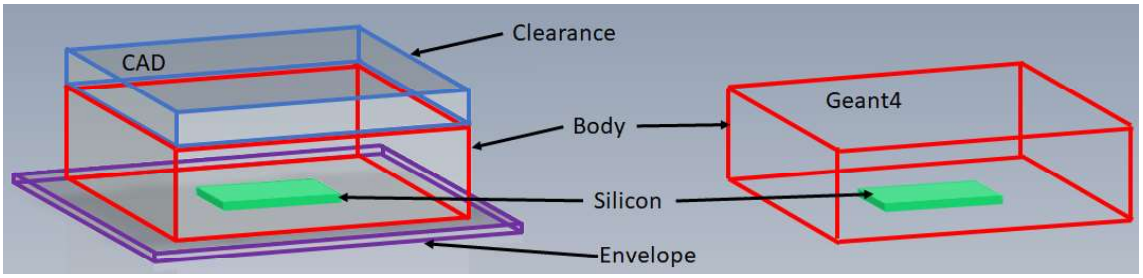

Figure 6.10: Representation of an EEE component (SRAM UT8R1M39 21XFC) in the CAD model (left) and in Geant4 (right). The body (Al_2O_3 and Si mixture) and the Silicon die are fully described in Geant4 with dimensions obtained from the datasheet and SMD of the component.

The major drawbacks of the geometry is related to the approximation of the spacecraft to a six-side aluminum box which does not reproduce accurately particle scattering, and the increased computing time associated with the tessellated nature of the solids surfaces. Nevertheless this was found to be the best solution compromising between accuracy and time.

6.2.4 Particle Source, Physics and Normalization

To simulate the radiation environment of Jupiter interacting with the instrument two particles were simulated, electrons and protons, in 5 and 4 energy intervals respectively as

described in Table 6.4. The energy limits were chosen considering the radiation environment specified in [28] and the instrument design (particles with energies lower than 100 keV have very low range in the instrument walls). Each energy interval was simulated using an inverse power law energy dependency. These options were considered because they allow to simulate low energy particles more, since they are less likely to reach the sensitive volumes, and normalize to multiple differential fluxes with only one set of simulations. The particles were generated from the 6 faces of a 40*cm sided cube surrounding the whole instrument with a 90° isotropic distribution with respect to the surface normal vector facing RADEM. Each of the faces were simulated independently again to allow bias towards low statistical significant regions when needed. Heavy ions were not simulated because they do not contribute significantly to TID and DDD. Also, they would add significantly to the computing time. Particle interactions and cross-sections were calculated with the space dedicated "Shielding" physics list already described in Chapter 3.

Table 6.4: Geant4 simulation energy intervals.

Particle	Energy Interval (MeV)
Electrons	0.1-2.0
	2.0-10
	10-30
	30-100
	100-1000
Protons	0.1-10
	10-100
	100-500
	500-1000

Because the simulation spectra is biased as an inverse power-law, the results must be convoluted with the mission phases differential fluxes post-simulation. The two fluxes (simulated and real) are related by a weighting factor, w_E, as follows:

$$\varphi_{real}(E) = w_E.\varphi_{simulated}(E) = w_E.(\frac{dN}{dE})_{simulated} \tag{6.1}$$

Knowing that the shape of the simulated spectra follows a 1/E dependence in energy:

$$\frac{dN}{dE}simulated = k.\frac{1}{E} \tag{6.2}$$

Where the factor k is related to the number of particles generated and to the spectrum shape by an absolute normalization factor, G_E, such that:

$$\frac{dN}{dE} = \frac{1}{G_E}.\frac{1}{E} \tag{6.3}$$

Solving this for the number of particles within the simulated energy interval:

$$N_{gen} = \frac{1}{G_E}\int_{E_{min}}^{E_{max}} \frac{1}{E}dE = \frac{1}{G_E}.\big[log(E_{max}) - log(E_{min})\big] \tag{6.4}$$

Where N_{gen} is the number of particles simulated, E_{min} and E_{max} are the minimum and maximum generated energies respectively. G_E can then be calculated as:

$$G_E = \frac{\left[log(E_{max}) - log(E_{min})\right]}{N_{gen}} \tag{6.5}$$

Replacing $\frac{dN}{dE}$ in equation 6.1 by the normalization factor, one obtains:

$$\varphi_{real}(E) = w_E . \frac{1}{E} . \frac{N_{gen}}{\left[log(E_{max}) - log(E_{min})\right]} \tag{6.6}$$

Adding the geometrical factor of the simulation, G_A, calculated with the area and opening of the particle source, w_E becomes:

$$w_E = \varphi_{real}(E).E.G_E.G_A \tag{6.7}$$

w_E must be calculated for each event and applied to the count number. The result is that the simulated spectrum is converted to a real one in the same way as the example given in Figure 6.11. The real spectrum corresponds to the environment flux measured or predicted. For this work, the fluxes given in [28] and shown in Figure 4.19 were used.

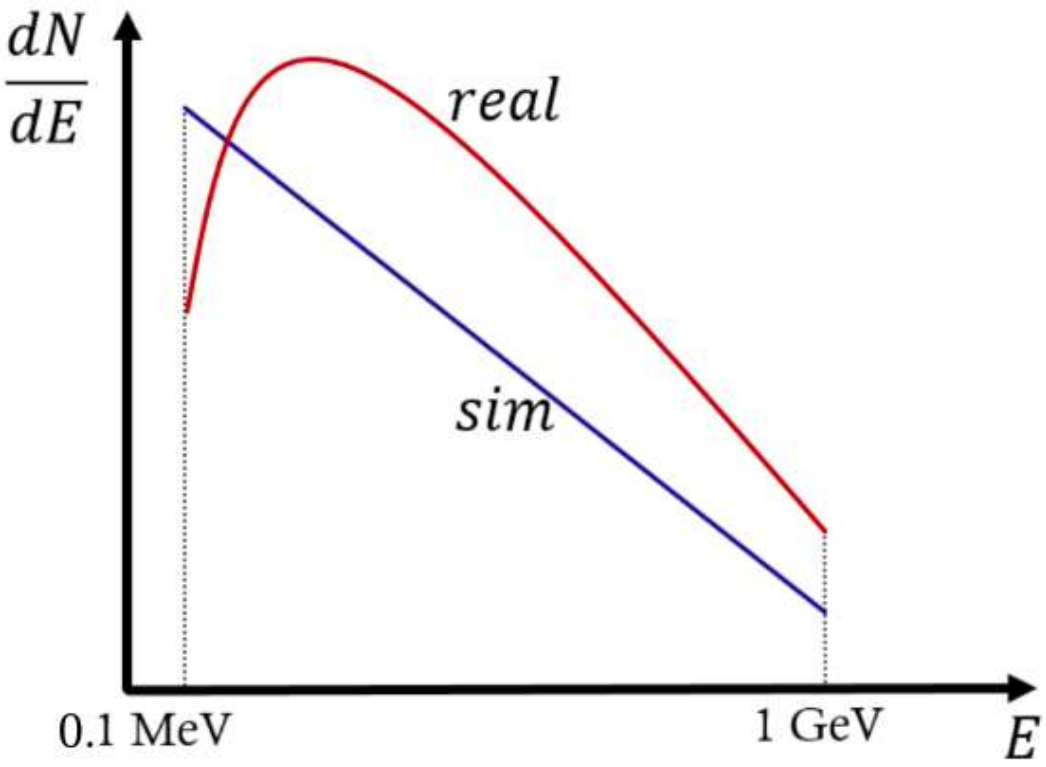

Figure 6.11: Comparison between the simulated and a possible real differential flux. Adapted from [173].

6.3 Radiation Sensitive Components

The first step in this type of analysis is to identify all sensitive parts. In RADEM, all parts were selected from the JUICE Preferred Part List [134] which is based on the technical performance, qualification status and heritage of available components. The only exceptions are the ASIC VATA466 [22] and the Silicon didoes which were custom designed for RADEM. For the ASIC, no test data was available when this thesis was written, but the device was built with the same architecture, its predecessor VATA465. For the purpose this analysis, the radiation data from the predecessor ASIC was used. It should be noted however that this does not replace actual testing of the ASIC and that the results obtained in this work here should accommodate future test data.

A list of all sensitive components and their TID and DDD sensitivity is given in A. SEEs are treated separately in Section 6.6. The first 49 components are the Silicon diodes of the detector heads described in Section 2.5. DDD sensitiveness of these components referred to as sensor diodes for the remainder of the chapter, corresponds to the level of 50 MeV proton fluence they were tested with. The test fluences are already a consequence of the results presented in this work. The rest of the list is diverse and will only be discussed where necessary. It is worth mentioning that all components besides sensor diodes have TID sensitivities of either 100 krad(Si) or 300 krad(Si).The DDD of the components is the one defined by the ECSS standards [26].

6.4 TID Analysis

The TID was obtained from the simulation, for each sensitive volume, as the sum of the deposited energy in all events normalized to the mission differential flux:

$$TID(rad) = 2.\frac{1}{m[kg]}.10^{2}.1.602^{-19}.[\frac{J}{eV}].10^{6}.[\frac{eV}{MeV}] \sum_{events} E_{dep}[MeV].w_E \tag{6.8}$$

The factor of two comes from the Radiation Design Margin (RDM). While not all deposited energy is from ionization processes (the contributions from non-ionizing energy loss (NIEL) is small [67][130]), it is a good approximation which reduces the number of operations and consequently the CPU time. Protons were not considered for TID before the final model of RADEM was achieved since according to [28] and confirmed by preliminary studies with a simplified modeled of RADEM [156], they account for less than 1% of TID. They were also considered for DDD and SEE analysis as it will be made clear in the next sections.

6.4.1 Baseline Results

TID values multiplied by 2 (RDM), obtained for all components for the first (baseline) model are shown in Table 6.5. These results were computed before a major re-design of the PCBs hence the different number of components when compared to Table A.1. The Silicon diodes' TID values are also not shown nor critical because they are less sensitive to radiation. TID levels of most components with 100 krad(Si) sensitivity vastly surpasses the limit. TID of some 300 krad(Si) sensitive components was also above their limits. Careful shielding optimization is then needed in order to bring TID levels below sensitive levels.

In Table 6.5 the results obtained with RADEM rotated by 90° are also presented. This hypothesis was considered because the SpaceWire Transceivers (responsible for interfacing RADEM with the spacecraft) have their larger surface facing the +Z face of RADEM, unlike all other components which face the top (+X) or bottom (-X) surfaces. Therefore these components would benefit from having the 10 mm equivalent Aluminum. from the spacecraft close to them. The rotation was effective for these components only but increased the average dose in all component since it covers less area of all other components. For this reason the initial configuration was maintained. TID levels of most components with 100 krad(Si) sensitivity vastly surpasses the limit. TID of some 300 krad(Si) sensitive components was also above their limits.

6.4.2 Shielding Optimization

The components with highest TID levels (>300 krad(Si)), were mostly near the bottom wall of the instrument as it can be seen in Figure 6.12 in pink. The ASIC VATA466 (id=87) with a TID level of 725.55±0.01 is particularly worrisome. This is mostly because of its position in the instrument, close to the bottom wall which only has 2 mm aluminum thickness, and its large surface area.

6.4.2.1 Dose Distribution

Taking the ASIC as a case-study there are two aspects that guide shielding implementation, angular and energy distributions. The former is shown in Figure 6.13. Two high dose regions can be identified in the former, the bottom wall (opposite to the detector heads) and the +Z wall where the connectors are located. The proximity and orientation of the ASIC are the main culprits of the high dose values from particles coming from the bottom of the instrument. Dose from particles coming from the side walls is not large because of the geometrical factor with an exception being the connector wall since it has weak spots where the connectors are located. Doses from the top are lower because the wall has 5 mm of aluminum and because the copper collimators cover a large part of the sky. Regarding the energy distribution of the dose it can be seen in Figure 6.14 that over 63% of the dose in the ASIC comes from electrons with initial energy below ∼3 MeV.

Table 6.5: TID values (x2) for the full JUICE mission obtained using the RADEM baseline model for a selection of 44 EEE RADEM components. From [157].

ID	Component	TID limit (krad(Si))	Computed TID (krad(Si))	
			0°	90°
50	MOSFET N-Channel	100	322.54±0.03	332.61±0.03
51	MOSFET P-Channel	100	325.05±0.03	340.72±0.03
52	Voltage Reference	100	141.12±0.13	133.31±0.12
53	Voltage Reference	100	140.84±0.12	139.97±0.13
54	Transistor NPN	100	116.50±0.24	110.15±0.28
55	Transistor NPN	100	234.97±0.25	225.1±0.24
56	Transistor NPN	100	420.63±0.29	403.84±0.28
57	Transistor NPN	100	118.70±0.29	103.67±0.24
58	Transistor NPN	100	400.83±0.25	406.94±0.26
59	Transistor NPN	100	221.19±0.27	235.13±0.29
60	Transistor NPN	100	430.97±0.26	452.72±0.26
61	Transistor NPN	100	395.17±0.27	451.87±0.26
62	Transistor Dual NPN	100	342.01±0.36	343.65±0.34
63	Transistor Dual PNP	100	203.41±0.33	164.6±0.33
64	Transistor Dual NPN	100	366.17±0.34	387.73±0.38
65	Transistor Dual PNP	100	192.84±0.36	162.52±0.38
66	Oscillator	100	143.41±0.05	162.41±0.05
67	uP GR712RC-MP	100	130.61±0.02	133.71±0.02
68	Multiplexed ADC	100	217.46±0.14	245.97±0.13
69	Multiplexed ADC	100	205.30±0.14	234.7±0.13
70	Multiplexed ADC	100	213.42±0.14	226.91±0.13
71	OPAMP	300	405.05±0.10	435.11±0.09
72	OPAMP	300	253.63±0.09	253.26±0.09
73	OPAMP	300	409.87±0.10	423.29±0.09
74	LDO	300	80.63±0.06	77.28±0.06
75	LDO	300	222.70±0.06	209.72±0.06
76	LDO	300	292.92±0.06	283.32±0.06
77	LDO	300	149.86±0.06	159.76±0.06
78	LDO	300	188.02±0.06	204.56±0.06
79	LDO	300	115.86±0.06	114.93±0.06
80	LDO	300	150.09±0.06	214.73±0.06
81	LDO	300	275.86±0.06	270.88±0.06
82	Voltage Supervisor	100	151.61±0.11	137.95±0.11
83	SpW Transceiver	100	288.98±0.09	159.72±0.09
84	SpW Transceiver	100	373.52±0.09	211.85±0.09
85	PWM Controller	300	379.66±0.04	364.02±0.04
86	ASVATA466 (DD)	TBA	184.89±0.01	211.5±0.01
87	ASVATA466 (P&ISD)	TBA	725.55±0.01	733.33±0.01
88	ASVATA466 (ESD)	TBA	188.67±0.01	184.12±0.01
89	Temperature Transducer	100	501.41±0.14	433.54±0.14
90	Temperature Transducer	100	201.58±0.14	173.82±0.14
91	MRAM 16Mb (2Mx8b)	100	92.15±0.02	97.98±0.02
92	SRAM 40Mb (1M x 39b)	100	78.65±0.01	76.37±0.01
93	PROM 256kb (32k x 8b)	100	98.78±0.03	103.93±0.03

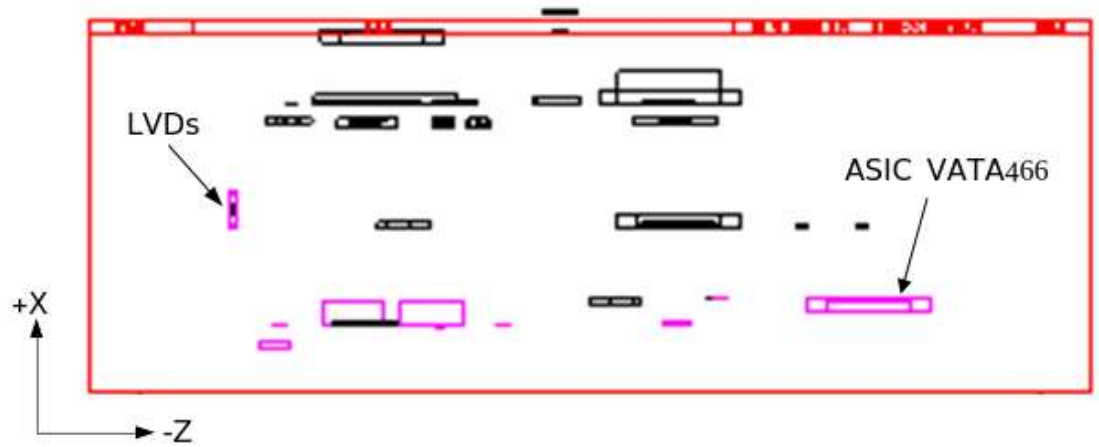

Figure 6.12: Location of the EEE components in RADEM. Components for which the values for the full mission exceeds 300 krad are represented in pink. RADEM structures providing shielding (red) are represented on the left, on the (Y,-Z) projection, where on the +Y face the 10 mm equivalent Aluminum shielding can be seen, as well as the 0.5 mm equivalent Aluminum shielding on the –Z face. From [158].

According to NIST [67], the range of these electrons in Aluminum is ∼6 mm.

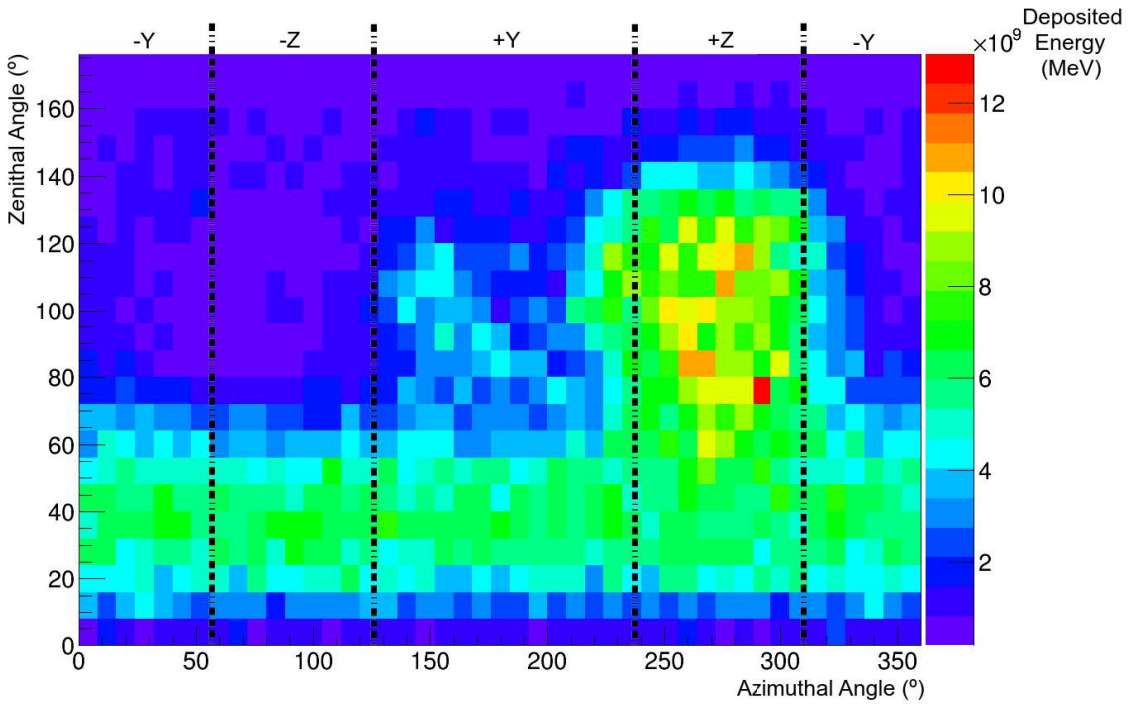

Figure 6.13: Deposited energy angular distribution in ASIC VATA466 (PIDH) for the entire mission. From [158].

6.4.2.2 Shielding Strategies

There are two main approaches to shield EEE components: Global and Local shielding. Global shielding consists of increasing the thickness of the instruments walls. It provides

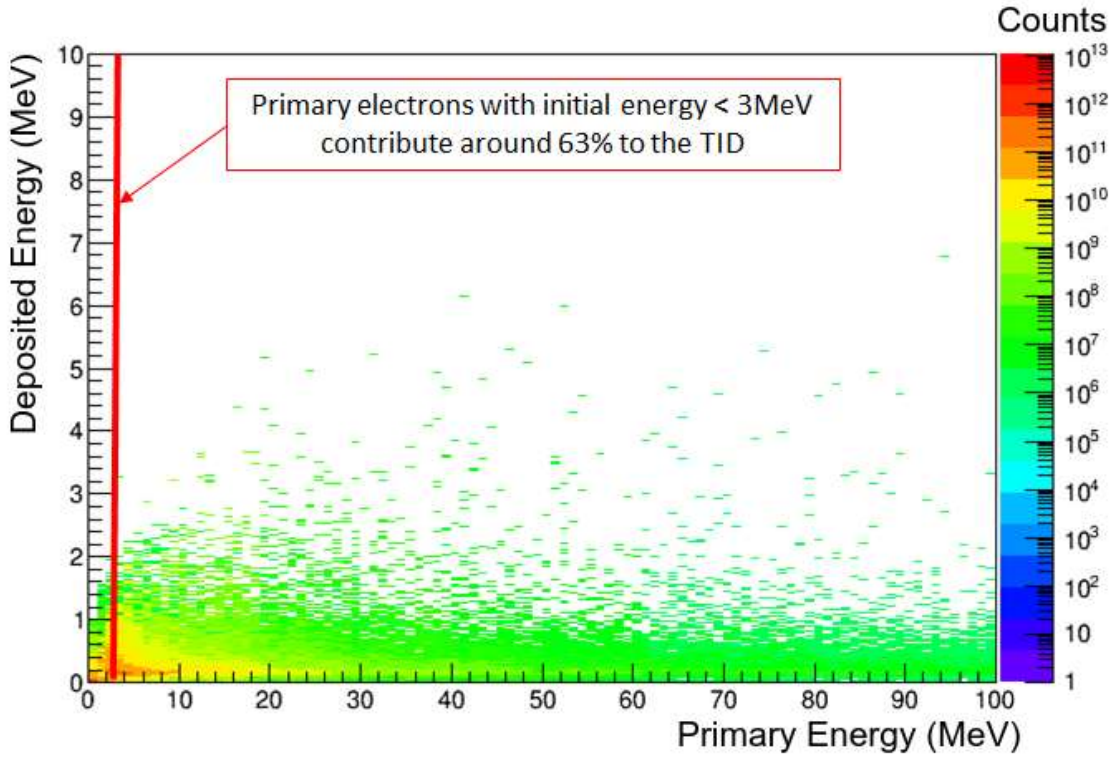

Figure 6.14: Deposited vs Primary energy in ASIC VATA466 (PDH and HIDH) for the entire mission. From [158].

general dose reduction for all components inside the instrument but has large mass cost. Local shielding on the other hand, as the name suggests, consists of adding small amounts of material in the form of slabs close to targeted sensitive devices or changing a component packaging. This solution is ideal when a relative small number of components is at risk.

For RADEMs baseline model, TID levels were found to be much larger than the components sensitivity overall. Therefore, different wall thickness increments to the side and bottom walls were coded with Geant4 classes as close as possible to the walls of the instrument. The results are compared in Figure 6.15. There are two noteworthy overall accomplishments of the shielding. First, all shielding scenarios lower TID of almost all components to values below 300 krad(Si). Second, side shielding greatly improves TID values of some of the components and decreases the overall dose of all components. It can also be seen that the best solution is the 6mm + 6mm, bottom and side increased wall thickness respectively, is the best solution to lower TID values. However, it also increases the mass by 1130g which is only surpassed by the 9.44mm + 4mm shielding scenario. Moreover, not all components are below in that scenario which means that more shielding would be necessary on top of the 1130g. To optimize the mass, the 6mm + 4mm solution was selected based on the number of components already below TID sensitivity levels, overall dose and incremented mass. Wall thickness of the final component is resumed in Table 6.6.

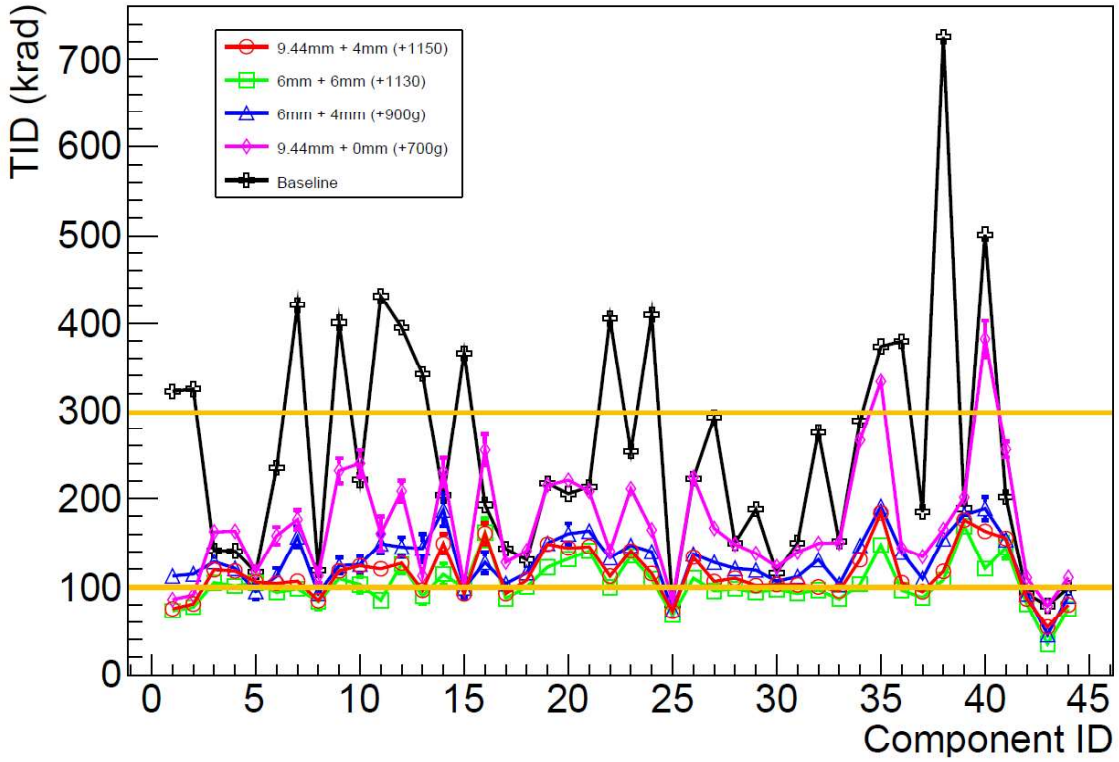

Figure 6.15: Component TID comparison for all shielding scenarios simulated. Left values are the bottom wall increased thickness and the right values the side walls increased thickness. TID sensitive limits of all components, 100 krad(Si) and 300 krad(Si), are marked in yellow. Adapted from [158].

Table 6.6: RADEM Wall thickness.

RADEM walls						
Side	z+	z-	x-	x+	y-	y+
Al. Thickness	6	6	8	5	6	6

6.4.3 Final Results

At this point, there an extensive re-design of RADEMs circuits was done. The final list of components is the one presented already in Table 5.1. To this model, local shielding was implemented on the form of Tantalum slabs in an iterative manner, since these offer the best dose reduction-to-mass ratio for the JUICE mission [28]. Tantalum was allocated to places inside the RADEM walls to decrease Bremsstrahlung energy loss from electrons as it can be seen in Figure 6.16. This was not always possible, especially for the SpW Transceivers, which were in a cluttered position making it difficult to shield these components. In fact, their shielding mass was of ∼120 g out of the total 1043 g of the local shielding and 2 kg of the total shielding. Despite this effort, one of the SpW Transceiver (ID=105) still remained above its sensitivity limit by ∼10% as it can be seen in Table 6.7. The only other component above its sensitivity level is the top diode of the Heavy Ion Detector head which has a large area and is directly exposed to the environment. Due to

its functionality it is not possible to shield the diode hence it was accepted that it will not last for the entire mission. The SpW Transceiver on the hand, is vital for mission success but has a fully redundant unit that should endure for the entire mission. Furthermore, as it can be seen in Figure 6.17, TID only exceeds the limits right at the end of the mission. The risk is then small and only a threat towards the end of the mission.

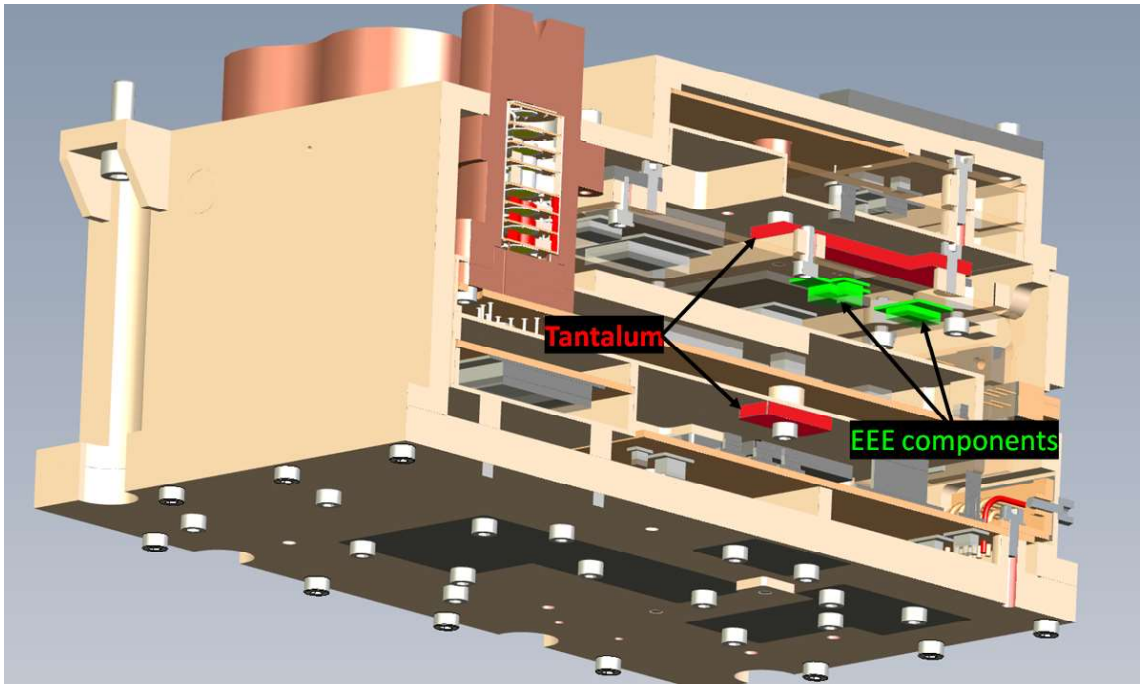

Figure 6.16: Example of Tantalum slabs placed inside RADEM walls to shield specific components. Two Tantalum slabs are highlighted in red and three EEE components are highlighted in green.

6.4.4 Materials

Materials can withstand larger doses of radiation but can also lose their integrity and/or physical properties due to radiation. The larger concern is usual with materials directly exposed to the environment such as the aluminum walls of the instrument, the copper collimators, kapton or the tantalum shielding. The dose of directly exposed materials can be estimated by the outer Heavy Ion Head sensor which is directly exposed as well. For this sensor the total computed dose was 2.5 Mrad(Si) which is acceptable for the aforementioned materials.

Internally, the most sensitive material is the PTFE (Teflon) which is used as a gasket. Its properties are guaranteed up to 1Mrad (Si). There are several PTFE gaskets locate inside RADEM. They are very thin and stuck between other volumes which can lead to overlaps in the Geant4 geometry. Taking into account the minimum thickness of RADEM walls (5 mm), only and no other volumes/materials, the expected dose inside an aluminum sphere from the Dose-Depth Curve in [28] is <787 krad(Si) which is a conservative estimation. Taking into account that the average size wall is 6 mm and that there are more

Table 6.7: TID values (a factor 2 was included to the generated electron and proton fluxes) due to electrons and protons for the full JUICE mission obtained with RADEM mechanical model v18.0 for a selection of 119 EEE RADEM components. From [158].

Component		Radiation Sensitivity	Electron Dose	Proton Dose	Total Dose
ID	Name	(krad)	(krad)	(krad)	(krad)
1	HI2	1000	777.54±3.47	14.07±0.06	791.61±3.47
2	PSD7	1000	46.43±0.24	1.39±0.01	47.82±0.24
3	PSD5	1000	19.71±0.08	1.36±0.01	21.08±0.09
4	PSD3	1000	56.77±0.57	2.69±0.01	59.47±0.57
5	PSD6	1000	17.44±0.10	1.21±0.01	18.65±0.11
6	PSD1	1000	929.77±7.47	27.05±0.20	956.82±7.48
7	PSD8	1000	68.41±0.38	1.43±0.01	69.85±0.38
8	PSD2	1000	175.36±1.49	5.35±0.02	180.72±1.49
9	PSD4	1000	26.76±0.20	1.59±0.01	28.35±0.20
10	HI1	1000	2,553.04±7.03	54.22±0.19	2,607.26±7.03
11	ESD7	1000	17.07±0.20	0.82±0.01	17.89±0.20
12	ESD4	1000	16.31±0.10	1.41±0.01	17.72±0.10
13	ESD8	1000	599.50±11.14	4.09±0.08	603.59±11.14
14	ESD2	1000	29.23±0.43	2.70±0.02	31.93±0.43
15	ESD6	1000	40.63±0.64	2.79±0.02	43.43±0.64
16	ESD5	1000	16.97±0.25	1.32±0.01	18.28±0.25
17	ESD3	1000	16.20±0.10	1.33±0.01	17.53±0.10
18	ESD1	1000	20.17±0.25	1.65±0.01	21.82±0.25
19	DD22.5	1000	105.97±5.58	1.67±0.07	107.64±5.58
20	DD45	1000	88.67±1.43	3.64±0.08	92.31±1.43
21	DD45	1000	86.88±2.63	3.80±0.10	90.68±2.63
22	DD45	1000	113.63±3.73	2.37±0.06	116.00±3.73
23	DD45	1000	102.41±1.91	3.72±0.09	106.13±1.91
24	DD67.5	1000	88.68±1.13	3.23±0.06	91.91±1.13
25	DD67.5	1000	97.09±2.71	2.94±0.06	100.02±2.71
26	DD67.5	1000	90.53±1.76	2.61±0.05	93.15±1.76
27	DD67.5	1000	83.07±2.06	3.24±0.06	86.31±2.06
28	DD22.5	1000	85.99±1.40	2.57±0.08	88.56±1.40
29	DD45	1000	105.69±4.31	3.22±0.08	108.91±4.31
30	DD45	1000	141.88±10.34	3.85±0.21	145.73±10.34
31	DD67.5	1000	86.20±0.93	3.74±0.07	89.93±0.93
32	DD22.5b	1000	79.96±1.42	1.87±0.06	81.83±1.42
33	DD22.5	1000	152.50±6.87	4.74±0.11	157.25±6.87
34	DD67.5	1000	85.69±1.14	4.61±0.08	90.30±1.14
35	DD45	1000	106.73±2.78	3.00±0.08	109.73±2.78
36	DD67.5	1000	80.37±0.99	4.69±0.09	85.06±1.00
37	DD22.5	1000	107.18±3.77	1.81±0.06	108.99±3.77
38	DD22.5	1000	152.45±10.45	2.87±0.08	155.33±10.45
39	DD45	1000	94.22±1.54	3.23±0.07	97.45±1.55
40	DD67.5	1000	89.02±2.33	3.88±0.07	92.89±2.33
41	DD45	1000	93.07±2.45	2.20±0.07	95.27±2.45

Component		Radiation Sensitivity	Electron Dose	Proton Dose	Total Dose
ID	Name	(krad)	(krad)	(krad)	(krad)
42	DD22.5	1000	173.77±7.92	3.09±0.06	176.86±7.92
43	DD22.5	1000	163.87±17.54	2.78±0.08	166.65±17.54
44	DD45b	1000	74.36±1.10	2.43±0.06	76.79±1.10
45	DD67.5b	1000	74.02±1.07	3.50±0.06	77.52±1.07
46	DD22.5	1000	140.07±9.33	2.09±0.07	142.15±9.33
47	DD67.5	1000	86.51±1.57	2.21±0.04	88.71±1.57
48	DD22.5	1000	124.62±2.15	5.07±0.14	129.69±2.16
49	DD0	1000	188.57±14.58	2.23±.08	190.81
50	Voltage Reference	300	66.32±0.56	2.62±0.02	68.94±0.56
51	Voltage Reference	300	108.48±1.08	3.70±0.07	112.18±1.08
52	Voltage Reference	300	86.69±0.74	2.87±0.06	89.56±0.74
53	Voltage Reference	300	65.75±0.79	2.89±0.03	68.64±0.79
54	Transistor NPN	100	90.59±1.67	2.96±0.06	93.55±1.67
55	Transistor NPN	100	77.08±1.27	3.31±0.09	80.39±1.28
56	Transistor NPN	100	68.17±1.40	3.33±0.15	71.50±1.41
57	Transistor NPN	100	90.55±2.20	3.30±0.14	93.86±2.20
58	Transistor NPN	100	85.24±1.84	3.90±0.05	89.14±1.84
59	Transistor NPN	100	78.04±1.53	2.77±0.05	80.81±1.53
60	Transistor NPN	100	78.22±1.28	4.29±0.08	82.52±1.28
61	Transistor Dual NPN	100	75.74±1.48	3.33±0.08	79.08±1.48
62	Transistor Dual PNP	100	81.35±2.01	2.70±0.06	84.05±2.01
63	Transistor Dual NPN	100	81.55±2.30	3.07±0.12	84.62±2.30
64	Transistor Dual PNP	100	84.23±2.39	2.77±0.12	87.00±2.39
65	Transistor Dual NPN	100	74.41±1.51	3.90±0.07	78.30±1.51
66	Transistor Dual PNP	100	73.59±1.51	2.97±0.05	76.57±1.51
69	Diode Ultra Power Rectifier	300	118.07±1.65	3.22±0.14	121.29±1.65
70	Diode Ultra Power Rectifier	300	135.90±1.74	2.62±0.06	138.52±1.74
71	Diode Ultra Power Rectifier	300	106.27±1.34	2.81±0.07	109.08±1.34
72	Diode Ultra Power Rectifier	300	102.17±1.42	3.51±0.07	105.68±1.42
73	Diode Ultra Power Rectifier	300	98.62±1.20	3.61±0.16	102.23±1.21
74	Diode Schottky 45V 1A	300	127.84±1.64	3.13±0.05	130.96±1.64
75	Diode Schottky 45V 1A	300	122.17±1.47	3.87±0.15	126.04±1.48
76	Diode Schottky 45V 1A	300	98.70±1.27	3.02±0.08	101.73±1.28
77	Diode Schottky 45V 1A	300	104.29±1.42	4.07±0.04	108.36±1.42
78	Diode Schottky 45V 1A	300	147.66±1.80	3.66±0.04	151.32±1.80
79	Diode Schottky 45V 1A	300	163.86±1.73	3.69±0.11	167.55±1.73
80	Diode Ultra Fast Recover 440V	300	100.73±2.90	3.68±0.14	104.41±2.91
81	Diode Ultra Fast Recover 440V	300	99.97±2.63	3.92±0.09	103.89±2.63
82	Diode Ultra Fast Recover 440V	300	82.82±1.73	3.43±0.12	86.25±1.74
83	Zener 12V	300	121.22±2.84	3.50±0.14	124.72±2.85
84	Zener 87V	300	113.66±1.83	3.93±0.08	117.59±1.83
85	Diode Ultra Fast Recover 440V	300	50.22±0.73	2.63±0.03	52.84±0.74
86	Diode Ultra Fast Recover 440V	300	80.40±1.47	2.85±0.05	83.25±1.47
87	Diode Ultra Fast Recover 440V	300	79.75±1.16	3.13±0.06	82.88±1.16
88	Oscillator 10MHz CMOS	100	80.28±0.32	3.72±0.01	84.00±0.32

Component		Radiation Sensitivity	Electron Dose	Proton Dose	Total Dose
ID	Name	(krad)	(krad)	(krad)	(krad)
89	uP Leon 3 FT Dual Core	300	87.98±0.17	2.87±0.10	90.85±0.20
90	Multiplexed ADC	100	70.20±0.81	3.00±0.07	73.20±0.81
91	Multiplexed ADC	100	68.23±0.78	3.31±0.04	71.54±0.78
92	Multiplexed ADC	100	76.46±0.70	2.72±0.05	79.18±0.70
93	OPAMP	300	87.59±0.91	2.88±0.02	90.46±0.91
94	OPAMP	300	90.03±2.42	3.22±0.12	93.25±2.42
95	OPAMP	300	81.99±0.50	3.17±0.08	85.16±0.51
96	LDO	300	91.15±0.60	2.93±0.04	94.08±0.60
97	LDO	300	77.97±0.37	3.18±0.07	81.15±0.38
98	LDO	300	133.76±0.71	3.58±0.03	137.34±0.71
99	LDO	300	118.88±0.69	3.28±0.05	122.16±0.69
100	LDO	300	124.45±0.95	3.64±0.02	128.08±0.95
101	LDO	300	93.06±0.46	2.84±0.01	95.90±0.46
102	LDO	300	85.63±0.48	4.14±0.07	89.76±0.48
103	LDO	300	132.11±0.59	3.48±0.05	135.59±0.59
104	Power Supervisor	100	78.18±0.61	2.87±0.05	81.05±0.62
105	SpW Transceiver	100	108.86±1.02	3.52±0.04	112.39±1.03
106	SpW Transceiver	100	75.77±0.53	3.53±0.07	79.30±0.54
107	Dual PWM Controller	300	87.81±0.32	3.19±0.02	91.00±0.32
108	ASIC VATA466	TBA	122.22±0.15	4.16±0.03	126.38±0.15
109	ASIC VATA466	TBA	85.25±0.10	3.26±0.12	88.52±0.16
110	ASIC VATA466	TBA	155.91±0.17	4.25±0.06	160.16±0.18
111	Temperature Transducer	300	250.78±8.66	4.10±0.05	254.88±8.66
112	Temperature Transducer	300	116.17±0.92	3.65±0.07	119.82±0.92
113	Temperature Transducer	300	161.37±1.56	4.62±0.10	165.99±1.56
114	Temperature Transducer	300	91.83±1.12	3.55±0.06	95.38±1.12
115	Temperature Transducer	300	120.24±2.83	3.65±0.07	123.89±2.84
116	QUAD COMP LM139A	100	71.70±0.76	2.54±0.04	74.24±0.76
117	MRAM 16Mb (2Mx8b)	100	79.92±0.16	3.08±0.09	83.00±0.19
118	SRAM 40Mb (1M x 39b)	100	72.81±0.22	3.26±0.11	76.07±0.24
119	PROM 256kb (32k x 8b)	100	73.49±0.35	2.69±0.09	76.18±0.36

materials inside and outside (spacecraft) it was deemed that the dose is low enough that no issues will come from it.

6.5 Displacement Damage Analysis

DDD is analyzed taking into account that its effect is proportional to the total Non-Ionizing Energy Loss (NIEL) (see Section 4.4.3). For the JUICE mission, a large population of electrons with energies larger than 10 MeV exist. As it was shown in Figure 4.17, at these energies, NIEL of electrons is less than two orders of magnitude lower than that of protons of the same energies. However, their flux is also very large when compared to protons, making them both important contributors for total DDD.

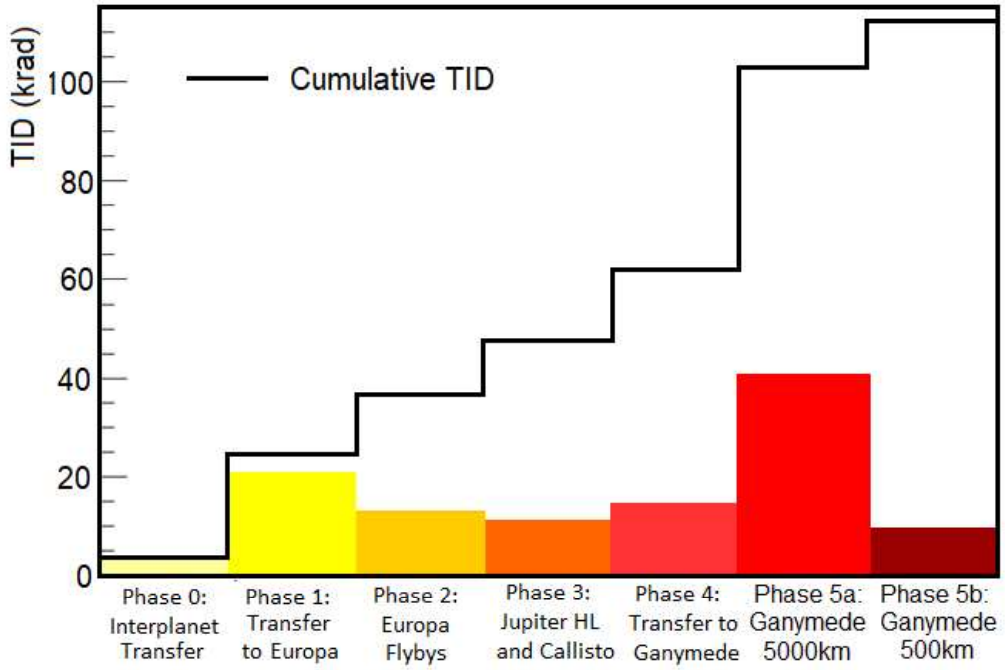

Figure 6.17: TID levels from of component #105, one of the SpW Transceivers, for all phases of the mission (colored). The cumulative dose is shown in black. From [158].

6.5.1 Non-Ionizing Dose Calculation

To calculate DDD, the results from Geant4 simulations of electrons and protons of the last TID model were analyzed. Knowing that the equivalent 50 MeV protons fluence can be calculated as:

$$Fluence(\frac{\#}{cm^2}) = \sum_{particles} \frac{\#}{A.cos\theta} . \frac{NIEL_{particle}(E_k, Si)}{NIEL_p(50MeV, Si)} \tag{6.9}$$

Where A is the total surface area of a component, θ is the incidence angle of the particles w.r.t. the surface's normal, NIEL(E_k) is the NIEL coefficient for an incident particle with kinetic energy E_k in the medium (Si) and $NIEL_p$(50MeV) is the NIEL coefficient for 50 MeV protons in Si. This formula breaks down for large angles which is not acceptable since particles are coming from all directions. Considering that the deposited energy from non-ionizing processes in Silicon is related to the NIEL by:

$$E_{dep}(Non - Ionizing) = NIEL(E_k, Si).\rho(Si).P_{length} \tag{6.10}$$

Where P_{length} is the length of the particles path in the sensitive volume. Replacing the particle NIEL in equation 6.9 it becomes:

$$Fluence(\frac{\#}{cm^2}) = \sum_{particles} \frac{\#}{A.cos\theta} . \frac{E_{dep}(Non - Ionizing)}{NIEL_p(50MeV, Si).\rho(Si).P_{length}} \tag{6.11}$$

Since P_{length} is in the denominator it can be approximated by the thickness, th, of the

volume divided by the cos of the entrance angle. While this is not exactly true it still gives the worst-case value. The cos term can then be dropped and the equivalent fluence calculated as:

$$Fluence(\frac{\#}{cm^2}) = \sum_{particles} \frac{\#}{A}.\frac{E_{dep}(Non-Ionizing)}{NIEL_p(50MeV,Si).\rho(Si).th} \tag{6.12}$$

Notice that the denominator in the right side is the average deposited energy through non-ionizing processes of a 50 MeV proton crossing a volume in a straight line.

6.5.2 Results

According to specifications, DD levels must be kept below 2E+11 protons/cm^2 for a 50 MeV equivalent proton fluence after a RDM of 2 is applied [26]. Table 6.8 shows the results for all 119 radio-sensitive components. Only four sensors of the Directionality Detector Head were above their sensitive limits, diodes number 33, 38, 42 and 47. However they have been tested after these results were obtained and are now qualified. Larger area sensors such as the HID1 had already been tested to higher fluence levels because they were expected to be subject to higher DDD. In fact this diode is the component with larger DDD levels for the whole mission. Most of the fluence is given in the Ganymede orbit due to a combination large fluxes at higher energies and duration of the phase [28]. In conclusion, no failure is expected from any of the devices due to DDD for the whole mission hence no further action was done.

Table 6.8: 50MeV proton equivalent fluence (RDM applied) for the full JUICE mission obtained with RADEM mechanical model v18.0 for 119 components. From [158].

#	Component	50 MeV proton Eq. Fluence (#/cm^2)	
		Sensitivity	Mission level
1	HID2	1.16E+012	1.57E+011 ± 1.57E+010
2	PSD7	1.16E+012	1.39E+010 ± 1.39E+009
3	PSD5	1.16E+012	1.47E+010 ± 1.47E+009
4	PSD3	1.16E+012	2.84E+010 ± 2.84E+009
5	PSD6	1.16E+012	1.24E+010 ± 1.24E+009
6	PSD1	6.70E+011	2.32E+011 ± 2.32E+010
7	PSD8	1.16E+012	1.36E+010 ± 1.36E+009
8	PSD2	1.16E+012	5.37E+010 ± 5.37E+009
9	PSD4	1.16E+012	1.76E+010 ± 1.76E+009
10	HID1	1.16E+012	4.58E+011 ± 4.58E+010
11	ESD7	6.70E+011	1.22E+010 ± 1.22E+009
12	ESD4	6.70E+011	1.40E+010 ± 1.40E+009
13	ESD8	6.70E+011	3.01E+010 ± 3.01E+009
14	ESD2	6.70E+011	1.16E+010 ± 1.16E+009
15	ESD6	6.70E+011	2.60E+010 ± 2.60E+009
16	ESD5	6.70E+011	1.31E+010 ± 1.31E+009
17	ESD3	6.70E+011	1.36E+010 ± 1.36E+009
18	ESD1	2.82E+011	6.54E+010 ± 6.54E+009
19	DD22.5	6.01E+010	5.57E+010 ± 5.57E+009
20	DD45	6.01E+010	4.59E+010 ± 4.59E+009
21	DD45	6.01E+010	4.49E+010 ± 4.49E+009
22	DD45	6.01E+010	4.61E+010 ± 4.61E+009
23	DD45	6.01E+010	4.88E+010 ± 4.88E+009
24	DD67.5	6.01E+010	4.24E+010 ± 4.24E+009
25	DD67.5	6.01E+010	4.42E+010 ± 4.42E+009
26	DD67.5	6.01E+010	4.39E+010 ± 4.39E+009
27	DD67.5	6.01E+010	4.19E+010 ± 4.19E+009
28	DD22.5	6.01E+010	5.22E+010 ± 5.22E+009
29	DD45	6.01E+010	4.55E+010 ± 4.55E+009
30	DD45	6.01E+010	5.31E+010 ± 5.31E+009
31	DD67.5	6.01E+010	4.37E+010 ± 4.37E+009
32	DD22.5b	6.01E+010	4.43E+010 ± 4.43E+009
33	DD22.5	6.01E+010	6.60E+010 ± 6.60E+009
34	DD67.5	6.01E+010	4.26E+010 ± 4.26E+009
35	DD45	6.01E+010	5.13E+010 ± 5.13E+009
36	DD67.5	6.01E+010	4.48E+010 ± 4.48E+009
37	DD22.5	6.01E+010	5.03E+010 ± 5.03E+009
38	DD22.5	6.01E+010	6.58E+010 ± 6.58E+009
39	DD45	6.01E+010	4.57E+010 ± 4.57E+009
40	DD67.5	6.01E+010	4.41E+010 ± 4.41E+009

#	Component	50 MeV proton Eq. Fluence (#/cm^2)	
		Sensitivity	Mission level
41	DD45	6.01E+010	4.32E+010 ± 4.32E+009
42	DD22.5	6.01E+010	6.03E+010 ± 6.03E+009
43	DD22.5	6.01E+010	5.65E+010 ± 5.65E+009
44	DD45b	6.01E+010	3.62E+010 ± 3.62E+009
45	DD67.5b	6.01E+010	3.73E+010 ± 3.73E+009
46	DD22.5	6.01E+010	5.19E+010 ± 5.19E+009
47	DD67.5	6.01E+010	6.27E+010 ± 6.27E+009
48	DD22.5	6.01E+010	3.94E+010 ± 3.94E+009
49	DD0	6.01E+010	5.12E+010 ± 5.12E+009
50	Voltage Reference	2.00E+011	3.94E+010 ± 3.94E+009
51	Voltage Reference	2.00E+011	5.68E+010 ± 5.68E+009
52	Voltage Reference	2.00E+011	4.88E+010 ± 4.88E+009
53	Voltage Reference	2.00E+011	3.76E+010 ± 3.76E+009
54	Transistor NPN	2.00E+011	5.04E+010 ± 5.04E+009
55	Transistor NPN	2.00E+011	4.54E+010 ± 4.54E+009
56	Transistor NPN	2.00E+011	4.25E+010 ± 4.25E+009
57	Transistor NPN	2.00E+011	4.89E+010 ± 4.89E+009
58	Transistor NPN	2.00E+011	5.29E+010 ± 5.29E+009
59	Transistor NPN	2.00E+011	4.35E+010 ± 4.35E+009
60	Transistor NPN	2.00E+011	4.43E+010 ± 4.43E+009
61	Transistor Dual NPN	2.00E+011	9.38E+009 ± 9.38E+008
62	Transistor Dual PNP	2.00E+011	8.32E+009 ± 8.32E+008
63	Transistor Dual NPN	2.00E+011	8.75E+009 ± 8.75E+008
64	Transistor Dual PNP	2.00E+011	9.58E+009 ± 9.58E+008
65	Transistor Dual NPN	2.00E+011	9.04E+009 ± 9.04E+008
66	Transistor Dual PNP	2.00E+011	8.46E+009 ± 8.46E+008
69	Diode Ultra Power Rectifier 150V	2.00E+011	5.98E+010 ± 5.98E+009
70	Diode Ultra Power Rectifier 150V	2.00E+011	6.44E+010 ± 6.44E+009
71	Diode Ultra Power Rectifier 150V	2.00E+011	5.32E+010 ± 5.32E+009
72	Diode Ultra Power Rectifier 150V	2.00E+011	5.29E+010 ± 5.29E+009
73	Diode Ultra Power Rectifier 150V	2.00E+011	5.53E+010 ± 5.53E+009
74	Diode Schottky 45V 1A	2.00E+011	6.17E+010 ± 6.17E+009
75	Diode Schottky 45V 1A	2.00E+011	6.41E+010 ± 6.41E+009
76	Diode Schottky 45V 1A	2.00E+011	5.21E+010 ± 5.21E+009
77	Diode Schottky 45V 1A	2.00E+011	5.07E+010 ± 5.07E+009
78	Diode Schottky 45V 1A	2.00E+011	5.91E+010 ± 5.91E+009
79	Diode Schottky 45V 1A	2.00E+011	7.28E+010 ± 7.28E+009
80	Diode Ultra Fast Recover 440V	2.00E+011	3.43E+010 ± 3.43E+009
81	Diode Ultra Fast Recover 440V	2.00E+011	3.43E+010 ± 3.43E+009
82	Diode Ultra Fast Recover 440V	2.00E+011	3.36E+010 ± 3.36E+009
83	Zener 12V	2.00E+011	5.46E+010 ± 5.46E+009
84	Zener 87V	2.00E+011	6.14E+010 ± 6.14E+009
85	Diode Ultra Fast Recover 440V	2.00E+011	2.94E+010 ± 2.94E+009
86	Diode Ultra Fast Recover 440V	2.00E+011	4.06E+010 ± 4.06E+009

#	Component	50 MeV proton Eq. Fluence (#/cm^2)	
		Sensitivity	Mission level
87	Diode Ultra Fast Recover 440V	2.00E+011	4.41E+010 ± 4.41E+009
88	Oscillator 10MHz CMOS	2.00E+011	4.50E+010 ± 4.50E+009
89	uP Leon 3 FT Dual Core	2.00E+011	4.85E+010 ± 4.85E+009
90	Multiplexed ADC	2.00E+011	3.89E+010 ± 3.89E+009
91	Multiplexed ADC	2.00E+011	4.06E+010 ± 4.06E+009
92	Multiplexed ADC	2.00E+011	4.30E+010 ± 4.30E+009
93	OPAMP RHF43BK-01V	2.00E+011	4.50E+010 ± 4.50E+009
94	OPAMP RHF43BK-01V	2.00E+011	4.55E+010 ± 4.55E+009
95	OPAMP RHF43BK-01V	2.00E+011	4.65E+010 ± 4.65E+009
96	LDO RHFL4913KPA-01V	2.00E+011	5.05E+010 ± 5.05E+009
97	LDO RHFL4913KPA-01V	2.00E+011	4.42E+010 ± 4.42E+009
98	LDO RHFL4913KPA-01V	2.00E+011	7.20E+010 ± 7.20E+009
99	LDO RHFL4913KPA-01V	2.00E+011	6.01E+010 ± 6.01E+009
100	LDO RHFL4913KPA-01V	2.00E+011	6.51E+010 ± 6.51E+009
101	LDO RHFL4913KPA-01V	2.00E+011	5.10E+010 ± 5.10E+009
102	LDO RHFL4913KPA-01V	2.00E+011	4.84E+010 ± 4.84E+009
103	LDO RHFL4913KPA-01V	2.00E+011	7.06E+010 ± 7.06E+009
104	Power Supervisor	2.00E+011	4.41E+010 ± 4.41E+009
105	SpW Transceiver	2.00E+011	5.69E+010 ± 5.69E+009
106	SpW Transceiver	2.00E+011	4.49E+010 ± 4.49E+009
107	Dual PWM Controller	2.00E+011	4.89E+010 ± 4.89E+009
108	ASIC VATA466	2.00E+011	6.74E+010 s± 6.74E+009
109	ASIC VATA466	2.00E+011	4.71E+010 ± 4.71E+009
110	ASIC VATA466	2.00E+011	7.83E+010 ± 7.83E+009
111	Temperature Transducer	2.00E+011	1.01E+011 ± 1.01E+010
112	Temperature Transducer	2.00E+011	6.02E+010 ± 6.02E+009
113	Temperature Transducer	2.00E+011	8.33E+010 ± 8.33E+009
114	Temperature Transducer	2.00E+011	5.07E+010 ± 5.07E+009
115	Temperature Transducer	2.00E+011	6.00E+010 ± 6.00E+009
116	QUAD COMP LM139A	2.00E+011	3.99E+010 ± 3.99E+009
117	MRAM 16Mb (2Mx8b)	2.00E+011	4.49E+010 ± 4.49E+009
118	SRAM 40Mb (1M x 39b)	2.00E+011	4.17E+010 ± 4.17E+009
119	PROM 256kb (32k x 8b)	2.00E+011	4.12E+010±4.12E+009

6.6 Single Event Effect Analysis

Single Event Effects are non-destructive/destructive occurrences in components from a single particle with high enough Linear Energy Transfer (LET). In RADEM, all components have a LET threshold for latch-up, LET$_{th}$, (minimum LET for an SEE to occur) >60 MeV.cm^2/mg hence its probability is very low and analysis is not required [27]. It does have however, four components sensitive to Single Event Upsets (SEUs) and Single Event Transients (SETs): the VATA466 ASICs [22], the 1103R10M000000BF 10MHz CMOS oscillator [174][175], the UT8R1M39 21XFC 40Mb (1M x 39b) SRAM and the UT28F256LVQLE 65UCC 256kb (32k x 8b) PROM [176]. SEU test data parameters for

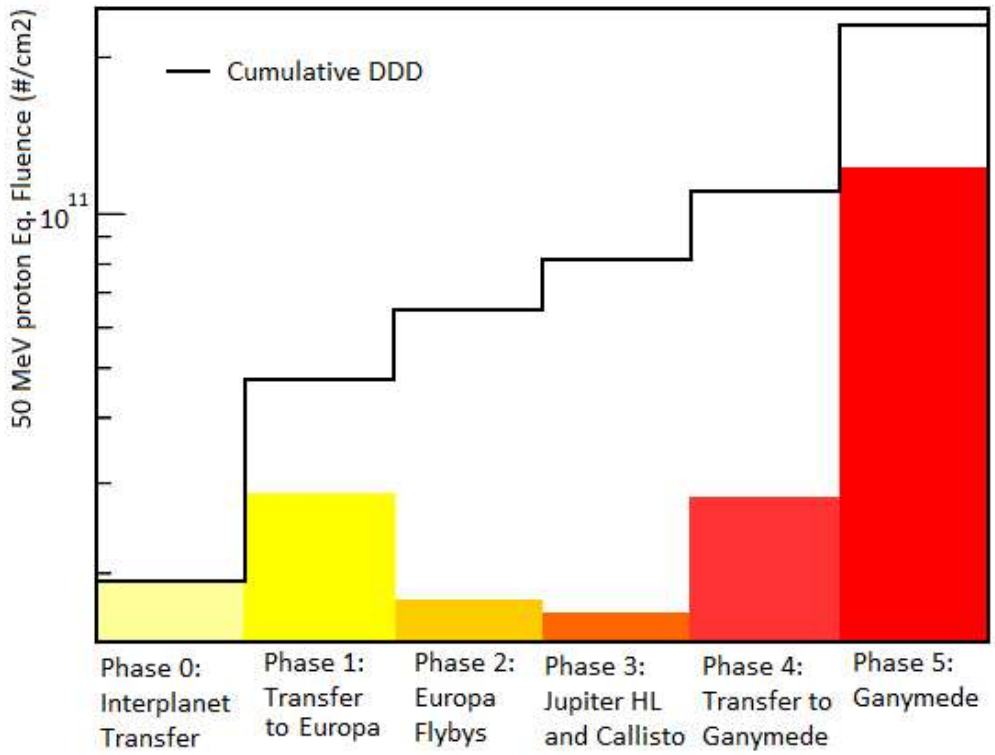

Figure 6.18: Equivalent fluence for component #6, top Silicon Diode of PSD, for all phases of the mission (coloured). The cumulative fluence is shown in black. From [158].

the ASIC VATA466, the SRAM and the PROM, and SET test data for the oscillator are presented in Table 6.9.

Table 6.9: Component parameters used in SEU rate predictions. From [158].

Component			Weibull Fit Parameters			
Name	Sensitive Vol. Area (μm)	Sensitive Vol. Thickness (μm)	LETth (MeV. cm^2/mg)	Csat (cm^2/Vol)	S	W (MeV. cm^2/mg)
ASIC	1.64*1.64	2	50	2.64E-08	2.83	13.49
SRAM[1]	2.82*2.82	2[2]	1	8.00E-08	0.8	60
PROM	17.32*17.32	2[2]	40	3,00E-06	1.6	45
Oscillator	173.2*173.2	2[2]	33	3,00E-04	1.1	135

Three of the components have LET$_{th}$ (>15 MeV.cm^2/mg). For these components, protons from radiation belts do not have enough LET to cause SEEs. It was then possible to calculate SEE rates using the CRÈME algorithm (constant LET)[27] in SPENVIS [12] assuming a shielding of 1 g/cm^2. Three LET spectrums were used as input in this analysis:

[1]No data was available for the selected SRAM. As such data from UT8ER512K32 SRAM produced by the same manufacturer was selected as reference for this analysis.

[2]No information was obtained for the thickness of the components. A typical value was selected for the analysis.

peak 5 minutes of a SEP, worst week and galactic cosmic ray background at solar minimum, all at 1 A.U. as recommended for interplanetary missions in [26], [158] since it represents a worst-case condition. In the SRAM, proton induced upsets was also calculated with the effective LET (LET_{eff}=LET/cosθ) fluence obtained from Geant4 simulations. This was necessary because the geometry of RADEM has a large impact on the number and energy of protons at the component level.

Before discussing SEU rate and impact in RADEM, first one needs to understand the dataflow in the instrument shown in Figure 6.19. There are four types of memories in RADEM: the PROM responsible for the boot; the MRAM, where the Application Software (ASW) is stored; the ASIC which has an embedded memory to store temporary data; and the SRAM which works as a typical Random-Acess Memory and that for the purpose of this thesis, integrates the data from the ASIC before sending it to the spacecraft. An important aspect of the dataflow is that the ASIC registers have 22-bit only. This constraints its hold-time since at maximum count rate, 1 MHz, the ASIC can only store data for ~5 s. Consequently data from the ASICs has to be transferred, first to the SRAM, and later to the spacecraft (each 30 s). This is of great importance for SEE analysis as it will be discussed below

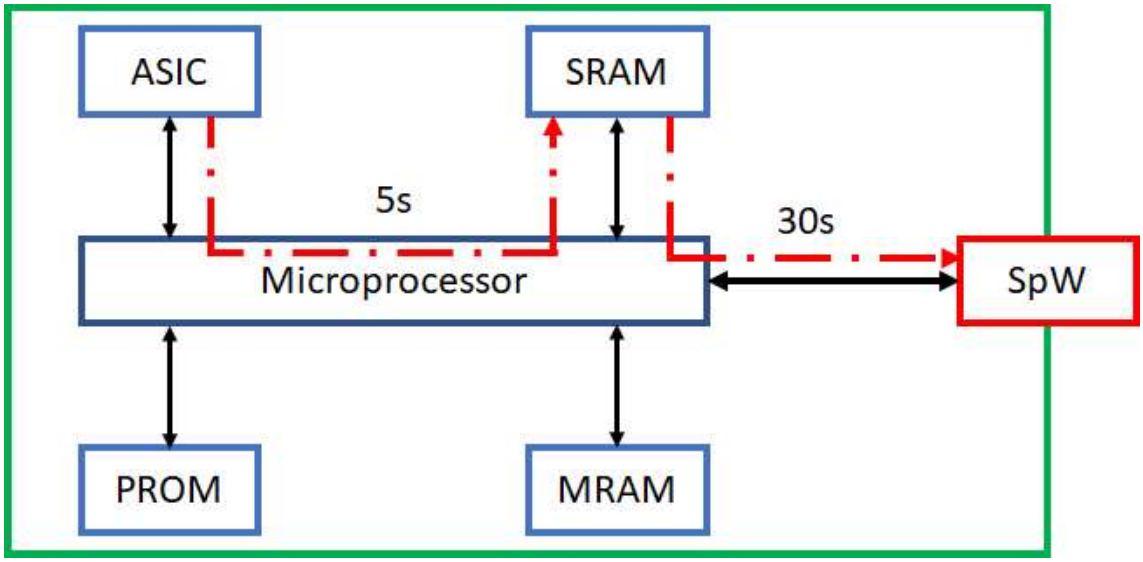

Figure 6.19: Dataflow in RADEM as described by the contractor (EFACEC). The PROM is responsible for the boot, the MRAM for the Application Software (ASW) and the SRAM for integrating ASIC register count rates before sending the data to the spacecraft via spacewire. The dashed red line shows the theoretical dataflow from the ASIC to the spacecraft.

6.6.1 ASIC

ASIC VATA466 [22] had not been tested yet at the time this thesis was written. However it is based on the same technology and processes of its predecessor. For this reason estimations were done with test data from ASIC VATA465 instead. Since LET_{th} is larger than 15 MeV.cm^2/mg, no proton induced SEUs are expected. SEU rates computed for this component are given in Table 6.10. The SEU rate is so low, 3.21E-11 bit^{-1}.day^{-1}, that the probability that an SEU occurs, even in the programable bits, for the entire mission, is negligible.

Table 6.10: SEU rates in the ASIC for the three reference LET spectrums. From [158].

Effect	GCR Quiet		GCR+Worst Week		GCR+Peak 5min	
	(bit.s)$^{-}$1	(bit.day)$^{-}$1	(bit.s)$^{-}$1	(bit.day)$^{-}$1	(bit.s)$^{-}$1	(bit.day)$^{-}$1
Direct Ionization	2.05E-18	1.77E-13	6.55E-17	5.66E-12	3.72E-16	3.21E-11
Total	2.05E-18	1.77E-13	6.55E-17	5.66E-12	3.72E-16	3.21E-11

6.6.2 PROM

The 2^{th} component is a Programmable Read-Only Memory (PROM) from AEROFLEX [176]. PROMs can only be written once. SEUs occur in the registers and not on the memory cells themselves. The registers can be returned to their original state by power-cycling the device. The PROM in RADEM has 32782 registers of 8 bits each. The rate at which SEUs occur per register due to GCR is shown in Table 6.11. Since LET_{th} is larger than 15 MeV.cm^2/mg, no proton induced SEUs are expected.

Table 6.11: SEU rates for each register of the PROM for the three reference LET spectrums. From [158].

Effect	GCR		GCR+Worst Week		GCR+Peak 5min	
	(s)$^{-1}$	(day)$^{-1}$	(s)$^{-1}$	(day)$^{-1}$	(s)$^{-1}$	(day)$^{-1}$
Direct Ionization	2.68E-12	2.32E-07	1.87E-10	1.62E-05	2.12E-09	1.83E-04
Total	2.68E-12	2.32E-07	1.87E-10	1-62E-05	2.12E-09	1.83E-04

If each register was used individually, no errors would be acceptable. However, while the probability that no errors occur in a register, calculated assuming a Poisson distribution, for the whole mission is very high, when combined for the whole PROM it is close to zero. In the case of RADEM, the PROM is responsible for booting of the instrument and no redundancy exists. This means that only a power cycle allows to recover from such error which may result in a significant downtime. Knowing this, the PROM was split into 6144 words (RADEM uses only 3/4 of the memory) of five registers where four of the registers contain the actual boot code and the the fifth works as an EDAC code. EDACs can detect any number of errors and correct one error only. This means that success can

be defined as each word having one or less errors. To calculate the probability of success, first one needs to calculate the probability that a register has one or less errors in a given time interval:

$$P(k=0,t) = P(0) = e^{(-r.t)}.\frac{(r.t)^0}{0!} \tag{6.13}$$

$$P(k=1,t) = e^{(-r.t)}.\frac{(r.t)^1}{1!} \tag{6.14}$$

Where r is the SEU rate displayed in Table 6.11. The probability of success of a word, $P_{w\_success}$, can then be calculated as:

$$P_{w\_success}(t) = P(0,t)^5 + 5.P(0,t)^4.P(1,t) \tag{6.15}$$

Finally, the probability of success of the PROM, $P_{PROM\_success}$, is obtained by combining the probability of success of all words:

$$P_{PROM\_success}(t) = P_{w\_success}(t)^{6144} \tag{6.16}$$

The $P_{PROM\_success}$ for different time intervals is shown in Figure 6.20. This probability is very high (>93%) for the whole mission duration (4066 days), especially taking into account that a power cycle of the instrument returns the PROM to its initial state. It is also noteworthy that this is a conservative approach as it does not take into account the rigidity cutoff from Jupiters magnetosphere during the planetary orbits. For the worst-case week and five minutes, the probability of success is very close to one for periods of the same order of magnitude as they are predicted, which means that the downtime of RADEM from due to the accumulation of SEUs in the PROM is negligible.

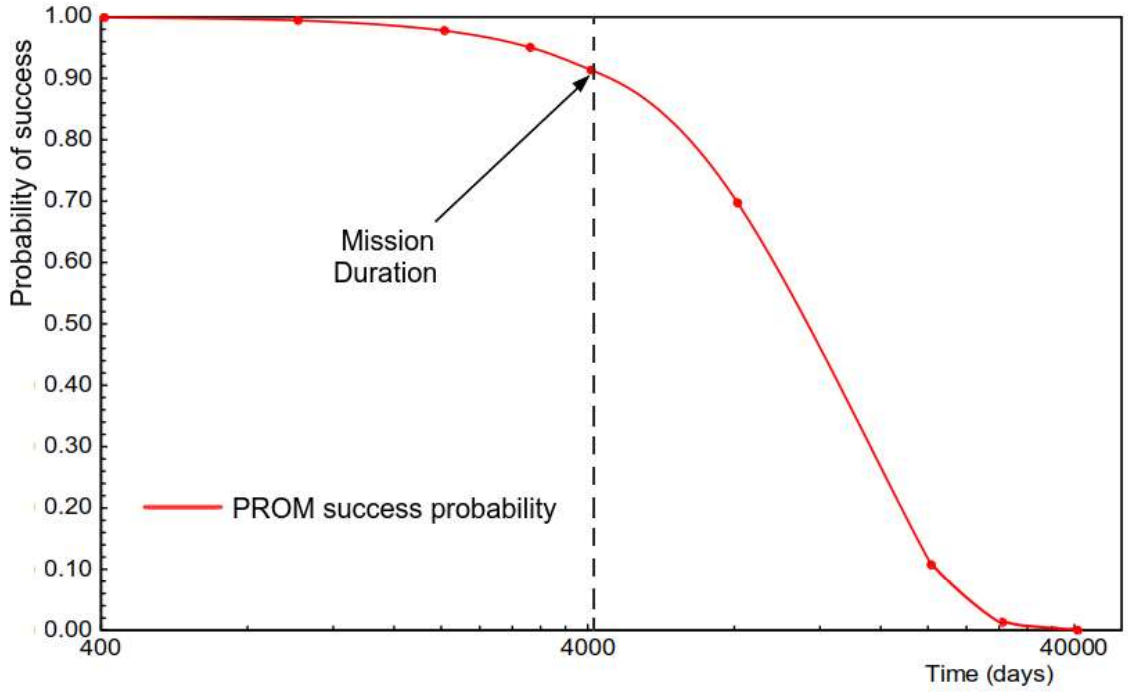

Figure 6.20: Probability that all words in the PROM will have less than SEU for different time intervals during GCR quiet times.

6.6.3 SRAM

The UT8R1M39 21XFC 40Mb (1M x 39b) SRAM is most sensitive device to SEUs in RADEM. Its has small LET_{th} which means that even protons from the radiation belts can trigger an SEU via indirect ionization (knock-off Silicon atoms). It has 1 million 39 bite words which contain a 7-bit Error Detection and Correction (EDAC) code. EDACs allow to detect an error in a word and correct it, and to detect more than one error without correcting it. However, EDACs require words to be read.

The SEU rate is shown in Table 6.12. Trapped protons are responsible for more SEUs than GCR during quiet times. Notice also that SEU rates are much higher than in the other components because of the low LET_{th}. To assess the impact of SEUs in the operation of the system let us calculate the probability that, in a given interval, a word has one or less errors. Assuming again a Poisson distribution, the probability that a word has less than two SEU, P_{word}(k<2, t), is given by:

$$P_{word}(k < 2, t) = P_{bit}(k = 0, t)^{39} + 39 * P_{bit}(k = 0, t)^{38} * P_{bit}(k >= 1, t) \tag{6.17}$$

Where P_{bit}(k=0,t) and P_{bit}(k>=1,t) are the probabilities that a single bit has 0 or at least one error in a time interval t respectively. The probability that N words have one or less errors can be calculated with P_{word}(k<2, t) to the power of N. Figure 6.21 shows this probability as a function of time for several sets of words, cause by the worst-case

trapped protons. Considering that the data is uploaded to the spacecraft every 30 s, it seems unlikely that more than a few words are uploaded correctly. However, the SRAM is used for different applications. One of them is for integrating data from the ASIC registers which is later uploaded to the spacecraft. Since the 22-bit register of the ASIC require that its information is uploaded to the SRAM every ∼5 s, the SRAM memory that stores this information is access and the EDAC allows to correct for single errors. There are 36 registers per ASIC and three ASICs hence the SRAM must be able to hold 108 words (registers) for ∼5 s. In this case the probability that all words remain correct is ∼0.75 during 5 s, and ∼0.18 ($0.75^{(30/5)}$) for 30 s which is not acceptable. Decreasing the time between data transfer from the ASIC to the SRAM to 1 s, the probability of success increases to ∼0.99 for 5 s and ∼0.70 ($0.99^{(30/1)}$) for 30 s which is also not acceptable. To have a probability of success of over 0.96 the transfer time must be decreased to less than 0.15 s. Of course this is a worst-case scenario inside the Jovian magnetosphere. Nevertheless, in the inner-belts one should consider smaller time-windows between data transfers or fast scrubbing rates of the words storing the data. For other parts of the mission inside the Jovian magnetosphere fluxes are low by at least ∼one order of magnitude. For solar events the rates are higher and data might be loss. This is considered acceptable since these are not the main focus of RADEM. In quiet times the SEU rate is low and no issues are forseen.

Table 6.12: SEU rates in the SRAM for the three reference LET spectrums and for Jovian worst-case trapped protons. From [158].

Effect	Rate	Direct ionization	Proton Induced Ionization	Total
GCR	$(\text{bit.s})^{-1}$	3.92E-12	3.22E-06	3.22E-06
Quiet	$(\text{bit.day})^{-1}$	3.38E-07	2.78E-01	2.78E-01
GCR +	$(\text{bit.s})^{-1}$	2.27E-10	2.64E-03	2.64E-03
Worst Week	$(\text{bit.day})^{-1}$	1.96E-05	2.28E+02	2.28E+02
GCR +	$(\text{bit.s})^{-1}$	3.15E-09	3.83E-02	3.83E-02
Worst 5m	$(\text{bit.day})^{-1}$	2.72E-04	3.31E+03	3.31E+03
Trapped	$(\text{bit.s})^{-1}$	4.45E-15	0.000339	0.000339
Protons	$(\text{bit.day})^{-1}$	3.84E-10	29.3	29.3

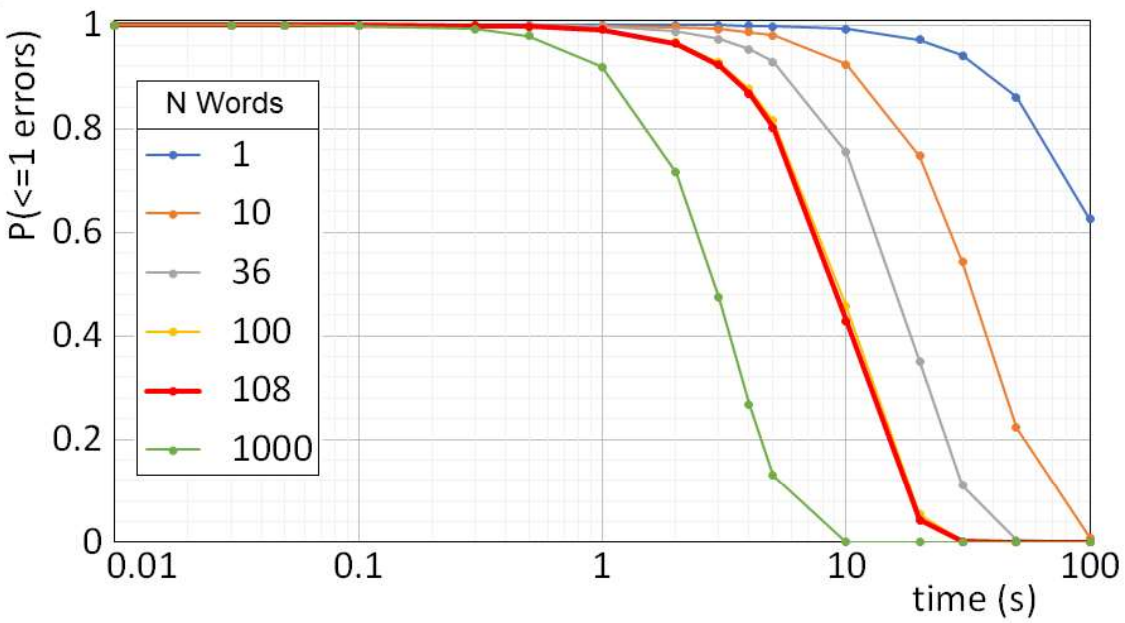

Figure 6.21: Probability N words in the SRAM will not have a double error in a time interval t.

6.6.4 Oscillator

The fourth component, the oscillator is senstive to SET. According to the producer of the this component, Vectron, the Oscillator has one sensitive part only, ACT3301, a Flexible AC Transmission IC which contains CMOS logic. A SET occurs when the output changes value due to a particle [174][175].

Average SET rates calculated for this component are shown in Table 6.13. All values are extremely low which is not surprising given its high LET_{th}. In fact, as it can be seen in Figure 6.22, the probability that a SET occurs in a time interval smaller than the mission duration is always less than 6%. For the worst week and worst five minutes the probabilities within their time frames are even lower, ∼0.93% and ∼0.01% respectively. Furthermore it was shown by EFACEC that transients are not a concern for any components hence full reliability is expected [177].

Table 6.13: SEU rates in the Oscillator for the three reference GCR LET spectrums. From [158].

Effect	GCR Quiet		GCR+Worst Week		GCR+Peak 5min	
	s^{-1}	day^{-1}	s^{-1}	day^{-1}	s^{-1}	day^{-1}
Direct Ionization	1.88E-10	1.63E-05	1.55E-08	1.34E-03	1.97E-07	1.70E-02
Total	1.88E-10	1.63E-05	1.55E-08	1.34E-03	1.97E-07	1.70E-02

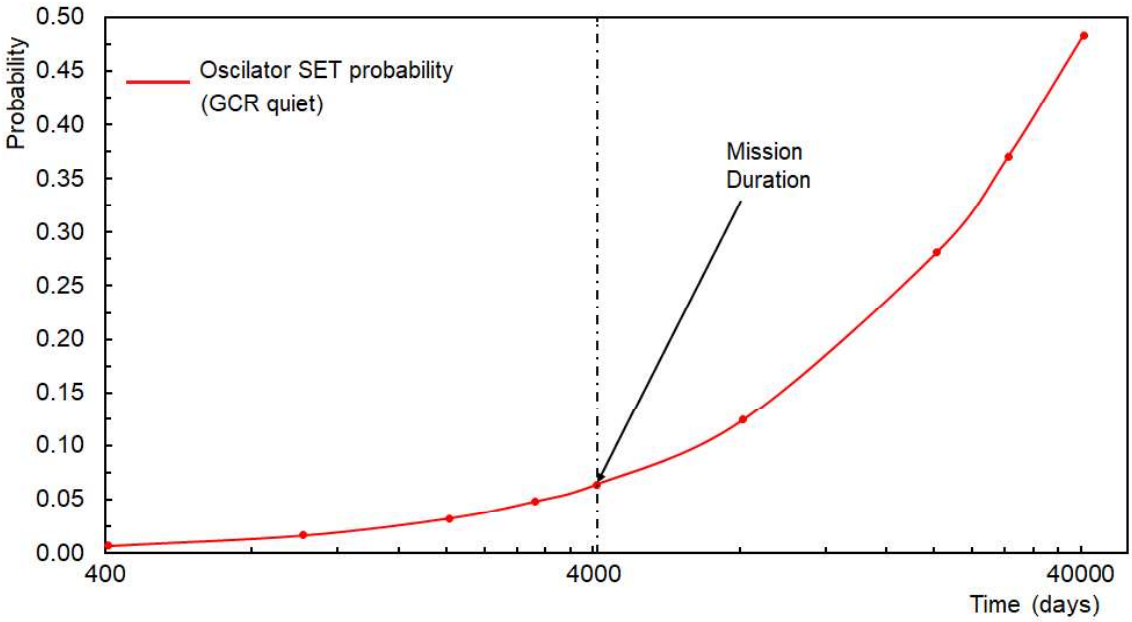

Figure 6.22: SET occurrence probability in the oscillator for different time intervals assuming a constant GCR quiet flux.

6.7 Discussion

In this chapter, radiation analysis regarding TID, DDD and SEE for all RADEM sensitive components was presented. This was a laborious task which combined ray-tracing of the spacecraft and full description of the instrument to obtain as accurately as possible the radiation levels for each sensitive part. The Jovian environment is particularly demanding because the dominant particle are electrons with energies high enough to produce Bremmstrahlung photons. For this reason it was essential to perform detailed Monte Carlo simulations which take into account secondary particles from interactions. The combined solution of modeling the spacecraft as a 6-sided box and fully describing RADEM was essential in this case since it takes a very long time (or a very large number of computing resources) to simulate particles interacting with all the spacecrafts materials. The description of all RADEM volumes, particularly the components package, is of utmost importance because they have a non-negligible mass that covers half the solid angle of the sensitive parts. This solution also took a long time to simulate electrons (~4 days with 20-80 cores depending on the availability), but still within reason regarding the mission schedule. Furthermore, Monte Carlo simulations are an essential part of the development and characterization of particle detectors which was done in parallel with the radiation analysis, specifically because of the method employed. This will be made clear in the Chapter 7 where the work performed to develop RADEMs Directionality Detector will be presented.

Shielding optimization against TID in components was the major challenge of this analysis. First because the initial design of RADEM was made with the assumption that

the instrument would be contained in a protective vault with only its detector heads exposed directly to the environment. Second because of the nature of particle interaction with matter and mass constraints. It is well established that TID does not decrease linearly with a material thickness. Therefore it is necessary to select the materials and/or combination of materials in order to keep the mass of the instruments as low as possible. Taking this into account Aluminum and Tantalum were used. The former for the RADEM structure in the form of increased thickness and the later for local shielding. It was also preferred to use Tantalum inside RADEM walls to keep Bremsstrahlung radiation dose contribution low. Bremsstrahlung occurs preferentially for energetic electrons and for high atomic number materials such as Tantalum (Z=73). The idea behind having Tantalum between Aluminum and the components is that electrons first slow down in the Aluminum before interacting with Tantalum resulting in lower Bremsstrahlung. This was not always possible however, because of spacing constraints inside RADEMs volume. Nevertheless, all these aspects were considered. While the total mass increase may seem large, more than ∼2.0 kg, one has to bare in mind that the contribution from the spacecraft to the overall shielding is low and therefore this adjustment is necessary.

An aspect that should be considered in future design of instruments is the orientation of components. In the case of RADEM, the Spacewire Transceivers have their larger surface facing a different direction than all other components. These components required 150 g of Tantalum alone and were the larger incentive to increase the side walls. Even after all this resource allocation the final TID computation for one of them was still higher than their radiation sensitivity. As they are fully redundant, and the limits are expected to be reached at the end of the mission only, the risk was deemed acceptable. However it is something that can be reduced by design choices. At the phase that shielding was optimized there were already several constraints in place so this should be addressed right from the beginning of a project.

Displacement Damage Dose on all components were within the limits for the final model. Only the diodes that were custom made had to be tested up to higher non-ionizing doses. Nonetheless, some results are noteworthy. While no further shielding was necessary to protect components from DDD, roughly half of DDD in the final model came from electrons. This means that the increased shielding also lowers the overall DDD in the components since the Non-Ionizing Energy Loss (NIEL) of electrons increases with energy as it was already discussed in Figure 4.17. Radiative energy loss is also important since the photons produced do not contribute to DDD. Lastly, the devices used are not substantially sensitive to DDD such as solar panels or optical devices further decreasing the need for DDD mitigation strategies [4][26].

Both TID and DDD were computed taking into account a 2x factor (RDM) to bound part-variability and stochastic enhanced dose absorption. Damage from cumulative effects is now contained and the risk of failure for RADEM is considered low. The only questionable component was one of the SpaceWire Transceivers which is fully redundant. The VATA466 ASIC also still needs to be tested but can easily be shielded since they are

located inside aluminum boxes that have room for the addition of material.

Regarding Single Event Effects, no latch-up modes were identified as threats. However, four components were considered susceptible to SEUs, the ASICs, the SRAM, the Oscillator IC and the PROM, have different functionalities, sensitivities and mitigation strategies. A case by case study was then done to each. The results showed that only the SRAM is vulnerable during worst-case proton fluxes. Limitations calculated in this thesis will be considered in the software design in order to avoid loss of data.

In conclusion, all components are expected to survive the entire duration of the mission and perform within specification. The only question mark are the VATA466 ASICs which will be tested during 2019. While no contingency plan exists, there is no particular reasons to expect that the devices will not work and that a replacement is needed. It is worth mentioning that this was the first work resorting to the GUIMesh software. It seems that this will be helpful for future instrument development as it allows a precise and fast method to describe solids from instrument designers in Geant4 for applications in several fields that resort to radiation interaction with matter.

7 Development of a Directionality Detector

Now that the Radiation Hardness Assurance of RADEM, and in some part JUICE, has been addressed, it is time to discuss the performance of the Radiation Monitor. Despite the fact that RADEM has four detector heads, only the Directionality Detector Head (DDH) is addressed in this thesis. The other detectors are based on standard Silicon stack detectors with layers of absorbers interlayed between Silicon diodes. These detectors, described in Chapter 2, will perform spectral analysis of the electron, proton and ion environment present in the Jupiter belts. The DDH will measure the electron flux angular variability. It is a key part of RADEM that will allow to correct the flux angular variance. This is of particular importance in Jupiter where the Total Ionizing Dose (TID) is very large and under or over-estimation from angular variability can have a large impact on the mission and on the construction of new radiation environment models.

7.1 Objective

Since the DDH is a novel design its concept needs to be characterized, and its read-out and response validated. Calibration is also necessary, but due to the time line of the project, it was not performed at the time this thesis was written. In this chapter, the work done regarding the characterization of the DDH and the validation of its concept as a stand-alone detector and as part of RADEM, presented in two International conferences, RADiation Effects on Components and Systems 2018 (RADECS2018) and Vienna Conference on Instrumentation 2019 (VCI2019), and published in [21] and submitted for publication in Nuclear Methods and Instruments A as a special issue of the latter, as well as the overall test plan and setup preparation for the future calibration will be discussed. The work here presented was supported by the European Space Agency ESA/ESTEC 175 Contract 1-7560/13/NL/HB.

7.2 Concept

The DDH was developed specifically for RADEM to compensate for the lack of a rotating mechanism such as the used by the Energetic Particle Detector (EPD) in the

Galileo mission [13][19]. Rotating mechanisms are heavier and require power that RADEM constraints do not allow. Therefore, the development of a different solution, the DDH, was necessary. The DDH consists of a semi-torus with 4 mm inner radius and 8 mm outer radius, united with a central cylinder with 12 mm radius and 8 mm height, copper collimator, with 28 holes, or entrances, each with a radius of 0.5 mm and 8 mm of length. The holes point to four zenithal directions, 0°, 22.5°, 45° and 67.5°, and 2*9 azimuthal directions interleaved by 40° for each zenithal direction. Due to spacing constraints, the 67.5° sensors are azimuthaly phased by 20° from the 22.5° and 45° directions. By definition only one sensor pointing to the zenith exists. A schematic of the geometrical form is shown in Figure 7.1.

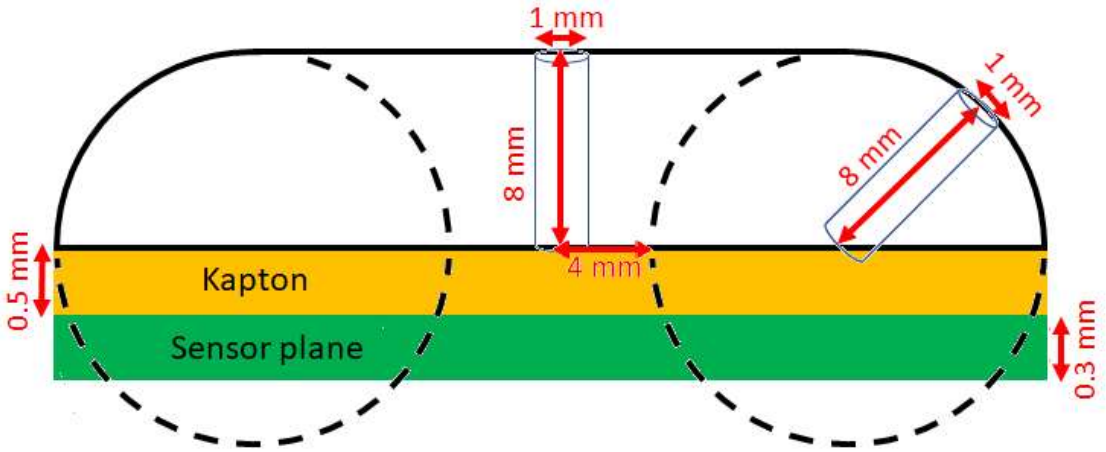

Figure 7.1: Directionality Detector Head concept cut view. The DDH is based on a semi-torus with 4 mm inner radius and 8 mm outer radius, united with a central cylinder with 12 mm radius and 8 mm height. The 28 collimator apertures corresponding to each direction are placed in away that each has approximately same length, 8 mm , and the same diameter, 1 mm . Figure dimensions are not to scale. From [21].

A thin, 505 μm thick Kapton absorber separates the semi-torus collimator and a custom-made, 31 pixel, 300 μm thick, 30 mm in diameter, n-well Silicon diode. 28 of the pixels are disposed below the Field-Of-View (FOV) of one of the collimator holes, with a geometrical area corresponding to its projection on the plane. Three extra pixels, which do not see any part of the sky, with different areas corresponding to those of the other 28 pixels, also exist in the Silicon wafer, with the purpose of measuring the particle background on a count rate basis. Each pixel is isolated and connected to one of the high-gain channels of an ASIC VATA466 [22] already presented in Section 2.5. The thickness of the Kapton absorber was selected as the CSDA range of electrons of 300 keV in that material [67]. The energy cutoff however, differs for the different directions, since the linear path length of particles incoming from steeper angles is larger. The same is true for protons which have an energy cutoff of 7 MeV. Table 7.1 summarizes the main characteristics of the DDH directions.

Table 7.1: DDH direction characteristics. From [21].

Zenithal Direction (°)	# of sensors (azimuthal directions)	Sensor Area (mm)	Energy Threshold (MeV)	
			Electrons	Protons
0	1	0.79	0.3	7
22.5	9	0.8	0.3	7
45	9	1.2	0.35	8.5
67.5	9	2.18	0.5	12.5

7.3 Proof-of-Concept

The response of the DDH to the different electron and proton fluxes expected in the JUICE mission was done at several points in its development. In this thesis, only the results of the last RADEM version, which is expected to be the flight model, are presented. The sensitivity to each direction during the phases in Jupiter was studied with Geant4 simulations. The parameters of the simulations were the same used in the radiation analysis presented in Chapter 6. The only difference was that a larger number of electrons were simulated from the top surface of RADEM with energies between 0.1 and 2 MeV to improve the statistical significance of the results. In this case, it was assumed that these electrons did not have enough energy to penetrate the side and bottom aluminum walls. In fact, according to NIST [67] the range of 2 MeV electrons in Aluminum is ∼0.45 cm while the Aluminum walls have a minimum of 0.5 cm thickness so this was thought to be a reasonable assumption. For reference, the ID of each sensor in the sensor plane color coded according to its zenithal direction is displayed in Figure 7.2.

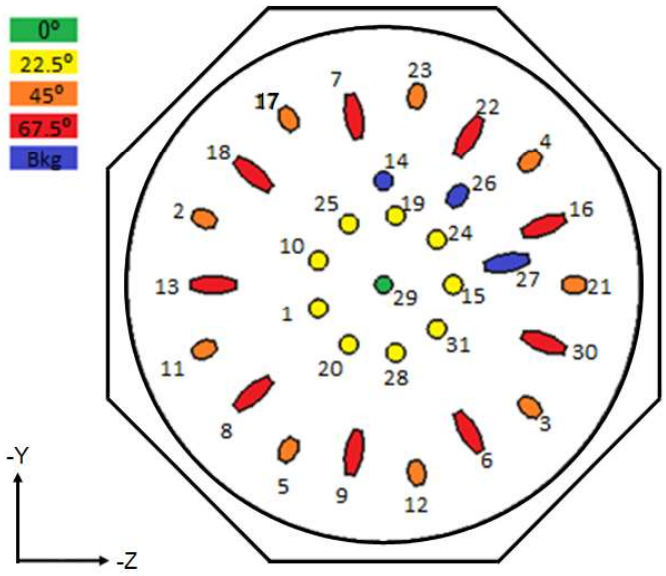

Figure 7.2: Sensor serialization. Sensors with the same color measure the same zenithal direction. The blind sensors, for background monitoring, are shown in blue. From [21].

7.3.1 Baseline Directional Response

The first step to understand the response of the DDH is to study the directional sensitivity to electrons, considering an omnidirectional, energetically flat differential flux (dN/dE=k). The four zenithal directions, 0°, 22.5°, 45° and 67.5° were analyzed independently. Figures 7.3 - 7.6 show the hit angular distribution in different energy ranges for all four directions. The background sensor (blind sensors) count rate is also shown. The results were averaged over the nine signal sensors (sensors below an aperture of the collimator) that point in each direction except for the 0° which only has one sensor. For energies higher than 2 MeV, the count rate in the blind sensors (background sensors) matches the one in the signal sensors within statistical uncertainty. This means that, it is reasonable to expect that the blind sensors will allow do discriminate the background from high part of the electron spectra. For the 2-10 MeV energy interval a smaller increase in count rate in the direction the sensors are pointed to when compared to their corresponding blind sensor exists. This is because 8 mm copper of copper can, in theory, stop electrons up to ∼10 MeV [67]. The difference actually works in the favour of the detector since it contributes positively to the signal. For energies low than 2 MeV it is clear that there is significance sensitivity in directions of interest. The sensitivity is lower for larger angles because of increase in threshold. This is more significant in non-uniform energies distributions as it will be seen in the response to the Jovian system analysis.

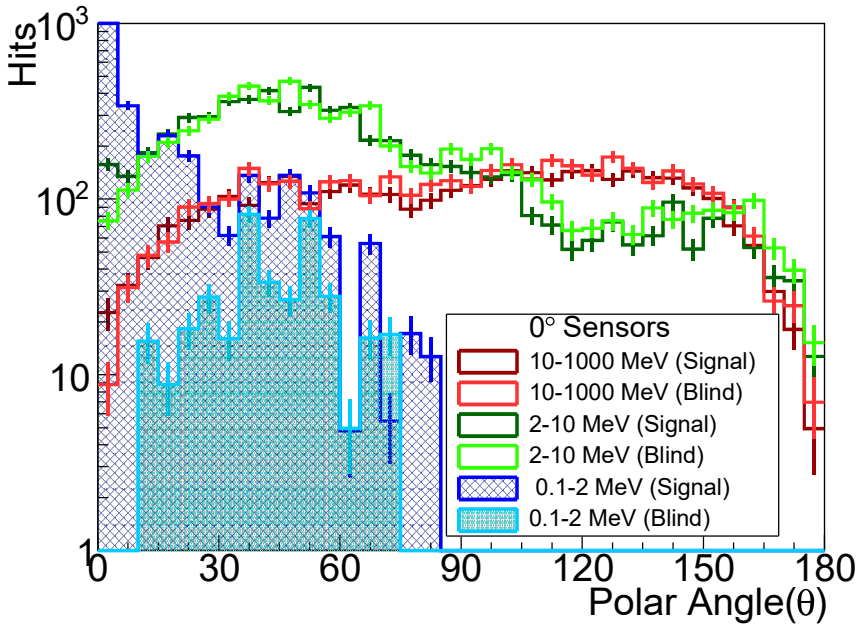

Figure 7.3: Directional response of the 0° signal sensor, and correspondent blind sensor response to electrons, for a simulated omnidirectional flux distributed uniformly in energy. Dark colors show the number of hits in the signal sensor and light colors in the blind sensor. Three energy intervals are considered, 0.1-2 MeV (blue), 2-10 MeV (green) and 10-1000 MeV (red). The number of hits in the blind sensor is in very good agreement with the response of the signal sensor for the two highest energy intervals and reasonably well for the lowest energy interval for directions outside the signal FOV. Directionality is seen only for energies below 2 MeV. From [21].

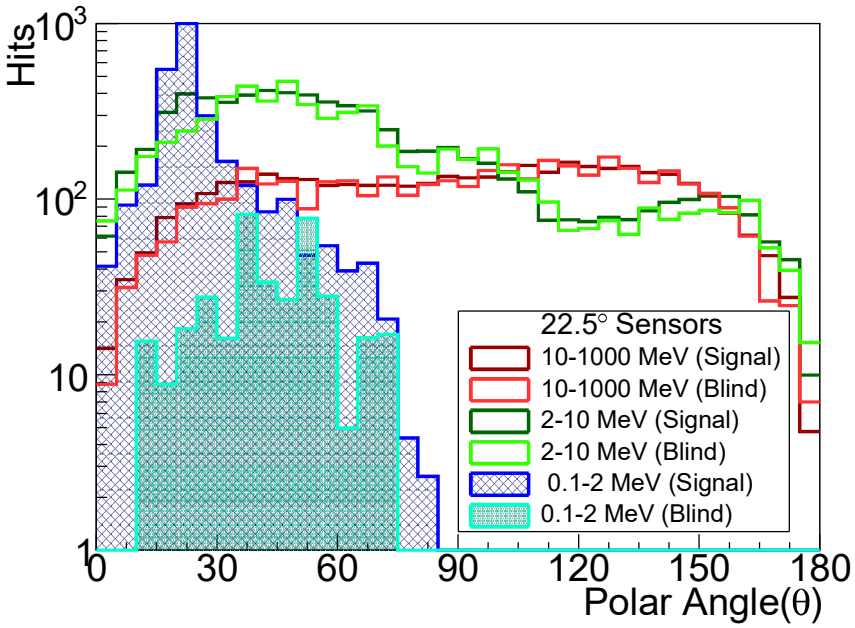

Figure 7.4: Directional response of the 22.5° signal sensors, and correspondent blind sensor response to electrons, for a simulated omnidirectional flux distributed uniformly in energy. Dark colors show the number of hits in the signal sensor and light colors in the blind sensor. Three energy intervals are considered, 0.1-2 MeV (blue), 2-10 MeV (green) and 10-1000 MeV (red). The number of hits in the blind sensor is in very good agreement with the response of the signal sensor for the two highest energy intervals and reasonably well for the lowest energy interval outside the signal FOV. Directionality is seen only for energies below 2 MeV.

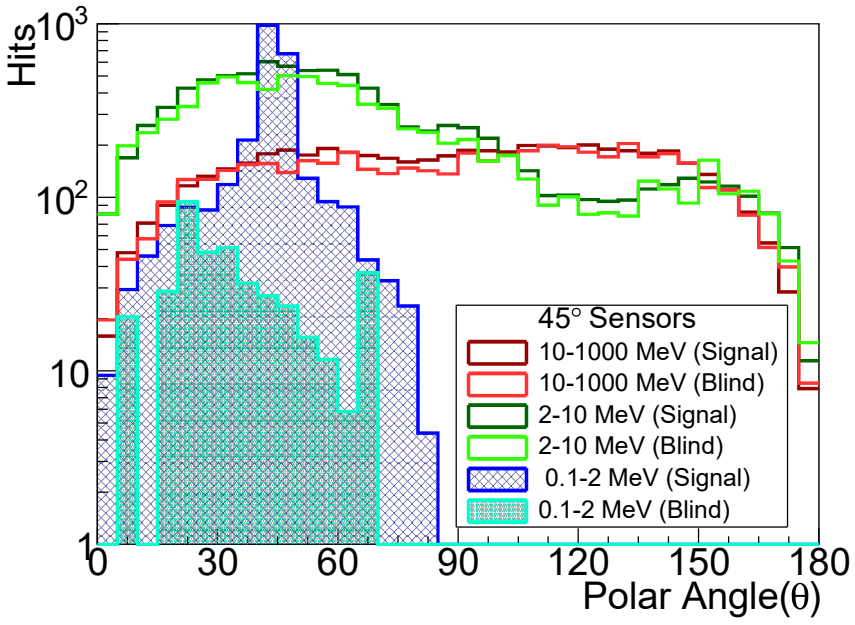

Figure 7.5: Directional response of the 45° signal sensors, and correspondent blind sensor response to electrons, for a simulated omnidirectional flux distributed uniformly in energy. Dark colors show the number of hits in the signal sensor and light colors in the blind sensor. Three energy intervals are considered, 0.1-2 MeV (blue), 2-10 MeV (green) and 10-1000 MeV (red). The number of hits in the blind sensor is in very good agreement with the response of the signal sensors for the two highest energy intervals and reasonably well for the lowest energy interval outside the signal FOV. Directionality is seen only for energies below 2 MeV.

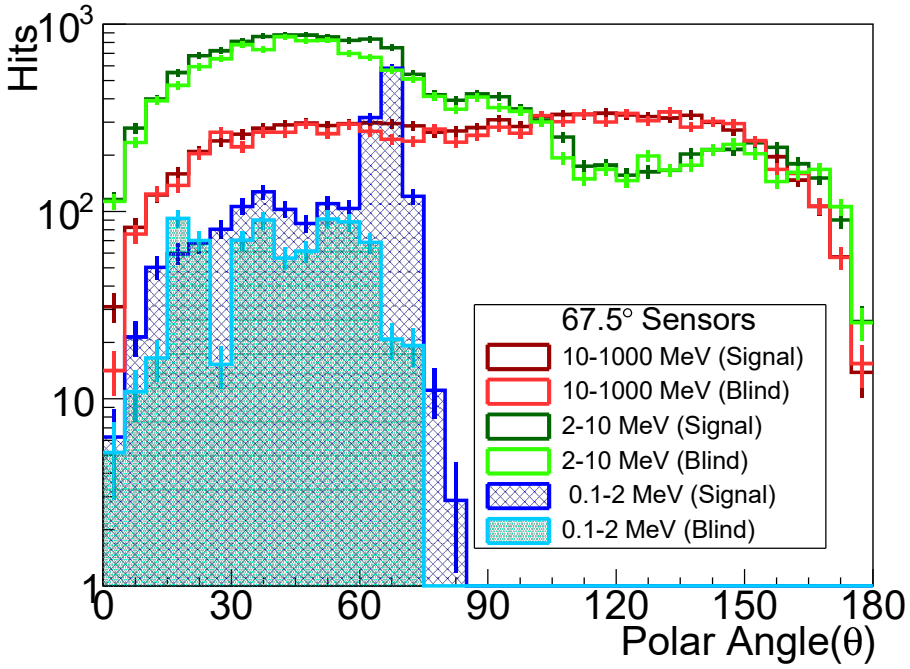

Figure 7.6: Directional response of the 67.5° signal sensors, and correspondent blind sensor response to electrons, for a simulated omnidirectional flux distributed uniformly in energy. Dark colors show the number of hits in the signal sensor and light colors in the blind sensor. Three energy intervals are considered, 0.1-2 MeV (blue), 2-10 MeV (green) and 10-1000 MeV (red). The number of hits in the blind sensor is in very good agreement with the response of the signal sensors for the two highest energy intervals and reasonably well for the lowest energy interval outside the signal FOV. Directionality is seen only for energies below 2 MeV. From [21].

Protons results are not shown here because the expected count rate expected is three orders of magnitude lower and can be discriminated by the ASIC. Nevertheless, they should be studied in more detail in the future since they are less prone to scattering and can be useful to cross-calibrate the DDH with the Proton Detector Head (PDH) [21].

7.3.2 Response to the JUICE radiation environment

Now that it was proven that the detector can differentiate between zenithal detectors in the presence of an omnidirectional energetically flat differential flux, one needs to verify if it can perform according to specification of the JUICE environment.

7.3.2.1 Count rate

The first aspect is to determine if the count rate does not surpass the ASIC specification, 1 MHz per channel for both electrons and protons. As it can be seen in Figure 7.7, this limit is not reached even in the worst-case instantaneous fluxes for all sensors. In all other phases the count rate is at least one order of magnitude lower which means that no pile-up problems are expected. Note that proton count rates are ∼3 order of magnitude lower. With this in mind, they will be neglected for the remainder of this section.

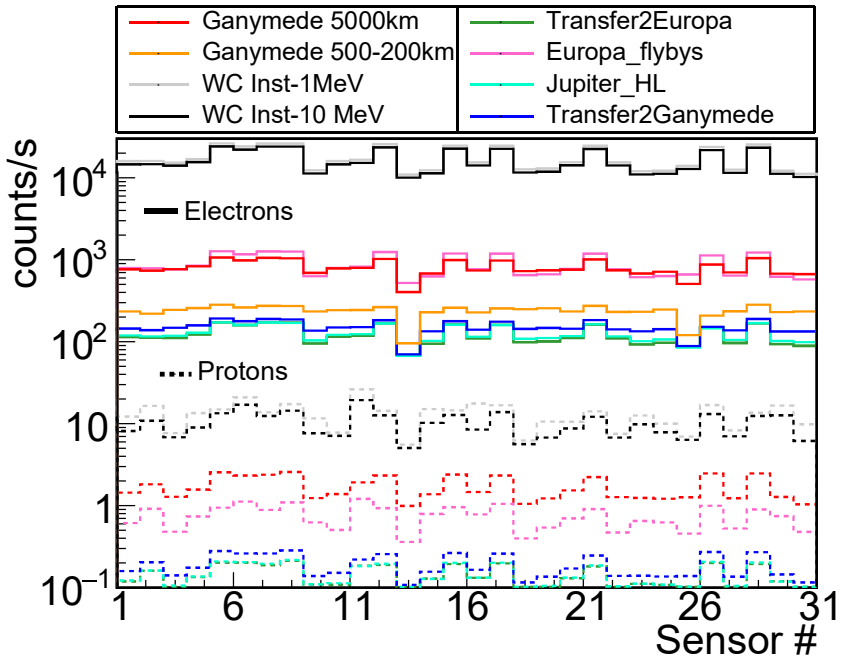

Figure 7.7: Electron and proton count rates in all 31 DDH sensors for all JUICE mission phases assuming isotropic incoming particle distributions. From [21].

7.3.2.2 Omnidirectional zenithal distribution

All phases have very different fluxes in the two energy ranges of interest, below and above 2 MeV, as it was already shown in Figure 4.19. If one considers the ratio of the total number of particles in the two energy regimes, the Europa phase presents the most challenging case since it has the larger number of electrons above 2 MeV and only the third larger number of electrons below this energy. The other phases have a much softer flux. With this in mind, only the results for Europa and Ganymedes 5000 km orbit, which has the larger integral flux, will be discussed. The count rate angular distribution for all zenithal direction and for both phases can be seen in Figure 7.8. The count rates corresponding to each direction were averaged over the corresponding nine azimuthal sensors. It can be seen that the response of each zenith angle differs, despite the omnidirectionality of the simulated electron flux. This is due to the angular dependence of the electron energy threshold set by the absorber and to the difference in the areas of the sensors, which are larger for steeper zenith angles (see Table 7.1) [21].

Though all directions are distinguishable in all phases, each direction sensitivity varies due to variability of electron spectra hardness during the mission. This can be seen when comparing phase 5a in Figure 7.8 (top) with the phase 2: Europa flybys in Figure 7.8 (bottom). In the latter, the count rate of the 45° and 67.5° signal sensors is lower than in the former. However, the opposite occurs for the 0° and 22.5° directions. The result is understandable by looking at the corresponding electron spectra. In fact, phase 5a flux is higher for energies below ∼10 MeV and is lower for energies above this energy. For the 45° and 67.5° directions, a combination of higher threshold and higher area are responsible for

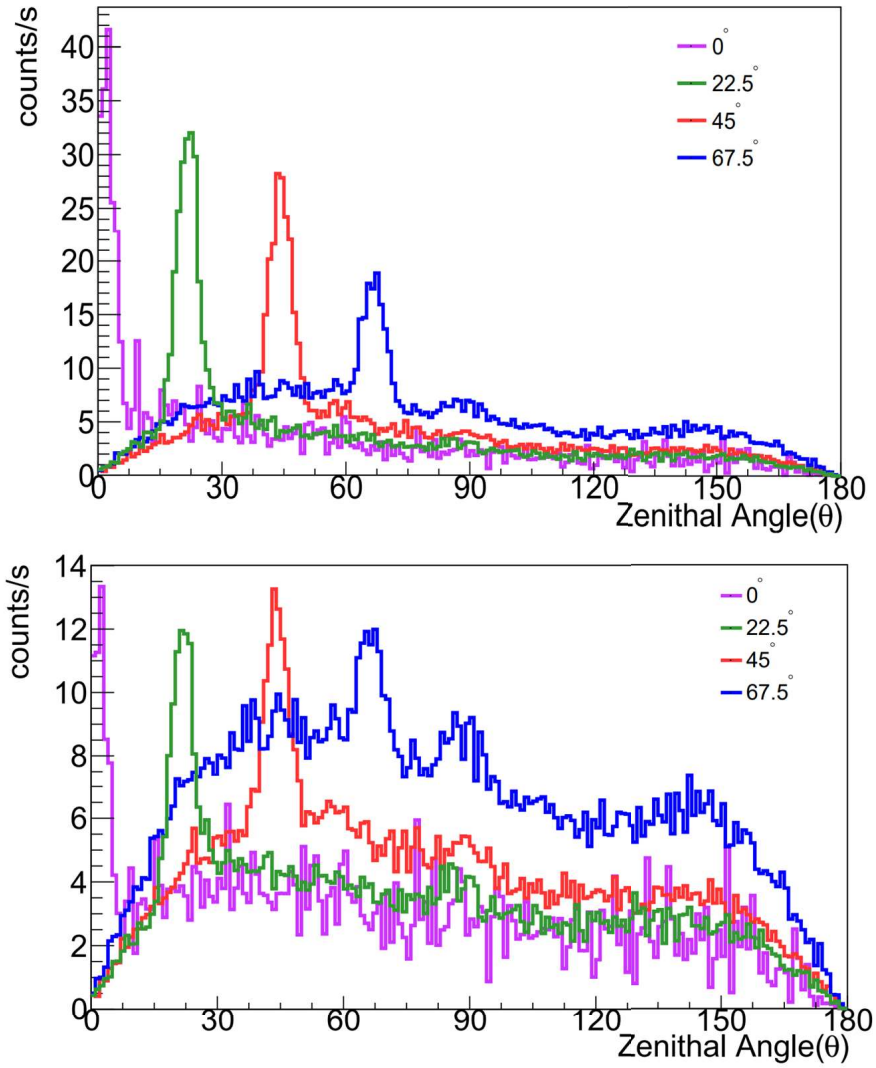

Figure 7.8: Omnidirectional response to each zenithal angle covered by the DDH for the Ganymede 5000 km orbit phase (top) and the Europa Flybys (bottom). 0° count rate accounts for sensor number 31 only. For the other directions the count rate is an average of the 9 sensors pointing in that corresponding direction. Increased threshold in steeper directions decreases count rate in the region of interest, hence lower count rate in 67.5° zenithal direction, while larger sensor area leads to increase in background. From [21].

the lower signal-to-background ratio. The same correlation can be seen in all the other mission phases [21].

To account for the different sensitivities to each direction and mission phase, the central sensor (0° signal sensor) will have to be inter-calibrated with the EDH. The two detectors will complement each other. The spectral data from the EDH will be used to calibrate the DDH sensitivity, and the DDH will correct the fluxes measured by the EDH for the angular variability of the environment. [21].

7.3.2.3 Background Removal

Given the results obtain for a flat spectrum, it is reasonable to assume that the blind sensors will correctly count the background flux of the signal sensors. To verify this, the full range count rate (0.1-1000 MeV) from the blind sensors was subtracted to the signal sensors count rate (averaged over the corresponding 9 sensors for the 22.5°, 45° and 67.5°) for the Europa phase. Figures 7.9, 7.10, 7.11 and 7.12 show the results for all angles. In all cases it can be seen that the signal sensor count rate subtracted by the blind sensor count rate for the full energy ranges is very similar to the results of the energy range of interest (<2 MeV) though some discrepancy exists. The differences are more prevalent in the 67.5° direction because of the proximity between the 45° and 67.5° signal sensors (see Figure 7.2). What happens is that particles coming from the 45° holes can easily reach the 67.5° signal sensors and vice versa. Since the 67.5° signal sensors are larger, this effect is more predominant in them [21].

Table 7.2 shows the signal-to-background ratio of the four zenithal directions for all mission phases. The signal is defined as the number of particles that hit the sensor after entering the collimator through the corresponding hole, and the background as all other particles that are not subtracted by the blind sensors. Notice that the ratios are larger in the Ganymede phases because of a combination of high flux at lower energy and low flux at higher energies. Another important result is in the Europa phase where the signal-to-background ratio in the 0° direction is high but is low in the 67.5° direction. The later is because of the particles entering through the 45° direction holes and hitting the 67.5° sensors due to the physical proximity of the sensors. The fact that Europa provides the larger fluxes are higher energies lead to this result. Although not critical, precise calibration and development of reconstruction algorithms can improve this characteristic of the detector.

Nevertheless, this method is limited by statistics only, but it is very efficient to veto electrons above 2 MeV that can go through the DDH copper collimator. This is especially true in phases where the spectrum is harder than in Ganymede, since the ratio between particles coming from outside and inside the field-of-view is larger. In these cases, the time-window for data analysis will have to be increased in order to improve signal-to-background ratios [21].

Also, it is made clear that to account for the different sensitivities to each direction and mission phase, the signal sensors will have to be inter-calibrated with the EDH measured spectra [21].

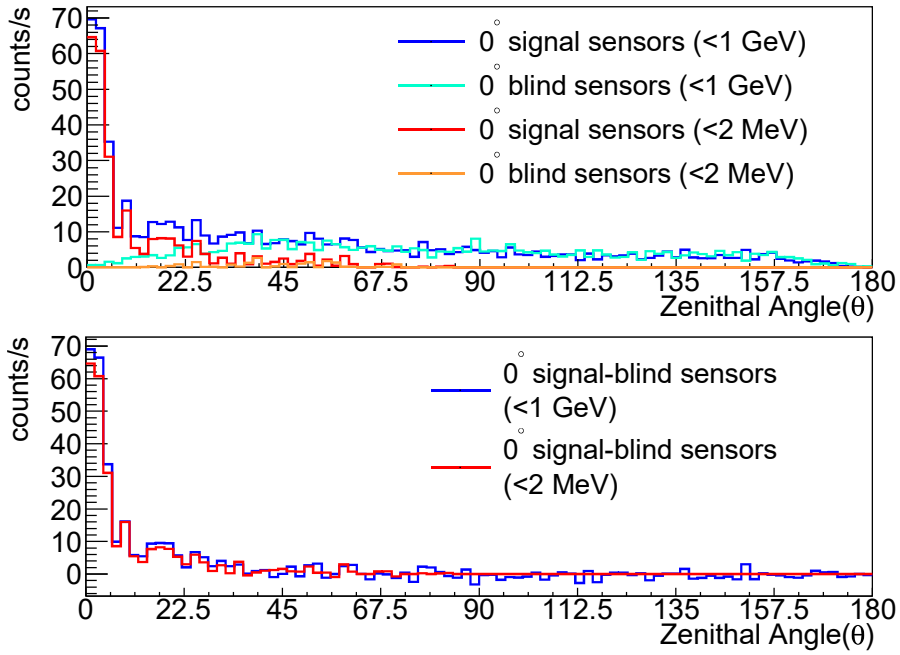

Figure 7.9: Top: Average signal sensor (light color) and blind sensor (dark color) count rates for the 0° zenith angle sensors for the Phase 5a of the JUICE mission for the full electron energy range (blue) and for electrons with energy below 2 MeV (red). Bottom: Comparison between the count rate zenithal distribution after background subtraction for the full energy range (blue) and E <= 2 MeV (red) for the same directions. From [21].

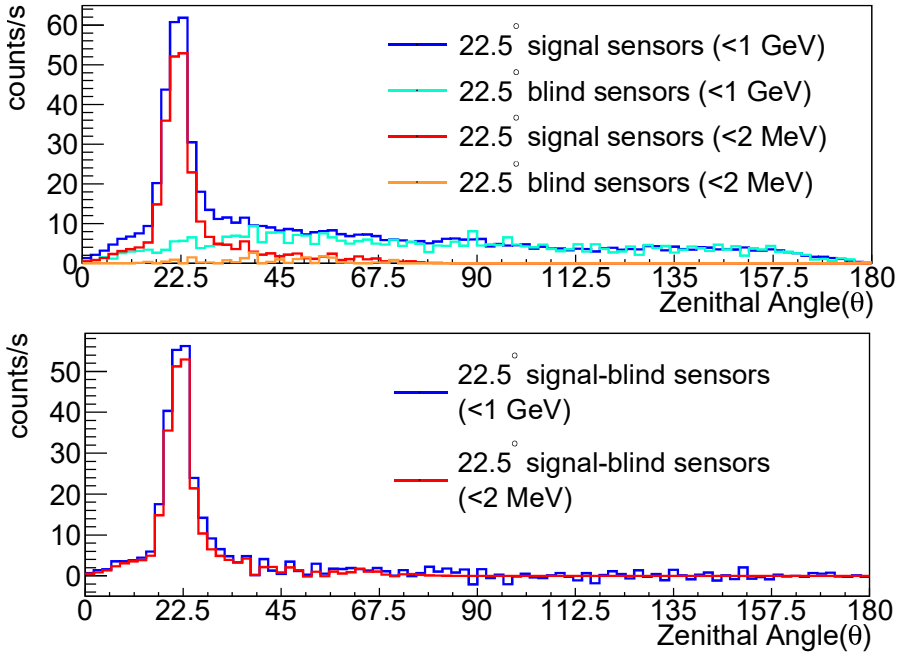

Figure 7.10: Top: Average signal sensor (light color) and blind sensor (dark color) count rates for the 22.5° zenith angle sensors for the Phase 5a of the JUICE mission for the full electron energy range (blue) and for electrons with energy below 2 MeV (red). Bottom: Comparison between the count rate zenithal distribution after background subtraction for the full energy range (blue) and E <= 2 MeV (red) for the same directions. From [21].

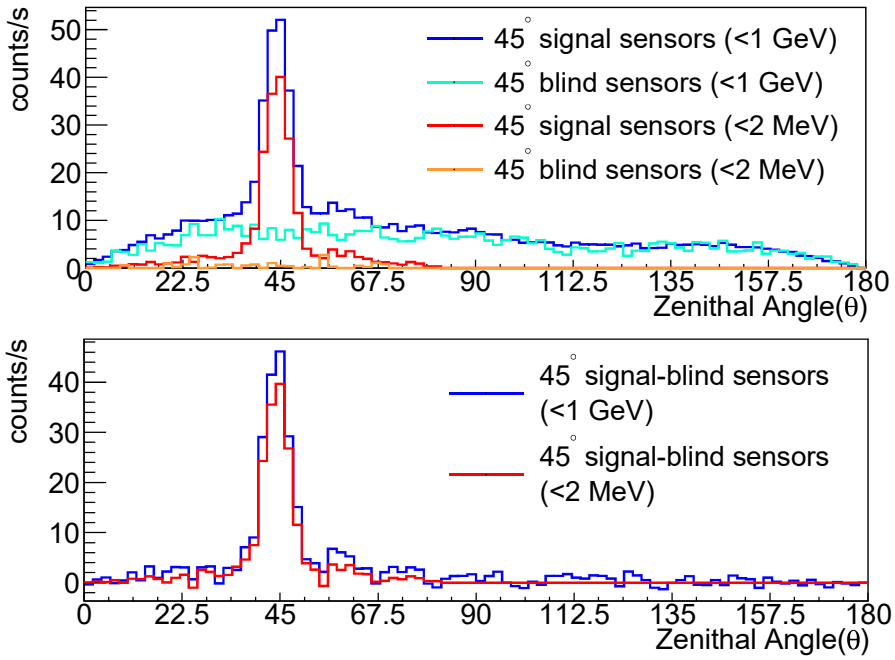

Figure 7.11: Top: Average signal sensor (light color) and blind sensor (dark color) count rates for the 45° zenith angle sensors for the Phase 5a of the JUICE mission for the full electron energy range (blue) and for electrons with energy below 2 MeV (red). Bottom: Comparison between the count rate zenithal distribution after background subtraction for the full energy range (blue) and E <= 2 MeV (red) for the same directions. From [21].

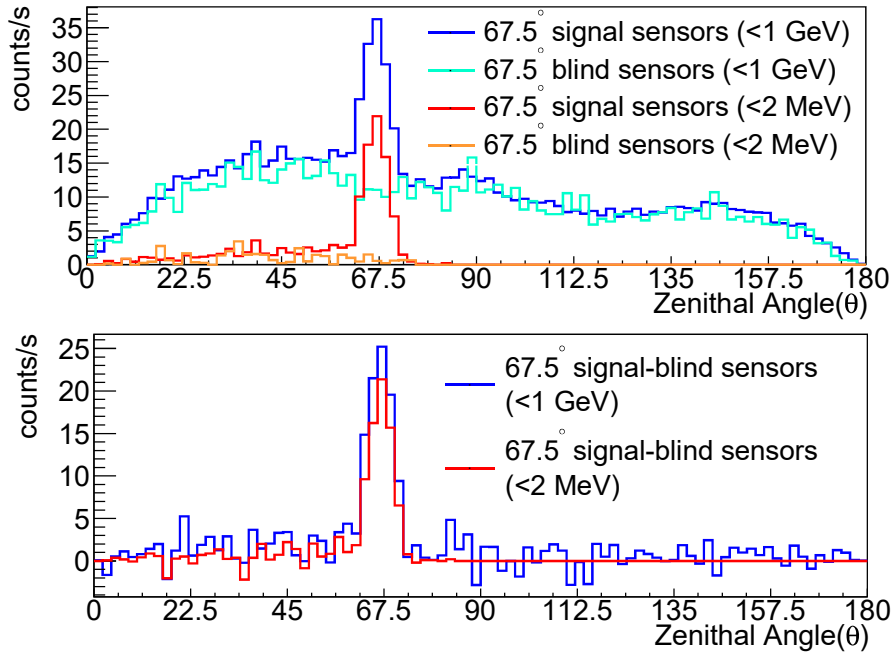

Figure 7.12: Top: Average signal sensor (light color) and blind sensor (dark color) count rates for the 67.5° zenith angle sensors for the Phase 5a of the JUICE mission for the full electron energy range (blue) and for electrons with energy below 2 MeV (red). Bottom: Comparison between the count rate zenithal distribution after background subtraction for the full energy range (blue) and E <= 2 MeV (red) for the same directions. From [21].

Table 7.2: Signal-to-Background ratio for the four zenithal directions for all phases.

Phase	Direction (°)			
	0	22.5	45	67.5
1: Transfer to Europa	4.8±0.42	4.64±0.4	3.08±0.27	1.55±0.13
2: Europa flybys	10.6±0.92	6.61±0.58	4.11±0.36	2.02±0.18
3: Jupiter high latitude phase with Callisto	5.75±0.5	6.33±0.55	4.39±0.38	2.25±0.2
4: Transfer to Ganymede	7.85±0.68	9.77±0.85	7.24±0.63	3.82±0.33
5a: Ganymede 5000km altitude circular orbit	16.4439±1.43	19.38±1.69	13.83±1.2	7.21±0.63
5b: Ganymede 500km altitude circular orbit	11.24±0.98	15.1375±1.32	11.97±1.04	6.55±0.57

7.3.3 Readout Validation

Another aspect of proof-of-concept was to validate the sensor and readout technologies both custom-made for RADEM. This was done in May 2017 by irradiating the DDH sensor plane coupled to a VATA466 ASIC [22] and performing low threshold scans for two proton energies, 42.8 and 62.7 MeV, and two electron energies, 0.68 and 82 MeV, at the Paul Scherrer Institute (PSI). The experimental setup at the PiM1 line is shown in Figure 7.13 where the proton and higher energy electron tests were done. The central diode in the sensor plane was aligned with the beam line. The beam profile was approximately homogeneous in an area larger than the sensor plane [21].

Since at the monochromator with electron energy of 0.68 MeV, the beam has an area smaller than the plane, only the central pixel was analyzed so far in order to study full energy range response [21].

The results of the scans for the central diode compared to Geant4 simulations of mono-energetic, uniform proton and electron beams are shown in Figure 7.14. Although it was not possible to perform measurements with a threshold below 4 fC because of noise issues it was shown that it is possible to discriminate protons from electrons. This is not true for high proton energies since they deposit less energy in the sensors but their flux will also be much lower. Even if the fluxes are higher than predicted the discrimination capabilities of the ASIC will allow to veto a large part of it while the background sensors can help to account for the high energy protons [21]. The fact that over 30000 counts per second were measured without reaching saturation is also important since it was shown that in worst-case flux conditions, where each signal sensor may reach 10000 counts per second, the sensor-ASIC coupling can then be used without expecting pile-up.

It can also be seen in Figure 7.14 that the experimental results are in good agreement with Geant4 simulations of the setup. They also show linearity between threshold and energy (deposited energy in the simulations was converted by assuming a 3.6 eV average electron-hole pair creation in Silicon and 100% efficiency), but calibration of the flight

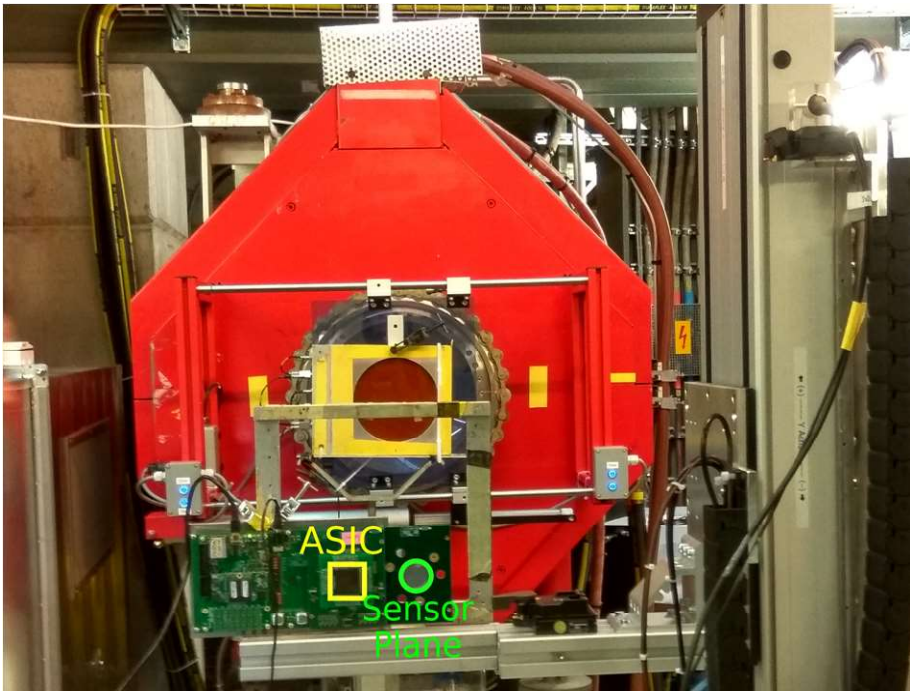

Figure 7.13: Experimental setup at PiM1 line. The sensor plane and the ASIC are highlighted in green and yellow respectively. From [21].

model is still critical to the development and future measurements [21]. At this point, there is a high level of confidence that the DDH concept is suitable to measure the electron flux variability in Jupiter in combination with the EDH.

7.4 Functional tests of RADEM Engineering Model

Another battery of tests was done to RADEM Engineering Model (EM), showed in Figure 7.15, with the purpose of identifying possible issues that may need correction in the Engineering Qualification Model (EQM) and Flight Model (FM). These tests consisted mostly in showing the overall functionality of RADEM and of the ASIC. Given that all detector heads have the same principle, a set of Silicon diodes connected to a VATA466 ASIC, it was not considered necessary to fully characterize all detectors at this stage. Different tests, separated into four categories, were done to the four detector heads: energy response of Low Gain and High Gain channels; flux scaling; coincidence logic functionality; and DDH sensor alignment.

The High-Gain channels and the coincidence logic were tested with the EDH since it had less noise than the PDH. The Low-Gain channels were tested with the HIDH since it is the only detector connected to them. Due to some issues with the top diode, only the bottom one was tested in this case. The response of the ASIC to a flux scaling was done with the DDH since multiple diodes could be tested at the same time.

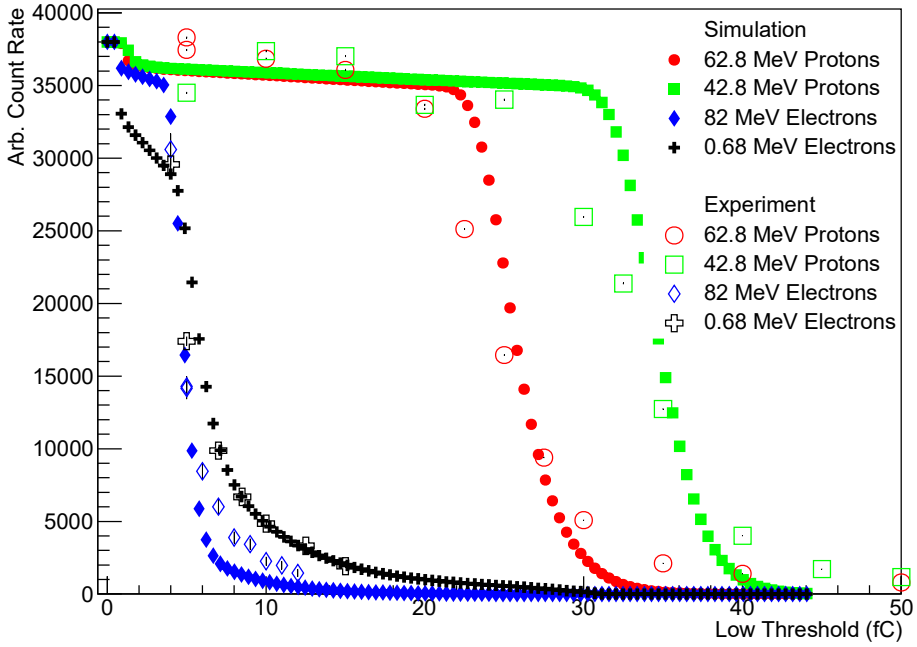

Figure 7.14: Low threshold scans in the central diode under four different beams, 62.8 MeV and 42 MeV proton beam and 86 and 0.68 MeV electron beams. Noise issues limited threshold only down to 4 fC (40DAC). From [21].

7.4.1 Energy response

The High-Gain channels of the EDH were tested with a point-like ^{90}Sr source that emits β^- particles with a continuous spectrum up to 2.3 MeV, a flat ^{137}Cs source which emits 662 keV gamma rays, and a 100 MeV parallel proton beam. The first two tests were done with the sources placed right on the top of the EDH collimator and the beam tests were done with the beam centered on the middle of the EDH top sensor. The three test results are shown in Figures 7.16, 7.17 and 7.18 respectively. Diodes are identified as D1, D2..., D7, D8 where D1 is top diode and D8 the bottom one. In all tests only the Low Threshold (LT) was scanned while the High Threshold remained disabled.

The ^{90}Sr test results showed significant count rates in the top three diodes and no counts in the other five. This is because the electrons lose energy in the absorbers between the diodes and the diodes themselves (see Section 2.5), and do not cross all the EDH diodes.

The ^{137}Cs are highly penetrating reaching all the diodes. The only issue is that the source used had low activity and not much time could be allocated for these tests. Nevertheless, particle counts were observed in all the diodes. The difference in count rate can be explained by the larger distance of the deeper diodes in the stack to the source, and to their smaller solid angle with respect to the source.

The protons tests were done at 200 MeV, an energy that allow to observe the peak of the energy distribution in all diodes. The peak can be seen at increasingly larger thresholds in Figure 7.18 because of the proton energy loss as it goes through the stack. The count rate decreases further into the stack because of the smaller solid angle and to

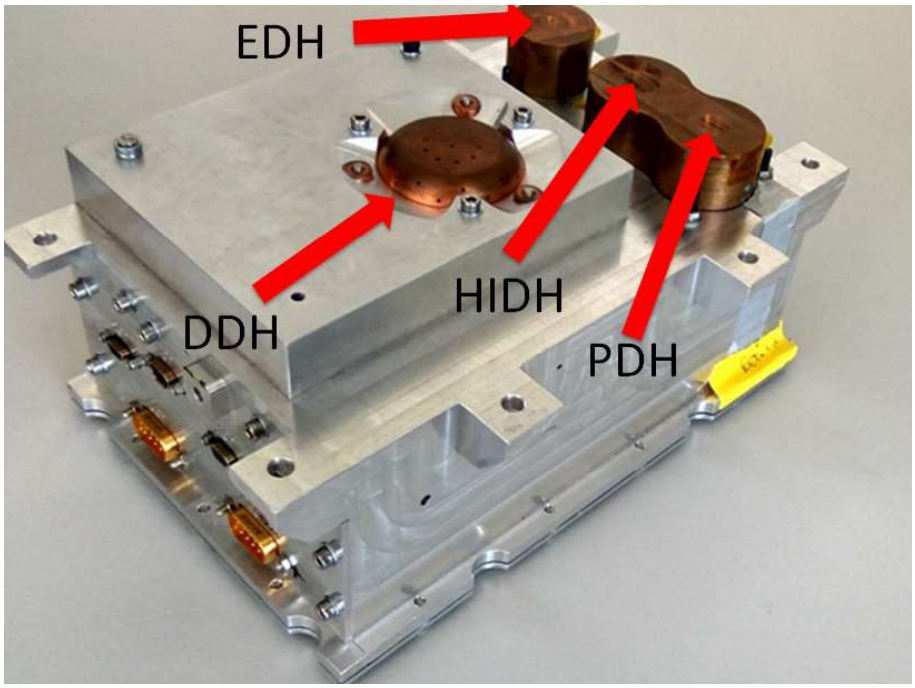

Figure 7.15: RADEM Engineering Model. The four detector heads: EDH; PDH; HIDH and DDH are indicated in the picture.

the scattering of the protons. The only exception is the top diode which has an area four times smaller than the others. These results show that the High-Gain channels work as required. In the future, these results will be compared to Geant4 simulations in order to obtain the full response function of the detector.

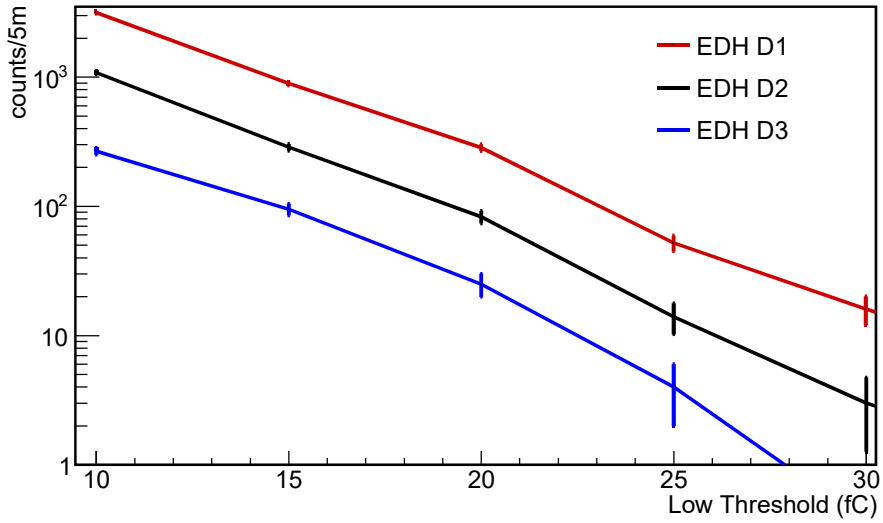

Figure 7.16: RADEM EDH response of the three top diodes to the ^{90}Sr electron source.

The Low-Gain channels on the other hand had to be tested with the HIDH. Since the proton energies available were not sufficient to reach the Landau peak in these channels (200 MeV protons were used), the beam was point to the side of the diode in order to try to increase the deposited energy of the protons. However, as it can be seen in Figure 7.19,

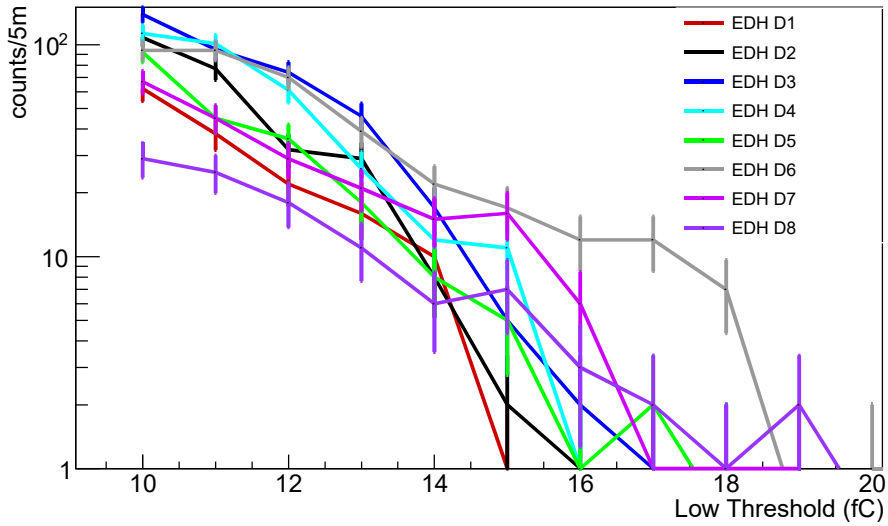

Figure 7.17: RADEM EDH Low Threshold scan of all eight diodes to the ^{137}Cs gamma source.

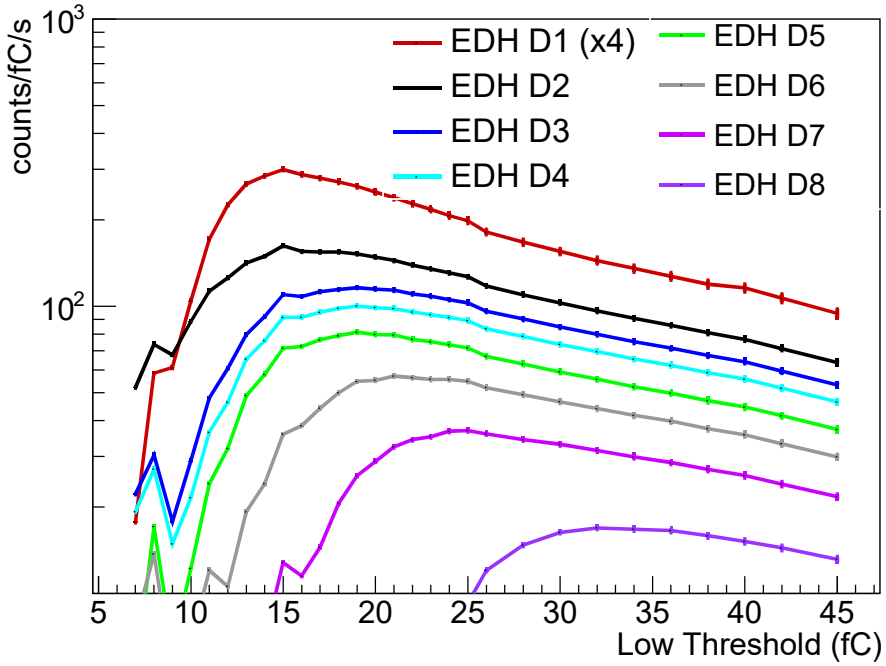

Figure 7.18: RADEM EDH LT scan with a 100 MeV proton beam. D1 counts are multiplied by four, the ratio between the area of the top diode (D1) and the other seven diodes (D2-D8) for visualization purposes only.

this was not sufficient. Nevertheless, particles were clearly observed and the functionality of the Low Gain channels was confirmed.

7.4.2 Flux Scaling

In DDH sensor plane coupling to the ASIC tests, it was already shown that the maximum count rate for the mission can be measured without pile-up (for the DDH). Despite this, it is also necessary to show that the count rate has a linear relationship to the flux.

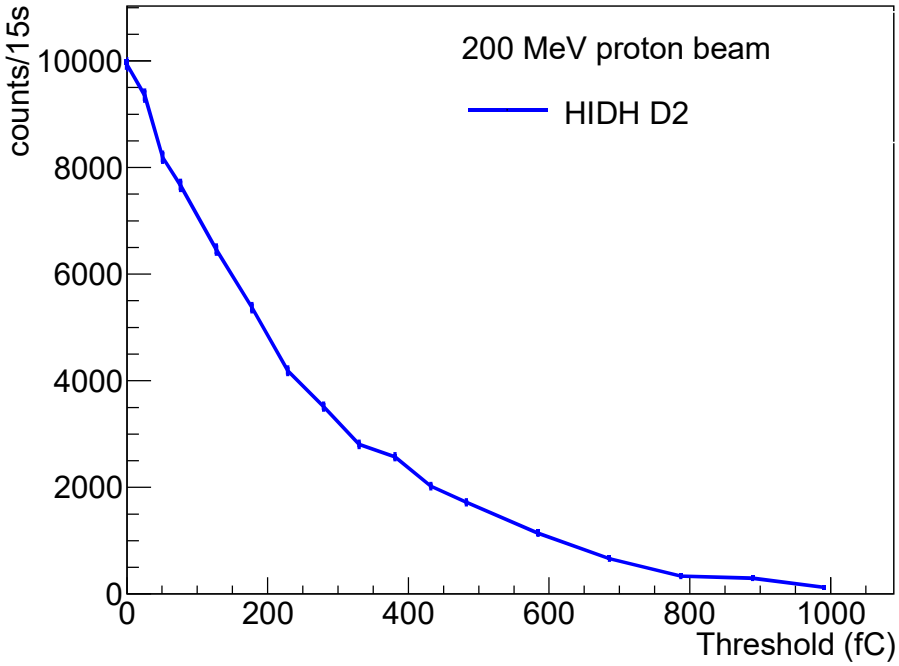

Figure 7.19: RADEM HIDH response to the 200 MeV proton beam.

This was done with a 200 MeV proton beam aligned with the DDH central sensor at three different flux leves, 2.28E+4, 4.56E+4 and 22.8E+4 particles/cm^2/s. The energy of the protons was high enough for them to fully cross the copper collimator and still deposit enough energy in the sensors. The DDH was used because it allowed to test several channels at the same time. The results of the irradiation, presented in Figure 7.20. As it can be seen, the count rate increases linearly with the flux for all diodes. The flux was not increased to higher levels to avoid activation of the copper collimators which would delay transport of RADEM to other experimental setups. This was not an issue because it had already been proven that pile-up does not occur up to flux magnitudes predicted for the mission.

7.4.3 Coincidence Logic

The last topic of ASIC functionality is the coincidence logic. To measure the energy of electrons (EDH) and protons (PDH), a coincidence channel must be able to determine the passage of a single particle in more than one diode within a predefined time interval. The depth of the inner-most diode where the particle deposited enough energy to trigger the readout channel, translates into an energy bin. For this reason, it is necessary to verify the capabilities of the ASIC coincidence channels, for different Mono-stable Coincidence Times (MCT).

Coincidence tests were done on the EDH with the same point-like ^{90}Sr source used to scan the Low Threshold of the ASICs. This was tested on the EDH for the two first diodes (as it was seen in Figure 7.16, electrons of these energies can only travel up to the third diode and only with low statistical significance). Three logic channels were selected:

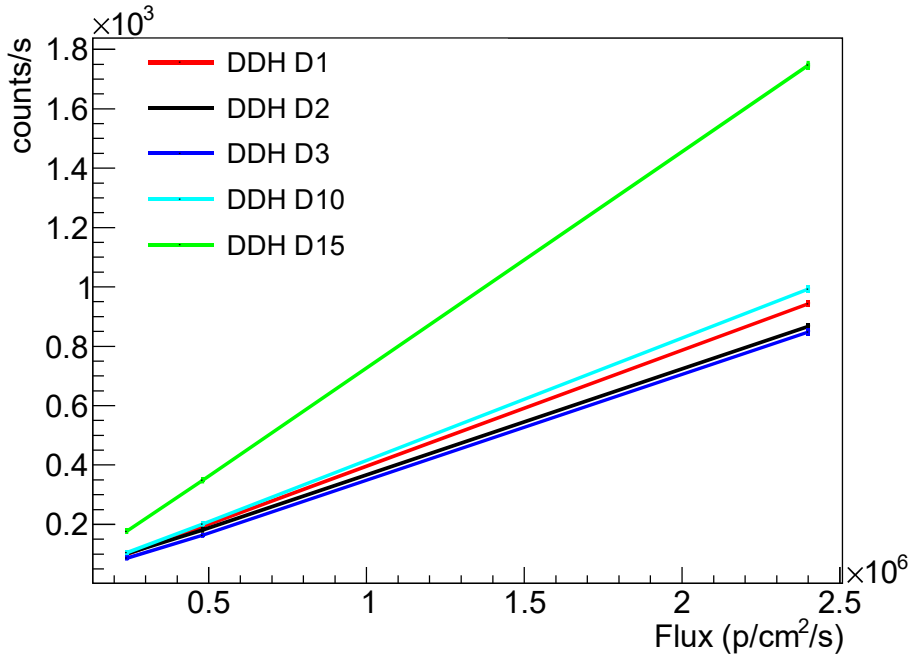

Figure 7.20: Flux scaling response of several DDH pixels. Count rate in all channels increased linearly with the flux as required.

D1 only; D2 only; and D1+D2. The Low Threshold was 6 fC in all channels and the High Threshold was disabled.

The results of the three channels are shown in Figure 7.21. It can be seen that the count rate in both D1 and D2 single channels has a very small, neglectable, dependence on the MCT. The coincidence channel shows increasing count rate from 50 ns to 300 ns. For higher MCTs it remains stable. This happens because of the front-end readout electronics which needs time to collect the charge from the interactions. This MCT is enough to guarantee a count rate of up to 3.3 MHz, which is much higher than the specification. Even if one assumes a worst-case 500 ns MCT the available count rate is 2 MHz so no issues are expected from this higher MCT values.

The results also show a large difference between the count rates in the second diode alone and the coincidence channel. Ideally, without background, the two should be the same. The reasoning behind this result is that it is a direct consequence of the energy cuts. For a particle to trigger a count in D2, it has to lose an amount of energy larger than the cut assigned to that channel. For the same particle to trigger the coincidence channel this must be true in both D1 and D2. Assuming the same trigger probability, P_t, that an electron loses enough energy to be counted, then the probability that there is a trigger in the coincidence channel is P_t^2. If there is no energy cut then P_t=1 and no difference in count rate exists between the second diode channel and the coincidence channel. By increasing the energy cut, P_t decreases and the ratio between D2 counts and coincidence channel counts also increases.

To assess the influence of the energy cut, a Geant4 simulation was done with the same RADEM model used in the proof-of-concept characterization. The only difference

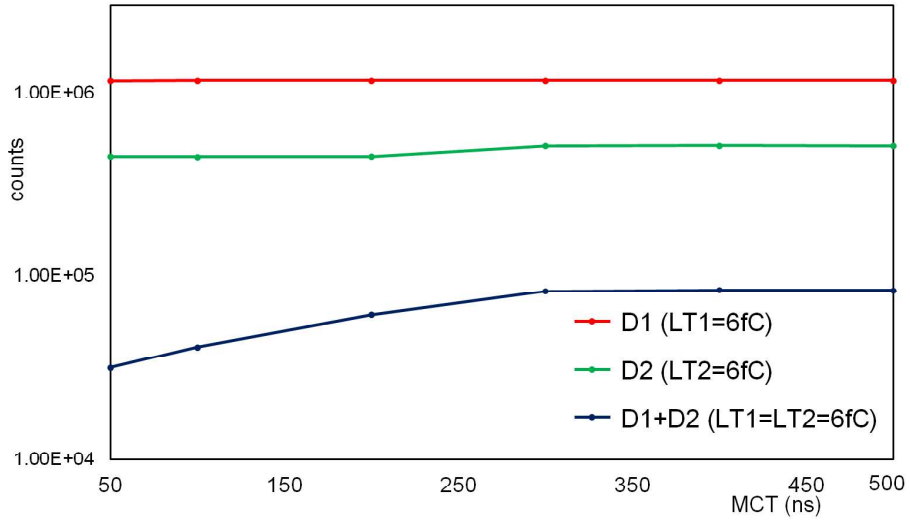

Figure 7.21: Total counts in D1 (red), D2 (green) and D1+D2 (blue) with to a ^{90}Sr source placed on top of the collimator for different MCT.

was that the source was defined as the ^{90}Sr decay spectrum. The number of events where electrons interacted with each of the two sensors, individually and together, was registered as a function of the deposited energy as it can be seen in Figure 7.22. As expected, the difference between the two channels increases with the energy cut. At 6 fC, approximately 0.12 MeV , the difference between the two is similar to the one obtained in the experimental data which not only reinforces the hypothesis, but also confirms the functionality of the ASIC logic and the modeling of the EDH in RADEM.

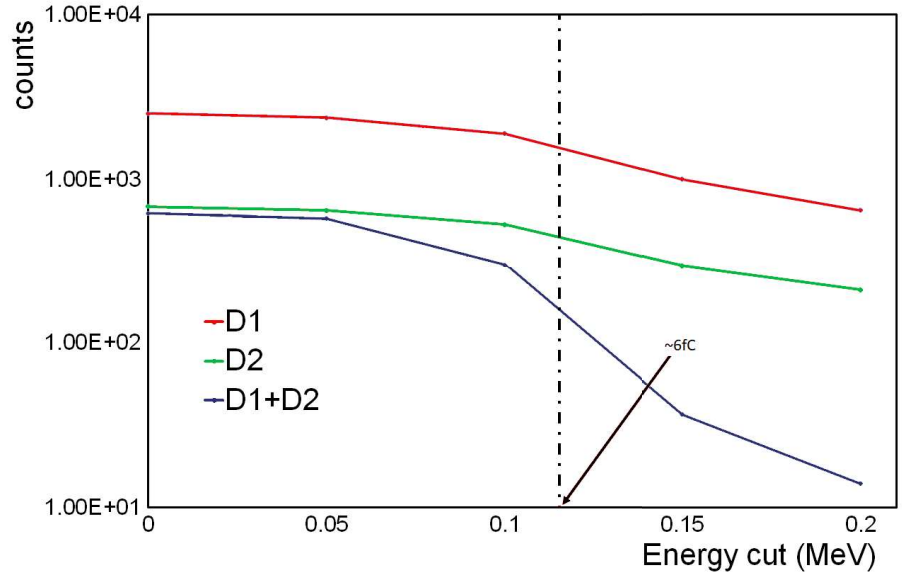

Figure 7.22: Count rate as a function the deposited energy in the top diode (D1), the second diode (D2) and in both diodes (D1+D2).

All tests regarding the ASIC, despite being done on other detector heads, are also

valid for the DDH. The ASIC readout and the sensor plane are therefore fully validated requiring only calibration in the EQM and the FM.

7.4.4 Directional Detector Alignment

The DDH also demands physical validation. The large number of apertures in its small collimator must be well aligned with the sensors below. This is critical for the correct measurement of all directions. In the Engineering Model an experimental setup was designed and tested in order to verify the alignment between the apertures and the sensors.

The setup consisted of mounting the ^{90}Sr source in a XY mechanical table, as close to the DDH collimator as possible, and registering the count rate in all sensors for different source positions. The source was mounted on the table because it is much smaller and lighter than RADEM and therefore easier to manipulate. The setup is shown in Figure 7.23. The Low Threshold was set to ∼10 fC in all 31 diodes to avoid decrease the noise. The value was high which meant that the sensitivity was much lower than the ideal scenario (peak deposited energy corresponds roughly to 5 fC). Despite the loss in sensitivity, the signal was clear without any need to study the noise in the channels. High Threshold was disabled for all channels.

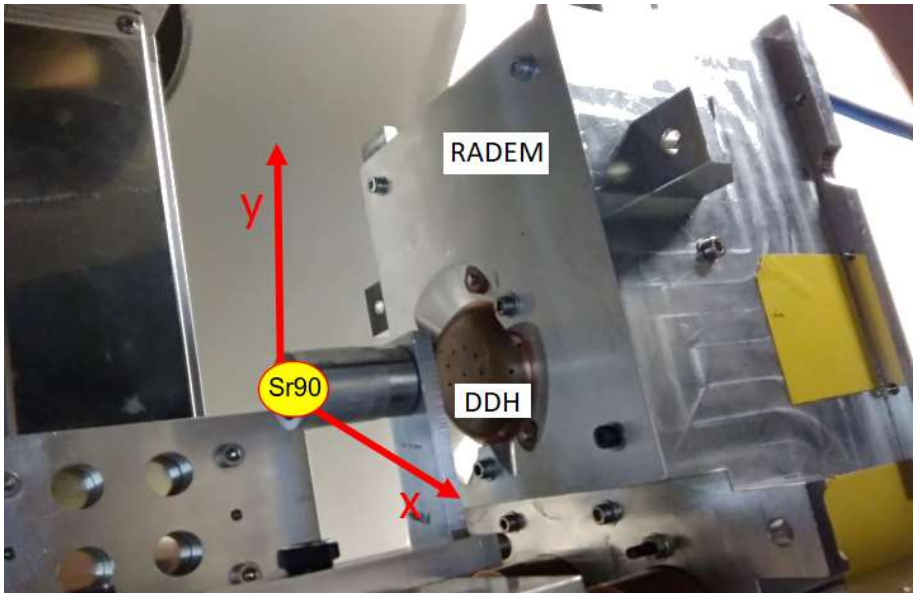

Figure 7.23: DDH alignment setup. The source was mounted on a XY table as close as possible in order to scan the count rates in all sensors for different source positions.

Although there was no angular degree of freedom, the source was always pointing in the same direction in relation to RADEM, the plane where the source was moved on, fully contains the projection of the FOV of each aperture in the same way that the sensors areas are the projection of the FOV in the sensor plane. The only limitation of this approach was that the source is slightly collimated (no precise information of the collimator is available) which makes it inefficient/impossible to test the 45° and 67.5° angles this way.

Nevertheless it was used to assess the potentiality of the setup. The results of the scans for the central diode (0°) and one of the 22.5° diodes are shown in Figure 7.24. The active area is relatively larger than the diodes areas and is directly related to the source distance. Although this distance could be measured because of the geometry of the source, it can be estimated knowing the distance between the maximum of the XY scans in both sensors and the sensor distance and the angle between the entrances. The distance from the source to the sensors was estimated as ∼33 mm , and used to simulate the setup with Geant4.

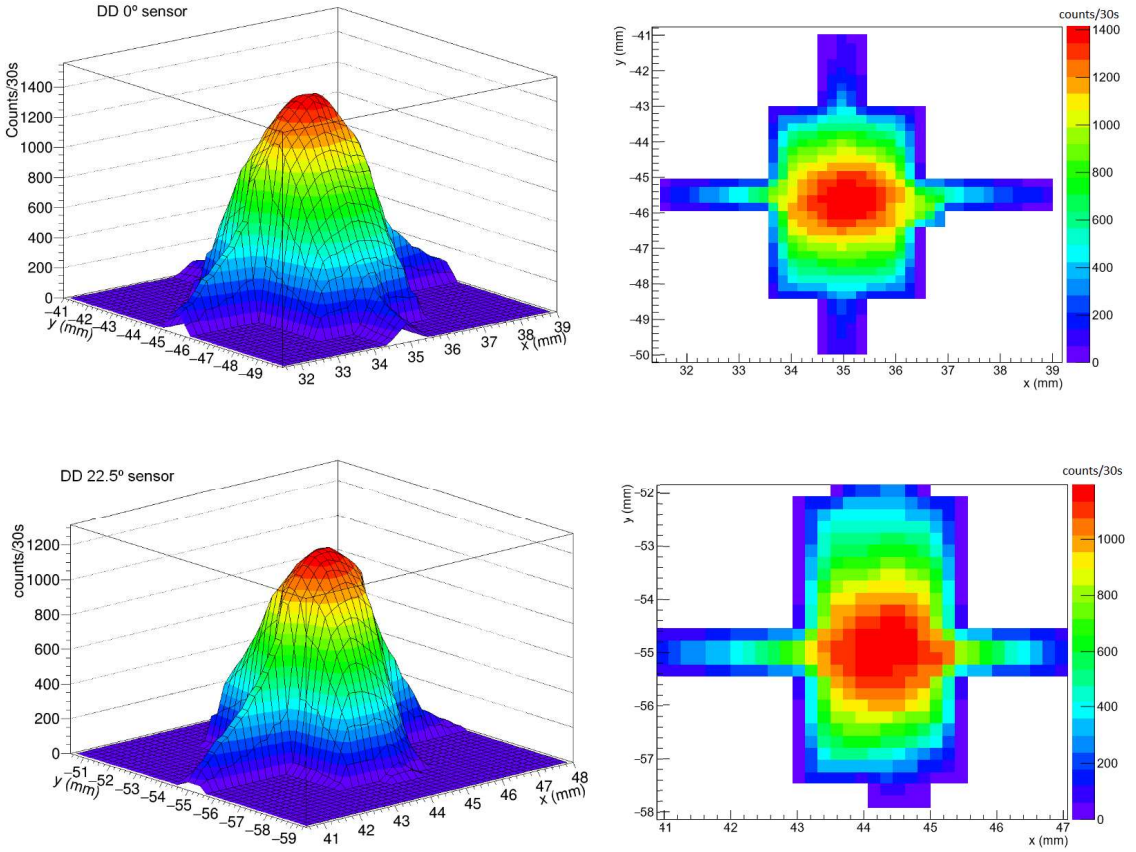

Figure 7.24: DDH 0° (top) and 22.5° (bottom) sensors XY scan 3D (left) and planar (right) intensity maps.

The Geant4 simulations were done with the final RADEM model and a ^{90}Sr point-like source, 33 mm away from the sensors (25 mm from the copper collimator). A full scan of 0.5 mm steps in the X and Y was done to simulate what was done experimentally. The comparison between simulation and experimental data of the X and Y maximum count rate row is shown in Figure 7.25. A 0.5 mm uncertainty was assumed for the experimental scan because there was no accurate way to center the source with the center of the DDH. The results show very good agreement between the results which leads to conclude that there is good alignment between the collimator and the sensor plane. However, this was done to a sub-set of the sensors only and does not validate the full detector. For the EQM and FM the alignment of all sensors with their respective collimator holes must be tested.

The method was limited by the point-source aperture. For the RADEM EQM and

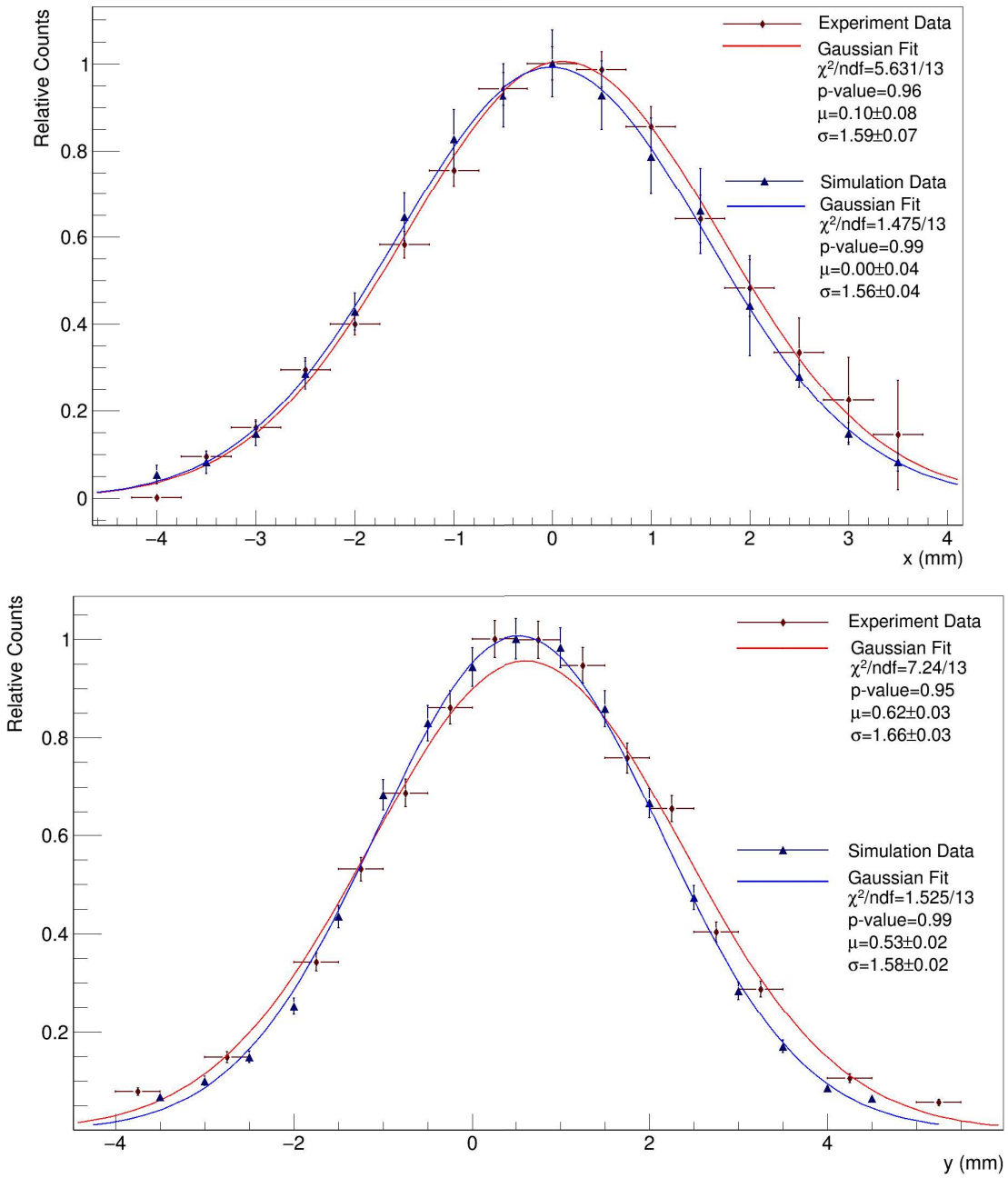

Figure 7.25: Geant4 simulation comparison to the experimental data of the DDH alignment tests. Gaussian fits were done to the X (top) and Y (bottom) scans with the highest number of counts. Experimental data closely matches simulation in both cases with geometrical uncertainties, such as detector tilting, responsible for the differences.

FM a new platform for the source is being designed. The platform must allow to position the source in the four zenithal directions, 0°, 22.5°, 45° and 67.5°and in all azimuthal angles. This can be done with a 360° rotating wheel with four supports corresponding to each of the zenithal directions. At the time this thesis was written this was still under development and no tests were done.

7.5 Discussion

In this chapter, all the work done regarding the development of RADEMs Directionality Detector was presented. The Directionality Detector is a fundamental piece of the radiation monitor that will allow to correct for the angular variability of the electron population in the Jovian system. It is a low mass, low power detector that will measure 28 different directions in a FOV close to half the sky.

The DDH sensitivity to incoming electron directions was studied for each JUICE mission phase, before and after background subtraction, based on the blind sensors count rates. A good discrimination between electron directions, particularly below 2 MeV, is obtained for all mission phases, especially after applying the background reduction technique, which is particularly useful for steeper zenithal angles. However, this technique does not consider the cross-contamination from particles coming through the 45° collimator apertures FOV and hitting the 67.5° signal sensors. Due to the varying sensitivity of the DDH between mission phases, a conseguence of the absorber and sensors single plane geometries, and to the variability in the electron spectral hardness, cross-calibration of the central DDH diode and the EDH needs be performed in order to calibrate the directionality response [21]. Also notice that the response of the DDH was obtained always assuming an omnidirectional flux. However this is not what is expected (if it was there would be no need for the DDH). The next step in the characterization will be model the angular dependence of the fluxes and use multivariate techniques to reconstruct them. The degree of precision must also be addressed.

Another important aspect of the proof-of-concept was to validate the sensor plane coupling to the ASIC and study its response to radiation. This was done with both electrons and protons. The results obtained showed that the detector will be able to differentiate electrons from low energy protons at a rate above the one that was estimated for the worst-case conditions in the Jovian system. The results were comparable to those of Geant4 simulations which increased the level of confidence in the functionality of the detector. For high energy protons this does not occur because their energy loss in Silicon is similar to electrons. However their flux should be low enough that they are neglectable. The blind sensors can also be used to count the high energy proton flux that can cross the materials in RADEM.

The ASIC was also tested already integrated in the RADEM Engineering Model. A large battery of tests was done to the three ASIC copies that are used in RADEMs detector heads. RADEM showed sensitivity to electrons, gammas and protons of different energies. Threshold scans showed the capabilities of both Low-Gain and High-Gain channels as well as the coincidence logic. The logic was shown to be dependent on the Mono-stable Coincidence Time (MCT) and to the energy cut (threshold) of the channels. Operation considering a 300 ns MCT should be sufficient to collect the charge in two channels working in coincidence mode without compromising the worst-case count rate. Sensitivity of the detectors will be highly dependent on the energy cut which should be kept as low as

possible especially if the coincidence is made between more than two channels.

Finally the mechanical alignment between the DDH collimator and its sensor plane was tested. This was done with a simple setup that must be upgraded for the full calibration of the Engineering Qualification Model and the Flight Model. Nevertheless, it was possible to show good alignment of the 0° sensor and of a 22.5° sensor. The results were compared to Geant4 simulations which showed very good agreement with the experimental data. The alignment is critical for the function of the detector and special attention will be given to the calibration of the future models.

The overall performance of the DDH is according to mission specification and will be an essential asset for both house-keeping and scientific analysis. Its concept is now fully validated. Calibration and development of algorithms for flux reconstruction should be done in the next year. Opportunities for early flights and studies of its capabilities to measure other environments and cross-calibrate it with other radiation monitors such as the ones in Earths radiation belts will also be addressed.

8 Conclusions and Future Work

The work presented in this thesis was developed in the framework of two ESA contracts: "RFQ/3-13975/13/NL/PA" - Verification of ^{60}Co Testing Representativeness for EEE components flown in the JUICE mission; and "1-7560/13/NL/HB" - Radiation Hard Electron Monitor (RADEM), for the same mission. The work was involved on almost all aspects of the Radiation Hardness Assurance process of RADEM and JUICE, as well as of future missions to Jupiter. It also addressed computational methods for the assessment of the radiation levels in complex geometries and for the characterization particle detectors, namely the development of the Directionality Detector.

The first aspect of Radiation Hardness Assurance process studied was the validity of ^{60}Co tests, as the worst-case radiation condition for components used in the Jovian environment. These tests were done due to current indications that these standard tests could under-estimate the effect of high energy electron environments (when compared to Earth) on semiconductor components. A large irradiating test campaign was done on several discrete and Integrated Circuit (IC), MOS and Bipolar technologies, with ^{60}Co at high and low dose rate, and 12 and 20 MeV electron beams at high dose rate. The effects from all irradiations campaigns were then compared. The tests were successful in showing that ^{60}Co testing is comparable to 12 and 20 MeV electron irradiation for all tested components. Only LM124, an operation amplifier, showed enhanced damage on three parameters, the $\pm$ bias currents and the common-mode rejection ratio. However, this effect was associated to the small DDD from the electrons since previous tests done with protons to the same component, showed increased damage from displacement damage to these parameters.

As a result of this study, ^{60}Co testing was deemed valid as the worst-case radiation conditions for components flown to Jupiter. This had important financial and scheduling impacts on the mission development. It assured that no further testing was necessary on components already approved for the mission. It also allowed to keep the Radiation Design Margins which would otherwise raise the mass budget of the spacecraft to shield components and/or render some components unacceptable for use.

^{60}Co test validation benefited both RADEM and the JUICE mission by enabling the Radiation Design Margins to be kept at 2. The Radiation Analysis here presented used and developed state-of-art-methods. Both ray-tracing and Monte Carlo (Geant4) simulations were combined to calculate TID, DDD and to some extent, SEEs, in all sensitive

components of RADEM. An open-source program, GUIMesh, was created for this purpose, allowing to quickly translate STEP geometries into GDML, a Geant4 compatible format. The range of applications of the tool extends past the space sector, to the medical, nuclear and high energy particle physics.

RADEM radiation analysis consisted of performing Geant4 simulations to estimate the TID at component level for the baseline configuration and in different shielding scenarios. Monte Carlo simulations are more accurate than ray-tracing but require a much larger computational time. For this reason, the spacecraft was modeled as a 6-sided box with wall thickness equal to its aluminum shielding equivalent obtained by ray-tracing. RADEM on the other hand was simulated with full detail. Though the scattering of particles and the production of secondaries in the spacecraft is not taken into account this way, this method allows to compute the radiation levels as accurate as possible within reasonable time.

The major challenge of the TID was that several components are qualified only up to 100 krad(Si) which demands a lot of shielding mass in order to be used in the JUICE mission. Also, in the baseline model analysis, TID of most components were above their sensitivity by a large margin. To decrease TID levels, several shielding scenarios, with increased aluminum wall thicknesses, were studied. Although none was fully capable of protecting all components, the overall dose of the components decreased for all scenarios with varying efficiency depending on the total mass and location of the shielding. A compromise between TID decrease and mass was done to select the best configuration.

In addition to the wall aluminum thickness increase, small tantalum slabs were placed strategically, according to the dose angular distribution, in an iterative manner, until all components were below their sensitivity levels. The major issue of the last approach were the two SpaceWire Transceivers, which had their large surface facing the side walls of RADEM, unlike all other components which faced the bottom/top walls of the instrument. These components were the driving force behind the Aluminum thickness increase in the side walls, as well as for the addition ∼10% of the tantalum mass. Furthermore one of the SpaceWire Transceivers still exceeds its TID limit by 8 krad(Si) but was approved as both as fully redundant.

The total mass of RADEM was increased by ∼2 kg from the baseline model. While this value may seem large, the shielding from the spacecraft is low and the radiation environment very demanding for the components. Nevertheless, this increase in mass allowed to assure that the TID of all components were below their sensitivity levels after the Radiation Design Margins were applied. It also benefited the components regarding the DDD since, for JUICE, the electron fluxes are so high, that only ∼50% of the DDD comes from protons. This means that shielding the components from electrons also decreases the DDD. Furthermore, electron radiative energy loss in high Z materials does not contribute to the DDD in the same way as it does for TID.

SEE rates were calculated for the four sensitive components: SRAM, PROM, ASIC and Oscillator. It was shown through standard calculations and Geant4 computed proton

fluxes that all components are expected to work during the entire mission with no significant downtime. All components have neglectable risk of latch-up. The combined risk of failure of RADEM is then very low and the instrument is expected to work during the entire mission.

The same Geant4 simulation were used to characterize and validate the Directional Detector (DDH) design concept for RADEM and the JUICE mission. The DDH is an essential detector that will allow to measure the electron flux angular variability and avoid under or over-estimation of the fluxes. The sensitivity of the DDH to electrons and protons was studied in detail for each mission phase. It was shown both through simulations, and through beam tests of the sensor plane of the detector coupled to an VATA466 ASIC, that the expected count rate is lower than the readout ASIC specification for all predicted flux conditions. The beam tests also showed that the system will be able to discriminate electrons from low energy protons based on the energy loss of the particles in the sensors. The ASIC logic was functional within the required parameters and comparez well with the simulation results that were obtained.

The DDH sensitivity to incoming electron directions was also assessed as well as the background subtraction method potential to measure the number of particles coming from outside the detector field-of-view. It was found that the detector is sensitive to the four zenithal directions that it will measure in all mission phases. Background reduction will be essential to measure the fluxes of high energy particles that can cross the whole instrument especially for the two larger zenithal angles measured. In their case, the surface area is larger and therefore the background count rate is larger as well. Their signal on the other hand is lower because of the increased threshold from the Kapton absorber. The method fails only to account for the contamination of particles that enter through the 45°apertures and lose energy in the 67.5°sensors due to being located right next to the 45°sensors.

One essential aspect of the sensitivity is that it is highly dependant on the electron energy spectrum. For this reason it is essential to combine the results from the Electron Detector Head (EDH) and the DDH, not only to correct for the angular variability, but also to calibrate the DDH directional sensitivity. The EDH will measure the electron energy spectrum which will be used to calibrate for the DDH sensitivity and the DDH will allow to convolute the electron flux with its angular dependence.

The DDH was also tested as part of the RADEM Engineering Model. The tests leveraged on the equivalent concepts of all RADEM detectors: a set of Silicon diodes connected to the low-gain and high-gain channels of a VATA466 ASIC. It was shown that the high-gain channels are sensitive to 622 keV gammas, electrons from ^{137}Cs decay, and 50-200 MeV protons. The ASIC logic was fully tested and showed that both thresholds cuts and coincidence logic perform within the detectors requirements. The response of low-gain channels to protons was also studied and approved. Though full calibration was not done to the Engineering Model it was shown that its concept and instrumentation are fully functional.

RADEMs Engineering Model was also used to test the alignment of the DDH, a critical

characteristic of the detector. A new experimental setup was designed in order to verify the alignment of the 0°sensor and the 22.5°sensors with respect to the corresponding collimator apertures. The tests were successful in showing that the pixels are correctly aligned with the collimator for the two aforementioned angles. The results obtained agreed well with Geant4 simulations of the setup. The setup was limited in the sense it that did not allow to irradiat the larger zenithal angle sensors. This was because of source collimator and lack of angular freedom, and not because of incorrect alignment. An upgrade to the setup is currently under design and will be available for the Qualification and Flight models of RADEM.

So far, RADEM has passed all tests successfully. The only remaining issue is the ASIC qualification that has been delayed until October 2019 because of mechanical malfunctions. Nevertheless, the Engineering Qualification and Flight models are now under construction and are scheduled to be tested and calibrated in 2019 and 2020 respectively. Calibration results will allow to fully validate the Geant4 model of RADEM and obtain its response functions. This will benefit the development of flux reconstruction algorithms for all four detector heads and ultimately analyze in-flight data during the cruise phase, especially in the Earth flybys where the monitor can be cross-calibrated with other instruments in orbit, and in Jupiter. It will also be evaluated the possibility of joint measurements with the Particle Environment Package (PEP). PEP is a plasma detector that covers the energy range between <0.001 eV to > 1MeV. Its range overlaps with RADEM which will give full sight of the particle population. Both detectors will also complement the J-Mag magnetometer to study the processes that accelerate electrons up to energies above 10 MeV.

GUIMesh still has margin for improvement. While the tool is already being used in several projects it is still largely dependent of CAD tools for visualization. The Open Cascade Library could be used to allow GUIMesh users to fully visualize their geometry. Functionally speaking ray-tracing algorithms could be included to perform quick radiation analysis when applicable. Other meshing algorithms could also be implemented to decrease the number of triangles for the same geometry precision. This would be useful to decrease the navigation time at simulation level. An alternative would be to implement GPU (Graphical Processing Unit) navigation algorithms. Navigation is done by solving the parametric equations of a particle and find the intersection with the solids in the simulation. This technique can be parallelized with GPUs without any need to change the kernel which would result in large decrease in computation time.

Appendices

A - Components List

Table A.1: List of components in RADEM and their TID and DDD sensitivity. Components 1-49 are the Silicon diodes of the four detector heads.

Component		TID sensitivity	DDD sensitivity
ID	Name	(krad(Si))	50 MeV Proton Fluence (p/cm^2)
1	HI2	1000	1.16E+12
2	PSD7	1000	1.16E+12
3	PSD5	1000	1.16E+12
4	PSD3	1000	1.16E+12
5	PSD6	1000	1.16E+12
6	PSD1	1000	6.70E+11
7	PSD8	1000	1.16E+12
8	PSD2	1000	1.16E+12
9	PSD4	1000	1.16E+12
10	HI1	1000	1.16E+12
11	ESD7	1000	6.70E+11
12	ESD4	1000	6.70E+11
13	ESD8	1000	6.70E+11
14	ESD2	1000	6.70E+11
15	ESD6	1000	6.70E+11
16	ESD5	1000	6.70E+11
17	ESD3	1000	6.70E+11
18	ESD1	1000	2.82E+11
19	DD22.5	1000	6.01E+10
20	DD45	1000	6.01E+10
21	DD45	1000	6.01E+10
22	DD45	1000	6.01E+10
23	DD45	1000	6.01E+10
24	DD67.5	1000	6.01E+10
25	DD67.5	1000	6.01E+10
26	DD67.5	1000	6.01E+10
27	DD67.5	1000	6.01E+10
28	DD22.5	1000	6.01E+10
29	DD45	1000	6.01E+10

Component		TID sensitivity	DDD sensitivity
ID	Name	(krad(Si))	50 MeV Proton Fluence (p/cm^2)
30	DD45	1000	6.01E+10
31	DD67.5	1000	6.01E+10
32	DD22.5b	1000	6.01E+10
33	DD22.5	1000	6.01E+10
34	DD67.5	1000	6.01E+10
35	DD45	1000	6.01E+10
36	DD67.5	1000	6.01E+10
37	DD22.5	1000	6.01E+10
38	DD22.5	1000	6.01E+10
39	DD45	1000	6.01E+10
40	DD67.5	1000	6.01E+10
41	DD45	1000	6.01E+10
42	DD22.5	1000	6.01E+10
43	DD22.5	1000	6.01E+10
44	DD45b	1000	6.01E+10
45	DD67.5b	1000	6.01E+10
46	DD22.5	1000	6.01E+10
47	DD67.5	1000	6.01E+10
48	DD22.5	1000	6.01E+10
49	DD0	1000	6.01E+10
50	Voltage Reference	300	2.00E+11
51	Voltage Reference	300	2.00E+11
52	Voltage Reference	300	2.00E+11
53	Voltage Reference	300	2.00E+11
54	Transistor NPN	100	2.00E+11
55	Transistor NPN	100	2.00E+11
56	Transistor NPN	100	2.00E+11
57	Transistor NPN	100	2.00E+11
58	Transistor NPN	100	2.00E+11
59	Transistor NPN	100	2.00E+11
60	Transistor NPN	100	2.00E+11
61	Transistor Dual NPN	100	2.00E+11
62	Transistor Dual PNP	100	2.00E+11
63	Transistor Dual NPN	100	2.00E+11
64	Transistor Dual PNP	100	2.00E+11
65	Transistor Dual NPN	100	2.00E+11
66	Transistor Dual PNP	100	2.00E+11
69	Diode Ultra Power Rectifier 150V	300	2.00E+11
70	Diode Ultra Power Rectifier 150V	300	2.00E+11
71	Diode Ultra Power Rectifier 150V	300	2.00E+11
72	Diode Ultra Power Rectifier 150V	300	2.00E+11
73	Diode Ultra Power Rectifier 150V	300	2.00E+11
74	Diode Schottky 45V 1A	300	2.00E+11
75	Diode Schottky 45V 1A	300	2.00E+11

Component		TID sensitivity	DDD sensitivity
ID	Name	(krad(Si))	50 MeV Proton Fluence (p/cm^2)
76	Diode Schottky 45V 1A	300	2.00E+11
77	Diode Schottky 45V 1A	300	2.00E+11
78	Diode Schottky 45V 1A	300	2.00E+11
79	Diode Schottky 45V 1A	300	2.00E+11
80	Diode Ultra Fast Recover 440V	300	2.00E+11
81	Diode Ultra Fast Recover 440V	300	2.00E+11
82	Diode Ultra Fast Recover 440V	300	2.00E+11
83	Zener 12V	300	2.00E+11
84	Zener 87V	300	2.00E+11
85	Diode Ultra Fast Recover 440V	300	2.00E+11
86	Diode Ultra Fast Recover 440V	300	2.00E+11
87	Diode Ultra Fast Recover 440V	300	2.00E+11
88	Oscillator 10MHz CMOS	100	2.00E+11
89	uP Leon 3 FT Dual Core	300	2.00E+11
90	Multiplexed ADC	100	2.00E+11
91	Multiplexed ADC	100	2.00E+11
92	Multiplexed ADC	100	2.00E+11
93	OPAMP	300	2.00E+11
94	OPAMP	300	2.00E+11
95	OPAMP	300	2.00E+11
96	LDO	300	2.00E+11
97	LDO	300	2.00E+11
98	LDO	300	2.00E+11
99	LDO	300	2.00E+11
100	LDO	300	2.00E+11
101	LDO	300	2.00E+11
102	LDO	300	2.00E+11
103	LDO	300	2.00E+11
104	Power Supervisor	100	2.00E+11
105	SpW Transceiver	100	2.00E+11
106	SpW Transceiver	100	2.00E+11
107	Dual PWM Controller	300	2.00E+11
108	ASVATA466	TBA-300	2.00E+11
109	ASVATA466	TBA-300	2.00E+11
110	ASVATA466	TBA-300	2.00E+11
111	Temperature Transducer	300	2.00E+11
112	Temperature Transducer	300	2.00E+11
113	Temperature Transducer	300	2.00E+11
114	Temperature Transducer	300	2.00E+11
115	Temperature Transducer	300	2.00E+11
116	QUAD COMP LM139A	100	2.00E+11
117	MRAM 16Mb (2Mx8b)	100	2.00E+11
118	SRAM 40Mb (1M x 39b)	100	2.00E+11
119	PROM 256kb (32k x 8b)	100	2.00E+11

Bibliography

[1] T. R. Oldham and F. B. McLean, "Basic Mechanisms of Radiation Effects on Electronic Materials, Devices and Integrated Circuits," *1987 IEEE NSREC short course notes*, July 1987.

[2] T. R. Oldham and F. B. McLean, "Total ionizing dose effects in mos oxides and devices," *IEEE Transactions on Nuclear Science*, vol. 50, pp. 483–499, June 2003.

[3] D. M. Fleetwood, "Total ionizing dose effects in mos and low-dose-rate sensitive linear-bipolar devices," *IEEE Transactions on Nuclear Science*, vol. 60, p. 1706–1730, June 2013.

[4] J. R. Srour, C. J. Marshall, and P. W. Marshall, "Review of displacement damage effects in silicon devices," *IEEE Transactions on Nuclear Science*, vol. 50, p. 653–670, June 2003.

[5] J. R. Srour and J. W. Palko, "Displacement damage effects in irradiated semiconductor devices," *IEEE Transactions on Nuclear Science*, vol. 60, pp. 1740–1766, June 2013.

[6] P. E. Dodd and L. W. Massengill, "Basic mechanisms and modeling of single-event upset in digital microelectronics," *IEEE Transactions on Nuclear Science*, vol. 50, pp. 583–602, June 2003.

[7] K. A. Soliman and D. K. Nichols, "Latchup in CMOS Devices from Heavy Ions," *IEEE Transactions on Nuclear Science*, vol. 30, pp. 4514–4519, December 1983.

[8] C. Plainaki *et al.*, "Planetary space weather: scientific aspects and future perspectives," *Journal of Space Weather and Space Climate*, vol. 6, June 2016.

[9] J. A. V. Allen, C. E. McIlwain, and G. H. Ludwig, "Radiation observations with satellite 1958 ϵ," *Journal of Geophysical Research*, vol. 64, March 1959.

[10] S. D. M. and J. I. Vette, "AP-8 trapped proton environment for solar maximum and solar minimum," *NASA-TM-X-72605, NSSDC/WDC-A-R/S-76-06*, 1976.

[11] J. I. Vette, "The AE[U+2010]8 trapped electron model environment," *NSSDC/WDC[U+2010]A[U+2010]R S 91[U+2010]24*, 1991.

[12] D. Heynderickx, B. Quaghebeur, J. Wera, E. J. Daly, and H. D. R. Evans, "New radiation environment and effects models in the European Space Agency's Space Environment Information System (SPENVIS)," *Space Weather*, vol. 2, pp. 2150–2160, October 2004.

[13] D. J. Williams, "The Galileo Energetic Particle Detector," *Space Science Reviews*, vol. 60, pp. 385–412, May 1992.

[14] S. J. Bolton *et al.*, "The JUNO Mission," *Space Science Reviews*, vol. 213, p. 5–37, November 2017.

[15] D. N. Baker and J. A. V. Allen, "Revised pioneer10 absolute electron intensities in the inner jovian magnetosphere," *Journal of Geophysical Research Atmospheres*, vol. 82, pp. 681–683, February 1977.

[16] J. A. V. Allen, B. A. Randall, D. N. Baker, C. K. Goertz, D. D. Sentman, M. F. Thomsen, and H. R. Flindt, "Pioneer 11 observations of energetic particles in the jovian magnetosphere," *Science*, vol. 188, pp. 459–462, May 1975.

[17] S. M. Krimigis, T. P. Armstrong, W. I. Axford, C. O. Bostrom, G. G. C. Y. Fan, and L. J. Lanzerotti, "The low energy charged particle (lecp) experiment on the voyager spacecraft," *Space Science Reviews*, vol. 21, p. 329–354, May 1977.

[18] E. Keppler, J. Blake, D. Hovestadt, J. Q. A. Korth, G. Umlauft, , and J. Woch, "The ulysses energetic particle composition experiment (epac)," *Space Science Reviews*, vol. 92, p. 317–331, January 1992.

[19] I. Jun, J. M. Ratliff, H. B. Garrett, and R. W. McEntire, "Monte Carlo simulations of the Galileo energetic particle detector," *Nuclear Instruments and Methods in Physics Research Section A: Accelerators, Spectrometers, Detectors and Associated Equipment*, vol. 480, pp. 465–475, September 2002.

[20] O. Grasset *et al.*, "JUpiter ICy moons Explorer (JUICE): An ESA mission to orbit Ganymede and to characterize the Jupiter system," *Planetary and Space Science*, vol. 78, pp. 1–21, April 2013.

[21] M. Pinto, P. Goncalves, H. Wojtek, A. Marques, and J. C. Pinto, "Development of a Directionality Detector for RADEM, the Radiation Hard Electron Monitor aboard the JUICE Mission," *IEEE Transactions on Nuclear Science*, vol. 13, March 2019.

[22] T. A. Stein *et al.*, "Front-end readout ASIC for charged particle counting with the RADEM instrument on the ESA JUICE mission," *Proceedings of SPIE 9905, Space Telescopes and Instrumentation 2016: Ultraviolet to Gamma Ray*, July 2016.

[23] A. Mohammadzadeh *et al.*, "The ESA Standard Radiation Environment Monitor program first results from PROBA-I and INTEGRAL," *IEEE Transactions on Nuclear Science*, vol. 50, pp. 2272–2277, December 2003.

[24] L. Arruda *et al.*, "SEP Protons in GEO measured with the ESA Multi-Functional Spectrometer," *IEEE Transactions on Nuclear Science*, vol. 64, pp. 2333–2339, August 2017.

[25] D. J. Williams, "Energetic electron beams in ganymede's magnetosphere," *Journal of Geophysical Research*, vol. 109, p. A09211, September 2004.

[26] "ECSS-Q-ST-60-15C: Space product assurance, Radiation Hardness assurance – EEE components." European Cooperation for Space Standardization (ECSS) Standard, October 2012.

[27] "ECSS-E-HB-10-12A: Space Engineering, Calculation of radiation and its effects and margin policy handbook." European Cooperation for Space Standardization (ECSS) Standard, December 2010.

[28] J. Team, "JUICE –Jupiter Icy moons ExplorerEnvironmental Specification, js-14-09, issue 5, revision 5," 2017.

[29] C. Poivey, "Radiation hardness assurance for space systems." 2002 IEEE Nuclear and Space Radiation Effects Conference Short Course Notebook.

[30] S. Agostinelli *et al.*, "Geant4 - A Simulation Toolkit," *Nuclear Instrumentation and Methods A*, vol. 506, pp. 250–303, July 2003.

[31] J. Allison *et al.*, "Geant4 Developments and Applications," *IEEE Transactions on Nuclear Science*, vol. 53, pp. 270–278, July 2006.

[32] J. Allison *et al.*, "Recent Developments in Geant4," *Nuclear Instrumentation and Methods A*, vol. 835, pp. 186–225, November 2016.

[33] "STEP-file, ISO 10303-21 – Industrial automation systems and integration – Product data representation and exchange."

[34] R. Chytracek, J. McCormick, W. Pokorski, and G. Santin, "Geometry Description Markup Language for Physics Simulation and Analysis Applications," *IEEE Transactions on Nuclear Science*, vol. 53, pp. 2892–2896, October 2005.

[35] "Cosmic vision 2015-2025." `http://sci.esa.int/cosmic-vision/`. (Last Access: 24-04-2019).

[36] Athena Study Team, "Athena The extremes of the Universe: from black holes to large-scale structure," *ESA/SRE(2011)17*, vol. 1, pp. 1–117, December 2011.

[37] LISA Mission Science Office, "LISA: Probing the Universe with Gravitational Waves," *LISA-LIST-RP-436*, vol. 1, pp. 1–117, July 2007.

[38] R. Moeller *et al.*, "Astrobiological Aspects of Mutagenesis of Cosmic Radiation on Bacterial Spores," *Astrobiology*, vol. 10, pp. 509–521, June 2010.

[39] M. Maalouf, M. Durante, and N. Foray, "Biological Effects of Space Radiation on Human Cells: History, Advances and Outcomes," *Journal of Radiation Research*, vol. 52, pp. 126–146, March 2011.

[40] I. C. on Radiological Protection (ICRP), "The 2007 Recommendations of the International Commission on Radiological Protection. ICRP Publication 103," *Annual ICRP*, vol. 38, pp. 1–332, 2007.

[41] T. P. O'Brien and J. E. Mazur, "Section II: The Space Radiation Environment," *2016 IEEE NSREC short course notes*, July 2016.

[42] G. Santin, D. Wright, and M. Asai, "Section III: Space Radiation Transport Models," *2006 IEEE NSREC short course notes*, July 2006.

[43] S. Bourdarie, "Section I: Comparative Earth and Jovian Space Environment," *2014 IEEE NSREC short course notes*, July 2014.

[44] M. G. Kivelson and K. T. Russel, *Introduction to Space Physics*. Cambridge University press, 1 ed., April 1995.

[45] `http://lasp.colorado.edu/home/mop`. (Last Access: 24-04-2019).

[46] A. Sicard-Piet, S. Bourdarie, and N. Krupp, "JOSE: A new Jovian Specification Environment Model," *IEEE Transactions on Nuclear Science*, vol. 53, pp. 923–931, June 2011.

[47] S. J. Bolton, "Ultra-relativistic electrons in Jupiter's radiation belts," *Nature*, vol. 415, pp. 987–991, February 2002.

[48] I. de Peter and C. Goertz, "Radial diffusion models of energetic electrons and Jupiter's synchrotron radiation 1. Steady state solution," *Journal of Geophysical Research*, vol. 95, pp. 39–50, 1990.

[49] D. W. Kerst, "Acceleration of Electrons by Magnetic Induction," *Physical Review*, vol. 58, November 1940.

[50] E. Fermi, "On the Origin of the Cosmic Radiation," *Physical Review*, vol. 75, April 1949.

[51] N. Divine and H. B. Garret, "Charged particle distribution in Jupiter's magnetosphere," *Journal of Geophysical Research*, vol. 88, pp. 6889–6903, September 1983.

[52] H. B. Garrett, S. M. Lvin, and S. J. Bolton, "A revised model of Jupiter's inner electron belts: Updating the Divine radiation model," *Geophysical Research Letters*, vol. 32, p. L04104, February 2005.

[53] J. E. P. Connerney *et al.*, "New Models of Jupiter's magnetic field constrained by the Io flux tube footprint," *Journal of Geophysical Research*, vol. 103, pp. 11929–11939, June 1998.

[54] S. Bourdarie and A. Sicard, "Physical electron belts model from Jupiter's surface to the orbit of Europa," *Journal of Geophysical Research*, vol. 109, pp. 1–13, February 2004.

[55] D. V. Reames *et al.*, "Particle acceleration at the sun and in the heliosphere," *Space Science Review*, vol. 90, pp. 413–491, 1999.

[56] A. Keating, *Mars Radiation Environment and Effects on EEE Components*. PhD thesis, Instituto Superior Técnico - Universidade de Lisboa, September 2008.

[57] "Sunspot Index and Long-term Solar Observations - Royal Observatory of Belgium." `http://sidc.be/silso/`. (Last Access: 24-04-2019).

[58] "Radiation Monitor Data - ESA." `https://spitfire.estec.esa.int/ODI/dplot_SREM.html`. (Last Access: 24-04-2019).

[59] M. Burrel, "The Risk of Solar Proton Events to Space Missions," 1972. NASA Report TMX-2440.

[60] M. A. Xapsos, G. Summers, J. Barth, E. G. Stassinopoulos, and E. Burke, "Probability Model for Cumulative Solar Proton Event Fluences," *IEEE Transactions on Nuclear Science*, vol. 47, pp. 486–490, June 2000.

[61] M. T. et al. (Particle Data Group), "Review of Particle Physics," *Physics Reviews D*, vol. 99, pp. 39–50, August 2018.

[62] S. E. Forbush, "On world-wide changes in cosmic-ray intensity," *Physical Review*, vol. 54, pp. 975–988, December 1938.

[63] O. Witass *et al.*, "Interplanetary coronal mass ejection observed at STEREO`[U+2010]`A, Mars, comet 67P/Churyumov`[U+2010]`Gerasimenko, Saturn, and New Horizons en route to Pluto: Comparison of its Forbush decreases at 1.4, 3.1, and 9.9 AU," *Journal of Geophysical Research Space Physics*, vol. 122, pp. 7865–7890, August 2017.

[64] "ECSS25100: Single Event Effects Test Methods and Guidelines." European Cooperation for Space Standardization (ECSS) Standard, October 2014.

[65] R. A. Nymmik, "Time lag of galactic cosmic ray modulation: Conformity to general regularities and influence on particle energy spectra," *Advanced Space Research*, vol. 26, pp. 1875–2000, August 2000. Also as ISO 15390 – Galactic Cosmic Ray model.

[66] A. Carlton, M. de Soria-Santacruz Pich, W. Kim, I. Jun, and K. Cahoy, "Using the Galileo Solid-State Imaging Instrument as a Sensor of Jovian Energetic Electrons," *IEEE Transactions on Nuclear Science*, vol. 66, January 2019.

[67] "NIST – estar : stopping power and range tables for electrons." http://physics.nist.gov/PhysRefData/Star/Text/ESTAR.html. (Last Access: 24-03-2019).

[68] "ESCC22900: Total Dose Steady-State Irradiation Test method." European Cooperation for Space Standardization (ECSS) Standard, June 2005.

[69] W. R. Leo, *Techniques for Nuclear and Particle Physics Experiments A How-to-Approach.* Springer-Verlag Berlin Heidelberg.

[70] "NIST – estar : stopping power and range tables for photons." https://physics.nist.gov/PhysRefData/Xcom/html/xcom1.html. (Last Access: 24-03-2019).

[71] W. S. C. Williams, *Nuclear and Particle Physics.* Clarendon Press, 1 ed., May 1991.

[72] J. E. Turner, *Atoms, Radiation, and Radiation Protection.* Wiley[U+2010]VCH Verlag, 2 ed., October 2007.

[73] "NIST – estar : stopping power and range tables for protons." https://physics.nist.gov/PhysRefData/Star/Text/PSTAR.html. (Last Access: 24-03-2019).

[74] H. Bichsel, "A method to improve tracking and particle identification in TPCs and silicon detectors," *Nuclear Instrumentation and Methods A*, vol. 562, pp. 154–197, June 2006.

[75] H. Merolia, D. Passeria, and L. Servolia, "Energy loss measurement for charged particles in very thin silicon layers," *Journal of Instrumentation*, vol. 6, June 2011.

[76] H. A. Bethe, "Molière's Theory of Multiple Scattering," *Physical Review*, vol. 89, March 1953.

[77] S. Goudsmit and J. L. Saunderson, "Multiple Scattering of Electrons," *Physical Review*, vol. 57, January 1940.

[78] H. W. Lewis, "Multiple scattering in an infinite medium," *Physical Review*, vol. 78, p. 526–529, June 1950.

[79] *MCNPX User's Manual, Version 2.3.0.* The University of Michigan, la-ur-02-2607 ed., 2002.

[80] A. Fassò, A. Ferrari, J. Ranft, and P. Sala, "Fluka: A multiparticle transport code," Tech. Rep. CERN-2005-10, INFN/TC 05/11, SLAC-R-73, CERN, 2005.

[81] G. Collaboration, "Guide for physics lists release 10.4," Tech. Rep. 1.0, 2017.

[82] H. Messel and D. Crawford, *Electron-Photon shower distribution.* Wiley-Interscience, 1 ed., September 1970.

[83] S. Seltzer and M. Berger, "Bremsstrahlung spectra from electron interactions with screened atomic nuclei and orbital electrons," *Nuclear Instruments and Methods B*, vol. 12, pp. 95–134, August 1985.

[84] S. Seltzer and M. Berger, "Bremsstrahlung energy spectra from electrons with kinetic energy 1 kev - 100 gev incident on screened nuclei and orbital electrons of neutral atoms with z = 1-100," *Atomic Data and Nuclear Data Tables*, 1986.

[85] L. Urban, "A multiple scattering model," *Technical Report CERN-OPEN-2006-077*, December 2002.

[86] V. N. Ivanchenko, O. Kadri, M. Maire, and L. Urban, "Geant4 models for simulation of multiple scattering," *Journal of Physics: Conference Series*, vol. 219, pp. 32–45, April 2010.

[87] J. Cugnon, C. Volant, and S. Vuillier, "Improved intranuclear cascade model for nucleon-nucleus interactions," *Nuclear Physics A*, vol. 620, pp. 478–509, July 1997.

[88] H. W. Bertini and P. Guthrie, "News item results from medium-energy intranuclear-cascade calculation," *Nuclear Physics A*, vol. 169, pp. 670–672, July 1971.

[89] B. Andersson, G. Gustafson, and B. Nilsson-Almqvist, "A model for low-pT hadronic reactions with generalizations to hadron-nucleus and nucleus-nucleus collisions," *Nuclear Physics B*, vol. 281, pp. 281–289, January 1987.

[90] B. Nilsson-Almqvist and E. Stenlund, "Interactions between hadrons and nuclei: The Lund Monte Carlo - FRITIOF version 1.6 -," *Computer Physics Communications*, vol. 43, pp. 387–397, January 1987.

[91] C. Poole, I. Cornelius, J. Trapp, and C. Langton, "Fast tessellated solid navigation in geant4," *IEEE Transactions on Nuclear Science*, vol. 99, pp. 1–7, 2012.

[92] S. M. Sze, *Physics of Semiconductor Devices.* Wiley-Interscience, 2 ed., September 1981.

[93] A. S. Sedra and K. C. Smith, *Microelectronic Circuits.* McGraw-Hill, 5 ed., 2004.

[94] J. E. Lilienfeld, "Method and apparatus for controlling electric currents." U. S. Patent No. 1,745,175, October 1926.

[95] "The nobel prize in physics 1956." `http://nobelprize.org/nobel_prizes/physics/laureates/1956/index.html/`. (Last Access: 22-03-2019).

[96] "Datasheet of 2n7000-d." `https://www.onsemi.com/pub/Collateral/2N7000-D.PDF/`. (Last Access: 22-03-2019).

[97] D. Kahng and S. M. Sze, "A floating gate and its application to memory devices," *The Bell System Technical Journal*, vol. 46, pp. 1288–1295, July 1967.

[98] R. J. Baker, *CMOS Circuit Design, Layout, and Simulation.* Wiley-IEEE Press, 3 ed., September 2010.

[99] F. M. Wanlass, "Low stand-by power complmentary field effect circuitry." U. S. Patent No. 3,356,858, June 1963.

[100] C. Poivey, "Section I: Total Ionizing and Non-Ionizing Dose Radiation Hardness Assurance," *2017 IEEE Nuclear and Space Radiation Effects Conference Short Course Notebook*, July 2017.

[101] P. Adell and J. Boch, "Section II: Dose and Dose Rate Effects In Microelectronics: Pushing the Limits to Extreme Conditions," *2014 IEEE Nuclear and Space Radiation Effects Conference Short Course Notebook*, July 2014.

[102] T. R. Oldham, "Section II: Basic Mechanisms of TID and DDD Response in MOS and Bipolar Microelectronics," *2011 IEEE Nuclear and Space Radiation Effects Conference Short Course Notebook*, July 2011.

[103] C. Poivey, "Total Ionizing Dose (TID) and TNID Total Non Ionizing Dose (TNID) Effects in Electronic parts." Presentation at SERESSA 2018.

[104] "MIL-HDBK-814: Ionizing Dose and Neutron Hardness Assurance Guidelines for Microcircuits and Semiconductor Devices," February 1994.

[105] "MIL-STD-883E: Ionizing dose rate procedure, method 1019.9," December 1996.

[106] "Mil-std-883e: Neutron irradiation, method 1017.2," December 1996.

[107] "ASTM F 1892-04: Standard Guide for Ionizing Radiation (Total Dose) Effects Testing of Semiconductor Devices."

[108] "ASTM F 1263-94: Standard guide for analysis of overtest data in radiation testing of electronic parts."

[109] "ASTM F 1190-99: Standard Guide for Neutron Irradiation of Unbiased Electronic Components."

[110] J. Guillermin *et al.*, "Part-to-part and lot-to-lot variability study of TID effects in bipolar linear devices," *16th European Conference on Radiation and Its Effects on Components and Systems (RADECS)*, 2016. DOI: 10.1109/RADECS.2016.8093124.

[111] E. Normand, "Single event upset at ground level," *IEEE Transactions on Nuclear Science*, vol. 43, pp. 2742 – 2750, December 1996.

[112] C. M. Hsieh, P. C. Murley, and R. P. O'Brien, "Dynamics of charge collection from alpha-particle tracks in integrated circuitss," *19th International Reliability Physics Symposium*, pp. 38–42, April 1981.

[113] R. C. Baumann, "Section III: Landmarks in Terrestrial Single-Event Effects," *2013 IEEE Nuclear and Space Radiation Effects Conference Short Course Notebook*, July 2013.

[114] R. C. Baumann, "Year-In-Review 2005-2006: Radiation-induced Soft Error Rate (SER)," *IRPS 2006*, March 2006.

[115] "RADEF - Univesity of Jyvaskyla." `https://www.jyu.fi/fysiikka/en/research/accelerator/radef/`. (Last Access: 01-04-2019).

[116] G. Hopkinson. Component testing, displacement damage, RADECS short course 2003.

[117] K. P. Rodbell and C.-Y. Cher, "Section V: Where Radiation Effects in Emerging Technologies Really Matter," *2013 IEEE Nuclear and Space Radiation Effects Conference Short Course Notebook*, July 2013.

[118] S. Duzellier, "Section 3-C: Radiation engineering methods for space applications - Radiation Effects Analysis: Single Event Effetcs," *Short Course Book, RADECS 2003*, 2003.

[119] E. L. Petersen *et al.*, "Rate prediction for single event effects-A critique," *IEEE Transactions on Nuclear Science*, vol. 39, pp. 1577–1599, December 1992.

[120] J. C. Pickel, "Single-Event Effects Rate Prediction," *IEEE Transactions on Nuclear Science*, vol. 43, pp. 483–495, April 1996.

[121] A. Tylka *et al.*, "CREME96: A Revision of the Cosmic Ray Effects on Micro-Electronics Code," *IEEE Transactions on Nuclear Science*, vol. 40, pp. 2150–2160, December 1997.

[122] "Space Radiation 7." `http://www.spacerad.com/index.htm/`. (Last Access: 23-03-2019).

[123] A. Varotsou and others, "OMERE space radiation environment and effects tool: new developments and new interface." ESA-CNES Radiation Final Presentation Days, March 2017.

[124] R. C. Baumann, "Section IV: Addressing device and environment variations in single event rate predictions Effects," *2018 IEEE Nuclear and Space Radiation Effects Conference Short Course Notebook*, July 2018.

[125] P. D. Edmondson, D. J. Riley, R. C. Birtcher, , and S. E. Donnelly, "Amorphization of crystalline si due to heavy and light ion irradiation," *Journal of Applied Physics*, vol. 105, July 2009.

[126] S. Wood *et al.*, "Simulation of radiation damage in solids," *IEEE Transactions on Nuclear Science*, vol. 28, pp. 1740–1766, December 1981.

[127] M. Boschini *et al.*, "Expression for the mott cross section of electrons and positrons on nuclei with z up to 118," *Radiation Physics and Chemistry*, vol. 90, pp. 39–66, September 2003.

[128] I. Jun, W. Kim, and R. Evans, "Electron nonionizing energy loss for device applications," *IEEE Transactions on Nuclear Science*, vol. 56, pp. 3229 – 3235, December 2009.

[129] I. Jun *et al.*, "Proton nonionizing energy loss (niel) for device applications," *IEEE Transactions on Nuclear Science*, vol. 50, pp. 1924 – 1928, December 2003.

[130] M.J. Boschini and P.G. Rancoita and M. Tacconi, "SR-NIEL Calculator: Screened Relativistic (SR) Treatment for Calculating the Displacement Damage and Nuclear Stopping Powers for Electrons, Protons, Light- and Heavy- Ions in Materials." `www.sr-niel.org`. (Last Access: 24-03-2019).

[131] E. Maddox, B. Taylor, and G. Vacanti, "Interplanetary Electron Model Tools Software Documentation." Report of ESA contract 22915/09/NL/AF, CSC-IEM-DOC003, 2011.

[132] D. Rodgers, "Jovian Electron Spectrum in near-Jupiter interplanetary space." ESA Technical note, TEC-EES/2011.747/DR, 20/06/2011, 2011.

[133] Seltzer S., "SHIELDOSE: A Computer Code For Space Shielding Radiation Dose Calculations." NBS Technical Note 1116, National Bureau of Standards, May 1980.

[134] M. Morales, "JUICE Preferred Part List (JPPL)." JUI-ATN-CPPA-LI-001.

[135] J. H. E. Boesch and J. M. McGarrity, "CHARGE YIELD AND DOSE EFFECTS IN MOS CAPACITORS AT 80 K1," *IEEE Transactions on Nuclear Science*, vol. 23, pp. 1520–1525, December 1976.

[136] M. R. Shaneyfelt, D. M. Fleetwood, J. R. Schwank, and K. L. Hughes, "CHARGE YIELD FOR COBALT-60 AND 10-keV X-RAY IRRADIATIONS OF MOS DEVICES," *IEEE Transactions on Nuclear Science*, vol. 38, pp. 1187–1194, December 1991.

[137] F. H. Attix, *Introduction to radiological physics and radiation dosimetry.* Wiley-VCH, 1 ed., January 1991.

[138] Casey *et al.*, "A comparison of high-energy electron and cobalt-60 gamma-ray radiation testing."

[139] "Nasa Test reports homepage." `radhome.gsfc.nasa.gov/`. (Last Access: 23-03-2019).

[140] M. Pinto *et al.*, "Representativeness of 60Co testing for EEE components to be flown in JUICE."

[141] M. Pinto *et al.*, "Verification of Co-60 testing representativeness for EEE components flown in the Jupiter electron environment (Eco60-LIP-FR-v2.1)."

[142] "St microelectronics "datasheet of str100h100n10"." https://www.st.com/resource/en/datasheet/. (Last Access: 01-04-2019).

[143] "Micron "Datasheet of MT29F32G08ABAAAWP-ITZ"." https://www.micron.com/products/nand-flash/slc-nand/part-catalog/mt29f32g08abaaawp-itz/. (Last Access: 01-04-2019).

[144] "ST Microelectronics "Datasheet of 2N2222"." http://www.st.com/content/ccc/resource/technical/document/datasheet/a0/75/d9/bd/fc/ca/42/15/CD00003223.pdf/files/CD00003223.pdf/jcr:content/translations/en.CD00003223.pdf/. (Last Access: 01-04-2019).

[145] "Texas Instruments "Datasheet of LM124"." www.ti.com/lit/ds/symlink/lm324-n.pdf/. (Last Access: 01-04-2019).

[146] K. Kruckmeyer, L. McGee, B. Brown, and D. Hughart, "Low dose rate test results of national semiconductor's eldrs-free bipolar amplifier lm124 and comparators lm139 and lm193," in *2008 IEEE Radiation Effects Data Workshop*, pp. 110–117, July 2008.

[147] "Texas Instruments "Datasheet of LM4050"." hthttp://www.ti.com/lit/ds/symlink/lm4050-n.pdf/. (Last Access: 01-04-2019).

[148] K. Kruckmeyer, T. Trinh, L. McGee, and A. T. Kelly, "Impact of reference voltage on the eldrs characteristics of the lm4050 shunt voltage reference," in *2011 12th European Conference on Radiation and Its Effects on Components and Systems*, pp. 926–930, September 2011.

[149] "ESTEC-ESA facilities." https://escies.org/webdocument/showArticle?id=251/. (Last Access: 01-04-2019).

[150] "Basic Information About the Estec Co-60 Facility." https://escies.org/webdocument/showArticle?id=251. (Last Access: 24-04-2019).

[151] "CTN-IST facilities." http://www.ctn.tecnico.ulisboa.pt/facilities/uk_utr.htm/. (Last Access: 01-04-2019).

[152] "Hospital Santa Maria." http://www.chln.pt/index.php/oncologia/radioterapia/. (Last Access: 01-04-2019).

[153] P. R. Almond *et al.*, "AAPM's TG-51 protocol for clinical reference dosimetry of high-energy photon and electron beams," *Medical Physics*, vol. 26, pp. 1847–1870, September 1999.

[154] R. M. Howell *et al.*, "Secondary neutron spectra from modern Varian, Siemens, and Elekta linacs with multileaf collimators," *Medical Physics*, vol. 36, pp. 4027–4038, September 2009.

[155] RUAG, "LM124 TID DD comparison."

[156] M. Pinto *et al.*, "RADEM Geant4 model Radiation Analysis (JUI-LIP-RDM-TN-002.6)."

[157] M. Pinto *et al.*, "RADEM EEE Component Radiation Analysis Total Ionising Dose (JUI-LIP-RDM-TN-004.2)."

[158] M. Pinto *et al.*, "RADEM Radiation Analysis - EEE Components, Sensors and Materials (JUI-LIP-RDM-TN-004.5-3)."

[159] M. Pinto and P. Goncalves, "GUIMesh: A tool to import STEP geometries into Geant4 via GDML," *Computer Physics Communications*, vol. 239, pp. 150–156, June 2019.

[160] C. Poole, I. Cornelius, J. Trapp, and C. Langton, "A CAD Interface for GEANT4," *Australasian Physical and Engineering Science in Medicine*, September 2012.

[161] "STL2GDML." `https://www.solveering.com/InStep/instep.aspx`. (Last Access: 26-04-2019).

[162] "3D Systems, Inc. Stereolithography Interface Specification, July 1988.."

[163] C. Vuosalo *et al.*, "A tool to convert cad models for importation into geant4," *Journal of Physics: Conference Series*, vol. 898, no. 042024, 2017.

[164] "Dassault Systèmes SOLIDWORKS Corporation, Waltham, Massachusetts.."

[165] "GDML USER's GUIDE Version 2.7." `http://gdml.web.cern.ch/GDML/doc/GDMLmanual.pdf/`. (Last Access: 26-04-2019).

[166] T. Beutier, E. Delage, M. Wouts, O. Serres, and P. Peyrard, "Fastrad new tool for radiation prediction," *Proceedings of the 7th European Conference on Radiation and Its Effects on Components and Systems*, pp. 181–183, September 2003.

[167] "ESABASE2." `https://esabase2.net/wp-content/uploads/2017/09/ESABASE2-Fact-Sheet.pdf`. (Last Access: 26-04-2019).

[168] "STEP Tools." `https://www.steptools.com/`. (Last Access: 26-04-2019).

[169] "FreeCAD." `https://www.freecadweb.org/`. (Last Access: 26-04-2019).

[170] "Python." `http://www.python.org/`. (Last Access: 26-04-2019).

[171] "TKinter." `https://wiki.python.org/moin/TkInter/`. (Last Access: 26-04-2019).

[172] J. M. Sampaio, P. Gonçalves and C. Povey, "Dose calculations from the radfets response onboard the alphasat cttb experiment," *2016 16th European Conference on Radiation and Its Effects on Components and Systems (RADECS)*, pp. 1–3, September 2016.

[173] A. L. Casimiro, *Efeitos do Ambiente de Radiac]ão Espacial em Missões Tripuladas a Marte, school = Instituto Superior Técnico - Universidade de Lisboa, year = 2016, month = June.* PhD thesis.

[174] RADIATION ASSURED DEVICES, INC, "Non-Destructive Single Event Effects Testing of the C1460A1-0015 and –0016 Oscillator Modules for Vectron." (Radiation test report obtained from supplier.).

[175] RADIATION ASSURED DEVICES, INC, "Destructive Single Event Effects Testing of the C1460A1-0015 and – 0016 Oscillator Modules for Vectron." (Radiation test report obtained from supplier.).

[176] "AEROFLEX "Datasheet of UT28F256LVQLE Radiation-Hardened 32K x 8 PROM"." `https://www.cobhamaes.com/pagesproduct/datasheets/256VQLE.pdf/`. (Last Access: 14-04-2019).

[177] A. Marques *et al.*, "RADEM SET Analysis (JUI-EFA-RDM-TN-003 1.1)."